Supramolecular self-assemblies for plasmonics : a bottom-up approach to efficient photonic nanodevices

Sylvain Le Liepvre

université PARIS-SACLAY

NNT : 2017SACLS330

Thèse de doctorat

Supramolecular self-assemblies for plasmonics : a bottom-up approach to efficient photonic nanodevices

Thèse de doctorat de l'Université Paris-Saclay
préparée au CEA Saclay (SPEC)

École doctorale n°572 Ondes et Matière (EDOM)
Spécialité de doctorat: Nanophysique

Thèse présentée et soutenue à Gif-sur-Yvette, le 26 septembre 2017, par

Sylvain Le Liepvre

Composition du Jury :

Jean-Jacques Greffet Professeur, IOGS	Président
Nathalie Katsonis Professeur Associé, University of Twente	Rapporteur
Joël Bellessa Professeur des Universités, Université Lyon 1	Rapporteur
Steven de Feyter Professeur, KU Leuven	Examinateur
Sylvain Barbay Professeur, C2N	Examinateur
Fabrice Charra CEA, SPEC	Directeur de thèse

Université Paris-Saclay
Espace Technologique / Immeuble Discovery
Route de l'Orme aux Merisiers RD 128 / 91190 Saint-Aubin, France

Contents

Remerciements

Après ces trois années passionnantes passées au Laboratoire d'Electronique et de Nanophotonique Organique (LEPO), j'aimerai remercier chaleureusement mon directeur de thèse Fabrice Charra pour sa gentillesse, sa disponibilité, ses observations toujours très pertinentes, son aide en toutes circonstances et sa patience pour expliquer clairement les points les plus obscurs abordés pendant ce travail de thèse.

J'ai été marqué pendant cette période par le cadre très sympathique du laboratoire et je voudrais remercier à ce titre tous les membres permanents de l'équipe qui créent cet environnement de travail si agréable, autant du point de vue humain que scientifique : Céline Fiorini, Ludovic Douillard, Simon Vassant, Bruno Delomez.

Cette expérience n'aurait pas été la même sans les bons moments passés avec les non-permanents de l'équipe : Maud Jaouen pour ses conseils en démontage de STM, Patrick Hsia et sa science cinématographique, Céline Molinaro et les frites bruxelloises, Sarra Mitiche et les fleurets anciens, Farid Kameche et ses théories sur les kebabs, Mohammed Houssat alias Barack Obama, Léa Constans, Alice Six, Morgan Auffray, Anaïs Gouesmel, Kim Nguyen, Tessnim Sghaier, Yasmine Nahas, Nathalya Kalashnyk, Quanbo Jiang, Martin Melgarejo, Bastien Jouy, Sébastien Jean-Louis, Milino Kerowgodage et Paul Bouteyre.

Je tiens à remercier l'équipe du C2N qui m'a accueilli pour quelques semaines d'expériences au sein de leur laboratoire, et avec qui il a été très agréable de collaborer tout au long de cette thèse: Sylvain Barbay, Alejandro Giacomotti, John Bigeon, Ariel Levenson.

Merci à toutes les personnes ayant collaboré aux différents projets de cette thèse, beaucoup de belles discussions scientifiques ou plus générales ont résulté de ces rencontres. Merci à toute l'équipe de l'UPMC : André-Jean Attias, Fabrice Mathevet, David Kreher, Lydia Sosa-Vargas, à Philippe Lang de Jussieu, à Ludovic Tortech, Quentin Arnoux, Sylvie Marguet, Vincent Derycke, Thomas Gustavsson et Valentin Mafféis du CEA Saclay ainsi que Jean-Paul Hugonin de l'IOGS.

Tout ce travail n'aurait pu voir le jour sans le soutien de mes proches. Pour éviter le côté un peu lourd de l'exercice des remerciements, je ne peux m'empêcher de citer le golfeur Greg Norman excellant dans ce registre : "Je dois beaucoup à mes parents, surtout à ma mère et à mon père". Bref merci papa merci maman et merci les frérots d'avoir appris plein de trucs au petit dernier.

Dans la catégorie abnégation, je dois une mention spéciale remerciement à ma femme Elise qui a fait et qui fait toujours l'effort de comprendre des parties de plus en plus vaste de ce travail de thèse, même si les liens avec l'électroménager rénové garanti restent quand même assez ténus.

Toujours grands seigneurs en termes de conseils avisés, constructeurs de l'extrême, aventuriers sans peurs et sans reproches, mais par-dessus-tout, colocs, j'aimerai claquer un tchek reconnaissant aux colocs de l'Hay Simon, Hadrien et Guillaume, et par extension à toute la famille de la dégaine. (Division d'Escalade Giffoise Aérienne Innovante Novatrice et Engagée). Mention spéciale à Goulven pour son caramel. (le plus goutû de tout landerneau !)

J'allume à cette ligne la flamme du copain non cité dans les remerciements, tragique sort pour celui qui a tant œuvré pour me soutenir, me distraire, m'essouffler au cours

de cette thèse, héros de l'ombre à qui les portes de l'immortalité du papier viennent de se fermer subitement. Puisse cette flamme porter ton âme en souvenir aux générations futures.

Sur ce, bouclez vos ceintures, repérez les issues de secours (qui peuvent se situer derrière vous !), PNC aux portes, on va décoller !

"Progress is the realisation of Utopias."
- Oscar Wilde

A Elise

Introduction

"There's plenty of room at the bottom". Here are the words of Richard Feynman at an American Physical Society meeting at Caltech in 1959, describing its vision of a technology working at the ultimate atom scale. This landmark can be considered as the beginning of the nanotechnology field which is devoted to the study and the manufacture of structures ranging in size from 1 to 1000 nm. The development of powerful tools such as the scanning tunneling microscope (STM),[1] the atomic force microscope (AFM)[2] and other scanning probe microscopes[3] in the 80s have fostered research at the nanoscale giving means to observe and manipulate systems as small as individual atoms.[4]

Furthermore, the discovery of low-dimensional materials such as fullerene,[5] carbon nanotubes,[6,7] graphene,[8] single layer boron nitride[9] has revealed the potential of nanotechnology for a vast number of fields such as energy (solar cells,[10] fuel cells,[11] batteries[12]), information and communications (transistors,[13] transparent conducting electrodes,[14] optoelectronics[15]), medicine (tissue engineering,[16] bioimaging,[17] drug delivery[18]), environment (contamination removal,[19] pressure sensors,[20] molecular sensor[21]). However, the nanotechnology era is just beginning and important progresses have to be made aiming at the design of matter at the nanoscale and at the development of practical applications in most of the fields mentioned above.

Two strategies can be mentioned when trying to miniaturize existing systems. The top-down approach pushes the limits of existing tools such as UV lithography or etching techniques to form smaller systems. This strategy is for example used by the semiconductor industry to scale the size of transistors down to $\sim$ 10 nm today.[22]

On the other side, the bottom-up approach is an additive technology using small building blocks such as molecules or atoms to create complex nanoscale systems. Supramolecular self-assembly is one of the most advanced techniques able to generate periodically-replicated well-ordered molecular architectures with well-controlled geometry. By chemical design of molecular building blocks, their molecular recognition abilities can be finely tuned so as to spontaneously arrange themselves, forming pre-programmed 1D, 2D or 3D supramolecular architectures.[23,24,25]

Various molecular-recognition processes are at the origin of the self-assembly architecture, from steric hindrance[26] to hydrogen bonding,[27] metal coordination[28] or interdigitation of alkyl chains.[29,30,31]

The fabrication of such systems is simple and does not require complex tools unlike top-down approaches. The formation of molecular self-assemblies can easily be obtained by drop casting or by dip coating techniques, which essentially consists in evaporating a solution containing the molecular building blocks on a targeted substrate. The self-assembly processes can also take place with molecules deposited in ultra-high vacuum environments using molecular beam epitaxy techniques to gain control over the formation of the supramolecular self-assembly.

Plasmonics exploits collective oscillation of electrons in metallic structures to confine optical fields on dimensions much below their wavelength. This offers unique opportunities for subwavelength optical waveguiding and enhancements of light-matter interactions through intense local fields and optical antennas.[32] Nanoplasmonics has made major

advances thanks to recent developments in nanoscale manufacturing techniques. The possible applications of this field in full development cover wide segments of technology: spectroscopy,[33] nanophotonics,[34,35] biological sensors,[36,37] imaging,[38] cancer treatment.[39]

In recent years, the physics and applications of plasmonic waves interacting with quantum emitters became a hot topic.[40] In particular, the coupling between a highly confined plasmonic waveguide and an optical gain medium attracted much attention since the prospect of overcoming propagation losses paves the ways to the development of photonic integrated circuits with subwavelength scale working at optical frequencies.[41] Furthermore, a robust active plasmonics device would find applications in the realization of photovoltaic cells and light-emitting diodes,[42] biomedical sensors, fluorescent labels and light-triggered actuators.[43]

Various gain media have been used to demonstrate Surface Plasmon Amplification by Stimulated Emission of Radiation (SPASER) such as semiconductors[44] or π-conjugated molecules dispersed in a polymer matrix.[45]

It has been shown that the distance and the orientation between the fluorophores and the metal surface plays a crucial role on the coupling between the gain medium and the plasmon mode.[46] At small distances, Dexter electron exchange quenching of emitter fluorescence is preponderant and overcompensates plasmonic enhancements. Moreover, the plasmon mode electric field is mainly perpendicular to the metal surface and thus interacts more strongly with emitters displaying the same orientation. Therefore, a gain of control over the hybrid plasmonic-emitter system structure, especially in the positioning of the emitter relatively to the metal surface could lead to a neat increase of the efficiency of such active plasmonics devices. Finally, the important spatial confinement of the plasmonic mode electromagnetic field requires a high density of photoactive species in the gain medium to increase the number of emitter interacting with the electromagnetic mode.

Supramolecular self-assembly offers the flexibility to finely tune molecular scale positioning on a targeted substrate through the chemical design of the molecular building blocks. the concept of Janus-like 3D molecular tectons introduced few years ago[47] could be used to reduce the Dexter quenching of self-assembled π-conjugated molecules on a metallic surface. In these systems, molecular building blocks display a dual-functionalization at two opposite faces linked by a rigid insulating spacer: a pedestal manages the 2D self-assembly on the substrate whereas a dye group provides the photonic functionality. Therefore, the lateral organization of the self-assembly array is maintained while lifting photoactive entities by a few angströms above the substrate surface thanks to the spacer group. Such Janus tecton approach paves the way for the precise distance and orientation positioning of a photoactive entity with reference to a substrate surface, potentially a plasmonic waveguiding surface. Furthermore, very high molecular volume or areal densities can be reached in supramolecular self-assemblies. Such hybrid systems would significantly increase the number of emitters interacting with a confined plasmonic mode.

However, the aggregation of dyes strongly affects their photonics properties. Intermolecular interactions lead to increasing or decreasing radiative recombination rates as well as frequency shifts in the absorption and fluorescence spectrum, depending on constructive or destructive intermolecular interactions. Experimental and theoretical work have to be done to determine how do supramolecular self-assemblies tune the photonics properties of an active layer through the precise design of intermolecular orientation and positioning.

In this work, we study the photonic properties of self-assembled molecular monolayers on graphene by correlating the self-assembly structure as deduced from scanning tunneling and atomic force microscopies to photonic properties as analyzed by optical spectroscopy measurements. We demonstrate the strong-coupling regime between a 3D molecular self-assembly and a propagating plasmon polariton mode, and show that the optical gain in

such dense optically active systems saturates at high excitation rate.

- In chapter 1, we study the optical absorption of perylene derivative self-assembled monolayers on graphene and explore the effect of intermolecular and molecule-graphene interaction on the absorption spectrum of such hybrid systems. An example of a three-dimensional perylene self-assembly optimized for interacting with propagating plasmon polariton is also demonstrated.

- Chapter 2 deals with fluorescence of molecular self-assemblies on graphene. The first fluorescent non-covalent functionalization of graphene by a supramolecular self-assembled monolayer is demonstrated using a Janus tecton approach. The fluorescence signals of three-dimensional supramolecular self-assemblies suitable for interacting with propagating plasmon polaritons are studied.

- Vibrational properties of self-assembled monolayers on graphene are explored in chapter 3. We show the appearance of a coupled vibrational mode between adsorbed molecules and graphene.

- In chapter 4, we study how to engineer plasmonic modes to reduce losses in the metal. We demonstrate an approach to design plasmonics resonators with high quality factors.

- Strong-coupling between a three-dimensional self-assembly and a propagating plasmon polariton mode is demonstrated in chapter 5. The photonics properties of such a system are studied through its absorption and emission responses.

- Finally, chapter 6 presents the conditions for amplifying plasmonic systems by comparing traditional gain media to molecular self-assemblies. The gain limitation of molecular self-assembly systems is studied, and important losses due to exciton-exciton recombination are evidenced.

  These chapters relate research projects carried out in collaboration with other teams without whom this work would not have been possible. André-Jean Attias group (UPMC) worked on designing and synthetizing spontaneously assembling molecules at the graphene surface (chapters 1 and 2), Matthew Williams and David Andrews (Univ. East Anglia) performed DFT calculations to compute Raman spectra in chapter 3, John Bigeon and Sylvain Barbay (C2N) carried out numerical calculations and experimental characterizations of the plasmonic systems in chapter 5, Valentin Mafféis and Thomas Gustavssonn performed time resolved fluorescent spectra on PTCDI thin films in chapter 6, Philippe Lang (ITODYS) performed IR experiments (Appendix B), Yannick Dappe (CEA/SPEC) performed DFT calculations to compute the density of states (DOS) of adsorbed molecules on graphene (Appendix B), Ludovic Tortech (CEA/NIMBE) was of a precious help for the realization of self-assembled thin films by its advice and the lending of its equipment (chapters 1-3 ,5 and 6).

Chapter 1

Supramolecular self-assemblies and optical absorption

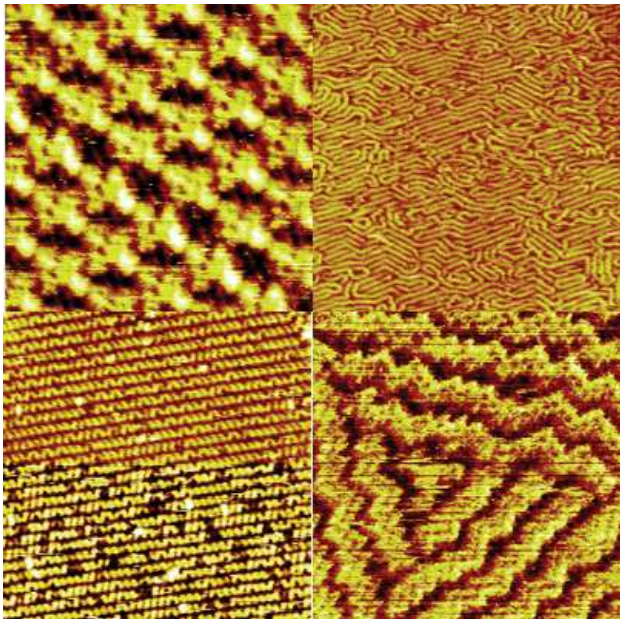

Supramolecular self-assemblies on highly ordered pyrolitic graphite (HOPG) probed by a scanning tunneling microscope (STM). The presence of molecules is indicated by the yellow color in the STM image. Self-assembled molecules: TBC8 (top left, 11 nm x 11 nm), TBC8-JT (bottom left, 100 nm x 100 nm), P3HT (top right, 65 nm x 65 nm), PTCDI-2C6a (bottom right, 45 nm x 45 nm).

Exotic molecular network patterns such as those displayed above can be drawn on various surfaces by designing carefully the structure of molecules that will form the self-assembly. When this system consists of self-assembled dye molecules, what color does it have? Would it be possible to engineer the color of self-assemblies by changing the geometrical parameters of the 2D molecular network?

Close-packed assemblies of dye molecules exhibit drastically altered photonic properties as compared with the isolated or diluted species.[48] These changes find their origin in near-field optical interactions between the constituent molecules, as early predicted by McRay and Kasha.[49] A well-known example is the spectral shift induced by the self-association of cyanine dyes in solution.[50] Depending on the aggregation pattern of the dyes, either bathochromically shifted J-bands or hypsochromically shifted H-bands are formed, corresponding to collectively excited states and energy bands of delocalized excitons.[51,52]

The giant transition dipole moments associated with such excitations result in enhanced optical interactions, e.g., with plasmon resonators in which case a strong-coupling regime can then be reached.[53,54] These collective excitations can also lead to remarkable light emission processes such as superradiance.[55]

Interactions between a dye and its surroundings at the molecular scale may also induce drastic changes in its photonic properties. Structural planarization of the adsorbed molecules,[56] or the immersion inside a polarizable medium[57] can induce uniform bathochromic shifts of the vibronic bands constituting the absorption spectrum.

Finally, when distances between π-conjugated systems are small enough to permit electron tunneling, quantum effects can also come into the play, at the origin, for instance, of new intermolecular charge-transfer absorption bands.[58,59]

Consequently, the fine tuning of molecular-scale organization of condensed dye assemblies appears critical for the control of photonic properties of matter and possibly for the generation of original photonic processes.

An atomically precise positioning of self-associated molecular dyes can be achieved either in vacuum or at the solution–substrate interface by self-assembly techniques.

A high level of control of the self-assembly geometry is possible by exploiting the interactions between alkyl side chains and the surface of highly oriented pyrolytic graphite (HOPG),[60] beyond H-bond-steered organizations.[61] Based on these principles, it has been possible to design molecular building blocks that arrange spontaneously according to various predetermined patterns.[31]

Graphene has focused intensive research in the past 10 years due to its unusually high electron mobility, atomic thickness, broadband optical absorption, and unique flexibility.[62,63,64,8] CVD-grown graphene, being easily transferable onto arbitrary substrates while preserving high electronic mobilities,[65] soon appeared as a tantalizing candidate for various applications in photonics,[15] such as solar cells,[66] high-speed photodetectors,[67] light sources,[68] ultrafast lasers,[69] and metamaterials.[70] However, as a zero-band-gap semimetal, pristine graphene has a narrow range of roles, merely limited to transparent electrodes. Advanced applications require graphene to be synergistically combined with nanomaterials providing complementary properties.

Recently, noncovalent functionalization of graphene with organic molecular building blocks has appeared as a promising way to modulate its properties in view of functional applications. Actually, graphene provides an atomic-scale crystallographic lattice acting as a template guiding supramolecular self-assembly.[71] This bottom-up elaboration process, which implies the physisorption onto graphene of mostly planar molecules (tectons), is now well mastered in view of electronic applications. For example, supramolecular self-assembly on chemical vapor deposition (CVD)-grown graphene was used to dope graphene, and back-gated graphene field-effect transistor (G-FET) devices were obtained.[72]

Surprisingly, by comparison with electronics, the noncovalent functionalization of graphene is still in its infancy as concerns applications in photonics. Yet, organic dyes offer a high flexibility in the design of innovative photonic devices. Actually, because of their high oscillator strengths, they can play the role of light harvesters, photon sources, exciton funnels, etc., and as such should provide opportunities to enhance or extend the properties of graphene toward light-based applications.

Molecular self-assembly techniques on HOPG substrates can be extended to monolayer CVD graphene as a substrate,[73] which offers optical transparency when transferred from its native CVD substrate usually copper– onto a transparent one such as quartz or polyethylene terephthalate (PET). This offers opportunities for advanced optical characterizations in a transmission geometry, such as polarized variable-incidence transmission spectroscopy. In addition, the electrical conductivity of a CVD graphene monolayer is sufficiently high to apply scanning tunneling microscopy (STM) and thus determine the structural data of the molecular assembly with atomic-scale accuracy.

Self-assembly of adsorbed conjugated molecules can influence the electronic properties of its substrate. Such a non covalent functionalization is especially suitable in the case of graphene because of its "surface only" nature[74,75] and has been applied to tailor its band structure[76] or its work function[77,78] with a monolayer of PTCDI and similar molecules, which can be laterally patterned[79] or even manipulated at the single-molecule level.[80]

Through the combination of optical characterizations and structural control of dye assemblies on CVD graphene, detailed studies about the influence of the dye organization on photonic properties become feasible.

In the following, we explore how the optical absorption spectrum of a dye can be changed once self-assembled on a surface or on a three dimensional network.

1.1 PTCDI on graphene

Perylene-3,4,9,10 tetracarboxylic-3,4,9,10-diimide (PTCDI) and its sibling molecule perylene-3,4,9,10-tetracarboxylic dianhydride (PTCDA) have become archetypes for photonic applications of dyes,[81] for self-organized adsorption on various atomically flat surfaces,[82] and for their combination. Indeed, optical differential reflectance spectroscopy,[83] photoluminescence, or Raman diffraction studies have evidenced optical responses attributed to strong interactions of PTCDA with metal[84,85] or semiconductor[86] substrates and between neighboring molecules when deposited on a dielectric substrate[87,88] or in multilayer structures.[89] The optical effects of interactions between close-packed PTCDA molecules deposited on epitaxial graphene have also been observed.[90]

1.1.1 Scanning tunneling microscopy.

The self-assembly was probed on two graphitic substrates, highly oriented pyrolytic graphite (HOPG) and monolayers of CVD graphene transferred either onto fused silica ("optical quartz") or PET. The resolution of carbon atoms is easily obtained on both systems. On CVD graphene samples, an additional moderate roughness is observed, which is attributed to the substrate (Figure 1.1). For example, in the case of graphene transferred onto a fused silica plate, this roughness attains 0.5 nm over distances of approximately 50 nm (Figure 1.1).

The PTCDI molecule has become a paradigm both as a self-assembly tecton and as a dye. For the present study, we chose an alkylated form of this dye, $N,N\prime-ditridecylperylene-3,4,9,10-tetracarboxylicdiimide$ (PTCDI-C13), forming a spontaneously self-assembled monolayer at the interface between the solution and graphene. The monolayer structures have been studied by STM at the solution–substrate interface.

Figure 1.2 displays STM images of PTCDI-C13 monolayers on HOPG, on as-grown CVD graphene monolayer on copper foil and CVD graphene monolayer transferred onto PET. The STM technique favors the signature of aromatic skeletons which present higher electronic surface density of states close to the Fermi level.[91]

Intramolecular resolution is possible both with HOPG and graphene as substrates (Figure 1.2).

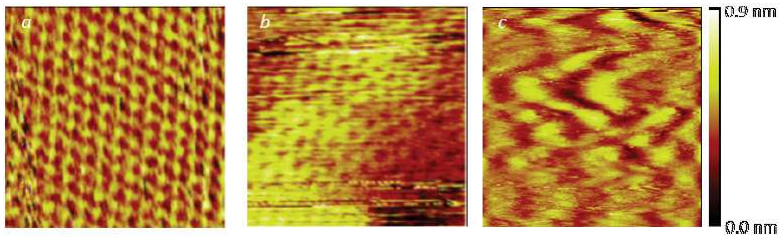

Figure 1.1: Structural characterization of the substrates. STM images ($2.3 \times 2.3nm^2$) of a HOPG surface (a) and CVD monolayer graphene transferred onto a fused quartz plate (b: $2.3 \times 2.3nm^2$ and c: $50 \times 50nm^2$). The images were acquired under air atmosphere, in the height (constant current) mode. The setpoint current was $I_S = 100pA$, and the bias was $V_T = 200mV$. The height scale is also shown for graphene on quartz (c).

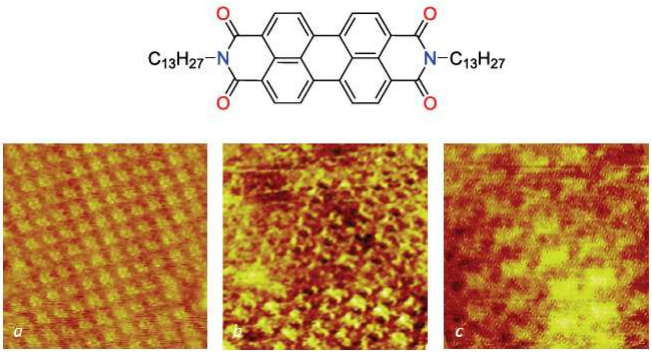

Figure 1.2: Structural characterization of the self-assembled PTCDI monolayers. Molecular formula of PTCDI-C13 and STM images of self-assembled monolayers on HOPG (a: $14 \times 14nm^2$) as-grown CVD monolayer graphene on copper foil (b: $11 \times 11nm^2$) and CVD graphene monolayer transferred onto a PET plate (c: $8 \times 8nm^2$). The typical current setpoint and sample bias were 10 pA and 800 mV, respectively. The images were acquired at the interface between the substrate and a ca. $10^{-5}M$ solution in phenyloctane at room temperature.

As expected from the atomically flat surface of HOPG, this substrate produces the largest domains. It permits an accurate determination of the lattice parameters, which correspond to a surface density of 0.45 molecules per nm^2 and a distance between closest neighbors of ca. 1.4 nm. The network obtained on CVD graphene is compatible with that obtained on HOPG, with one molecule per unit cell. The various domains have a finite number of lattice orientations, indicating an epitaxial relationship with the graphitic lattice. These results are fully consistent with the expected formation of a self-assembled monolayer in which the molecules are lying flat on the substrate, with n-alkyl chains standing away from the graphene surface due to steric constrains of oxygen atoms.[92]

By randomly inspecting various regions of drop-cast samples, it appears that a nearly complete coverage (about 80%–90%) is obtained whereas the droplet spread on the sample contained the exact quantity of molecules needed to form a monolayer. The formation of a second layer is avoided by the presence of alkyl chains standing away from the surface that act as a buffer layer.

1.1.2 PTCDI-C13 Transmission spectra.

The solution spectrum of PTCDI-C13 is reported in Figure 1.3 (labelled "SOL"). It presents a typical vibronic signature of a π–π^* transition. Vibronic transitions, involv-

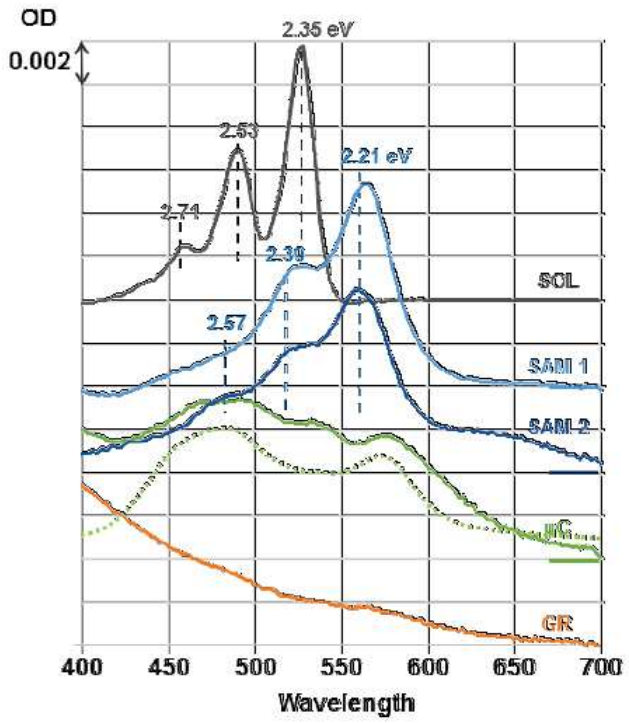

Figure 1.3: Normal incidence transmission spectra T, expressed as an optical density $DO = -log(\frac{T}{T0})$. SOL: a $10^{-6}M$ solution of PTCDI in toluene, cell thickness: 2 mm (black curve). SAM1 and SAM2: two self-organized PTCDI-C13 monolayers on graphite, formed following two methods: drop casting (light blue, SAM1) or dip coating (dark blue, SAM2). μC: 10 equivalent monolayers of PTCDI-C13 deposited by solvent evaporation on a fused-quartz substrate, that is without CVD graphene (green curve) and PTCDI-C13 microcrystalline thin film (dotted green curve) reproduced after Mizuguchi et al.[96] and rescaled for easier comparison. GR: monolayer CVD graphene transferred onto a fused-quartz plate (orange curve). All spectra are referenced (T0) to their corresponding naked substrate (GR for SAM1 and SAM2, quartz plate for μC and GR) or pure solvent (SOL). The energies of the 0-0, 0-1 and 0-2 vibronic bands are indicated for solution and monolayer spectra.

ing a change in both electronic and vibrational energy, can here be understood in the Franck-Condon approximation: electronic transitions are most likely to occur without changes in the positions of the nuclei in the molecular entity and its environment. As a consequence, the intensity of a vibronic transition is proportional to the square of the overlap integral between the vibrational wavefunctions of the two states that are involved in the transition.[93] Bands in the absorption spectrum are then attributed to electronic vertical transitions from the ground vibrational state of the PTCDI-C13 highest occupied molecular orbital (HOMO) to the 0, 1 and 2 vibrational states of the lowest unoccupied molecular orbital (LUMO). The observed 0.18 eV (1450 cm^{-1}) energy difference between 0-0, 0-1 and 0-2 sub-bands is characteristic from π-conjugated systems as present in the PTCDI core where p orbitals of neighbor carbon atoms overlaps.[94]

The main band is the 0–0 at 2.35 eV and corresponds to an absorption cross section $\sigma_{SOL} = 3.3 \times 10^{-16}\ cm^2$ consistent with the molar attenuation coefficient reported in the literature for alkylated PTCDI.[95] Quantum chemical calculations have shown that the transition dipole moment corresponding to the π–π^* transition is aligned along the N–N'-axis.[94]

The difference transmission spectra between self-assembled monolayer on a substrate of monolayer CVD graphene transferred onto fused quartz are shown in Figure 1.3. Two types of depositions are reported: (i) drop casting of a droplet of a toluene solution containing the exact amount of molecules needed for a coverage of 0.45 molecule per nm^2 (SAM 1) and (ii) dipcoating in a ca. $10^{-5}M$ solution in toluene followed by rinsing in toluene and ethanol (SAM 2).

The transmission spectra of SAM1 and SAM2 are nearly identical and correspond to a bathochromic shift of 0.14 eV (1130 cm^{-1}) of the whole vibronic system. This quantitative similarity further supports the homogeneous formation of one monolayer by dip coating, as was shown in the case of drop casting. At the maximum of the 0-0 absorption band, shifted to 2.21 eV, the relative transmission $\frac{\Delta T}{T}$ is ca. 2.1% (SAM1) and ca. 1.9% (SAM2).

For an absorbing monolayer deposited on a lossless dielectric substrate, the relative transmission depends only on the absorptive part of the molecular optical response.[97] Given the molecule surface density of 0.45 molecule per nm^2 measured by STM, the molecular absorption cross section can be thus evaluated to $\sigma_{ML} = 4.5 \times 10^{-16}\ cm^2$. By assuming an in-plane orientation of the N–N'-axis, which gives a factor of 3/2 corresponding to a 2D orientational averaging of the transition dipole moments instead of the 3D averaging in solution, the above value is fully consistent with that obtained in solution ($3.3 \times 10^{-16}\ cm^2$). Notice that accounting for the Lorentz local field correction to σ_{SOL}, $[\frac{n^2+1}{3}^2 \frac{1}{n}$ with n being the index of refraction of toluene, and for the substrate-index correction to σ_{ML}, $\frac{n+1}{2}$ with n being the index of the substrate,[97] does not change this conclusion (ca. 1.33 and ca. 1.25, respectively).

Microspectroscopy sampling of the sample, averaged over a spot of about $3\mu m$ in diameter have shown a high homogeneity of the absorption in the range of millimeters. Remarkably, in the absence of graphene coverage on the fused quartz substrate prior to PTCDI-C13 deposition, completely different transmission spectra are observed. Actually, no measurable absorption is recorded after using the dip coating technique and the spectrum observed for drop casting is very similar to the one reported in the literature for PTCDI microcrystalline films[96] (μC, solid and dotted lines). Moreover, microspectroscopy has shown a high inhomogeneity of the absorption strength, whereas the measured spectra acquired at different places remain homothetic.

Finally, we have measured the dependence on the incidence angle of the PTCDI absorption spectral feature in the polarized absorption for SAM1 and SAM2 samples (Figure 1.4). Whereas the absorption increases with incidence for TE polarization (blue triangles in Figure 1.4), it decreases monotonically with increasing incidence for TM polarization (red squares). In both cases, the molecule spectrum changes homothetically, that is preserving the balance between vibronic bands. These observations confirm that the orientations of the transition dipole moments of the molecule are parallel to the substrate surface (graphene layer), as shown by the theoretical model[98] (continuous lines). This can be easily seen at grazing incidence where the TM polarized incident electric field is almost perpendicular to the surface, and therefore can't be absorbed by optical dipoles parallel to the surface. This effect is even visible to the naked eye looking through a tilted plate through a polarizer. Notice that, for a thin film with random 3D molecule orientation, both TE and TM polarizations should exhibit an increased absorption at grazing incidence because the number of molecules illuminated by the incident beam increases.

The quantitative spectral analysis shows that the characteristic optical absorptions of drop-cast (SAM1) and dip-coated (SAM2) samples result from a homogeneous assembly of flat lying molecules with a surface density equivalent to one monolayer. Together with STM observations, this permits to unambiguously assign the spectral features observed at 2.21, 2.35 and 2.57 eV to the absorption of the PTCDI-C13 monolayer self-assembled onto the graphene substrate with a planar geometry of the molecules.

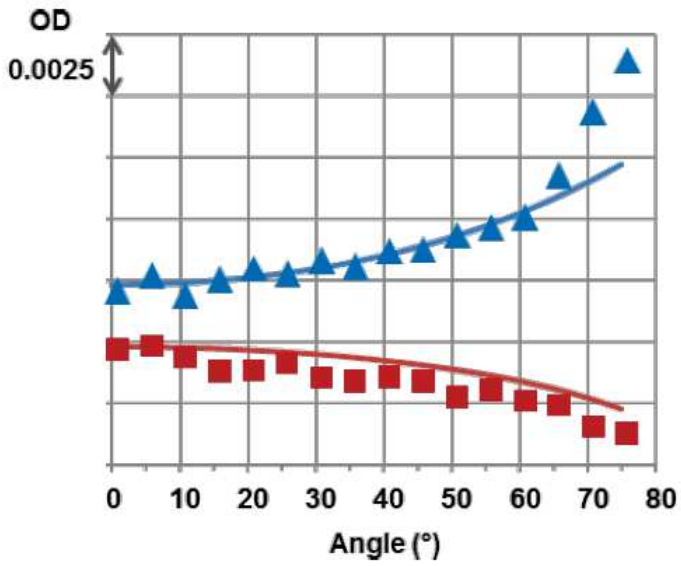

Figure 1.4: Optical signature of orientations of self-organized PTCDI-C13. Variable-incidence polarized-transmission analysis of the contribution of the self-assembled molecular monolayer to the absorption (blue triangle: TE, red squares: TM). The optical density at the absorption maximum ($\lambda = 561nm$), as obtained from a fit of the absorption line of the molecule, is plotted. The continuous lines represent the TE and TM theoretical absorption variations[98] considering molecular transition dipole moments lying flat on graphene. For randomly oriented transition dipole moments, both TE and TM should increase with incidence following the blue line.

The most striking feature of the self-assembled monolayer spectra is the uniform red-shift of the whole vibronic spectral line, which results from the self-assembly. This shift is not accompanied by an important blurring of the spectral structures, consistent with the high homogeneity of molecular organization and environments obtained through the atomically precise self-assembly process on graphene. The energy difference between 0–0, 0–1 and 0–2 sub-bands is preserved, at 0.18 eV. This value is characteristic of the π-conjugated C–C double bond vibration and shows that the absorption remains dominated by the π–$\pi*$ transition.

2D ordered aggregation of similar molecules on metals have been reported to induced drastic changes in optical spectra, attributed to new electronic transitions.[85] Less pronounced rigid spectral shifts have been reported previously for molecules deposited on crystalline dielectrics such as hexagonal boron nitride (h-BN).[56,88] The cited possible origins of such shifts are optical interactions between molecules or between molecules and the substrate and the deformation of molecules induced by van der Waals interactions between molecules and substrate.

1.2 Intermolecular interactions

Intermolecular optical interactions are a consequence of the local electric field resulting from the induced dipoles of molecules at neighboring sites.[99] The Coulomb interaction between close molecules can result in the creation of a Frenkel exciton, a bound electron-hole pair whose hole is localized at the molecule position.

Intermolecular distances in self-assembled systems are typically on the order of a nanometer. Thus, the retarded field can be neglected in the following and all calculations are performed in the quasi-static regime.

The field emitted by a dipole $\overline{d}$ at a distance $\overline{r}(r,\theta)$ is:

$$\overline{\mathbf{E}}(r,\theta) = \frac{1}{4\pi\epsilon r^3}(3(\overline{d}.\overline{u})\overline{u} - \overline{d}) \tag{1.1}$$

The dipole moment μ for a molecule at a certain frequency ω is related to the excitation local electric field through the polarizability α.

$$\mu(\omega) = \alpha(\omega)E_{loc}(\omega) \tag{1.2}$$

Since the incident electric field drives the molecular oscillator, all dipole moments in a molecular assembly are coherent in presence of an excitation field, in contrast to the case where molecules fluoresce.

In the following, molecules are considered identical and unidimensional. Therefore, the polarizability tensor has only one coefficient. It is possible to model in a classical picture (not quantum) the polarizability of the lone molecule applying Newton's law to the electron cloud of mass m and charge q represented by its barycenter at position x:

$$m\frac{d^2x}{dt^2} = \overline{F}_{Elocal} + \overline{F}_{tension} + \overline{F}_{damping} \tag{1.3}$$

The first term represents the Coulombic interaction with the incident electric field, the second term represents the Coulomb force between the electron cloud and the molecule nuclei (spring force or Hooke's law) that builds the electronic resonance, the third term represents oscillator losses from which results the quality factor of the resonance. Considering a sinewave excitation at frequency ω, the above expression can be rewritten:

$$-\omega^2 mx = qE_{local} - k(x - x_0) + i\gamma_0\omega x \tag{1.4}$$

Multiplying the two parts of equation 1.4 by the charge q, dividing by the mass m and replacing the dipole moment by its expression $\mu = qx$, we can write:

$$-\omega^2\mu + \omega_0\mu - i\gamma\omega\mu = \frac{q^2E_{local}}{m} \tag{1.5}$$

The theoretical expression of the polarizability can then be written:

$$\alpha(\omega) = \frac{q^2/m}{\omega_0^2 - \omega^2 - i\gamma\omega} \tag{1.6}$$

At resonance, the real part of the polarizability is zero. The imaginary part of the polarizability can be evaluated through the absorption cross-section σ from:

$$\sigma = \frac{Im(\alpha_0)\omega_0}{3\epsilon_0 c} \tag{1.7}$$

It is experimentally determined by a molar absorptivity ϵ ($L \times mol^{-1} \times cm^{-1}$) measurement through:

$$\sigma = 1000ln(10)\frac{\epsilon}{N_A} = \epsilon \times 3.82 \times 10^{-21}\ cm^2 \tag{1.8}$$

Where N_A is the Avogadro number, ω_0 is the resonant frequency, and c the speed of light.

We plot in figure 1.5 the electric field emitted by a perylene dye as a function of the distance from this dye in vacuum ($n = 1$). We use the PTCDI molar absorptivity to compute the polarizability ($\epsilon = 87000\ Lmol^{-1}cm^{-1}$). We compare these values to the incident electric field of a linearly polarized plane wave created by a continuous-wave (CW) laser at the PTCDI resonance wavelength (530 nm). In microscopy experiments, it

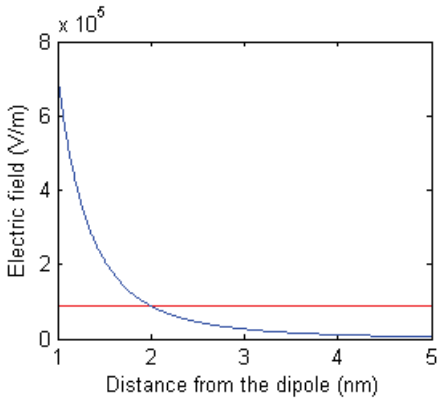

Figure 1.5: Electric field emitted by a perylene dye (blue curve) in the quasi-static limit and electric field of a plane wave created by a laser beam (10 $\mu W.\mu m^{-2}$) (red curve)

is common to focus a 10 μW beam onto a 1 μm^2 surface. The typical irradiance (energy flux) of such plane wave can be written as:

$$I = \frac{n\epsilon_0 c}{2} E^2 \tag{1.9}$$

Far from the dipole, the field emitted by the dipole is negligible in comparison to the exciting laser field. Close to the dipole, the dipole field becomes predominant. The characteristic length delimiting these two regime is a few nanometers, as shown in figure 1.5. This characteristic length does not depend on the amplitude of the incident electric field since the field emitted by the dye at a certain distance is proportional to the incident electric field.

The local electric field is the sum of the incident electric field and the field re-emitted from the molecules, i.e. the field experienced by a given molecule in the assembly. We introduce a geometrical parameter k which accounts for the distance and the orientation between neighboring dipoles.

$$E_{loc}(\omega) = E_{inc}(\omega) + k\mu_(\omega) \tag{1.10}$$

The combination of equations 1.2 and 1.10 gives a new expression for the dipole moment of the molecule as function as the incident electric field rather than the local one.

$$\mu_(\omega) = \frac{\alpha(\omega)}{1 - k\alpha(\omega)} E_{inc}(\omega) \tag{1.11}$$

One can then introduce from equation 1.11 an effective polarizability $\alpha_p(\omega)$:

$$\alpha_p(\omega) = \frac{\alpha(\omega)}{1 - k\alpha(\omega)} \tag{1.12}$$

To get insight about the effective polarizability, we consider two identical molecules with parallel dipole moment spaced by a distance r and with an angle θ between the dipole moment axis of one molecule and the line joining the two molecules. The k geometrical factor is:

$$k = \frac{1}{4\pi\varepsilon r^3}(3cos^2(\theta) - 1) \tag{1.13}$$

The k factor can be positive if $\theta = 0$ (dipoles are aligned) or negative if $\theta = \frac{\pi}{2}$ (dipoles are parallel, sideways).

Using the expression of the polarizability developed in equation 1.6, the effective polarizability can be rewritten as:

$$\alpha_p(\omega) = \frac{q^2/m}{\omega_0^2 - \frac{kq^2}{m} - \omega^2 - i\gamma\omega} \tag{1.14}$$

Figure 1.6 displays the k geometrical factor in SI units computed for several geometries of interacting PTCDI and associated imaginary part of the effective polarizability deduced from the geometrical factor k and a fit to the polarizability of isolated PTCDI diluted in a toluene solution as described in equation 1.14.

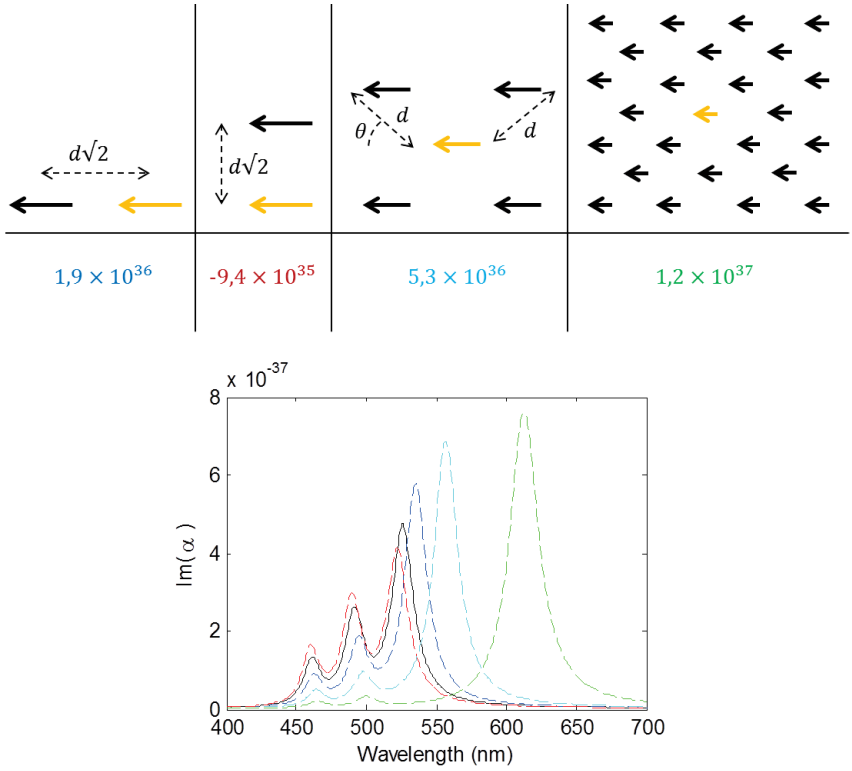

Figure 1.6: Top. Interacting dipoles geometry and associated geometrical factor k in SI units. To model the PTCDI network on graphene, $d = 1.5\ nm$ and $\theta = 45°$.[92] Bottom. Imaginary part of the polarizability for isolated PTCDI when diluted in a toluene solution (black, fit to the experimental data), computed effective polarizabilities for geometrical parameters (SI units) : 1.9×10^{36} (blue), -9.4×10^{35} (red), 5.3×10^{36} (cyan), 1.2×10^{37} (green).

A negative k constant (alongside parallel dipole configuration) produces a blue shift and a lowering of the peak absorption. A positive k constant (aligned dipoles configuration or PTCDI 2D network configuration) results in the red shift and an increase of the peak absorption. This classical theoretical description is sufficient to retrieve the behavior of H/J aggregates of the Kasha model.[52] The frequency shift is computed to be $80\ THz = 325\ meV$ when considering an important number of neighbors participating in the perturbation of the local electric field.

For an assembly of PTCDI-C13 in free space ($n = 1$), the relative change in local electric field can be analytically expressed as:

$$\frac{\Delta E}{E} = \frac{K}{4\pi}\frac{\sigma\lambda}{r^3} \tag{1.15}$$

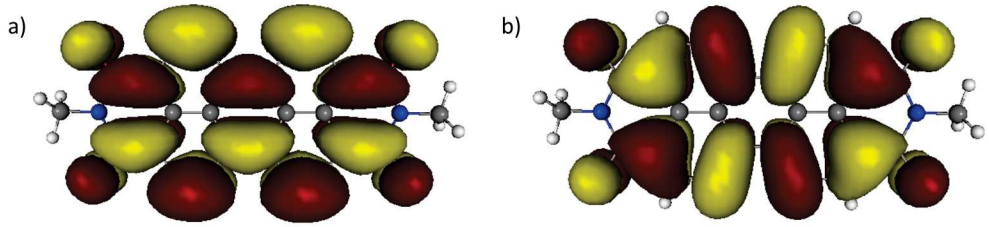

Figure 1.7: LUMO (a) and HOMO (b) of PTCDI-C1. The relaxed geometry has been calculated with the constraint DFT at the B3LYP/TZ level. Reproduced from U. Heinemeyer et al.[100]

where σ is the absorption cross-section ($3.3\times10^{-16}cm^2$), λ the excitation wavelength in vacuum (ca. 0.5 μm), r the distance between molecules (1.4 nm), and K a factor typically of the order of unity. This change in the local electric field in the case of self-assembled PTCDI-C13 is about 50%, which would be more than sufficient to explain the large red shift in the absorption spectrum observed experimentally.

However, this theoretical model does not explain the PTCDI vibronic replicas global band redshift nor oscillator strength redistribution observed experimentally. A perturbation Hamiltonian could then be used to describe electromagnetic interactions between dyes displaying virbonic replicas to predict more accurately both the shift and the oscillator strength of PTCDI vibronic replicas by considering multiple-particle states.[52]

A refined model taking into account non perturbative and high order multipolar interactions between charges, and the simultaneous interaction with several molecules of the 2D network is developed in the following section to attempt to reduce the mismatch between the predicted theoretical and experimental frequency shift.

1.2.1 Non pertubative multipolar 2D model

Figure 2.1 represents the wavefunction of the HOMO and LUMO states of a perylene derivative, PTCDI-C1.[100] The transition dipole moment is computed by taking the product of the LUMO and HOMO wavefunctions. As displayed in the figure, charges participating in the dye-light interaction are delocalized over the whole aromatic core of the dye molecule.

The distance between the two extreme nitrogen atoms of PTCDI is 1.2 nm and roughly corresponds to the delocalization length of charges through the aromatic core of the molecule. Since self-assembled PTCDI-C13 on graphene are approximately 0.3 nm apart, the dipole approximation that holds for computing electric fields far from an emitting dipole can't be used.

To develop a simpler classical model to predict the frequency shift of interacting self-assembled dyes, charges representing the transition dipole moment between S0 and S1 singlet states will be considered to be localized at the extremities of the dye conjugated parts. In the following, they are assumed to be 1.2 nm apart, which correspond to the N-N distance in the PTCDI-C13 molecule. This hypothesis is consistent with the Kekule approach where charges appear at the extremity of the sp^2 conjugated orbitals. This consideration is also consistent with longer conjugation length in dye molecules shifting resonances to the red. The problem is solved in the quasistatic regime since distances are far smaller than the wavelength. Typically, the electric field is computed in a $5\ nm\times5\ nm$ spatial window.

From a spatial charge distribution deduced from a scanning tunneling experiment we can compute the electric field at every point of the molecular network. We then compare the local electric field between the two opposite charges representing the molecular dipole

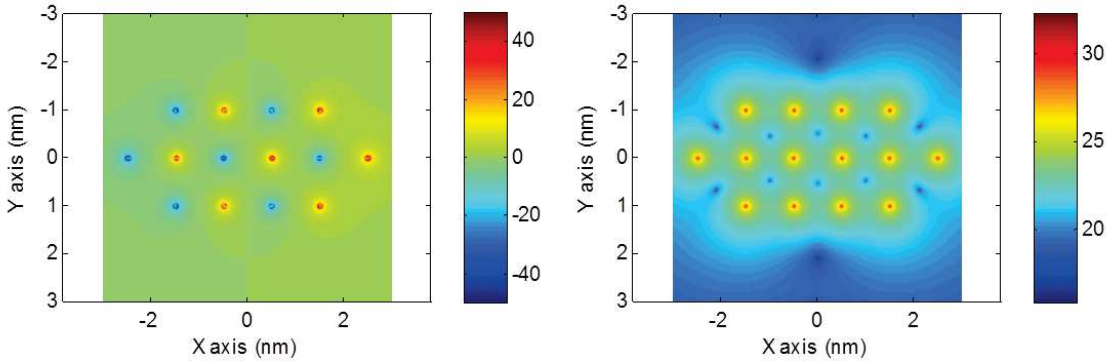

Figure 1.8: Left. 2D charge potential network deduced from PTCDI-C13 on graphene network. Right. Resulting absolute electric field (log scale).

between a lone molecule and an assembly of close molecules. This comparison allows a derivation of the change in the oscillator frequency between the lone molecules and the assembled molecules situations.

$$\frac{\omega_{network}}{\omega_{alone}} = \sqrt{\frac{E_{network}}{E_{alone}}} \tag{1.16}$$

Figure 1.8 displays the 2D network of charge potential and the logarithm of the electric field absolute value resulting from the PTCDI-C13 self-assembly on graphene network geometry. We consider only a central molecule and its nearest neighbors. The extension of the perylene conjugated core is computed to be $(5 + 6 \times \frac{1}{2}) \times 0.15 \simeq 1.2\ nm$ assuming a C-C bond length of 150 pm.

The change in the electric field between the two charges of the central molecule is computed to be zero at a charge position and non zero between the two charges. It results a frequency shift of the resonance that is comprised between 0 and 115 $THz = 480\ meV$ at different location between the two charges. Considering that the overall effect of the local electric field on the resonance frequency shift is the mean of every locations between the charges, we compute a frequency shift of 50 $THz = 200\ meV$ which is consistent with the experimental observation (160 meV).

However, such resonant interactions should also lead to a concentration of the oscillator strength on the 0-0 vibronic transition.[101] Yet, in the present case, a fit of the absorption line accounting for the spectral broadening of the vibronic structures gives an increase of the 0-0 to 0-1 ratio of about 20%, which is not consistent with the 280% value found computing the effective polarizability for a 200 meV frequency shift.

Therefore, the strong resonant molecule–molecule interaction evaluated above in free space may thus be screened by the presence of the highly polarizable graphene substrate. Graphene-molecule interactions should be explored to understand the role of these interactions on the absorption spectrum of self-assembled PTCDI on graphene.

1.3 Graphene-molecule interactions

1.3.1 Electromagnetic interactions

We show hereafter how the strongly increased polarizability of the environment[102] of the adsorbed molecules as compared with nearly isolated ones when diluted in toluene solution

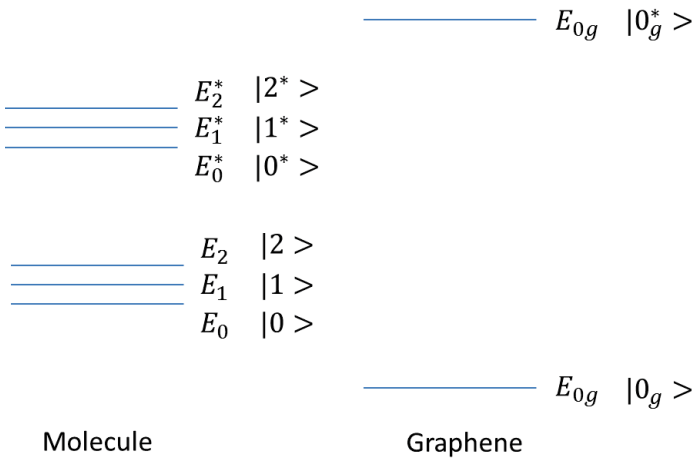

Figure 1.9: Jablonski diagram for a model dye and a simplified model of graphene.

could explain a large red-shift.

Models described in previous sections fail to predict the absorption spectrum of a dye displaying vibronic replicas signatures. In this paragraph we model the electromagnetic interactions between the dye and its environment by a perturbation Hamiltonian. We deduce the new transition energy through a perturbative approach. Graphene have high energy transition in the UV range (4.6 eV for the graphene Van Hove singularity). We then consider that the graphene transition energy is largely greater than the dye transition energies. States of a model dye and simplified model of graphene are defined as sketched in figure 1.9.

In the quantum treatment, the stationary states of the system are first derived as eigenvectors of the Hamiltonian. Then, the optical response is derived from the energies and transition dipole moments between those stationary states. The derivation of eigenvectors is done by applying the perturbation theory. The perturbation Hamiltonian H_1 depends on the dipole moment operators of the molecule and the graphene $\overline{\mu}$ and $\overline{\mu_g}$ respectively. It also depends on a coupling constant κ that characterizes the Coulomb interaction between $\overline{\mu}$ and $\overline{\mu_g}$.

$$H_1 = \kappa \overline{\mu} \overline{\mu_g} \tag{1.17}$$

Infrared transitions between vibronic replicas inside the ground or excited electronic state manifold are neglected. For simplicity, molecule and graphene are defined with no permanent dipole moment: diagonal terms of dipole moment operators are zero. This applies for instance to symmetrical molecules. Dipole moment operators act on states as described in the following:

$$\overline{\mu_g}|00_g >= \mu_g |00_g^* > \tag{1.18}$$

$$\overline{\mu}|00_g >= \mu \sum\nolimits_{j=0,1,2} < j^*|0 > |j^* 0_g > \tag{1.19}$$

The dye fundamental state $|00_g >$ at energy E_{00_g} sees its energy varying with the coupling constant κ. The perturbed energy $E_{00_g p}$ can be computed as:[103]

$$E_{00_g p} = E_{00_g} + < 00_g|H_1|00_g > + \sum\nolimits_{i,j} \frac{| < ij_g|H_1|00_g > |^2}{E_{00_g} - E_{ij_g}} \tag{1.20}$$

$$\Delta E_{00_g} = E_{00_g p} - E_{00_g} = (\kappa \mu \mu_g)^2 \sum\nolimits_{j=0,1,2} \frac{| < j^*|0 > |^2}{E_{0_g} - E_{0_g^*} + E_0 - E_0^* - j\Delta E} \tag{1.21}$$

where ΔE is the energy difference between two vibronic replicas. For conjugated molecules, the most strongly coupled vibration is the vinyl stretching mode around 1600 cm^{-1} or

180 meV. Since the solvent transition is in the UV range and the dye transition in the visible range, we neglect this IR transitions for j=0,1,2. We obtain the energy shift for the $|00_g>$ state:

$$\Delta E_{00_g} = \frac{(\kappa\mu\mu_g)^2}{E_{0_g} - E_{0_g^*} + E_0 - E_0^*} \tag{1.22}$$

with the sum rule:

$$\sum\nolimits_{j=0,1,2} |<j^*|0>|^2 = 1 \tag{1.23}$$

The first respectively second excited state of the molecule $|0^*0_g>$ (resp. $|1^*0_g>$)at energy $E_{0^*0_g}$ (resp. $E_{1^*0_g}$) sees its energy perturbed by a factor $\Delta E_{0^*0_g}$ (resp. $\Delta E_{1^*0_g}$):

$$\Delta E_{0^*0_g} = E_{0^*0_g p} - E_{0^*0_g} \tag{1.24}$$

$$\Delta E_{1^*0_g} = E_{1^*0_g p} - E_{1^*0_g} \tag{1.25}$$

$$\Delta E_{0^*0_g} = \frac{(\kappa\mu\mu_g)^2}{E_{0_g} - E_{0_g^*} + E_0^* - E_0} \tag{1.26}$$

$$\Delta E_{1^*0_g} = \Delta E_{0^*0_g} \tag{1.27}$$

The transition energy shift $\Delta_{gap} = \Delta E_{0^*0_g} - \Delta E_{00_g}$ induced by the interaction with the solvent for the dye can then be written:

$$\Delta_{gap} = \frac{-2(\kappa\mu\mu_g)^2(E_{0^*} - E_0)}{(E_{0_g^*} - E_{0_g})^2 - (E_{0^*} - E_0)^2} \tag{1.28}$$

This energy shift is identical for the three vibronic replicas. For a positive coupling $\kappa > 0$ the shift is negative, meaning that all vibronic replicas absorption bands shifts to the red.

The transition energy shift can also be computed for the graphene. In this case, the transition energy shifts to the blue:

$$\Delta_{gap\ graphene} = \frac{-2(\kappa\mu\mu_g)^2(E_{0_g^*} - E_{0_g})}{(E_{0_g^*} - E_{0_g})^2 - (E_{0^*} - E_0)^2} \tag{1.29}$$

Note that one can then deduce the solvent shift knowing the dye shift since the ratio of the two shifts only depends on the transitions without any perturbations:

$$\frac{\Delta_{gap\ graphene}}{\Delta_{gap}} = \frac{E_{0_g^*} - E_{0_g}}{E_{0^*} - E_0} \tag{1.30}$$

This perturbative quantum model can be tested by comparing the graphene transmission spectra with and without PTCDI-C13 self-assembly. The molecule-solvent coupling model predicts a blue-shift of the Van Hove singularity once PTCDI-C13 are adsorbed at the graphene surface. From the PTCDI-C13 on graphene transmission spectrum considering that the red-shift is entirely produced by the PTCDI-C13-graphene interaction, the graphene Van Hove transition is predicted to shift by:

$$\Delta_{graphene} = \Delta_{PTCDI-C13} \times \frac{4.6eV}{2.3eV} = 0.32eV \tag{1.31}$$

where $\Delta_{PTCDI-C13} = 0.16\ eV$ is the shift of PTCDI-C13 absorption bands. Since $4.6\ eV = 270\ nm$ the transmission spectrum should reveal a shift from 270 nm to 252 nm. UV-VIS transmission spectra of graphene on quartz, PTCDI-C13 functionalized graphene on quartz, and the quartz substrate are displayed in figure 1.10.

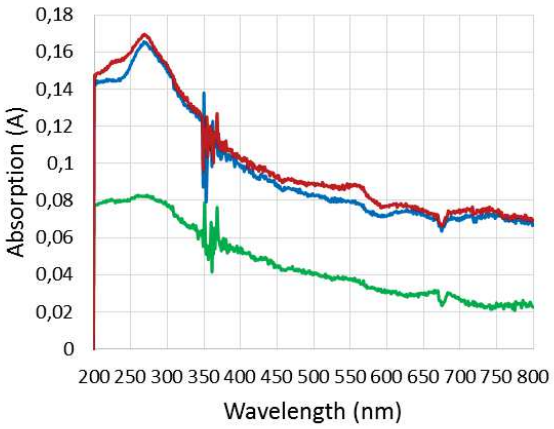

Figure 1.10: Absorption spectra of a reference quartz plate (green curve), graphene on quartz (blue curve) and self-assembled PTCDI-C13 on graphene on quartz (red curve).

The Van Hove singularity is clearly visible at 270nm in the graphene on quartz curve. Its absorption peaks at 9 percent at 270 nm, whereas it converges to 2 percent for visible-IR wavelengths. The functionalization of graphene by the non-covalently bound PTCDI-C13 self-assembly produces a clear new band in the UV range at 230nm. This is too far energetically from the predicted 252 nm to be attributed to a shift of the Van Hove singularity. We explain this new band by the UV absorption of PTCDI-C13 molecule. A precise fit on the graphene van Hove band reveals a 10 meV shift that could be the sign of the graphene-molecule coupling. It then means that graphene-molecule interactions are negligible in comparison to intermolecular interactions. However, only couplings between molecular states and van Hove transition states are considered in this model. The contribution of all other graphene possible transitions has to be considered to fully represent the interaction between graphene and adsorbed molecule on top of it.

The electronic properties of graphene can be modeled in a tight-binding approach.[104] In this framework, graphene electrons energy depends on the wavevector through the 2D dispersion relation:

$$E(k_x, k_y) = \pm t\sqrt{3+f} - tt \times f \tag{1.32}$$

$$f = 2cos(a \times k_y\sqrt{3}) + 4cos(\frac{a \times k_y\sqrt{3}}{2})cos(a \times k_x\frac{3}{2})$$

where a is the graphene lattice constant ($a = 0.24612 \times 10^{-9}\ m$), t is the hopping energy ($t = 2.8\ eV$) and tt is the nearest neighbor hopping energy ($tt = 0.1\ eV$). This 2D dispersion relation is represented in figure 1.11. This dispersion relation displays Dirac cones where the electronic density of states is constant and thus where electrons behave like a 2D electron gaz.

The density of states (DOS) and thus the absorption spectrum of graphene can then be computed. Figure 1.12 displays the density of possible electronic transitions that is closely related to the absorption spectrum. This transition density peaks at 5.6 eV whereas experimentally the absorption spectrum of graphene peaks at 4.6 eV. This band is usually referred as the graphene van Hove singularity.

For simplicity purposes the 2D dispersion relation of graphene electrons will be projected on the k_x axis in the following. We discretize the dispersion relation of graphene by a orthogonal base of eigenvector states corresponding to $\mathbf{k}$ wavevectors. The orthogonal characteristic is given by the orthogonality of propagating waves with different wavevectors (Fourier decomposition). The state defined by the wavevector $\mathbf{k}$ has an energy $e(k)$ defined by the dispersion relation of graphene electrons.

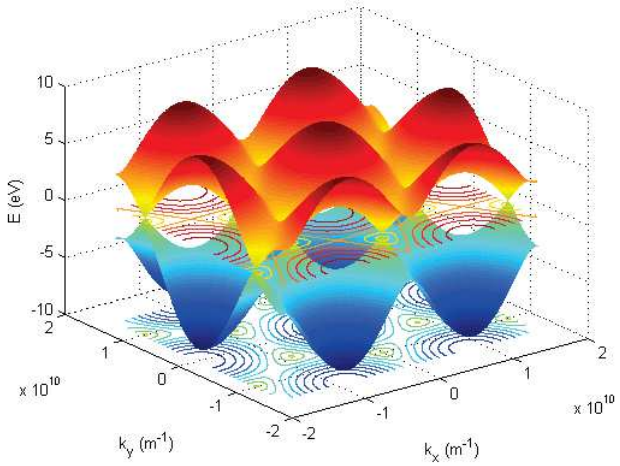

Figure 1.11: Electron dispersion relation in graphene in a tight-binding model.

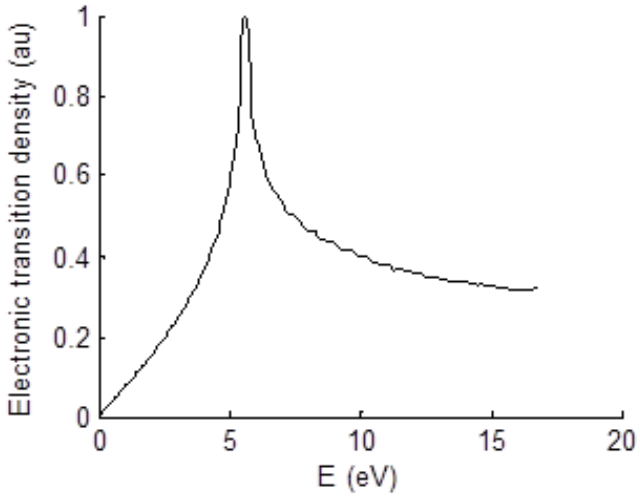

Figure 1.12: Graphene density of electronic transitions in a tight-binding framework.

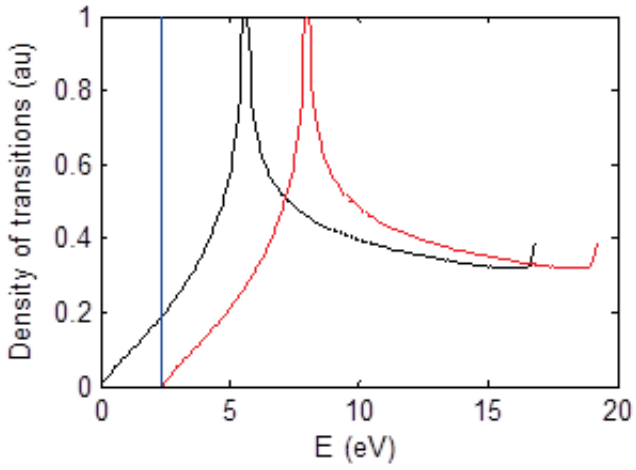

Figure 1.13: Density of transitions for the coupled unperturbed graphene-dye system. photon absorption in the dye (blue), in graphene (black) and simultaneous absorption in graphene and the dye (red).

In the following, we make a notation distinction between state of energy above or below the Fermi energy E_F that we place at the Dirac cone discontinuity. We note $|e_g(k)>$ and $|e_g(k)^*>$ the state corresponding to the wavevector $\mathbf{k}$ that have an energy below and above respectively E_F. We model the dye by a fundamental state of energy E_0 and an excited state of energy E_0^*. We thus define the base of the coupled system graphene-molecule in four parts to describe all possible states.

$$|e_g(k), 0> \ , \ E = e_g(k) + E_0$$

$$|e_g(k)^*, 0> \ , \ E = e_g^*(k) + E_0$$

$$|e_g(k), 0^*> \ , \ E = e_g(k) + E_0^*$$

$$|e_g(k)^*, 0^*> \ , \ E = e_g^*(k) + E_0^*$$

Figure 1.13 displays normalized density of transitions for an unperturbed graphene-dye system where the dye HOMO-LUMO gap is 2.4 eV. The HOMO is placed at -2 eV and the LUMO at 0.5 eV. The absorption of a photon is possible in the dye uniquely (blue curve) and correspond to a Dirac at 2.4 eV. The absorption of a photon is also possible in the graphene only (black curve). In this case, the density of transition for graphene corresponds to the one computed for graphene alone. Finally, it is also possible to absorb one photon in a molecule-graphene mixed state that results from their coupling. This process correspond to the red curve in figure 1.13.

The coupling between graphene and molecule dipole moments, $\overline{\mu}_g$ and $\overline{\mu}$ respectively, is defined by the coupling constant κ through the perturbation Hamiltonian $H_1 = \kappa \overline{\mu}_g \overline{\mu}$.

Perturbed energies for coupled molecule-graphene states described above can be then calculated as follow:

$$E_{e_g,0,p} = E_{e_g,0} + \frac{(\kappa \mu^* \mu_g)^2}{e_g(k) + E_0 - e_g^*(k) - E_0^*} \tag{1.33}$$

$$E_{e_g,0^*,p} = E_{e_g,0^*} + \frac{(\kappa \mu^* \mu_g)^2}{e_g(k) + E_0^* - e_g^*(k) - E_0} \tag{1.34}$$

$$E_{e_g^*,0,p} = E_{e_g^*,0} + \frac{(\kappa \mu^* \mu_g)^2}{e_g(k)^* + E_0 - e_g(k) - E_0^*} \tag{1.35}$$

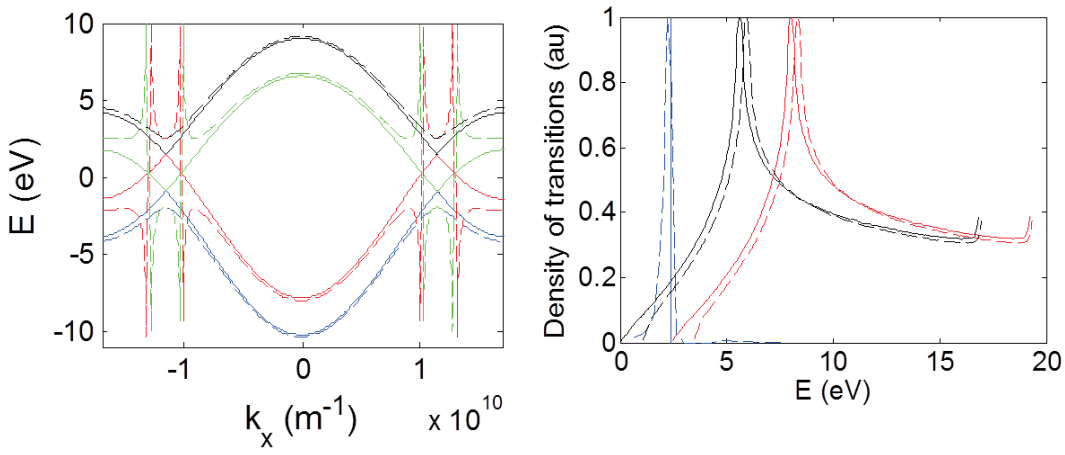

Figure 1.14: Density of transitions for the uncoupled unperturbed (plain lines) and perturbed (dash lines) graphene-dye system. photon absorption in the dye (blue), in graphene (black) and simultaneous absorption in graphene and the dye (red).

$$E_{e_g^*,0^*,p} = E_{e_g^*,0^*} + \frac{(\kappa\mu^*\mu_g)^2}{e_g^*(k) + E_0^* - e_g(k) - E_0} \tag{1.36}$$

Figure 1.14 displays the dispersion relations of electrons for perturbed and unperturbed coupled molecule-graphene electronic states.

$|e_g(k), 0>$ (respectively $|e_g(k)^*, 0^*>$) states are shifted to lower (resp. higher) energies regardless of the wavevector. A gap is thus opened at the graphene Dirac cone location.

When $e_g^*(k) - e_g(k) > E_0^* - E_0$, $|e_g(k), 0^*>$ (resp. $|e_g(k)^*, 0>$) states are shifted to lower (resp. higher) energies. When the inequality is inverted, $|e_g(k), 0^*>$ (resp. $|e_g(k)^*, 0>$) states are shifted to higher (resp. lower) energies. If $e_g^*(k) - e_g(k) = E_0^* - E_0$, the energy of the $|e_g(k), 0^*, p>$ and $|e_g(k)^*, 0>$ states diverge to infinity. This unphysical behavior is compensated by the fact that the density of state is null since the slope tends to infinity.

The resulting density of transitions for the unperturbed and perturbed graphene-dye system is displayed in Figure 1.14. One photon absorption in graphene and mixed molecule-graphene state are shifted to the blue due to the lowering of the $|e_g(k), 0>$ states and the increase of the $|e_g(k)^*, 0^*>$ states. The Van Hove singularity absorption band is thus blue-shifted. The transition in the molecule alone is shifted to the red. In fact, the higher transition density of graphene electrons at energies above the dye energy gap explains the overall red-shift of dye transitions. Computations also reveal that a transition is now possible in the molecule at higher energy (approx. 5 eV). However, the density of transitions at this energy is much lower than the low energy transition. Finally, the distribution of electronic graphene states in energy explain a broadening in the dye electronic transitions. These results are coherent with the simpler sovent-dye coupling model since they retrieve the shift to the red of the dye transition.

This analysis estimates the energy perturbation of electronic states of graphene and an adsorbed molecule on top of it. However, it considers the interaction between one electron of the molecule and one electron of graphene. Since the supramolecular network do not covers entirely the graphene surface, one should renormalize the effect on graphene states taking in account the number of affected states over the total number of states. In π-conjugated aromatic systems, one electron per carbon atom participate in the sp^2 delocalized electron cloud. The PTCDI core displays 24 conjugated carbon atoms, and forms a supramolecular network on graphene with a 0.5 $molecules/nm^2$ surface density. Therefore, the assembled monolayer have a $12e^-/nm^2$ conjugated electron surface density.

The graphene has two conjugated electrons per unit cell, corresponding to a $39e^{-}/nm^{2}$ conjugated electrons surface density. Therefore, only one third of graphene electrons are perturbed as described by this model and the rest of electrons are not affected by the presence of the supramolecular network.

This model shows that a clear energy shift for all graphene transitions should be produced by the coupling. Since this energy shift is not observed, we can confidently say that this coulombic coupling plays a minor role in the photonic properties of self-assembled PTCDI-C13 on graphene.

1.3.2 Change of molecular conformation

The overlapping of neighbor carbon atoms sp^2 orbitals in organic molecules allows the formation of a delocalized electron cloud that can be resonant at excitation frequencies in the visible range. When sp2 orbitals are twisted with reference to each other, their overlapping decreases resulting in a shortening of the electron cloud delocalization length. Since the delocalization length determines the resonant frequency of the oscillator, the twist of sp^2 orbitals produce a color shift in the absorption spectrum of the dye molecule. In a classical framework, a capacitance oscillator sees its resonant frequency shifting to the red when the distance D between charges increases ($\omega \sim \sqrt{D}$ demonstrated previously in a 1D model). An increase of the electron cloud delocalization length in an organic dye will shifts its resonance to the red, whereas a decrease of the delocalization length will shifts its resonance to the blue.

Although the interaction between a geometrically complex solvent and an organic dye is hard to imagine, the interaction between a flat surface (like graphene) and an organic dye is easier. One can expect the flattening of the aromatic dye through the π-π interaction with the surface. This effect should result in an increase of the delocalization length and thus a red-shift of the dye resonator.

An interesting case is the adsorption of conjugated dyes on carbon nanotubes. In the axis of the nanotube direction, the delocalization length of the electron cloud should be increased, like on graphene. However, in the perpendicular axis direction, the curve of the nanotube should bends the aromatic dye resulting in a decrease of the electron cloud delocalization length.[105]

A substrate-induced planarization was invoked for hydrogen bonded porphyrins on h-BN.[56] However, the PTCDI molecule already present a rigid intrinsically planar covalent structure and substrate-induced planarization cannot explain the even larger shift observed here.

1.3.3 Electronic interactions

Electronic interactions between conjugated π-electron systems of molecule and graphene (π-stacking), as evidenced by STM spectroscopy for non-alkylated PTCDI,[80] or by DFT computations[106] may also play a role in changes of the optical bandgap.

When HOMO and/or LUMO orbitals of a dye are participating in the dye adsorption process to a conductive or semiconductive (including pi-conjugated) substrate, one can expect a dramatical change in the electronic properties of dye through quantum interactions.

The charges can be redistributed between the interacting systems, and new coupled states can be created such as mixed charge-transfer (CT) and Frenkel excitons with incidence on optical properties.

Unlike Frenkel excitons arising from the Coulomb interaction between induced dipoles at molecular sites, charge-transfer excitons result from the overlap of nearest neighbor molecules orbitals wavefunctions. However, at required distances for the CT exciton to

exist (approx. 0.3 nm) the Frenkel exciton is also present resulting in a mixed CT-Frenkel exciton.

For example, the stacking of perylene dyes considerably change the optical absorption spectrum with the appearance of a new band related to the transition from the S0 vibrational ground state to the CT-Frenkel exciton state.[107] Such stacking of dye molecules is usually associated with an inhomogeneous broadening of the absorption spectrum since multiple stacking conformation are often possible.

The spatial partition of charges is a complex multibody problem defined through the unique structures of each molecule. Density functional theory (DFT) calculations can give an insight into these changes, but at such scale a small distance perturbation produces important modifications on electric fields. DFT calculations are then to be taken with precautions. Hence, the prediction of changes in the absorption spectrum due to charge redistribution in the dye molecule is a difficult task.

These interpretations are consistent with the observation of a concentration of the oscillator strength for dense assemblies of PTCDA deposited on a dielectric substrate,[87] in which case no significant spectral shift was observed.

In summary, we have realized the self-assembly of alkylated PTCDI molecules onto a monolayer CVD graphene transferred on a transparent substrate. The molecules form a well-organized dense assembly, the parameters of which being accurately determined by STM. The polarized optical transmission spectra have been acquired at variable incidence thanks to the high optical transparency of the monolayer CVD graphene substrate. This confirms that the transition dipoles of adsorbed PTCDI are all oriented parallel to the substrate. The absorption is consistent with the measured density of molecules and presents mainly a rigid red-shift of the absorption line compared with the free molecules dispersed in solution. These changes are attributed to non-resonant interactions with the graphene layer and the neighboring molecules. The intermolecular coupling results from the Coulombic interaction between dipole moments and the graphene-PTCDI-C13 coupling from an electronic coupling that modifies the electronic structure of both graphene and PTCDI-C13.

However, the preservation of the absorption line-shape and the balance between vibronic contributions in PTCDI-C13 experimental absorption spectra means that the strong resonant molecule–molecule interaction evaluated in free space is screened by the presence of the highly polarizable graphene substrate. An exciting perspective could be given by hexagonal boron nitride (h-BN) monolayers, which combine a dielectric nature with an atomic-scale template similar to that of graphene.[108]

Additional measurements have to be performed on different self-assembled systems to understand the contribution of intermolecular and molecule/graphene interactions in the modification of dye photonic properties once adsorbed on the graphene surface. This is the object of the next section.

1.4 Dependence on the intermolecular distance

To get insight about the origin of the spectral redshift observed for self-assembled dyes on graphene, we made comparisons with other self-assembled dyes on graphene. The two key physical parameters (intermolecular distance and graphene-molecule distance) should be varied to evaluate the strength of each coupling. However, one should take extra care when varying these parameters since they are not fully independent.

A first strategy to modify the 2D supramolecular network could be to change the length of alkyl chains which often play a role of spacer between assembled molecules.[60,47] The contribution to the adsorption force of a ten carbon alkyl chain should not change that much the molecule graphene distance in comparison to a 6 carbon atoms alkyl chain for

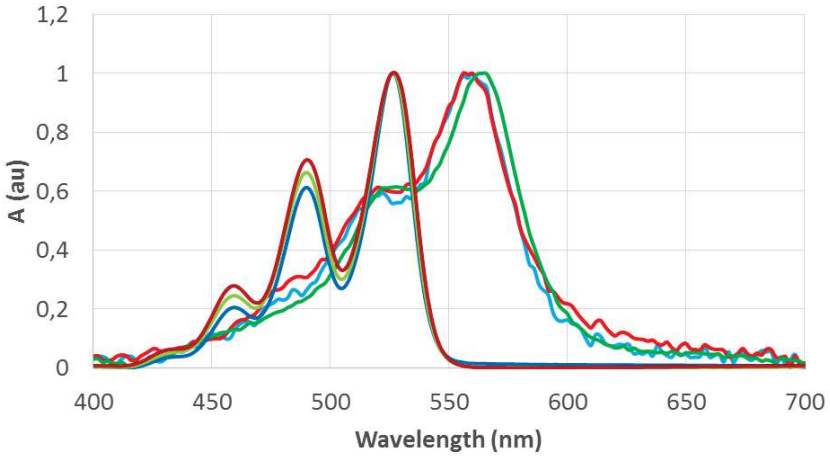

Figure 1.15: Normalized transmission absorption spectra of PTCDI-C7 (red), PTCDI-C8 (blue) and PTCDI-C13 (green) diluted in a toluene solution (dark curves) and self-assembled on a graphene on PET surface (light curves).

example.

However, a change in the number of carbon atoms do not have a major impact on the PTCDI-C13 on HOPG supramolecular network, as shown by Ludwig et al.[109] PTCDI-C13 alkyl chains do not participate in the adsorption force but seem to stand away from the graphene surface. This conformation originates from the steric constrain produced by the terminal oxygen atoms.

The measured network parameters are $a = 1.5\ nm$, $b = 1.7\ nm$, $\alpha = 87.5°$ for PTCDI-C8 and $a = 1.6\ nm$, $b = 1.7\ nm$, $\alpha = 88.2°$ for PTCDI-C13. Absorption spectra of PTCDI-C7, PTCDI-C8 and PTCDI-C13 diluted in solution and self-assembled on the graphene surface are displayed in figure 1.15. The absorption spectra of the three molecules in toluene peak at the same wavelengths. The difference in the distribution of the oscillator strength over the vibronic replicas is observed when the concentration of PTCDI dye molecules is varied. This difference can be attributed to a mismatch between PTCDI-C7, PTCDI-C8 and PTCDI-C13 concentrations during the measurement. The three spectra in solution can therefore be considered as identical, which seems reasonable since a change in the alkyl chain length should not affect the conjugation of perylene core that produce the visible absorption.

As expected from scanning tunneling experiments that show no major changes in the 2D molecular network, the absorption spectra of PTCDI-C7, PTCDI-C8 and PTCDI-C13 are almost identical once self-assembled on a graphene on PET surface. However, a small change in the position of the 0-0 transition is observed between PTCDI-C7 and PTCDI-C8 on one hand and PTCDI-C13 on the other hand. The redshift for PTCDI-C7 and PTCDI-C8 (140 meV) is slightly smaller than for PTCDI-C13 (155 meV). Moreover, the absorption peak is slightly smaller for PTCDI-C7 and PTCDI-C8 (2.0%) than for PTCDI-C13 (2.3%). Since the ratio between 0-0 and 0-1 transitions is identical for the three molecules, the intermolecular interaction should also be identical. This is consistent with the fact that molecular network geometries are not affected that much by the change in the alkyl length.

The presence of longer alkyl chains changes the dielectric environment around perylene dye dipoles. The refractive index surrounding aromatic cores is increased when alkyl chains are lengthened from eight to thirteen carbon atoms. The resulting dielectric constant ϵ_r of the mixture comprising aromatic cores and alkyl chains with respective polarizabilities

α_c and α_a and densities N_c and N_a can be found with the Clausius-Mossotti relation extended to mixture of species:

$$\frac{\epsilon_r - 1}{\epsilon_r + 2} = \frac{N_c \alpha_c}{3\epsilon_0} + \frac{N_a \alpha_a}{3\epsilon_0} \tag{1.37}$$

Alkyl chains are assumed to have a dielectric constant at optical frequencies ϵ_a when the perylene aromatic cores are not present. The polarizability of the aromatic core is a lorentzian oscillator describing a two level dye molecule such as:

$$\alpha_c = \frac{A}{\omega_0 - \omega + i\gamma} \tag{1.38}$$

The resulting dielectric constant of the mixture can be rewritten:

$$\epsilon_r = \epsilon_a \frac{\omega_0 - \omega + i\gamma + \frac{2N_c A}{9\epsilon_0 \epsilon_a}(\epsilon_a + 2)}{\omega_0 - \frac{N_c A}{9\epsilon_0}(\epsilon_a + 2) - \omega + i\gamma} \tag{1.39}$$

An increase of the surrounding material real part of the dielectric constant yields a decrease of the resonance frequency and a rise of the imaginary part of the dielectric constant of the mixture at resonance:

$$\Delta\omega_0' = -\frac{N_c A}{9\epsilon_0}(\Delta\epsilon_a + 2) \tag{1.40}$$

$$\Delta Im(\epsilon_r(\omega_0')) = \frac{2N_c A}{9\epsilon_0 \gamma}(\epsilon_a + 2)\Delta\epsilon_a \tag{1.41}$$

Consequently, the redshift mismatch in absorption spectra of PTCDI-C7, PTCDI-C8 and PTCDI-C13 on graphene could be attributed to an increased refractive index of the perylene core surroundings due to the presence of longer alkyl substituents. However, this difference may also result from a difference in the adsorption strength related to the steric constrain between neighbor alkyl chain.

The alkyl chain length variation strategy to obtain different PTCDI supramolecular networks on graphene is thus usable only if alkyl chains are forced to lay on the graphene surface overcoming the steric constrain produced by the terminal oxygen atoms.

Figure 1.16 displays the molecular structure of N-(1-hexylheptyl) - 3,4,9,10 - perylenedicarboximide (PTCDI-2C6a) and a scanning tunneling microscopy image of this molecule at the liquid/HOPG interface.

A second alkyl chain has been added at one extremity of the perylene core increasing the steric constrain between hypothetical neighbors in the self-assembled system. The molecular network obtained at the HOPG surface is of lamellar type, and differs completely from the PTCDI-C13 network. The distance between lamellae normal to the main direction of the line is about 3.5 nm. Interestingly, features can be distinguished inside these lines. First, lines turn very frequently with a constant angle of about 100°. Second, square features can be observed inside the lines. The distance between the points inside squares is measured to be 1.1 nm. Considering the building block molecular structure and the observations on the STM image of PTCDI-2C6a on HOPG, the proposed model for the molecular conformation in the 2D network on HOPG is displayed in figure 1.17.

The perylene core is adsorbed on the HOPG surface and the assembly geometry follows the same rule as for PTCDI-C13. However, the steric constraint produced by the double alkyl chain group at one extremity avoids the propagation of the square pattern. Building blocks are grouped by dimers forming a line instead of a 2D periodic pattern. Since the distance between the two nitrogen atoms of PTCDI is about 1.2 nm, the width of the line that should be observed in a STM experiment is about 2 nm considering a 0.4 nm spacing between the two molecules constituting the dimer. The C6 alkyl chains actually play the

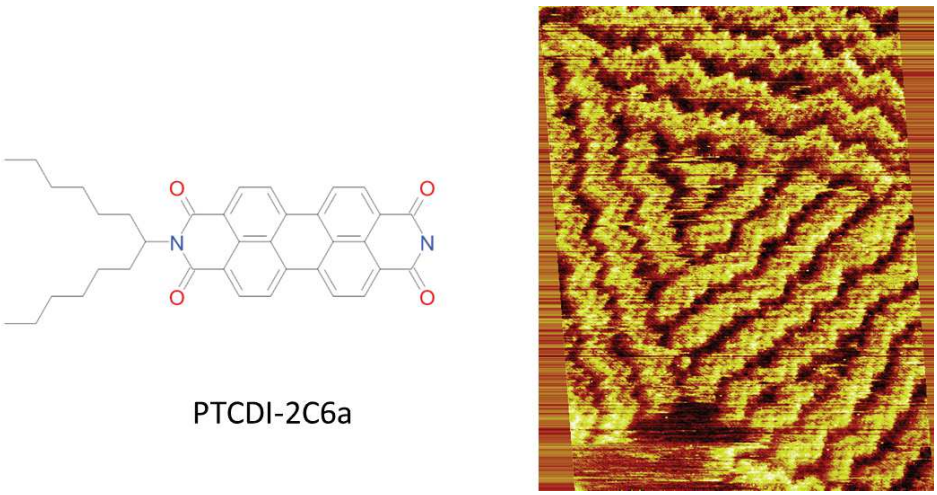

Figure 1.16: Structural characterization of the self-assembled PTCDI-2C6a monolayer. Left. PTCDI-2C6a molecular structure. Right. STM image of self-assembled monolayer on HOPG (53 nm $\times$ 65 nm, 11 pA, 900 mV), acquired at the interface between the substrate and a ca. 10^{-5} M solution in phenyloctane at room temperature.

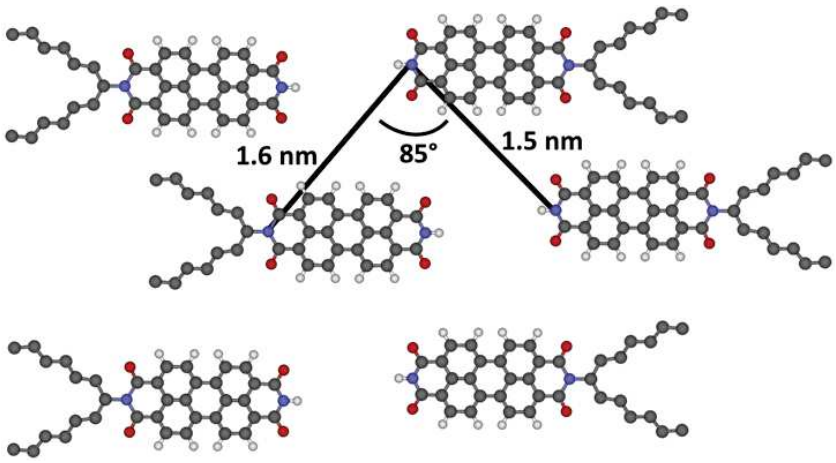

Figure 1.17: Model for the self-assembled PTCDI-2C6a monolayer on graphitic surfaces. Color represents the nature of atoms: grey (carbon), blue (nitrogen), red (oxygen), and white (hydrogen).

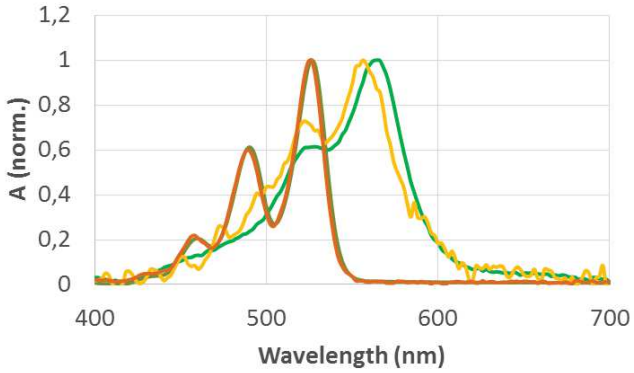

Figure 1.18: Normalized transmission absorption spectra of PTCDI-C13 (green) and PTCDI-2C6a (orange) diluted in a toluene solution (dark curves) and self-assembled onto a graphene on PET surface (light curves).

role of spacers, with a length of about 0.6 nm, giving an interline distance of 3.2 nm, consistent with the observed 3.5 nm. Moreover, this model explains the angle of about 100° that characterizes the turns of PTCDI-2C6a lines once self-assembled on HOPG. The average length of the line before it changes direction is measured to be 2 dimers, revealing that the direction of the line is entirely random and that the double alkyl chain do not play any role on the direction of the line. The resulting packing density from this model is 0.3 mol/nm^2 which represent a 33% reduction in comparison to the PTCDI-C13 assembly.

Figure 1.18 compares the optical absorption spectra of PTCDI-C13 and PTCDI-2C6a diluted in a toluene solution and self-assembled on the graphene surface.

As expected, the modification of the molecular structure does not affect the absorption spectrum in a toluene solution since conjugated aromatic cores are identical. However, three clear differences appear when the two molecules are self-assembled on the graphene surface. First, the 0-0 transition is shifted from 528 nm in a toluene solution to 556 nm (123 meV redshift)for PTCDI-2C6a and to 564 nm (155 meV redshift) for PTCDI-C13 once self-assembled on graphene. A 30 meV difference separates then the two self-assembled systems. In what follows, we show that this difference can be understood with the help of the 2D model developed in section 1.2.1. Figure 1.19 displays the models for the PTCDI-C13 and PTCDI-2C6a supramolecular networks on graphene with the charges resonantly induced by the excited transition modeled as being located on the extremities of the conjugated kernel, that is on the nitrogen atoms.

The application of the model results in a blueshift of $143meV = 34\,THz$ which overestimates once again the observed phenomenon. The absence of a J-like nearest neighbor in the case of PTCDI-2C6a as shown in figure 1.19 shifts the resonance to the blue.

Second, a neat difference appears in the partition of the oscillator strength. The 0-1 transition is much stronger in the PTCDI-2C6a system ($\frac{S_{0-0}}{S_{0-1}} = 1.39$) than the PTCDI-C13 system ($\frac{S_{0-0}}{S_{0-1}} = 1.64$) and than PTCDI-C13 and PTCDI-2C6a diluted in solution ($\frac{S_{0-0}}{S_{0-1}} = 1.66$). The transfer of oscillator strength form the 0-0 transition to the 0-1 transition reveals a H-type intermolecular coupling.[52] This behavior is thus consistent with the observed blueshift. Finally, the absorption peaks at 0.9% for PTCDI-2C6a and at 2.3% for PTCDI-C13. The decrease of the $\frac{S_{0-0}}{S_{0-1}}$ ratio contributes in this 60% reduction of the absorption band which corresponds to the S0-0 transition. Nevertheless, the integral of the absorption spectra over frequencies reveals that the overall oscillator strength is decreased by about 40% from the PTCDI-C13 to the PTCDI-2C6a self-assembled system. Considering the molecular network exposed above, a computed 33% reduction of

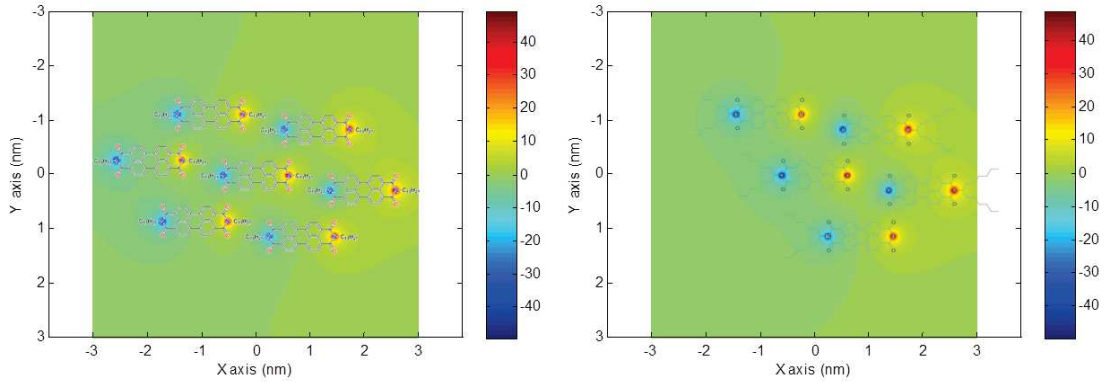

Figure 1.19: Model for PTCDI-C13 and PTCDI-2C6a on graphene supramolecular networks and associated potential resulting from their transition dipole moment.

the molecular surface density could explain the main part of the experimental oscillator strength decrease.

From these observations it is clear that a coupling between neighbor perylene optically induced dipole moments is effective since the oscillator strength of self-assembled PTCDI can be redistributed over the vibronic replicas by changing the supramolecular network geometry. However, this coupling does not explain the large redshift observed for all dye molecules since such shift should be accompanied by a major redistribution of the oscillator strength in absorption spectra. The redshift may find its origin in the high refractive index of the nearby environment produced by the presence of alkyl chains and other groups of PTCDI molecules that do not participate in the visible resonance. The graphene monolayer, which displays a high polarizability in the visible region, could also be responsible for the observed large redshift. Moreover, other phenomena such as charge transfer between the self-assembled dye and the graphene monolayer might change the transition energy of the adsorbed dye.

1.5 Dependence on the molecule-graphene distance

Recently, a versatile platform has been conceived in order to add physical properties to carbonated surfaces thanks to a new family of 3D self-assembled building blocks called Janus Tectons.[110] These molecules can be decomposed to three distinctive groups: an adhesive group, a spacer group, and a functional group. The adhesive group or "pedestal" consists of two molecular clips that strongly bind to carbon sp^2 surfaces. The pedestal forms 2D networks on HOPG and graphene surfaces. The spacer group decouples the substrate surface and the pedestal from the functional group thanks to a disulfur bridge of height evaluated to 0.31 nm. An aromatic dye is used as functional group to add optical properties to the substrate surface. The dye group is composed of two benzothiadiazoles units linked to a central benzene ring by a thiophene ring. At both extremities, another thiophene unit terminated by an octane chain complete the structure. The overall structure called TBC8-JT and related compounds are sketched in figure 1.20.

Scanning tunneling microscopy shows that both TBC8 and TBC8-JT molecules form well organized 2D networks on HOPG at the liquid-solid interface (Figure 1.21). Network parameters for TBC8 ($a = 2.5nm, b = 2.1nm, \alpha = 53°$) and for TBC8-JT ($a = 3.9nm, b = 2.4nm, \alpha = 80°$) show a clear difference in the molecular surface density σ_{surf}.

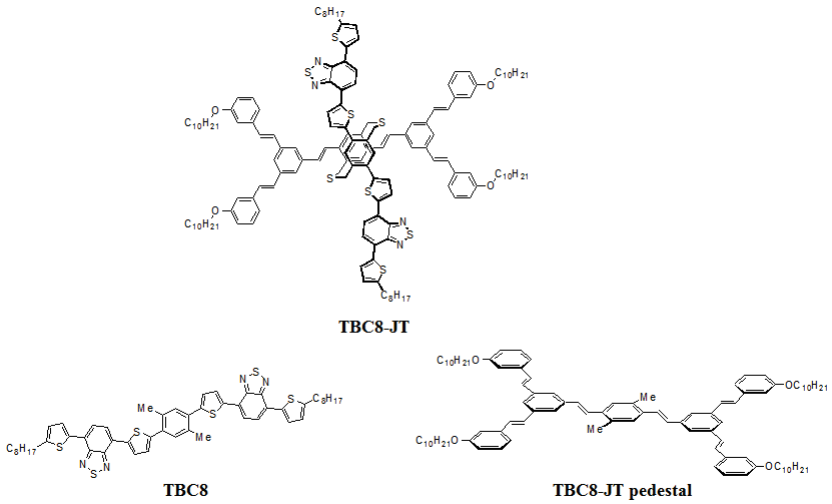

Figure 1.20: Schematic structures of the Janus Tecton TBC8-JT, TBC8-JT pedestal and TBC8 molecules.

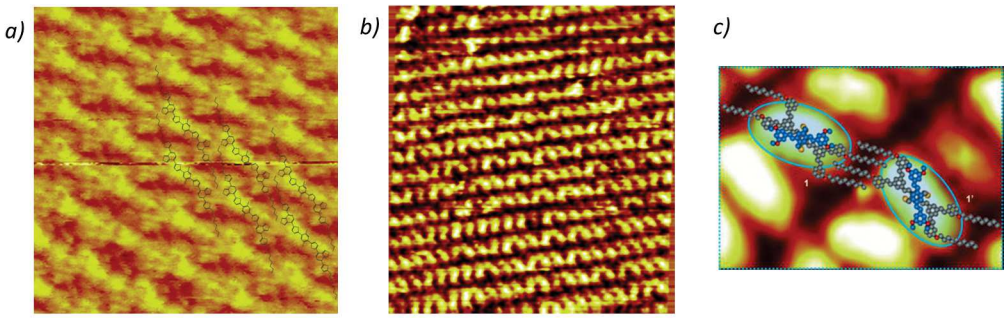

Figure 1.21: STM images at the liquid/HOPG interface at room temperature: (a) TBC8 ($11nm \times 11nm, I_t = 90pA, V_t = -460mV$); (b) TBC8-JT ($51nm \times 54nm, I_t = 9pA, V_t = -1320mV$); (c) model for the TBC8-JT supramolecular network on HOPG geometry, reproduced from ref.[47]

$$\sigma_{TBC8surf} = 0.24\ molecules/nm^2$$
$$\sigma_{TBC8-JTsurf} = 0.11\ molecules/nm^2$$

TBC8 molecules seem to be aligned on the HOPG surface forming a 2D network with closely packed lines separated by TBC8 terminal alkyl chains that are clearly visible on the STM image (Figure 1.21 a)). The proposed model for the 2D supramolecular network is superimposed to the STM image. Molecular mechanics calculations evaluate the distance between the terminal thiophene rings of a TBC8 molecule to be 2.7 nm. To verify the observed network parameters of the TBC8 lattice on HOPG, the conjugated cores of the molecule once adsorbed on the HOPG surface should then be fairly close to one another in a J-type coupling configuration.

The TBC8-JT STM image displays the conjugated aromatic core of the upper part of the TBC8-JT molecule, corresponding to the functional TBC8 group attached to the pedestal part by a spacer. These dye functional groups are forming lines in which conjugated cores have two distinct preferential orientations with respect to the line direction. The parameters of the TBC8-JT supramolecular network correspond to the parameters of the pedestal supramolecular network on the graphite surface ($a = 3.8\ nm$, $b = 2.1\ nm$, $\alpha = 64°$).[111] Therefore, the pedestal unit only seems to drive the formation of the TBC8-JT supramolecular network on the HOPG surface, though the presence of the pedestal and the functional dye group may produce minor steric constrains on nearest neighbors and changes in the adsorption strength that slightly modify the pedestal network parameters. The observation of two favored orientations for functional dye groups on top of TBC8-JT is explained by the presence of the two enantiomers corresponding to the meta or para positioning of the disulfur bridge.[47]

The model of the TBC8-JT network on HOPG proposed in (Figure 1.21 c)) is based on the pedestal supramolecular network model. It predicts the lines of parallel dye functional groups that are observed in the TBC8-JT STM image and the two possible orientations of the functional dye group when the sulfur atoms are varied from a para to a meta position. In contrast with the TBC8 on HOPG network where dyes lay in a J-like interaction geometry, TBC8-JT dye groups are more in a H-like interaction geometry since nearest neighbor dipoles are mainly parallel.

Toluene solution absorption spectra of TBC8 and TBC8-JT are displayed in figure 1.22. The absorption observed for TBC8-JT below 450 nm corresponds to the absorption of the pedestal of the Janus tecton. The large absorption band at 490 nm corresponding to the absorption of the TBC8 aromatic core is identical for TBC8 and TBC8-JT. The spacing action of the disulfur brigde is thus sufficient to decouple the aromatic unit of the pedestal group from the dye functional group and avoid any charge transfer between these two groups.

Absorption spectra of TBC8 and TBC8-JT on graphene are displayed in figure 1.22. The band at 491 nm in toluene has been shifted to 590 nm for TBC8 (424 meV redshift) and to 532 nm for TBC8-JT (180 meV redshift). The red-shift of TBC8 is surprisingly important, representing a 17% decrease of the HOMO-LUMO gap. Even more singularly, the redshift is accompanied with a 90 meV decrease of the absorption band width. A planarization of the molecule could explain a redshift in the absorption spectrum by increasing the conjugation length. It could also justify a reduction of the inhomogeneous broadening responsible for the absorption bandwidth by forcing molecules in a more homogeneous planar configuration. However, molecular mechanics simulations show that the TBC8 equilibrium configuration in vacuum is flat. It weakens thus the hypothesis of a planarization of the molecule on the graphene surface. Yet, since calculations are performed at zero temperature, the planarization of molecular motion at ambient temperature may still partially explain the observed redshift.

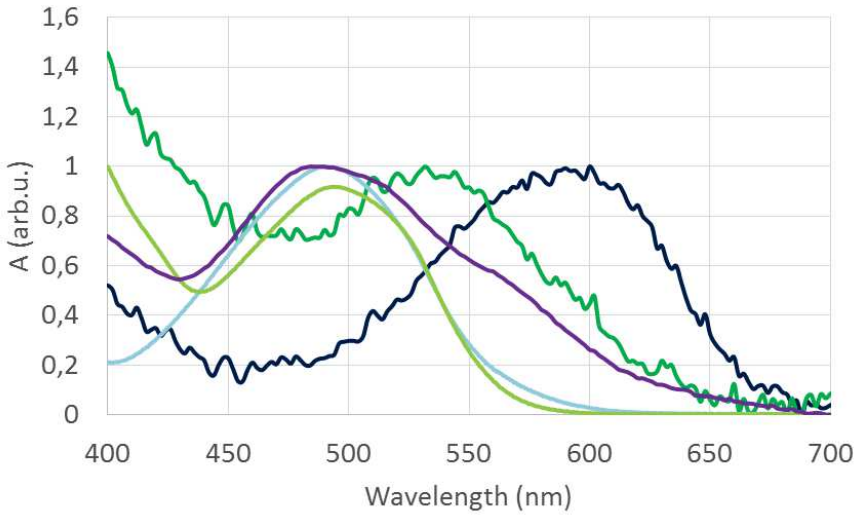

Figure 1.22: Normalized absorption spectra of TBC8 and TBC8-JT in toluene (resp. light blue and light green), self-assembled on graphene (resp. dark blue and dark green), and TBC8 microcrystals on glass (violet). The measurements were done in transmission, referenced to naked graphene for the self-assembled molecules on graphene.

The particularly favorable supramolecular network geometry for intermolecular J-type coupling may then explain this large reduction of the absorption band width. The observed large redshift should then be the combination of the intermolecular coupling and the interaction between dipole and the environment that is mostly responsible for the redshift as shown in the previous part with perylene systems on graphene.

The evolution of the TBC8-JT absorption band width is more difficult to evaluate since the redshift of the blue part of the spectrum coming from the pedestal blurs the band of interest. A Gaussian fit gives a broadening of 55 meV that reveals a H-type intermolecular coupling. However, this broadening can also be due to heterogeneous environment around dye molecules.

It is worth to notice that although TBC8-JT dye group is in a H-like intermolecular interaction geometry, the spectrum is shifted to the red by a large amount (180 meV). Since TBC8-JT dye group is electronically decoupled from the pedestal group, it is also electronically decoupled from the graphene surface. Therefore, the observed redshift for TBC8-JT does not come from electronic interactions with graphene but mostly from interaction with the high refractive index environment.

In the previous part, the comparison of PTCDI-C13 and PTCDI-2C6a demonstrated that a major change in the supramolecular network does not have a major impact on the redshift. Here, a significant reduction of the HOMO-LUMO gap (244 meV) is observed when comparing TBC8-JT to TBC8. Therefore, increasing the distance between the self-assembled dye and the graphene decreases the redshift considerably.

Two simultaneous effects could explain this result. First, the 0.6 nm spacer height of TBC8-JT moves the dye dipole moment away from the high refractive index graphene surface thus lowering the average refractive index of the environment. Second, the TCBC8 charge delocalization that could occur once adsorbed on graphene is not present in the TBC8-JT on graphene system. Therefore if it exits, this charge transfer effect should enlarge the delocalization length of the conjugated aromatic core.

The absorption spectrum of TBC8 microcrystals is displayed in figure 1.22. The main band of absorption is not shifted with reference to TBC8 in a toluene solution. Since

molecular densities in a TBC8 microcrystal or in a self-assembly of TBC8 on graphene are equivalent, the neighbor molecules do not participate in an increase of the local refractive index that could produce the redshift observed for self-assemblies on graphene. Consequently, only graphene is responsible for most of the redshift through an increase of the refractive index around self-assembled molecules on its surface and through a modification of the dye resonant frequency caused by charge transfer phenomena.

1.6 PTCDI multilayer thin film

Molecular self-assemblies of dyes on metallic surfaces are convenient for topographical studies since scanning probe microscopy experiments can reveal their organisation at the nano scale. However, their two-dimensional nature makes them difficult to integrate into actual optical applications since their absolute signal is weak: about 1% transmission absorption. Techniques to control the formation of three dimensional supramolecular self-assembly networks are needed to aim for photonics applications, such as light-emitting diodes or solar cells.

Self-assembled perylene diimide derivatives thin film received recently a lot of attention for their large molar absorption coefficients, high electron affinities and mobilities, and good thermal and photochemical stabilities.[112,113,114,115] They have been under intense investigation to replace fullerenes as the electron accepting component in organic photovoltaics.[116,117]

The study of these molecular aggregates reveals the presence of several physical phenomena disrupting the optical properties of the self-assembled dye. As suggested by Kasha, the Coulombic coupling of dye optical dipoles induces energetic shifts in the transition responsible for the main absorption spectral band and changes in the radiative decay rate. Moreover, the π-stacking of aromatic cores induces overlaps between nearest neighbor frontier orbitals that lead to variations in the delocalization length of the sp^2 conjugated electron cloud responsible for the dye photophysical properties.[118]

Since this short-range coupling is extremely sensitive to very small displacements between neighboring dye molecules (typically 0.1 nm),[59] predicting the photophysics of perylene derivative thin film is a challenging task and a systematic characterization of the thin film is needed.

Interestingly, alkyl substitutions at the imide-nitrogen position in perylene derivatives lead to significant changes in thin-film self-assembly.[113] For example, Ferguson et al. show the possibility to tilt the short molecular axis of PTCDI-Me at $\sim 60^\circ$ with reference to the substrate surface with the long molecular axis approximately parallel to the surface.[107] In the following, we study three perylene derivatives aiming at obtaining highly efficient emitting media.

In a first experiment, we deposited PTCDI-C7 by molecular beam epitaxy at a very low deposition rate (0.2 $nm.min^{-1}$) on heated substrates such as gold, indium titanium oxide, mica, glass and graphene on mica surfaces. The substrate heating temperature was set close to the evaporation temperature of PTCDI-C7, that is about $200°C$.

Figure 1.23 shows the Atomic Force Microscopy (AFM) topographic study of two PTCDI-C7 thin film on mica and on gold obtained by deposition of respectively 1.6 nm (figure 1.23 a)) and 30 nm (figure 1.23 d)). The AFM is operated in a non-contact (tapping) mode.

It is clear for the PTCDI-C7 thin film on mica that less than a monolayer has been deposited on the surface. Islands have been formed resulting from growth around nucleation sites. Lines can be distinguished forming sub-domains inside islands. It is worth noting that island heights are constant over all image, and are equal to 2.7 ± 0.2 nm which corresponds to the PTCDI-C7 total length (figure 1.23 b) and c)). Since no dispersion

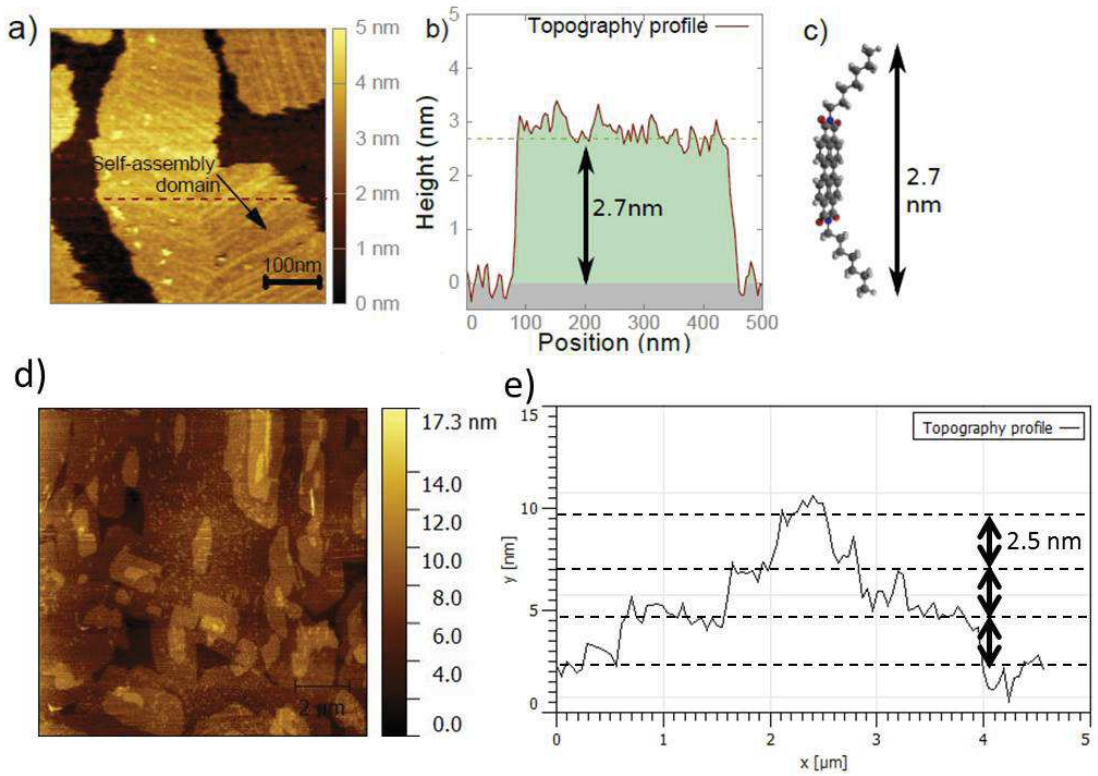

Figure 1.23: (a) AFM topographic image of a 1.6 nm thick PTCDI-C7 self-assembled thin film on mica revealing growth domains with different orientations. (b) Corresponding height profile (along red dashed line) which confirms the deposition of molecules standing on the substrate as sketched on (c). (d) AFM topographic image of 30 nm thick PTCDI-C7 self-assembled thin film on a gold thin film. (e) Height profile along the blue dashed line showing height jumps corresponding to a single monolayer.

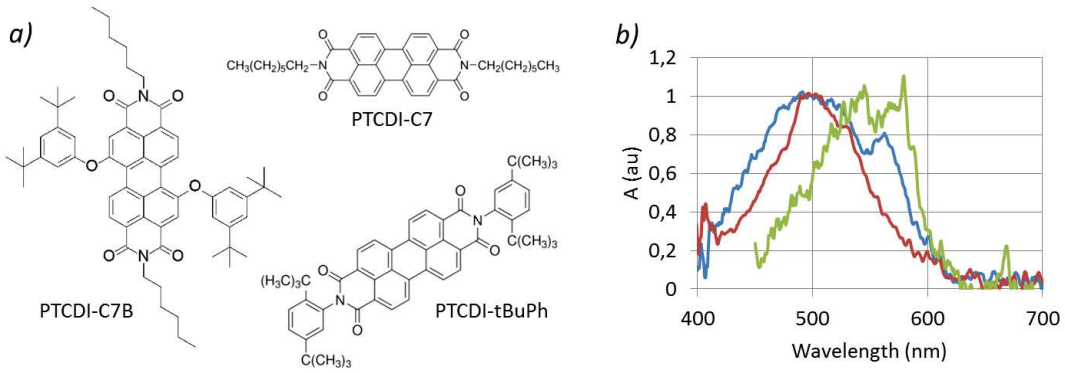

Figure 1.24: a): Molecular structures of PTCDI-C7, PTCDI-tBuPh and PTCDI-C7B. b): Normalized transmission absorption spectra of a 30 nm thick PTCDI-C7 thin film on a SiO2 coverslip coated with ITO (blue), of a PTCDI-tBuPh microcrystal (red) and of a 0.2 nm thick PTCDI-C7B thin film (green), both deposited on a SiO2 coverslip.

in the height of islands are observable, the islands are formed from one single layer of vertically-standing PTCDI-C7 molecules.

The film growth is controlled by the kinetics and not the thermodynamics. The organization taking place at high substrate temperature deposition does not result from an entropy increase but from the overcoming of kinetics barriers towards the most thermodynamically favorable state. The kinetics barriers probably consist of the conjugated core adsorption energy.[119] The deposited molecules lay flat on the substrate surface and a certain level of thermal energy is needed to take them off the surface and that they reorganize in a vertical position thanks to the pi-stacking with their nearest neighbor.

Therefore, the self-assembly model for this system consists in adjacent lines of stacked PTCDI-C2 oriented vertically inside the lines.

Interestingly, these findings also hold for gold, SiO2 and ITO substrates, but are not verified for the graphene on mica substrate. In this case, no islands can be distinguished on the graphene surface. The heating may then be not sufficient to avoid the adsorption of PTCDI-C7 molecules onto the graphitic surface. However, increasing the temperature could lead to retrodiffusing of the deposited molecule.

Figure 1.23 d) shows the surface of the 30 nm thick PTCDI-C7 thin film on mica as observed by AFM microscopy. Several layers are visible on the mica surface with domains of various sizes. A topography profile in 1.23 e) reveals that these domains are essentially flat terraces the height of which fluctuates by about ~ 2.5 nm, close to the PTCDI-C7 molecule length. The first layer is almost complete, continuously covering the substrate surface. The second layer consists in ~ 2 μm long islands randomly distributed on the first layer. Small groups of molecules are visible in the center of the image, before their aggregation in a more continuous domain. The third and fourth layers are visible at few locations on the image on top of the previously grown islands. This image demonstrates a layer-by-layer growth process that should result in a highly ordered molecular structure where PTCDI-C7 molecules are oriented perpendicularly to the substrate surface.

Absorption spectra of three perylene derivative crystals are displayed in figure 1.24. Side groups attached to the perylene core are varied to change the intermolecular interactions between the molecules inside the crystal.

The PTCDI-C7 thin film absorption spectrum displayed in figure 1.24 (b) peaks at 500 nm. The oscillator strength has been shifted to the blue in comparison to PTCDI-C7 diluted in toluene confirming the picture of H-aggregated perylene cores. Interestingly, a new band appears at 560nm in the absorption spectrum. It correspond to the transition

from the vibrational ground state to a mixed charge-transfer Frenkel excitonic state which is delocalized on several dye units.[107] A broadening of the vibronic replicas is observable since the corresponding bands can't be resolved anymore. This broadening may result from differences in the stacking of perylene cores and from inhomogeneities of local environments. In the case of π-stacked H/J aggregates, minor differences in the stacking geometry may induce large spectral changes, from J-type to H-type aggregates.[59]

PTCDI-tBuPh microcrystal absorption spectrum peaks at 500 nm and differs from PTCDI-C7 spectrum for two reasons. First, the absorption band is much thinner. The PTCDI-tBuPh microcrystal has been formed by evaporating a droplet of PTCDI-tBuPh in toluene solution on top of a glass coverslip at ambient conditions. Crystallization processes being quite different for the two systems, the decrease of the absorption band width may come from an improved crystal homogeneity. As a result, vibronic replicas are almost distinguishable and show a clear concentration of the oscillator strength in the 0-1 transition at 500 nm instead of the 0-2 transition at 475 nm or the 0-0 transition at 525 nm. This concentration of the oscillator strength confirms the π-stacking of aromatic cores in a H-like geometry. Second, the feature at 560 nm corresponding to the transition to the Frenkel state is not present in the PTCDI-tBuPh microcrystal. Therefore, even if molecules are stacked together, a collective state may not exist. The additional ter-butylphenyl groups at the extremities of the perylene core seem to be effective at reducing the exciton delocalization while keeping dyes molecules relatively close to each other.

The PTCDI-C7B thin film absorption spectrum is different from the two previous spectra since it peaks at 540 nm showing a red-shift of the 0-0 transition. Furthermore, the absence of other absorption bands at lower wavelength revealing a concentration of the oscillator strength in the 0-0 transition may show that PTCDI-C7B behave as a J-aggregate inside the thin film. In this system, an important part the oscillator strength is contained in the transition at 570 nm attributed to the transition from the S0 vibrational ground state to the excitonic Frenkel state. Therefore, chemical groups attached to the perylene core seem to favor the formation of excitons delocalized on several molecules over short-range CT-Frenkel excitons.

The dependence on the incidence angle of the 1.6 nm thick PTCDI-C7 thin film on mica TE and TM polarized transmission absorption is displayed in figure 1.25. Whereas the absorption increases with incidence for TM polarization, it decreases with increasing incidence for TE polarization. Random 3D molecule orientation should result in an increased absorption at grazing incidence for TE and TM polarizations, and the decrease of the TE signal can be only due to a mostly perpendicular orientation of the dipoles to the surface.[98] These experimental findings confirm AFM observations of this self-assembled system showing also a perpendicular orientation of the PTCDI-C7 dipole moments to the substrate surface.

1.7 Conclusion

The transparency of graphene and the fact that molecules self-assembled on its surface as they do on the HOPG substrate offered to characterize for the first time simultaneously the optical and topographical properties of supramolecular networks on graphene.

We have realized the self-assembly of several dye molecules onto graphene. The studied molecules form two-dimensional networks on the graphene surface which were characterized by scanning tunneling microscopy. Transmission absorption spectra acquired on these systems show an important redshift in comparison to the same dyes dispersed in a toluene solution. The distribution of the oscillator strength among vibronic replicas and the position of the main absorption band have been modulated by changing the supramolecular network geometry. The comparison of several self-assembled dyes on graphene show that

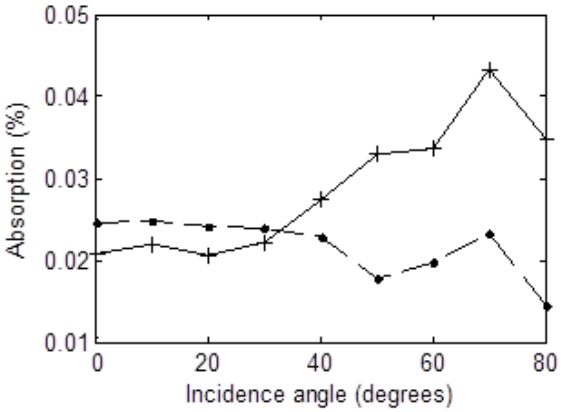

Figure 1.25: Variable incidence polarized-transmission analysis of the contribution of the self-assembled PTCDI-C7 monolayer to the absorption (cross: TM, points: TE). The mean optical density around the absorption maximum (460 nm to 500 nm)is plotted.

absorption spectra characteristics are correlated to intermolecular and dye-graphene interactions. A minor part of the redshift and oscillator redistribution results from the near-field Coulombic interaction between nearest neighbors and can thus be varied through modification of the supramolecular network. The major part of the absorption spectra modification is the consequence of dye-graphene interactions that can be separated into two effects. First, the graphene high refractive index produces an important redshift through the modification of the dye dielectric environment. Second, transfers of charges result from the adsorption of dye onto graphene that modifies the conjugation inside the dye and thus changes its photonic properties. Variable incidence transmission spectra confirmed that transition dipoles of adsorbed PTCDI are all oriented along the graphene surface. Other orientations of perylene derivatives transition dipoles inside self-assembled systems were obtained in a MBE setup by heating the substrate surface. Atomic force microscopy and variable incidence transmission spectra showed that normal orientations were obtained for PTCDI-C7 molecule transition dipole with reference to the substrate surface.

Chapter 2

Supramolecular self-assemblies and fluorescence

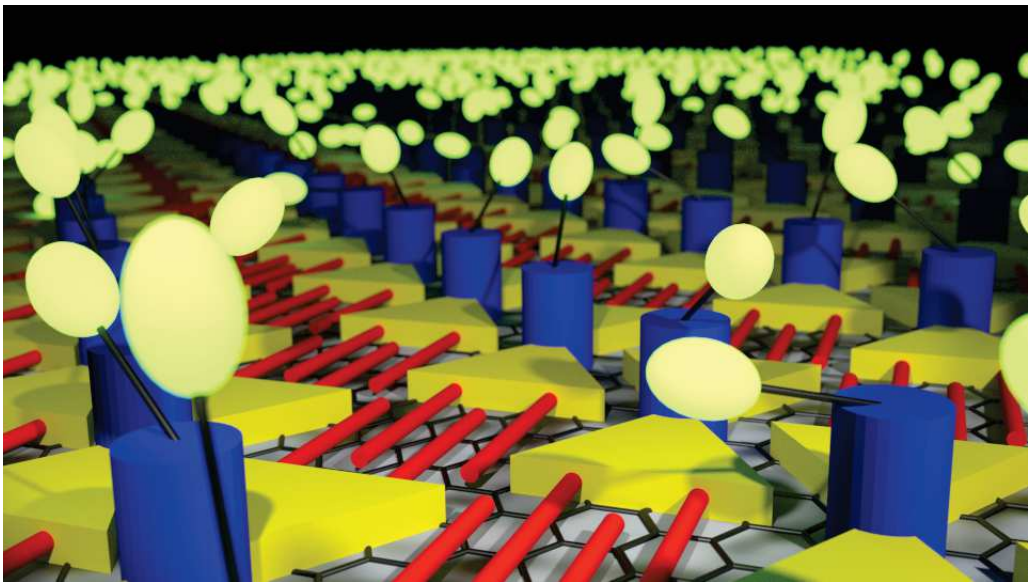

Artist view of a fluorescent Janus Tecton self-assembly on graphene.
Very surprisingly, a self-assembled dye monolayer on graphene, the thickness of which is of the order of a nanometer, can add a macroscopic optical absorption to the graphene surface. Since dye molecules can emit light, would it be possible to add a fluorescent character to graphene thanks to a self-assembled dye monolayer?

Contents

2.1 Theoretical considerations

2.1.1 Relaxation paths

When a photon is absorbed by a dye molecule, the electron cloud distribution is changed to form the excited state of the molecule. Figure 2.1 displays the highest occupied molecular orbital (HOMO) and the lowest inoccupied molecular orbital (LUMO) depicting the highest energy orbital occupied by an electron for the fundamental and the excited state respectively of the Me-PTCDI molecule.

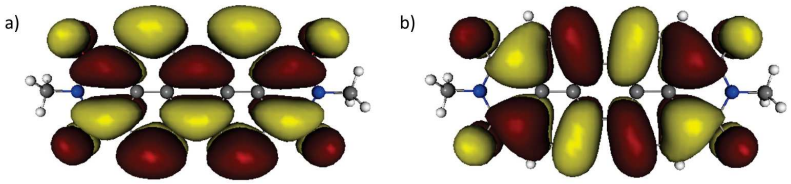

Figure 2.1: LUMO (a) and HOMO (b) of Me-PTCDI. The relaxed geometry has been calculated with the constraint DFT at the B3LYP/TZ level. Figure from ref.[100]

It is clear that an incident electro-magnetic field, a photon, can act on the electron distribution through the Coulombic force to excite the dye molecule from its S0 to S1 state. How a dye molecule can relax the absorbed energy? Several competing mechanisms take place in molecules, due to their unique properties and complexity.

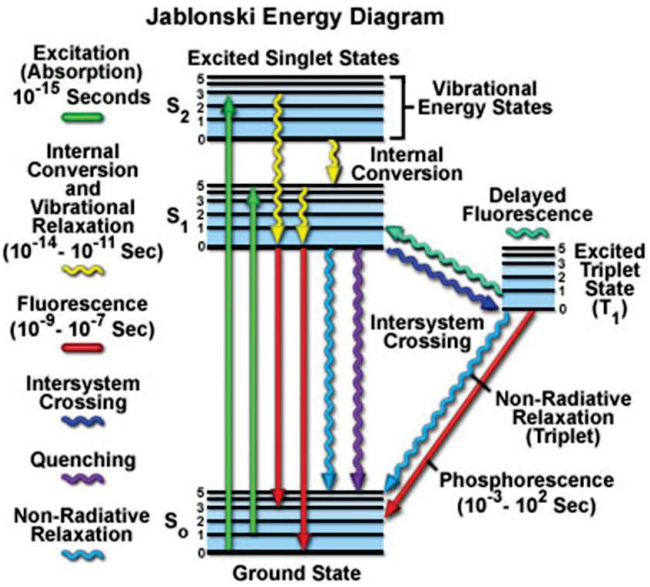

Figure 2.2: General Jablonski Energy diagram for light-molecules interactions .

The possible desexcitations mechanisms are displayed in Figure 2.2. A molecule in its excited state usually relaxes rapidly to a more stable vibrational state by emitting an IR radiation. The presence of these vibrational modes is at the origin of the red-shift between the absorption and fluorescence band of a dye molecule, named Stokes shift. When an excited state is stable enough in time, the energy can be radiatively relaxed with the emission of a visible photon (fluorescence).

The energy can also be transferred to a long-lived triplet state through a so-called intersystem crossing mechanism. From this triplet state, the energy is relaxed into the ground state either by a radiative process (photoluminescence) or by a chemical process (electron transfer). The chemical process is responsible of reactive oxygen species (ROS)

formation, which is supposed to eventually cause the dye fluorescence bleaching by modification of the dye chemical structure. Finally, a last mechanism consists in total internal conversion of the energy by the emission of multiple IR radiations. For example, ADN and melanin relax more than 99% of their absorbed energy through rapid internal conversion. This characteristic avoids the formation of ROS and thus can be considered as a protection since they avoid their degradation. Efficient dyes can reach very high rates of fluorescence. In free space the probability for a molecule to spontaneously emit photons is described by the A_{21} Einstein coefficient. However, the fluorescence rate is strongly affected by the environment surrounding the molecule. It is possible to favor a radiative relaxation when the local electromagnetic density of modes is increased, the so-called Purcell effect.[120] But the electromagnetic mode to which the dye molecule is coupled can be dark. For example, dye molecules on top of a metal surface can relax very rapidly their excited-state energy into a plasmon polariton mode that involves both charge motion in the metal and electromagnetic waves. However, surface plasmon polaritons do not radiate in free space (i.e. dark modes) unless certain conditions are filled.

2.1.2 Energy transfer mechanisms

Photonics active systems, such as loss compensators or lasers, require maximizing the radiative recombination probability (either spontaneous or stimulated). Physical phenomena that non-radiatively absorb the excited-state energy and thus lower radiative recombinations are defined as quenching mechanisms, and can be categorized as either Förster or Dexter mechanisms. Förster mechanism describes radiative transfer of the dye molecule excitation energy to any other excitation mode, mediated by the near-field, that is describable in the quasi-static approximation, usually donor dipole - acceptor dipole interactions. Depending on the either dark or radiative nature of this excitation acceptor mode, the Förster transfer produces a quenching or an enhancement of the radiative decay, respectively. In the latter case, the acceptor plays the role of an optical antenna.

The above example of a dye on top of a metallic substrate enters the quenching category. The dye molecule can possibly have a higher probability of transferring excitation energy to the plasmon polariton mode than to vacuum electromagnetic modes when isolated, but the plasmon mode does not radiate unless a wavevector matching mechanism, usually a prism or a grating, decouples the surface plasmon polariton to a photon.

Dexter mechanism describes excitation energy transfer through a direct exchange of charges by electron tunneling with another quantum system. As for the Förster mechanism, such energy transfer can result in an enhancement or a quenching of the radiative decay depending on the electron acceptor radiative or dark nature respectively. However, in practice Dexter mechanism most often leads to a quenching of the molecule radiative decay.

This mechanism happens when the dye molecule is at a tunneling distance from another system. For example, if a dye is very close from a metallic surface (typically 1 nm or less), the overlap between the LUMO and the electronic wavefunction of the metal is not zero. An electron transfer probability arises, thus competing with the radiative decay path.

At typical aromatic molecules π-stacking distances (0.3 nm), Dexter energy transfer is sensibly faster than Förster energy transfer.[121]

The understanding and the control of a dye molecule environment is therefore essential to engineer its radiative emission.

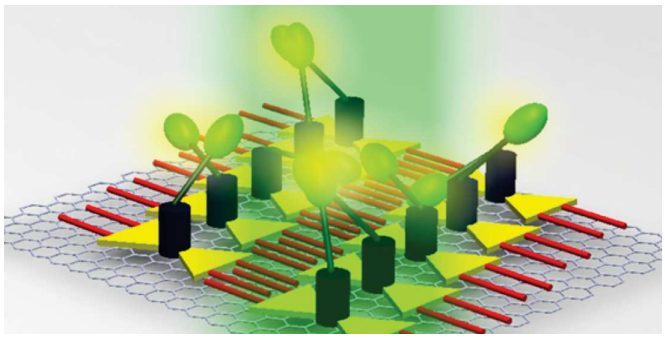

Figure 2.3: Artist view of graphene fluorescent non-covalent functionalization by a PTCDI-JT supramolecular self-assembly.

2.2 Janus Tecton on graphene

2.2.1 PTCDI-JT

In chapter 1, we have seen that the distinctive optical absorption signatures of self-assembled dye-graphene architectures, the structure of which were confirmed by scanning tunneling microscopy, can be analyzed by absorption microspectroscopy.[122] However, the main challenge remains the emission of light by such systems, since graphene is known as a strong quencher through Dexter excitation transfer between the dyes and the graphene.[123,124,125] Hence, the realization of light-emitting devices based on dye-graphene assemblies requires overwhelming Dexter transfers through introduction of an accurately controlled dye-to-graphene electron barrier, from which planar flat-lying molecules are deprived. Self-assembling building blocks of increasing three-dimensional (3D) complexity emerged recently, in particular following the so-called Janus tecton paradigm.[126,127] These systems have been proposed as a platform to attach functional molecular moieties at a controlled distance from graphene.[47]

In this chapter, we demonstrate the first fluorescent supramolecular self-assembly on graphene with a specifically designed 3D Janus tecton. We investigate its two-dimensional ordering by scanning tunneling microscopy (STM) and its surface optical properties by absorption and fluorescence spectroscopies.

Results and Discussion. The 3D Janus tectons are dual-functionalized and present two faces linked by a rigid spacer. One face is designed so as to steer the self-assembly on graphene, and, for the present study, the other is a dye unit.[126,127,47] More specifically, the dual-functionalized 3D tecton consists of a 3,4,9,10-perylenetetracarboxylic diimide (PTCDI) fluorophore linked to a graphene-binding pedestal by a dithiaparacyclophane pillar and a long leash made of one flexible alkyl chain and a stilbenic unit (Figure 2.4).

The pedestal also prevents the direct adsorption of the dye onto graphene and forms a tunneling barrier for electrons. It is thus expected to slow down Dexter energy transfers from the dye to the graphene layer. The pedestal unit consists of two molecular clips likely to steer the self-assembly of the whole entity. The clipping motif consists of two $C_{10}H_{21}$ alkyl chains, which, upon physisorption, lay flat on the surface and aligned along the (110) crystallographic direction of graphene. When two such units interdigitate, their lateral self-assembly leads to the formation of lamellae whose crystallographic structure is equivalent to the one observed upon adsorption of linear alkanes. The resulting enhanced 2D crystallization energy is at the origin of the binding nature of the clip.[123] In the following paragraphs, this functional 3D Janus tecton will be designed as PTCDI-JT. The spectroscopic properties of PTCDI-JT either in solution or self-assembled on graphene will be compared to those of a PTCDI-C13 model system studied in chapter 1.The self-assembly

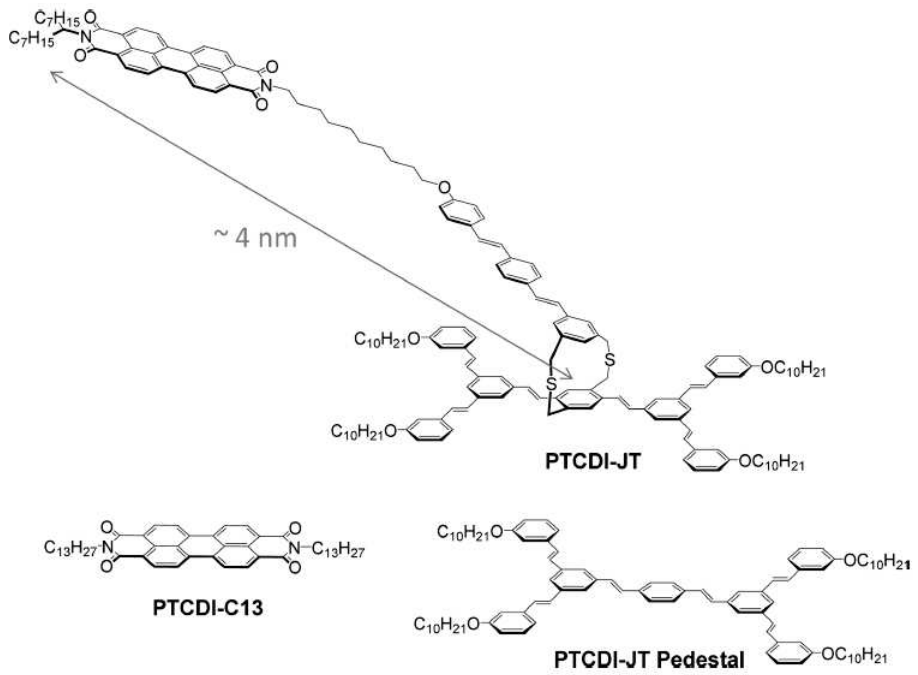

Figure 2.4: Schematic Structures of the Two-Faced Janus Tecton PTCDI-JT, PTCDI-JT Pedestal, and N,N′-Ditridecyl-3,4,9,10-perylenedicarboximide PTCDI-C13 Molecules.

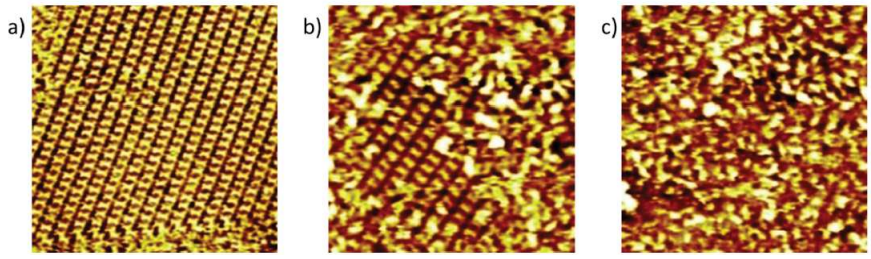

Figure 2.5: STM images at the liquid/HOPG interface at room temperature: (a) 1:4 mixture of Janus tecton and pedestal molecule ($60nm \times 60nm$, $It = 8.6pA$, $Vt = -1320mV$); (b) 1:1 mixture of Janus tecton and pedestal molecule ($50nm \times 50nm$, $It = 9.9pA$, $Vt = -1602mV$); (c) Janus tecton solution ($50nm \times 50nm$, $It = 8.6pA$, $Vt = -1596mV$).

properties of PTCDI-JT on sp^2-hybridized carbon-based substrates were investigated by STM at the liquid/solid interface at room temperature. As already observed in chapter 1, the roughness imposed on the CVD graphene monolayer by the underlying polyethylene terephthalate (PET) substrate makes STM observations difficult due to the poor contrast of molecules compared to this roughness. (Figure 2.6) More accurate observations are obtained with an HOPG substrate and will be preferentially used in what follows.

The image sequence displayed in Figure 2.5 corresponds to observations recorded at the liquid/HOPG interface for three different solutions: (a) 1:4 ratio solution of PTCDI-JT to the PTCDI-JT pedestal, i.e., the naked precursor clipping unit, which constitutes the base of the Janus tecton; (b) an equimolar mixture of the PTCDI-JT and PTCDI-JT pedestal; and (c) a solution of pure PTCDI-JT.

The independent pedestal unit is known to self-organize at the graphite surface, forming a two-dimensional network with the following parameters: $a = 3.8nm, b = 2.1nm, \alpha = 64°$.[128] Accordingly, STM images obtained with the 1:4 mixture (Figure 1a) display large domains of a well-ordered arrangement of the clipping molecules forming the same surface

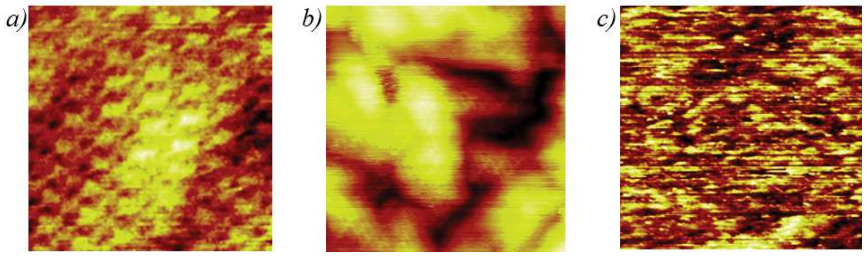

Figure 2.6: Structural characterization of the self-assembled a) PTCDI-C13 ($18nm \times 18nm, 10pA, -800mV$), b) PTCDI-JT pedestal ($75nm \times 75nm, 3pA, -1350mV$) and c) 1:1 ratio of PTCDI-JT and PTCDI-JT pedestal ($38nm \times 38nm, 5pA, -1560mV$) monolayers on graphene on PET. The images were acquired at the interface between the substrate and a $10^{-5}M$ solution in phenyloctane at room temperature.

lattice. Experimentally, due to a smaller molecule size, which reduces its steric constraints, the clipping molecule is shown to self-assemble more easily on graphite than the 3D Janus tecton. Upon increase of the PTCDI-JT relative concentration in the applied solution, STM images of the surface display smaller domains of the clipping molecule arrangement together with areas presenting bright spots with rough alignments reminiscent of the underlying ordered regions. Both domains appear in similar proportions to that in the solution. These misaligned bright features are the signature of the physisorbed PTCDI-JT molecules. Indeed, as far as molecular contrast is concerned, STM favors the signature of aromatic skeletons which present higher electronic surface density of states close to the Fermi level.[91] In the present case, the long and flexible alkyl spacer permits various locations of the PTCDI upper group relative to its pedestal, concealing the periodic signature of the clipped pedestals in the horizontal plane. Still, the spatial distribution of these terminal PTCDI groups is not completely random, suggesting that neighboring dye groups do aggregate themselves to form few-dye clusters.

For a pure solution of PTCDI-JT, the STM images show a quasi-random distribution of bright spots tentatively associated with clusters of aggregated neighboring PTCDI dye moieties, and the pedestal network is completely hidden. To get rough estimates of the dye cluster size and spatial distribution, we built an approximate model based on simple molecular mechanics. Estimating the distance between the end of the fluorescent unit and the dithiaparacyclophane bridge in PTCDI-JT to be 4 nm (see Figure 2.4), we computed the possible number of overlapping fluorescent units in every point of the overlying 3D space based on the known surface lattice parameters of the two-dimensional clipped network (Figure 2.7).

In this rough model, the aggregation of independent molecules was modeled with all molecules found at the same location; that is, the dimensions of the cluster itself are neglected. This simulation shows the possible aggregation of up to nine fluorescent groups belonging to different neighboring PTCDI-JTs. Looking at the dimensions of the clipped network surface lattice, the parameter a along the interdigitated alkyl chain direction is approximately twice the parameter b along the lamella axis. Consequently, the dye upper groups are expected to interact more importantly with their respective neighbors along the b direction. One can then reasonably predict the existence of stronger interacting subclusters of an even number of molecules. More specifically, the detailed simulation yields a bimodal distribution of the subcluster sizes, whose principal band corresponds to a cluster size value of 6 ± 1 (Figure 2.8).

The most probable location of such a six-dye cluster is computed to be 1.6 nm above the dithiaparacyclophane rigid pillar and 2.8 or 4.2 nm away from the bridge in the horizontal plane. The pillar height amounts to about 0.6 nm. The adsorption of the PTCDI-JT

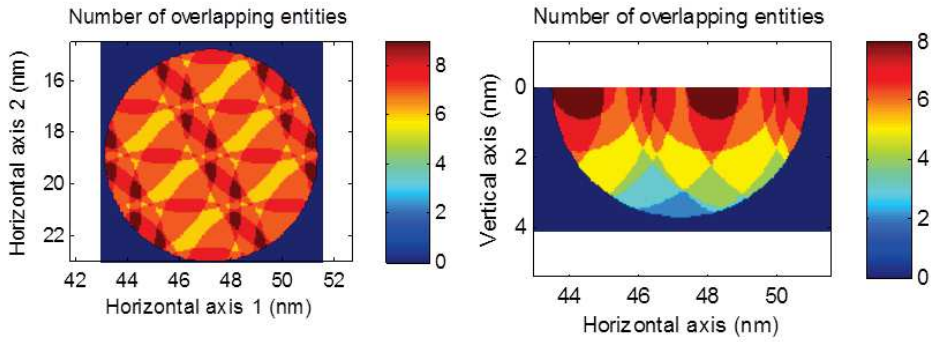

Figure 2.7: Map of the self-assembled PTCDI-JT tecton indicating the maximum number of aggregated dye moieties in a parallel (left) and perpendicular (right) plane to the substrate, obtained as the number of intersecting half-spheres assuming each dye is located within a 4 nm distance from the center of its pedestal.

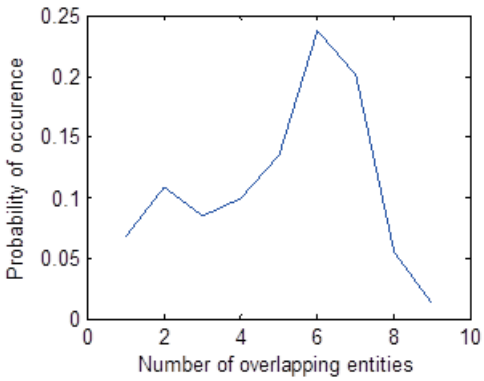

Figure 2.8: Occurrence probability of dye aggregate size.

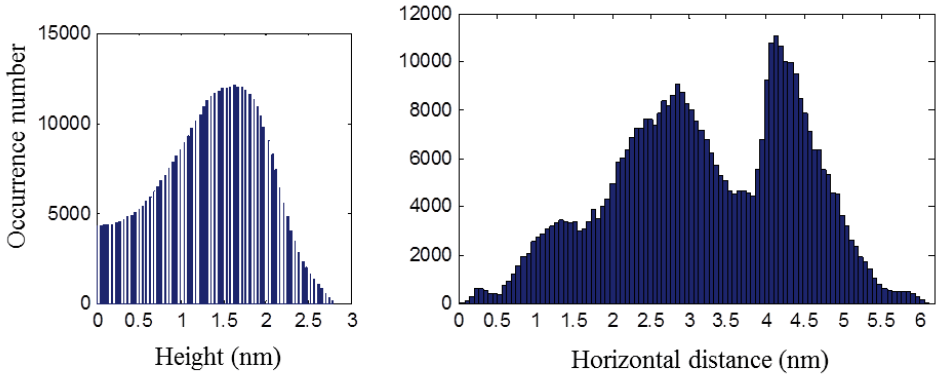

Figure 2.9: Spatial distribution above and away from the disulfur pillar of the 6 sized dye aggregate.

pedestal is driven by the physisorption of its aliphatic chains. The aromatic core of the basal unit lies flat on the graphene sheet at a respective distance of 0.33 nm.17 So, adopting a static view of the PTCDI-JT arrangement, the clusters of dye moieties lay at about 0.33 + 0.6 + 1.6 = 2.53 nm above the graphene substrate (Figure 2.9).

Experimental UV-visible absorption spectra of the PTCDI-JT and the PTCDI-C13 molecules in toluene are reported in Figure 2.10.

The light absorption by the clipping motif manifests itself in the UV range of the spectrum ($\lambda < 420nm$) and corresponds to the one recorded for the independent PTCDI-JT pedestal. The band at 330 nm and the shoulder at 375 nm are assigned respectively to the four terminal stilbene units and to the central distilbene unit. This shoulder in the PTCDI-JT absorption spectrum appears to be 2 times larger in accordance with the presence of another distilbene on top of the disulfur pillar. In the visible range $420nm < \lambda < 550nm$, the PTCDI-JT absorption matches very well that of the independent PTCDI-C13 dye. This unaltered spectroscopic signature of the core dye moiety demonstrates that the spacer effectively decouples the conjugated electron systems of fluorophore and pedestal units. The absorption spectra of self-assembled monolayers of PTCDI-JT and PTCDI-C13 on graphite are compared with a corresponding toluene solution in Figure 2.11.

The relative band absorption level of the PTCDI-JT monolayer (0.4%) is nearly 6 times smaller than that of PTCDI-C13 (2.3%). Considering a similar absorption cross section, a surface density of PTCDI-C13 of 0.5 $molecules/nm^2$, and a 2/3 orientational factor since the PTCDI-C13 molecules are lying flat on the graphene surface[122] whereas PTCDI-JT dye moieties are randomly oriented, one can estimate a Janus tecton surface density of 0.12 ± 0.03 $molecules/nm^2$. This value is consistent with the surface density derived from the surface lattice determination by STM of a PTCDI-JT self-assembled monolayer on HOPG:[127] 0.14 $molecules/nm^2$. This numerical estimate further supports the conclusion that PTCDI-JT are regularly self-assembled on the graphene surface following the expected binding scheme of the clipping pedestal units taken independently.

Both PTCDI-JT and PTCDI-C13 absorption lines drastically change when self-assembled onto graphene as compared with a toluene solution (Figure 2.11). Whereas the PTCDI-C13 absorption merely consists in a rigid red-shift compared with the solution, the situation is more complex for PTCDI-JT. Despite a reduced signal-to-noise ratio, an increased

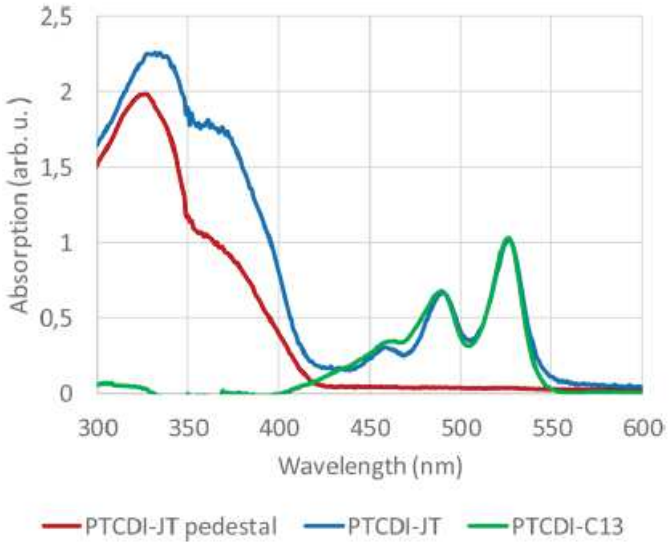

Figure 2.10: Normalized solution absorption spectra of the PTCDI-JT pedestal, PTCDI-JT, and PTCDI-C13 in toluene.

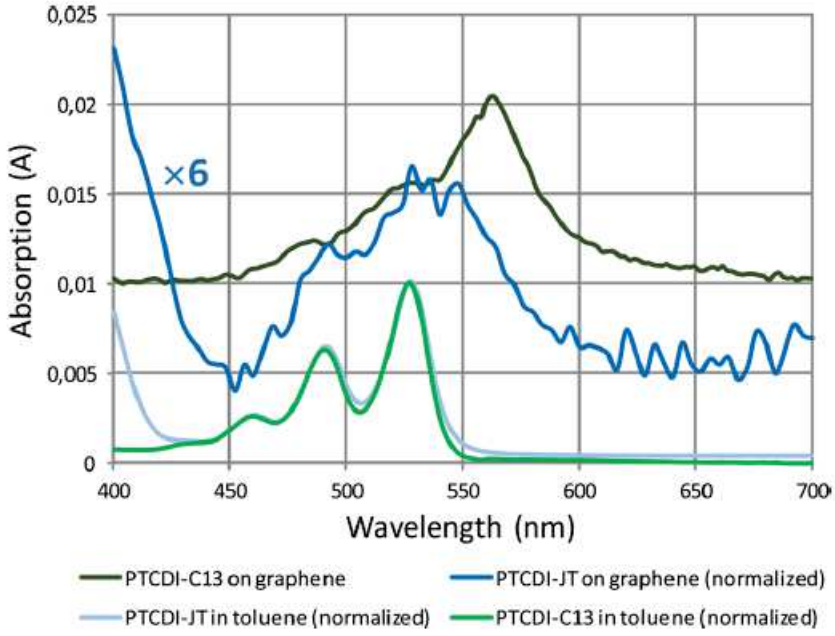

Figure 2.11: Absorption spectra of PTCDI-JT and PTCDI-C13 self-assembled on graphene. The CVD graphene sheet has been transferred from Cu onto a transparent PET substrate prior to self-assembly. The measurements were done in transmission, referenced to naked graphene. Because of the absorption of PET in the UV, the spectra are limited to $\lambda > 400$ nm.

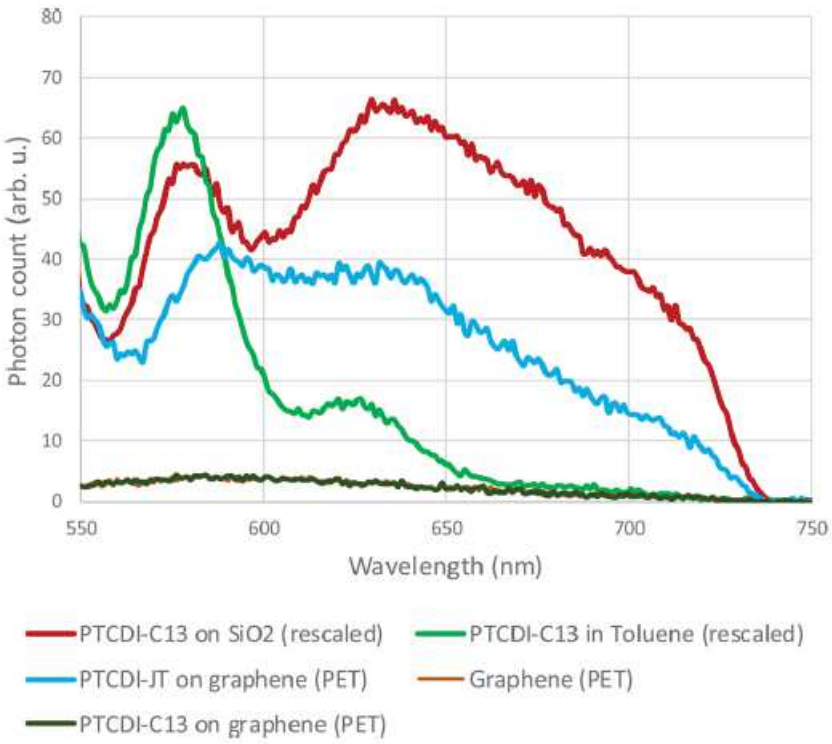

Figure 2.12: Photoluminescence spectrum of self-assembled PTCDI-JT on graphene (blue) compared with PTCDI-C13 reference signals in toluene (green, rescaled), self-assembled on graphene (black), and in the microcrystal solid state (red, rescaled). The molecules are excited by a continuous wave laser operating at 532 nm wavelength, which hides the principal fluorescence band (0-0 line) for all the systems.

weight of higher-order vibronic replicas is perceptible and the rising edge appears less abrupt, which can correspond to a spectral broadening. The red-shift observed for PTCDI-C13 is explained by the adsorption of its aromatic core, which lies flat on graphene at a typical π-stacking distance of 0.33 nm.[122] As inferred from STM analysis in the previous section, for PTCDI-JT, the corresponding distance is much larger. According to the static model discussed above, the distance from the dye moieties to the graphene is typically 7 times larger (2.5 nm), which prevents such interactions. In contrast with PTCDI-C13, the dye moieties of PTCDI-JT form few-molecule clusters. The increase of higher-order vibronic bands is typical of a H-aggregate behavior which can result from a π-stacking configuration inside clusters.[129,130,59] The spectral broadening of the vibronic spectral features, already present in self-assembled PTCDI-C13, is further increased for PTCDI-JT. This probably reflects the inhomogeneity of the dye-moiety assembly, as evidenced by STM imaging of the PTCDI-JT tectons, which evidence dye clusters with various sizes.

The main result of this chapter is presented in Figure 2.12, in which the fluorescence signals of the PTCDI-JT molecule self-assembled on graphene are compared with those of the PTDCI-C13 reference as recorded in solution, in a self-assembled monolayer on graphene, or in solid-state microcrystals as formed by casting the same PTCDI-C13 toluene solution onto naked fused silica instead of graphene.

A photoluminescence signal of the PTCDI-JT self-assembly on graphene is readily measurable, whereas no such signal can be detected from the PTCDI-C13 ordered domains on the same substrate. Hence, the design of PTCDI-JT based on a spacer between the dye and graphene actually reduces the energy transfer rate. The measured fluorescence quantum yield is still low, estimated in the range of 2×10^{-5} to 2×10^{-6} by integrating

the fluorescence signal between 560 and 745 nm for an excitation at 532 nm. Since the radiative decay rate of PTCDI is on the order of $10^{-9}s^{-1}$, the quenching rate is in the range $10^{14}s^{-1}$ to $10^{15}s^{-1}$. Although still high, this value is compatible with a residual Förster resonance energy transfer, the Dexter transfer being slower for the distances between dye and graphene that were estimated above. The formation of clusters also strongly affects the characteristics of luminescence. Although the above-mentioned H-aggregate coupling is supposed to slow the radiative decay in favor of the quenching, PTCDI-C13 is fluorescent in the solid state, as shown with the fluorescence of microcrystals formed on silica. Nonradiative relaxations are thus hindered by the strong interactions between stacked molecules. The fluorescence spectrum of PTCDI-JT self-assembled onto graphene (Figure 2.12, blue curve) is intermediate between that of the PTCDI-C13 solvated in toluene (green curve) and that of PTCDI-C13 microcrystals on silica (red curve), showing a progressive displacement of the oscillator strength toward higher vibrational replicas with cluster size, consistent with the H-aggregate-like coupling deduced from absorption spectroscopy. A shorter exciton coherence length in self-assembled clusters is consistent with the involvement of a small number of dye groups, spatially limiting the coherent delocalization of the exciton, which is on the order of 2 nm for similar crystals.[130,131] Furthermore, the H-aggregation geometry could be perturbed from a perfect π-stacking by the spacer steric hindrance. Instead of being parallel, aromatic cores can adopt an angle that partially decouples the transition dipole moments. This suggests that the controlled formation of few-molecule dye clusters plays a role in the restoration of luminescence. Note that the Janus tecton surface fluorescence band is slightly redshifted from the PCTDI-C13 ones, consistent with its redshifted absorption.

2.2.2 TBC8-JT

PTCDI-JT forms small aggregates once self-assembled on the graphene surface due to a long and flexible alkyl chain linking the disulfur bridge and the perylene dye group. A more rigid Janus tecton is desired to gain control on the optical properties of such graphene non-covalent functionalization, for example avoiding the formation of small aggregates. The Janus tecton approach is further explored with TBC8-JT (see chapter 1) which does not possess such flexible group in its structure. The optically active group is directly linked to the disulfur bridge. Scanning tunneling images confirm a periodic network formation without any aggregation. Figure 2.13 displays the absorption and photoluminescence spectra of TBC8-JT either dissolved in phenyloctane or self-assembled on graphene.

A fluorescence signal is detected from the self-assembled TBC8-JT monolayer on graphene (green curve). Surprisingly, the photoluminescence spectrum band and global shape of self-assembled TBC8-JT monolayer on graphene is quite similar to the same molecule in a phenyloctane solution. Since the absorption band is redshifted once adsorbed on the graphene surface, one should have expected to see this effect also on the photoluminescence spectrum that is a preservation of the Stokes shift. The 420 meV Stokes shift of TBC8-JT in a phenyloctane solution is reduced to 230 meV once self-assembled on the graphene surface.

The measured fluorescence lifetime of TBC8-JT in solution when exciting at 400 nm by a doubled femtosecond Ti:Sapphire laser is 4.0 ns. When self-assembled on graphene, the fluorescence lifetime is reduced to 2.7 ns. Hence, even if no differences can be observed on fluorescence spectra, fluorescence lifetime measurements reveal the decrease of the radiative desexcitation lifetime and thus the increase of the non-radiative decay. A Förster quenching by the graphene layer may be the cause of this fluorescence lifetime perturbation since the optical active group seems too far away from the graphene surface for charge transfer to occur. However, it is still not clear why the fluorescence spectrum is not shifted identically to the absorption spectrum and we prefer to do not draw a conclusion due to the

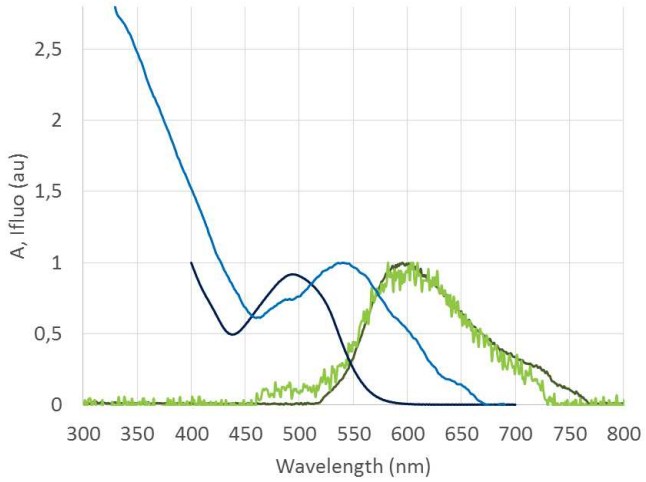

Figure 2.13: Normalized photoluminescence and absorption spectra of self-assembled TBC8-JT on graphene (photoluminescence: light green, absorption: light blue) compared with TBC8-JT reference signals in phenyloctance (photoluminescence: dark green, absorption: dark blue). The molecules are excited by a doubled femtosecond Ti:Sapphire laser operating at 400 nm wavelength.

resemblance between the solution and self-assembled spectra and to the long fluorescence lifetime. Small molecular aggregates decoupled from graphene have possibly remained on the surface, taking little part in the absorption spectrum due to their limited number but having a significant weight in the fluorescence spectrum due to their decoupling from graphene.

2.3 Multilayers of Perylene derivatives

Few dyes molecules display fluorescence in solid state. Their aggregation often dramatically changes their photophysics properties by shifting absorption band and increasing radiative decay rate. Non radiative path are usually favored due to interactions of molecules with the close environment, such as charge transfers resulting in Dexter quenching. However, fluorescent dyes in the solid state are highly desirable since this state represents the highest reachable density for these emitters. Such compact emitter systems could lead to the miniaturization of gain media for laser systems and become perfect media for interacting with highly confined electromagnetic modes paving the way to the realization of nanolasers.

In the following, we study the optical response of perylene derivatives in a solid state. Figure 2.14 displays the molecular structures and the fluorescence spectra of a 30 nm thick PTCDI-C7 thin film, a 1 nm thick PTCDI-C7B thin film and a PTCDI-tBuPh crystal produce by the evaporation of a PTCDI-tBuPh in toluene solution on a glass coverslip at ambient conditions.

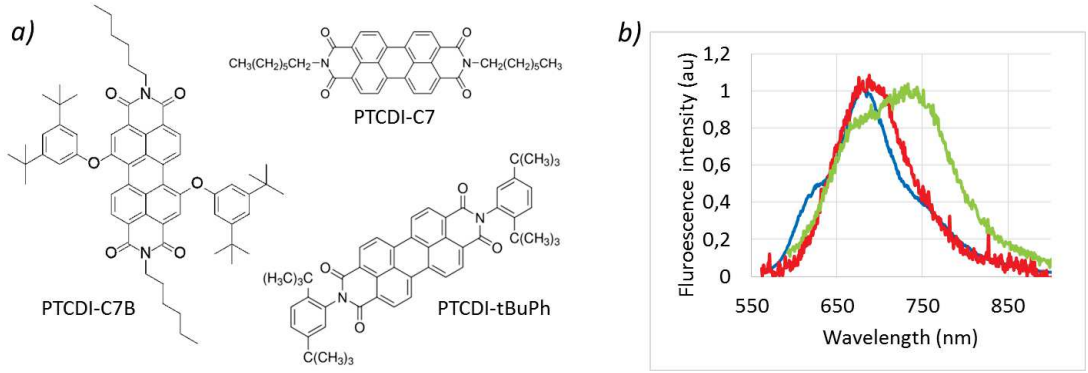

Figure 2.14: a). Molecular structures of PTCDI-C7, PTCDI-tBuPh and PTCDI-C7B. b). Normalized fluorescence spectra from a 30 nm thick PTCDI-C7 thin film (blue), a 1 monolayer PTCDI-C7B thin film (green) and a PTCDI-tBuPh cristal evaporated under ambient condition on a SiO2 coverslip (red). The systems are excited with a 532 nm continuous wave laser.

From the different perylene derivative spectra three main bands can be isolated at 630 nm, 680 nm and 730 nm that correspond to transitions from an excitonic state to the vibrational replicas of the molecule fundamental state.[132] The energy gap between these three bands are respectively 145 meV (1170 cm^{-1}) and 125 meV (1010 cm^{-1}). These values are a slightly smaller than C-C vibrational modes in conjugated aromatic molecules that fall around 174 meV (1400 cm^{-1}).

The fluorescence spectra peak at 680 nm for the PTCDI-C7 and PTCDI-tBuPh systems and at 730 nm for the PTCDI-C7B system, revealing a large Stokes shifts since the optical absorption peaks at 500 nm for the PTCDI-C7 and PTCDI-tBuPh systems and at 560 nm for the PTCDI-C7B system (Chapter 1). The formation of self-trapped excitons due to strong exciton-phonon coupling results in low energy states (ST), lower than free exciton states, that can explain such large Stokes shifts in these solid state systems.[133]

A direct comparison with a R6G/PMMA reference system gives a fluorescent quantum yield of approximately 10% for the 30 nm thick PTCDI-C7 thin film.

Each systems display various oscillator strength distributions over these bands. The PTCDI-C7 film decays mainly radiatively with the ST-1 path corresponding to a transition between the ST state and the first vibronic replica of the electronic fundamental state (680 nm band), as PTCDI-tBuPh does. However, the 630 nm band is not visible for the latter. Finally, the ST-2 transition (730 nm band) is the preferential radiative decay path for the PTCDI-C7B. These various oscillator strength distribution over vibronic replicas may result from H/J aggregate behavior arising from differences in the π-stacking geometry of the perylene aromatic cores.[59]

2.4 Conclusion

In summary, we have achieved the first fluorescent molecular self-assembly on graphene. This milestone has been made possible thanks to the development of a 3D Janus tecton embedding a PTCDI dye away from the substrate plane together with the use of CVD graphene as an optics-compatible 2D substrate. A fluorescent noncovalent functionalization of graphene could help to alter the photonic properties of this zero-gap semiconducting monolayer or to alter photonic properties of any third-party surfaces through transfer of monolayer CVD graphene. Furthermore, we obtained a dense three dimensional dye self-assembly displaying relatively good quantum fluorescence efficiency. This dense packing of fluorescent molecules could be of prime importance for maximizing the coupling between

emitters and strongly confined electromagnetic modes such as plasmonic waves.

Chapter 3

Vibrations of supramolecular self-assemblies on graphene

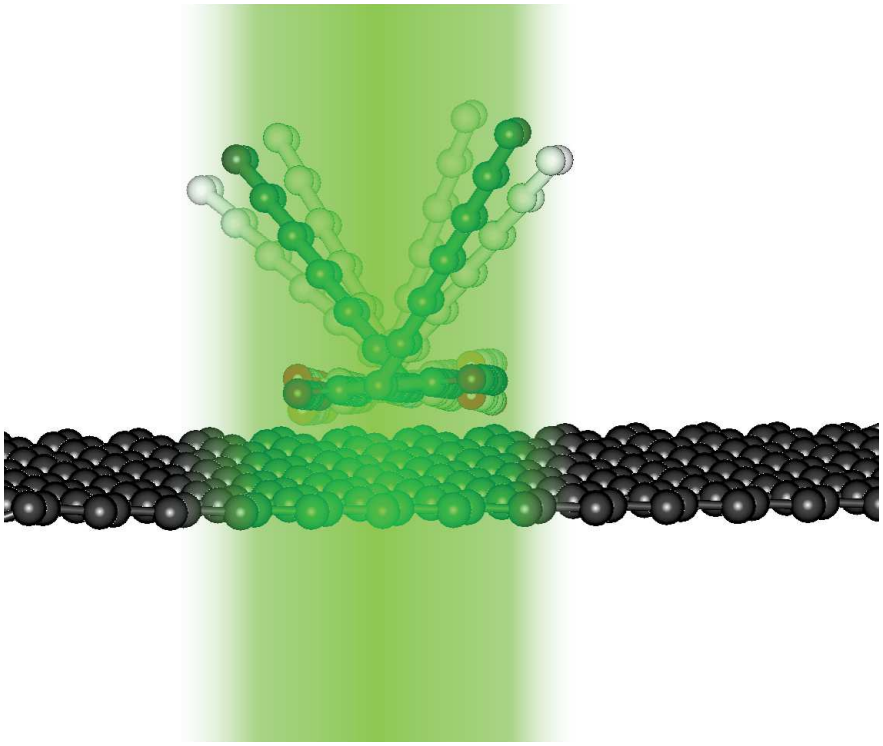

Artist view of the Mambo mode, a vibrational mode coupled between graphene and a self-assembled molecule on its surface.
The study of this mode characteristics may lead to the development of a sensor identifying aromatic molecules adsorbed on the graphene surface.

Contents

As explained in previous chapters, supramolecular self-assemblies on graphene provide opportunities for the design and the manufacturing of innovative hybrid photonic devices.

On its part, Raman spectroscopy has become an invaluable tool to characterize graphene with or without any functionalization since the active vibrations convey important information about graphene purity, defects or doping.[134] In the framework of chemical doping, most of the information about electron transfer is given by the width and the position of the G and 2D bands of graphene.[135] To our knowledge, other couplings, in particular mechanical coupling between graphene and adsorbed organic molecules, have not yet been explored.

The complete fluorescence quenching of resonant dyes adsorbed on graphene, by Dexter processes, allows a clear observation of Raman scattering. Actually, even under resonant conditions, Raman signals are orders of magnitude weaker than fluorescence. Moreover, it has been recently discovered that graphene can enhance the Raman signal of adsorbed molecules by a process which is physically similar to the chemical contribution to surface-enhanced Raman scattering (SERS).[136] These two effects represent a unique opportunity to explore the physical vibrational properties of systems comprising self-assembled molecules adsorbed on graphene by resonance Raman spectroscopy.[137] Recent theoretical work on the interpretation of Raman spectra modified by neighbor interactions will opportunely supplement such studies.[138,139]

In this chapter, we study the vibrational coupling between a free-standing graphene membrane and organic molecules self-assembled on its surface: a DFT simulation illustrates in a simple system the nature of coupled graphene-adsorbate vibrational modes. Experimental Raman spectra of a self-assembled resonant dye on graphene confirm the existence of such coupled modes. Scanning tunneling microscopy is performed to study the effect of the molecular network on the graphene-molecule vibrational coupling.

3.1 Introduction to Raman scattering

The vibrational modes of a system manifest themselves in the interaction with light. The signature of such low frequency modes (usually in the $0-90\ THz$ or $0-3000\ cm^{-1}$ or $0-370\ meV$ or $3.3-\infty\ \mu m$ range) can be probed by several ways. In the case of a dye absorbing in the visible range, these vibrational properties can be seen in the visible absorption spectrum, in the infrared absorption spectrum and in the Raman scattering of light.

The origin of Raman scattering can be understood by approximating the system polarizability α in a Taylor series approach.

When atom vibrations are involved in the polarizability resonance, one can introduce the displacement parameter dq which describes the motion of atoms in time about their equilibrium position.

$$dq = q_0 cos(\omega_v t) \tag{3.1}$$

where ω_v represent the angular frequency of a vibrational mode. Since the atom displacement remains quite small, the polarizability can be evaluated around the atom equilibrium position with a Taylor series:

$$\alpha = \alpha_0 + \frac{d\alpha}{dq}(0)dq + \frac{1}{2}\frac{d^2\alpha}{dq^2}(0)dq^2 \tag{3.2}$$

The dipole moment μ of the system can then be expressed with an incident electric field $E = E_0 cos(\omega t)$:

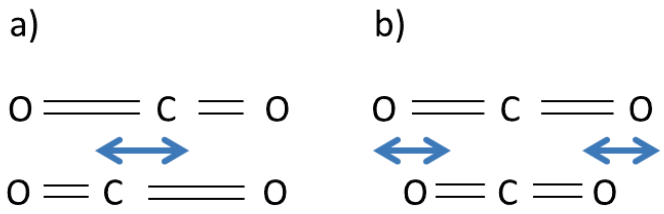

Figure 3.1: Anti-symmetric (a) and symmetric (b) vibrational mode of the CO_2 molecule. (a) is not Raman active whereas (b) is.

$$\mu = \alpha E = \alpha_0 E_0 cos(\omega t) + \frac{d\alpha}{dq}(0) q_0 E_0 cos(\omega t) cos(\omega_v t) + \frac{1}{2}\frac{d^2\alpha}{dq^2}(0) E_0 q_0 cos(\omega t) cos^2(\omega_v t) \tag{3.3}$$

$$\mu = \left[\alpha_0 + \frac{1}{4}\frac{d^2\alpha}{dq^2}(0) q_0^2\right] E + \frac{1}{2}\frac{d\alpha}{dq}(0) q_0 E_0 \left[cos((\omega + \omega_v)t) + cos((\omega - \omega_v)t)\right] + \frac{1}{8}\frac{d^2\alpha}{dq^2}(0) E_0 q_0^2 \left[cos((\omega + \omega_v)t) + cos((\omega - 2\omega_v)t)\right] \tag{3.4}$$

The above equation shows that induced dipole moments are created at the frequency ω which correspond to elastic scattering but also at inelastic frequencies $\omega - \omega_v$ and $\omega + \omega_v$ which are respectively referred to Stokes and anti-Stokes Raman scattering. From the above equation, these processes exist if the derivative of the polarizability with reference to the displacement is non null at the equilibrium position. As an example, figure 3.1 represents two vibrational modes of the CO_2 molecule. The polarizability in the anti-symmetric mode has a symmetrical behavior with reference to atom displacement about the equilibrium position. Therefore, $\frac{d\alpha}{dq}$ evaluated at the equilibrium position is zero and the mode is not Raman active, meaning no Raman processes can exist. This is not the case for the symmetric vibrational mode since the polarizability does not behave identically for positive or negative atom displacement about their equilibrium position. $\frac{d\alpha}{dq}(0)$ is non zero meaning that this mode is Raman active. The above equation also shows that overtones in Raman spectra are related to higher-order derivatives of the polarizability with reference to displacement. For example, first harmonic exist if $\frac{d^2\alpha}{dq^2}(0)$ is non zero.

We compare in a Jablonski diagram (figure 3.2) the different processes where vibrational modes are involved for a dye absorbing light in the visible.

The presence of vibrational states can be probed by the absorption of IR photons with energy corresponding to the energy gap between two vibrational modes, corresponding to process (a) in figure 3.2. Vibrational modes are observable if a small atom displacement induces a variation of dipolar moment, i.e. $\frac{d^2\mu}{dq^2}(0)$ is non zero. Raman scattering can occur at any incident photon energy. When this photon energy is not able to excite any state of the molecule, the process involves a virtual state and is referred as non-resonant Raman diffusion (process (b) in figure 3.2). In the reverse situation, that is when the photon energy is able to excite a molecular level, one refers to resonant Raman scattering. In the case of a fluorescent dye, the fluorescence signal can then hide the Raman scattering signal since it displays exactly the same energy.

Finally, the presence of vibrational states can be probed in both the absorption and fluorescence spectrum since photon absorption (respectively photon spontaneous emission) is possible from the lowest energy vibrational state of the electronic fundamental (respectively excited) state to the various vibrational states of the electronic excited (respectively fundamental) state.

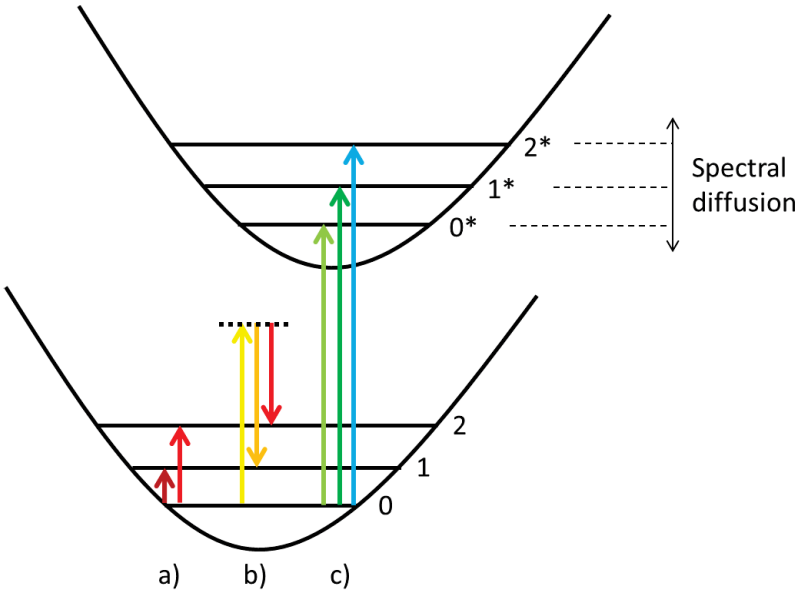

Figure 3.2: (a). Infrared absorption between the vibrational states 0-1 and 0-2 of the electronic fundamental state. (b). Non resonant Raman scattering implying a virtual state. (c) Visible absorption between the 0 electronic fundamental state and the 0*, 1* and 2* vibrational replicas of the electronic excited state.

The major difference between IR absorption and Raman scattering on one side and visible absorption on the other side is the fact that the energy of vibrational states is not probed with the same accuracy. Since visible absorption involves two different electronic states, spectral diffusion comes into the play and broadens consequently the transitions at ambient conditions. Thermal fluctuations ($kT = 25\ meV$ corresponding to a wavenumber of 200 cm^{-1}) and other dephasing processes significantly broadens the absorption lineshape. Raman scattering and IR absorption do not have these limitations and widths as small as 20 $cm^{-1} = 2.5\ eV$ can be observed under ambient conditions.

3.2 Graphene Raman spectrum

Raman spectroscopy is a powerful tool for the characterization of graphene. It can give insight about its purity in terms of defect density, number of stacked sheet, dopants.[135] A detailed understanding of graphene vibrational processes is needed before studying vibrational coupling with self-assembled monolayers on its surface.

Figure 3.3 displays the honeycomb lattice formed by the carbon atoms of graphene. The primitive cell of this Bravais lattice can be defined by the two primitive vectors in the direct space $\mathbf{a_1}$ and $\mathbf{a_2}$. In the reciprocal space, primitive vectors $\mathbf{b_1}$ and $\mathbf{b_2}$ are deduced from the two direct space primitive vectors as indicated in figure 3.3 where R represents a 90° rotation matrix.

The center of the Brillouin zone is called Γ point, vertices are referenced as K points, and the edge middles as M points.

Example Raman spectra of pristine graphene and damaged graphene are presented in figure 3.4. As displayed in spectra, three bands named D, G and 2D at 1350 cm^{-1}, 1580 cm^{-1} and 2700 cm^{-1} respectively are predominant. These bands correspond to two main vibrational modes on which we will focus in the following.

Scheme 3.5 represents the graphene lattice deformation due to the carbon atom motion of the vibrational mode implicated in the G band.

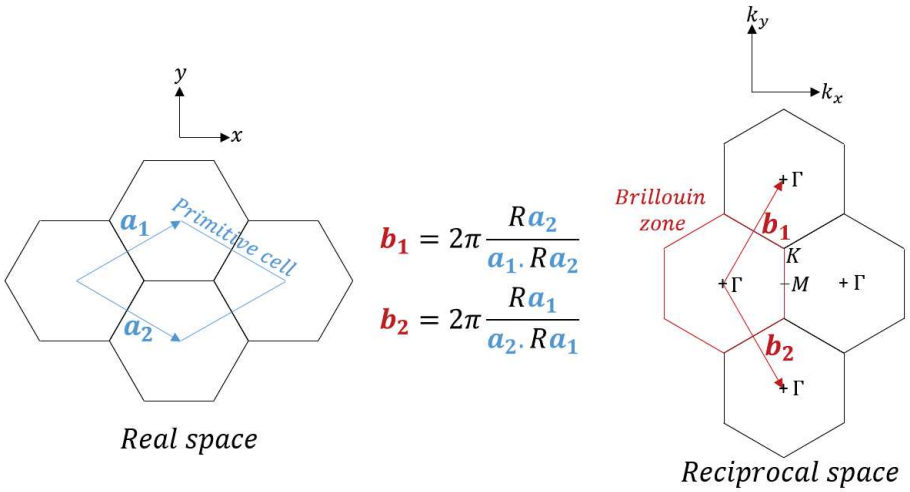

Figure 3.3: Graphene lattice in real and reciprocal space.

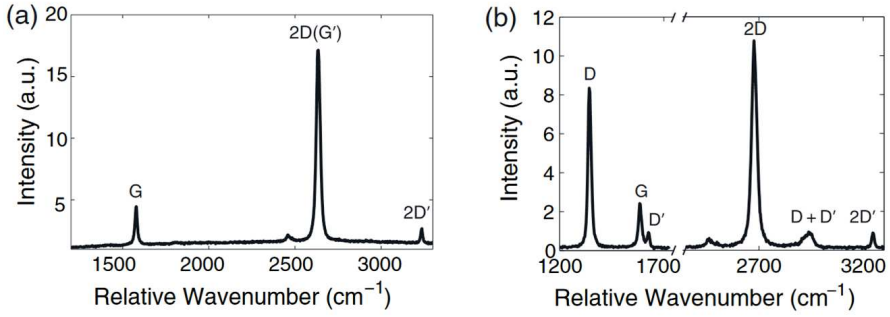

Figure 3.4: Example spectra : graphene flake. (a) A pristine flake showing only the G, 2D and 2D' bands. (b) A damaged flake, which shows the D and D' bands, as well as their combination D+D'. Reproduced from ref.[135]

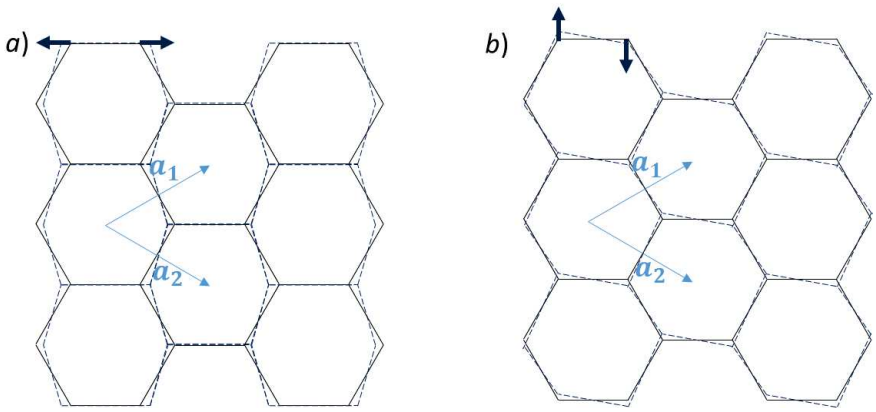

Figure 3.5: Graphene lattice (black) and its deformation (dash dark blue) for normal vibrational modes (a) and (b) corresponding to the G band in graphene Raman spectrum.

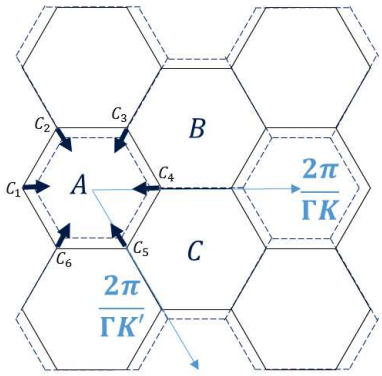

Figure 3.6: Graphene lattice (black) and its deformation (dashed dark blue) for the benzene breathing mode involved in graphene Raman spectrum D and 2D bands.

The deformed lattice maintains the same primitive vectors as the initial graphene lattice. Therefore, the G band vibrational mode is located at the Γ point in the reciprocal space, meaning that it has no momentum. This mode can thus interact with photons whose momentum is zero, since the momentum conservation law has to be verified. The graphene lattice rotational symmetry of order 3 implies the existence of these three modes which can be shown to be linked by a linear combination, reducing these three modes to two independent modes. These two modes are displayed in scheme 3.5 and will be referenced as iTO and iLO modes[135] with respective overall displacement dq_T and dq_L. It is clear that the graphene polarizability is different at extreme displacements, thus $\frac{d\alpha}{dq_T}$ and $\frac{d\alpha}{dq_L}$ are non zero at the equilibrium position. Since these two modes are independent, they can't interact to cancel the change in graphene polarizability. Therefore, these two modes are Raman active.

Scheme 3.6 represents the graphene lattice deformation due to the carbon atom motion of the vibrational mode implicated in the D and 2D band. It corresponds to a breathing mode of every third benzene ring.

The 2D periodicity of this mode differs from the graphene periodicity in length and direction. This consideration has two consequences. First, this mode is located at the K point in the graphene Brillouin zone meaning that momentum is needed to interact with this vibrational mode. Second, the primitive cell comprises three benzene rings called in scheme 3.6 A, B and C (with respective displacements q_A, q_B and q_C) instead of one benzene ring for graphene. Three vibrational modes can then be equiprobably excited in the graphene lattice, corresponding to the breathing of the A, B and C modes. Interestingly, these three modes are linked by a linear combination. Careful description of the atom motion shows that:

$$q_A + q_B + q_C = 0 \tag{3.5}$$

For each of these modes, the polarizability is different at extreme displacements meaning that taken alone, these modes are Raman active at the fundamental frequency and we have:

$$\frac{d\alpha}{dq_A}(0) = \frac{d\alpha}{dq_B}(0) = \frac{d\alpha}{dq_C}(0) = \frac{d\alpha}{dq}(0) \tag{3.6}$$

Taylor development of the polarizability can then be computed and since these three modes are equiprobable, the total polarizability is:

$$\alpha = \alpha_0 + \frac{d\alpha}{dq}(0)\frac{dq_A + dq_B + dq_C}{3} + \frac{1}{2}\frac{d^2\alpha}{dq^2}(0)\frac{dq_A^2 + dq_B^2 + dq_C^2}{3} \tag{3.7}$$

Since the sum of displacements for the three modes is null, the polarizability can be

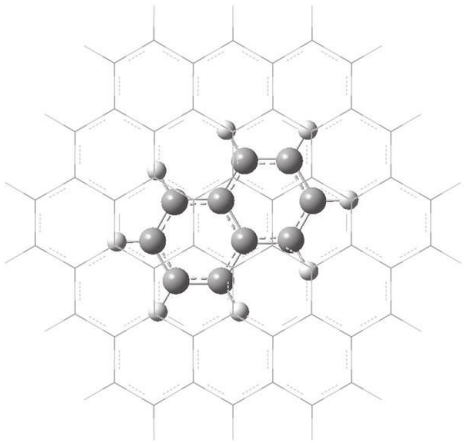

Figure 3.7: Top view of naphthalene on circumcoronene in the lowest energy conformation.

rewritten:

$$\alpha = \alpha_0 + \frac{1}{2}\frac{d^2\alpha}{dq^2}(0)\frac{dq_A^2 + dq_B^2 + dq_C^2}{3} \tag{3.8}$$

The breathing mode is thus non Raman active due to the presence of three benzene rings in the primitive cell. However, if a defect is present in the graphene lattice, the symmetry between the three modes can be broken, the relation $q_A + q_B + q_C = 0$ doesn't hold anymore, and the breathing mode becomes Raman active. It corresponds to the D band in the graphene Raman spectrum. Interestingly, since $q_A^2 + q_B^2 + q_C^2 \neq 0$, Raman scattering at $\omega \pm 2\omega_v$ is always allowed and corresponds to the 2D band in the graphene Raman spectrum.

It is worth noting that it is possible to define a normal mode to the breathing mode. These two modes are then independent, but the normal mode is not Raman active since the polarizability is identical for the two extreme displacements.

From another point of view, the non-zero momentum of the breathing mode prohibits any direct coupling to photons. This mode can then be only excited through the coupling to a defect that is localized and thus can couple to all wavevectors, or through a double resonance process involving two breathing modes with opposite momentum.

3.3 DFT computations

To obtain an insight into the general mechanisms of vibrational couplings between the graphene surface and a molecule that is adsorbed upon it, we first compared the simulated Raman spectra of a simple aromatic molecule: (i) in isolation; (ii) adsorbed on graphene. For computational expedience, we used naphthalene as a model aromatic molecule and circumcoronene to simulate the graphene sheet. In the adsorbed case, the geometry of the adsorption has been optimized to be evaluated at the lowest energy conformation. The resulting distance between the two molecules was $0.3nm$, which is typical of aromatic core adsorption on graphene.[140,141] A top view of naphthalene on circumcoronene in the lowest energy conformation can be found in Figure 3.7.

The Raman intensities of vibrational modes were obtained by computing the derivative of the zero-frequency electronic molecular polarizability with respect to the nuclear displacement of the corresponding normal mode. Hence, the intensity estimations do not account for hypothetical resonances between specific vibronic modes and the pump beam. The simulated Raman spectra obtained for naphthalene, both in isolated form and adjacent to circumcoronene, are displayed in Figure 3.8.

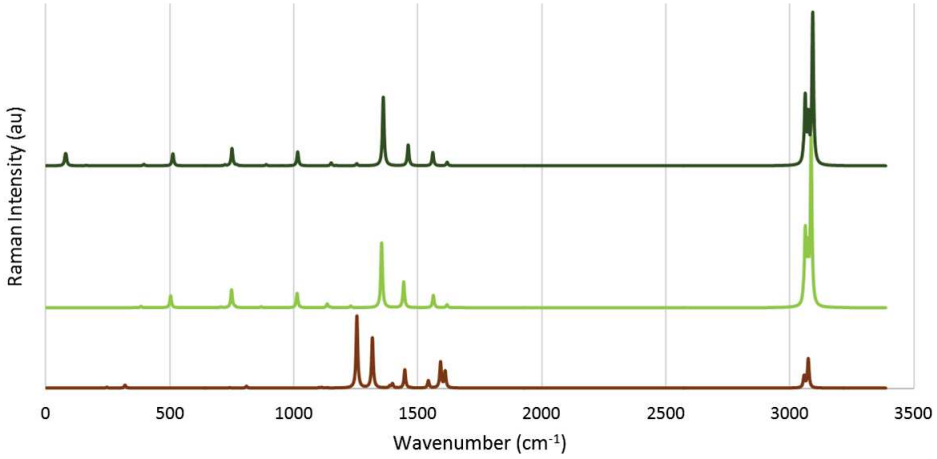

Figure 3.8: From bottom to top: Simulated Raman spectrum for circumcoronene (orange), naphthalene (light green), and naphthalene adjacent to circumcoronene (dark green) where only the naphthalene Raman signal is considered even if the circumcoronene is present.

The results obtained for the isolated molecule are consistent with other computations and experimental measurements,[142] as concerns both the vibrational frequencies and their assignments. The coupling between naphthalene and circumcoronene manifests itself in two effects.

First, a subset of the Raman-active resonances are shifted by $10-20cm^{-1}$ toward higher frequencies. A detailed comparison of vibration assignments and adsorption-induced high-frequency shifts of the corresponding bands shows that the affected vibrations are systematically those involving out-of-plane nuclear motions, in particular the out-of-plane C-C-C bending ($508cm^{-1}$) and the modes combining in-plane aromatic C-C stretching with out-of-plane C-H bending ($1166cm^{-1}$, $1240cm^{-1}$, $1459cm^{-1}$). In contrast, the in-plane normal modes involving only aromatic C-C stretching are not affected by the adsorption ($759cm^{-1}$ breathing-like mode, $1017cm^{-1}$, $1375cm^{-1}$, $1572cm^{-1}$ and $1626cm^{-1}$ ring-deformation modes). Notice that the in-plane CH-stretching group around $3050cm^{-1}$ is also not affected by the adsorption. The increase of the frequencies with adsorption shows that the distance of the adsorbate corresponds to a repulsive contact. The absence of shift induced by adsorption for in-plane vibrations shows that this contact doesn't affect the in-plane potential, and $\pi - \pi$ interactions have no significant influence on aromatic C-C bond strengths.

Secondly, a new vibration, absent from both isolated naphthalene or circumcoronene, appears at low frequency ($80cm^{-1}$) in the Raman spectrum of naphthalene when adsorbed onto circumcoronene. The visualization of nuclear motion in this combined molecular structure shows that this vibrational mode is delocalized on naphthalene and circumcoronene, and may be described as a swinging motion of the whole naphthalene molecule around its longer axis. For this reason, it will hereafter be referred as "molecular mambo" mode. Similarly with the first observation, this mode involves exclusively vertical nuclear motions, i.e. motions perpendicular to the graphene plane. The non-covalent nature of the corresponding vertical bonds explains the low frequency of the mambo mode compared e.g. to the stretching of covalent C-C bonds. Notice also that this mode is Raman-active thanks to a lateral shift of the naphthalene equilibrium position compared to circumcoronene, which breaks the symmetry between both sides of the tilt deformation. The absence of such a shift in the other in-plane direction justifies that no short-axis mambo mode is predicted.

Although based on a simplistic model, these illustrative observations will provide guide-

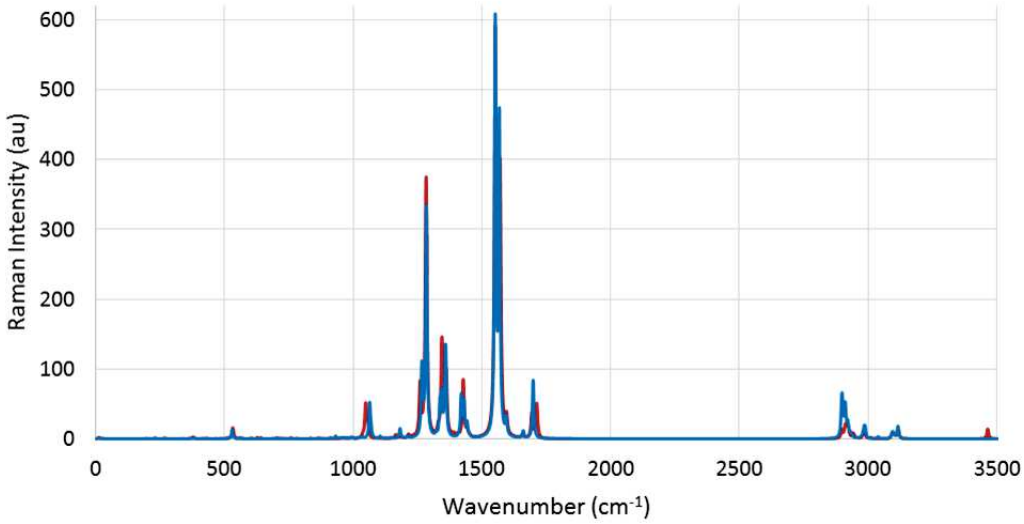

Figure 3.9: DFT computed Raman spectra for PTCDI-C13 (blue) and PTCDI-2C6a (red) in vacuum.

lines for analyzing the Raman spectra of more complex self-assembled dye monolayers on graphene.

3.4 Resonant self-assembled monolayer on graphene

In chapter 1, we have seen that PTCDI-C13 and PTCDI-2C6a form self-assembled monolayer at the graphene surface with two distinct geometries. Furthermore, transmission absorption spectra showed that both systems absorb light at a wavelength of 532 nm, and may thus be good candidates for resonant Raman scattering experiments.

Figure 3.9 displays the computed Raman spectra of isolated PTCDI-C13 and PTCDI-2C6a. The two spectra are highly similar. The computation only predicts a difference in the frequency of the $\sim 1050\ cm^{-1}$ vibrational mode: from $1050\ cm^{-1}$ for PTCDI-C13 to $1040\ cm^{-1}$ for PTCDI-2C6a. The visualization of the $1050\ cm^{-1}$ vibrational mode shows that this vibration involves aromatic C-C stretching with a symmetric elongation of the aliphatic C-N bonds at both extremities of the PTCDI aromatic core. The substitution of the highly inertial alkyl chain by a light hydrogen atom explains the predicted low-frequency shift for this normal mode. As most of the vibrational normal modes are already Raman-active in the symmetric PTCDI-C13 molecule, no new active Raman modes are produced by the breaking of this symmetry. PTCDI-C13 has twice as many C-H bonds as PTCDI-2C6a. Consequently, the associated $2900\ cm^{-1}$ Raman vibration group is twice as intense as in the PTCDI-C13 case.

For both molecules, the overlap between graphene sp^2 orbitals and the aromatic core in the self-assembled structures results in an ultrafast quenching of the electronic excitations.[143] Hence, these systems are not fluorescent as shown for PTCDI-C13 in chapter 2.[111] We can therefore observe Raman signals by using resonant excitation of the molecular dye, without disturbance from any fluorescence. The resonance enhancement is necessary to detect a signal from only one monolayer of molecules and to filter out other contributions from non-resonant systems such as the substrate. Moreover, the surface density in self-assembled PTCDI derivatives on graphene is very high: 0.45 $molecules.nm^{-2}$.(cf. chapter 1) Since Raman intensity is proportional to the number of probed molecules, this approach enables the experimental observation of molecular vibrations with an unprecedented signal to noise ratio. Finally, the Raman enhancement by graphene also facilitates

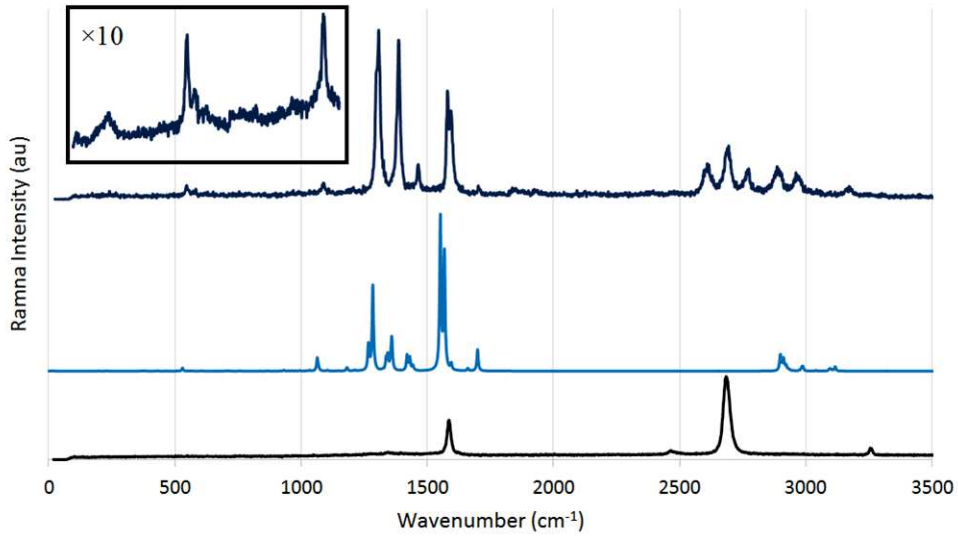

Figure 3.10: From bottom to top: Experimental Raman spectra for suspended graphene (black), DFT computed Raman spectrum for PTCDI-C13 (light blue, rescaled for easier comparison) in vacuum, and self-assembled PTCDI-C13 on suspended graphene (blue). Inset: self-assembled PTCDI-C13 on suspended graphene x10.

observation of self-assembled PTCDI-C13 and PTCDI-2C6a Raman signals.[136]

Figure 3.10 displays the experimental Raman spectrum of graphene, PTCDIC13 as well as DFT computed PTCDI-C13.

First, we compare in figure 3.10 the Raman experimental spectra of self-assembled PTCDI-C13 with that of the neat graphene and with the simulated Raman spectrum of isolated PTCDI-C13. As concerns neat suspended graphene film, the G band peak has a width of 19 cm^{-1} (full width half maximum); the 2D band corresponding to the mechanism involving two iTO phonons is located at 2685 cm^{-1} and its Raman intensity ratio to the G band intensity is 2.2. We detect a D band at 1345 cm^{-1} with very low Raman intensity, indicating a small density of defects. Such characteristics are usually considered reliable indicators of high quality graphene. The D+D$''$ band is also present at 2465 cm^{-1} as well as the 2D$'$ band at 3257 cm^{-1}. We see also a three-phonon process at 4275 cm^{-1} which we assign to G+2D.

The Raman spectrum of self-assembled PTDCI-C13 on graphene, displayed in figure 3.10, is in accordance with the DFT computed spectrum in the spectral range below 1700 cm^{-1}, within the limit of fundamental frequencies (since, as mentioned earlier, our computations do not predict overtones and combinations). Two differences appear in this part of the experimental Raman spectrum in comparison with the result of DFT modeling. First, a rigid shift of the spectrum toward higher frequencies can be observed. Secondly, and most interestingly, a broad low frequency band appears at 230 cm^{-1}. This observation echoes the low frequency coupled molecule-graphene mambo modes evoked before. Thus, by analogy, we assign this band to such mambo modes corresponding to oscillations around the N-N axis of PTCDI-C13.

In the spectral range above 1700 cm^{-1}, the experimental Raman spectrum of self-assembled PTDCI-C13 on graphene presents bands to be attributed to replicas of lower energy fundamental modes involving single vibrational quanta. As expected, these overtones and combinations of frequencies appear at multiple and sum frequencies of fundamental modes. Accordingly, their intensities can be reproduced by a simple autocorrelation $S * S$ of the spectrum S comprised in the $[0 - 1700\ cm^{-1}]$ region – a technique that provides for vibrational combinations to be excited in a single Raman event with a sum-frequency

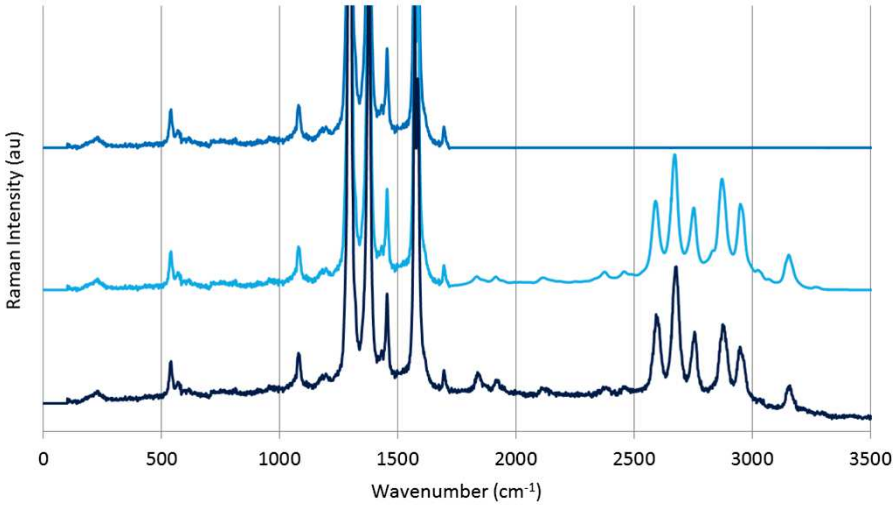

Figure 3.11: From top to bottom: Fundamental vibrational Raman spectrum (blue) for PTCDI-C13, Reconstructed spectrum (light blue), and full experimental spectrum (dark blue).

Stokes shift.

As shown in Figure 3.11, this operation faithfully replicates the spectrum above 1700 cm^{-1} by introducing one single overall scale parameter k such that the total reconstructed spectrum is written:

$$S_t = S + kS * S$$

The weighting factor k characterizes the strength of the process associating two vibrational quanta with respect to fundamental transition processes; from a classical point of view this reflects anharmonicity in the potential corresponding to each oscillator. This property illustrates the common nature of the vibrations that are the most Raman active under resonance conditions at a wavelength of 532 nm, which correspond to combinations of aromatic C-C stretching. Consistently, the common ratio of second-order to first-order Raman bands is the same as the ratio of the second (0-2) to the first (0-1) vibronic replica in the absorption spectrum. Notably, the Raman response of neat graphene doesn't follow the same rule. This difference is due to selection rules arising from the 2D-translational invariance of graphene.

By subtracting the full experimental spectrum from the convoluted spectrum, no 2900 cm^{-1} response that could be attributed to C-H stretching group emerges from the noise. This low efficiency is attributed to a resonance effect: only the conjugated aromatic part of the molecule is excited, and aliphatic CH vibrations are not electronically coupled to it. Graphene Raman bands, in particular the large 2D one, are also not discernible, indicating a surprisingly low response of graphene compared to PTCDI-C13.

We compare in Figure 3.12 the experimental Raman spectrum of self-assembled PTCDI-C13 and PTCDI-2C6a on suspended graphene. Once again, DFT computed spectra of isolated molecules displayed in figure 3 match very well their experimental data when adsorbed onto graphene. This shows the weakness of interactions between graphene and the conjugated kernels of adsorbed molecules as concerns in-plane aromatic C-C stretching vibrations, consistent with our conclusions on the illustrative simulation of naphthalene on circumcoronene. In particular, the predicted 10 cm^{-1} low-frequency shift of the 1050 cm^{-1} mode from PTCDI-C13 to PTCDI-2C6 is clearly observable experimentally, whereas the other bands keep the same frequencies. This illustrates the accuracy of predictions from

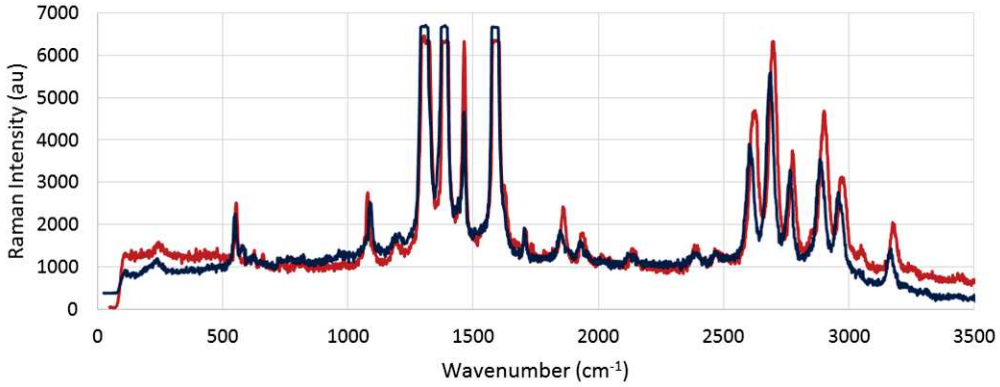

Figure 3.12: Experimental Raman spectra of self-assembled PTCDI-C13 (blue) and PTCDI-2C6a (red) on suspended graphene.

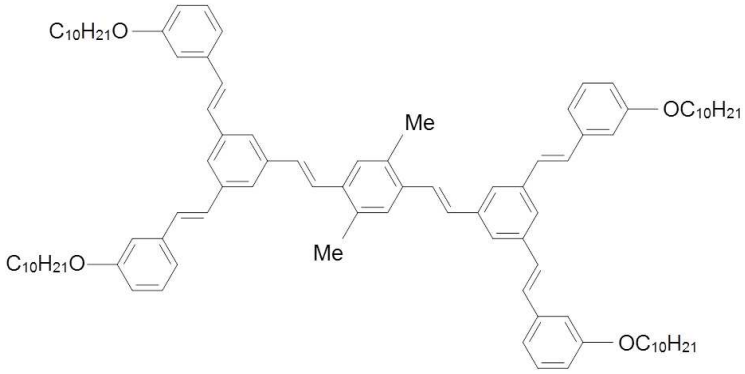

Figure 3.13: Molecular structures of BS-C10.

molecular simulations as concern vibrational modes frequencies.

Regarding out-of-plane vibrations, we retrieve for PTCDI-2C6a a signature of the molecular mambo mode which is not predicted for the isolated molecule. Moreover, this mode is shifted to higher frequencies ($\sim$ 240 cm^{-1}) in comparison with PTCDI-C13 ($\sim$ 230 cm^{-1}), as a consequence of the absence of an alkyl substituent on one side. This shift could also be explained by an increased participation of alkyl chains in the adsorption process of PTCDI-2C6a on graphene, increasing the force constant associated with the mambo mode.

3.5 Non-resonant self-assembled monolayer on graphene

A self-assembly that doesn't interact with visible light affords the best means of probing vibrational properties, in order to explore how graphene properties are affected by this non-covalent functionalization. As a non-resonant adsorbate, we chose BS-C10 molecule, (Scheme 3.13) which forms molecular self-assemblies on the graphene surface and is transparent at the wavelength of the Raman pump (532 nm).[144] BS-C10 can be described as two bistilbenes bound by a pi-conjugated benzene central core. Four alkoxy chains at the extremities of the bistilbenes groups control the adsorption on the surface in a Groszek model.(Chapter 2)

We compare in figure 3.14 the experimental Raman spectrum of suspended graphene either alone or non-covalently functionalized with self-assembled BS-C10 at its surface. This system consisting of a self-assembly of non-resonant molecules on resonant graphene

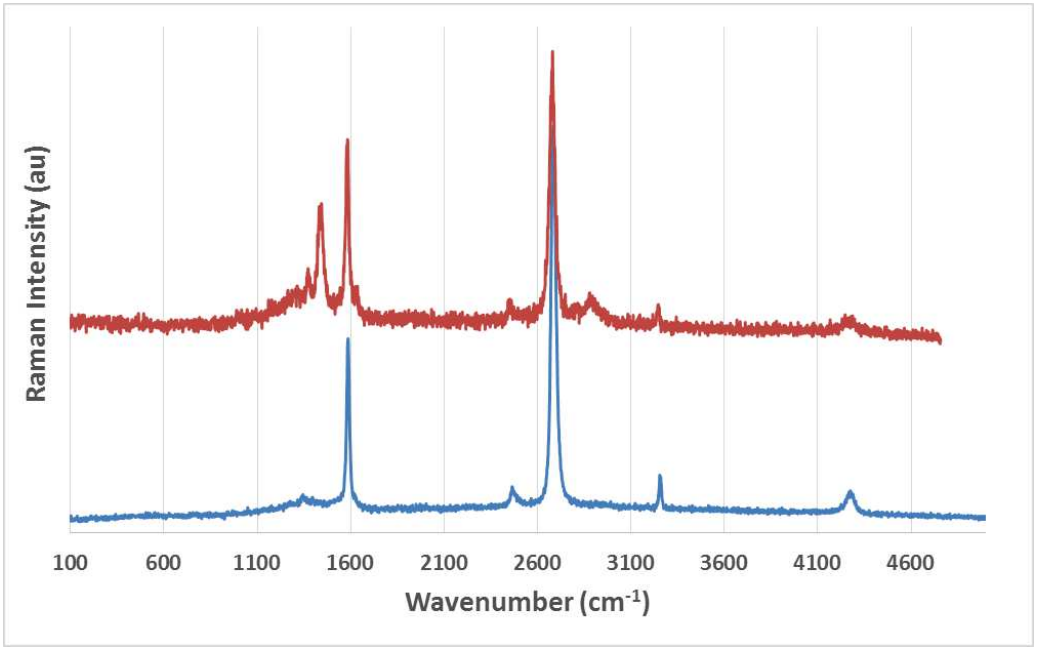

Figure 3.14: Experimental Raman spectrum of neat suspended graphene (blue curve) and with self-assembled BS-C10 (red curve).

allows us to acquire distinctively the graphene Raman spectrum and thus study modifications induced by the non-covalent supramolecular self-assembled network.

The Raman spectrum of the neat suspended graphene film demonstrates the high quality of suspended graphene utilized. The G band peak has a width of 19 cm^{-1} (full width at half maximum). The 2D band corresponding to the mechanism involving two iTO phonons is located at 2685 cm^{-1} and its Raman intensity ratio to the G band intensity is 2.2. We detect a very small D band at 1345 cm^{-1} with very low Raman intensity, indicating a small density of defects. The D+D" band is also present at 2465 cm^{-1} as well as 2D' band at 3257 cm^{-1}. We see also a three-phonon process at 4275 cm^{-1} which we assign to G+2D.

The Raman spectrum of graphene as modified by BS-C10 shows the appearance of two new bands at 1376 and 1444 cm^{-1}, supplemented by their combination band at 2815 cm^{-1} ($1376 + 1444 = 2820$) and an overtone at 2890 cm^{-1} ($2 \times 1444 = 2888$).

It would not be possible for these bands to result from a 1444 cm^{-1} line in the vibrational spectrum of BS-C10 since this molecule does not absorb the 532 nm excitation laser light - whereas graphene absorbs approximately 2% of this incident light. The non-resonant Raman intensity resulting from an intermediate virtual state would be much lower than those of the graphene bands.

The bands associated with suspended graphene are still present, and no frequency shifts are observed. Since the 2D band doesn't experience any shift, the TO phonon band around the K Brillouin zone corner is not affected by the presence of the supramolecular self-assembly. These propagating phonons correspond to the breathing mode of six-atom rings in graphene. Therefore, the coupling between graphene breathing mode and the aromatic core breathing modes of the adsorbed molecules is not strong.

Since the 2D band did not shift, and since a D band at 1345 cm^{-1} is not observable in the experimental Raman spectrum of graphene functionalized with a supramolecular network, we are confident that our deposition technique did not affect the quality of graphene.

The other main difference between the two experimental Raman spectra is the decrease

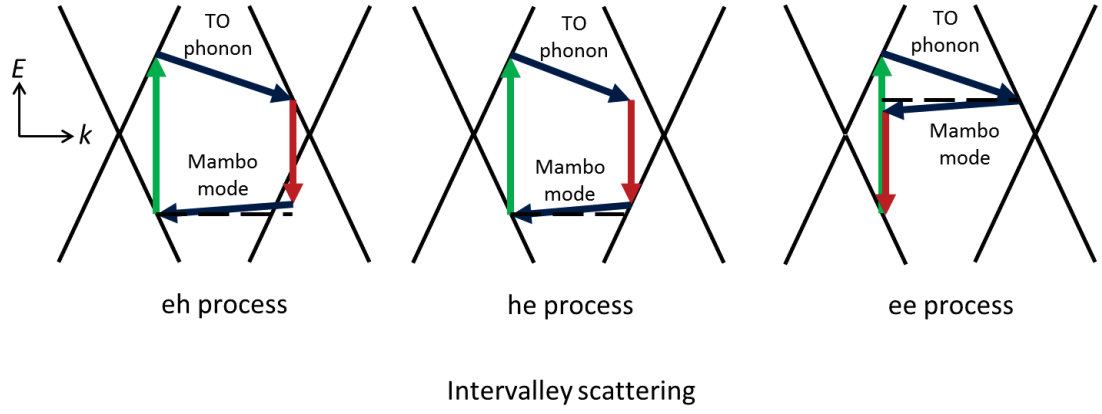

Figure 3.15: Proposed mechanisms to explain the appearance of 1372 cm^{-1} and 1444 cm^{-1} bands in the experimental Raman spectrum. These mechanisms involve a TO phonon and a coupled graphene-adsorbed "mambo mode".

of the 2D/G ratio from 2.2 for neat suspended graphene to 1.3, when functionalized by the supramolecular assembly. It is worth noting that the integration of the spectra over all frequencies gives exactly the same result for graphene alone and functionalized graphene. Consequently, the oscillator strength of the 2D band in the neat graphene spectrum appears as being transferred to the two new bands at 1376 and 1444 cm^{-1} in the BS-C10 on graphene spectrum.

Since the G band intensity is not affected by the presence of the supramolecular self-assembly, the 2D band decrease is the sign that a new mechanism is competing with the 2D mechanism, thus reducing the probability for the latter to occur. Since the only difference between the two systems is the presence of the supramolecular network, and since no defects have been introduced by the deposition technique, the competing mechanism clearly involves the adsorbed molecules. The redistribution of the oscillator strength indicates a new Raman-active mode for graphene due to the presence of the supramolecular network.

By breaking the translational invariance of the graphene lattice, vibrationally active molecules on the graphene surface allow the optical excitation of D-band phonons with non-zero wavevectors. They can then be seen as phonon launchers like localized defects. However, unlike structural defects, adsorbed molecules do not affect significantly graphene structure. Thus, the vibrational coupling must be resonantly enhanced through the mediation of a coupled vibration mode.

We demonstrated in previous sections that a molecule adsorbed on graphene can have vibrational mambo modes spatially delocalized on both graphene and the molecule. Moreover, these modes have low frequencies typically in the range of 100 cm^{-1}. This suggests that the 1376 and 1444 cm^{-1} bands in the experimental Raman spectrum results from mechanisms involving TO phonons and such mambo modes. These mechanisms are similar to those producing the D band where the electronic wavevector conservation is ensured during the process of transforming photons into phonons by the fact that localized defects can compensate for any phonon wavevector. The only difference is the fact that phonon defect modes are coupled at any frequency, whereas the mambo mode interacts with phonon modes at the given frequency of the involved coupled mode. We identify electron-hole, hole-electron, electron-electron intervalley scattering processes as principal mechanism producing the 1376 and 1444 cm^{-1} bands. These processes are displayed in figure 3.15.

Since the D band is not shifted (because the 2D band did not shift), according to

this interpretation, the two new bands should involve two molecular mambo modes with frequencies 101 cm^{-1} and 34 cm^{-1} as derived from the experimental spectrum. Such orders of magnitude are consistent with DFT calculations of molecular mambo modes which predict resonant frequency on the order of 80 cm^{-1}.

3.6 Conclusion

Adsorption on graphene offers a unique opportunity to apply resonance Raman spectroscopy to fluorescent molecules, thanks to the fast quenching of molecular excited states. When self-assembled molecules on graphene interact with their substrate, the Van der Waals forces that allow the adsorption result from the overlapping of graphene sp^2 orbitals with either sp^2 molecular orbitals or H atoms. Whereas these electronic interactions significantly perturb the electronic excited levels of the adsorbed molecule,[122] the vibrational properties involving in-plane motions are kept almost intact. However, the presence of the graphene surface in the vicinity of such an adsorbed molecule gives rise to new out-of-plane low frequency molecule-graphene coupled vibrational modes. The frequencies of such "mambo mode" resonances are determined by the size of the adsorbed molecule and the strength of the adsorption force, and are typically of the order of 100 cm^{-1} for aromatic molecules. These findings open new perspectives in the engineering of graphene properties. The identification of mambo modes could be explored to build a bridge between visible and IR optics, for example in optically triggering phonon launcher. More generally, our work emphasizes the capability, when engineering graphene-based self-assembled systems, to interrogate the nature of their adhesion to graphene through Raman spectroscopy.

Chapter 4

Plasmon engineering

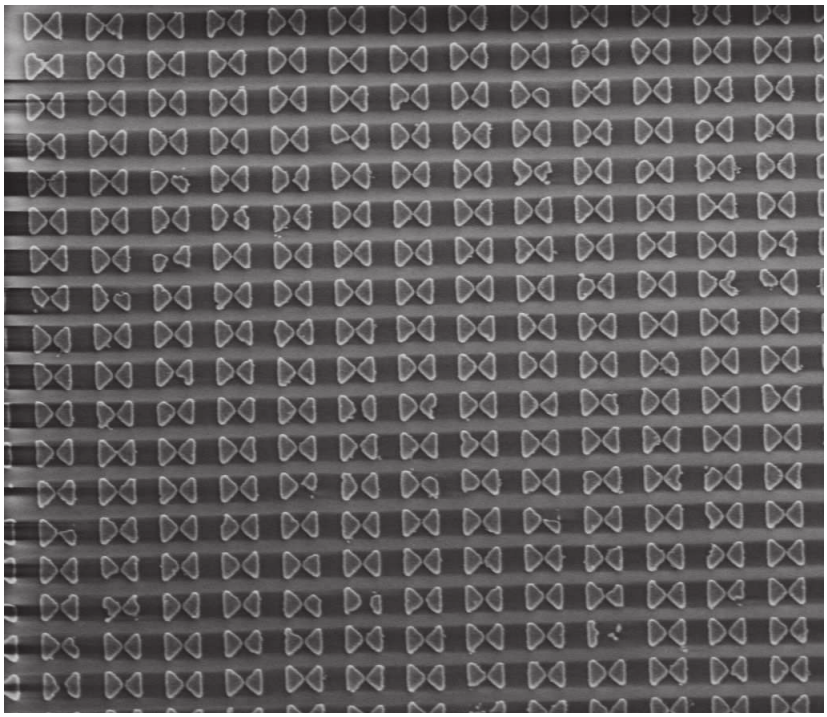

Scanning electron microscope (SEM) image of nanoscale gold bowties measuring 240 nm long and 170 nm large. (John Bigeon / C2N)

Metallic nanostructures have been used for centuries to produce colorful materials. One can cite the Lycurgus cup crafted in the Roman empire or the multitude of stained glass windows decorating cathedrals. These structures have the ability to confine light at the nanoscale and thus very high electric field can be reached at their close vicinity. A deep understanding of how metallic nanostructures interact with light is needed depending on their shape, size, aggregation to extend today applications through the careful design of such nanoscale objects and networks.

Contents

4.1 Characteristics of plasmon modes

4.1.1 Rabi frequency

Surface plasmons polaritons are strongly coupled plasma electronic oscillations of a metal to the electromagnetic field of photons. They propagate at the metal surface. For a simple metal/dielectric interface, an analytic dispersion relation for the surface plasmon can be obtained from the wave equation derived from Maxwell-Lorentz equation. A surface plasmon polariton can propagate if its wavevector β verifies the relationship:

$$\beta = \frac{\omega}{c}\sqrt{\frac{\epsilon_m \epsilon_d}{\epsilon_m + \epsilon_d}} \tag{4.1}$$

Where ϵ_m $(resp.\epsilon_d)$ is the dielectric constant of the metal (resp. the dielectric). Figure 4.1 represents the dispersion relation of a surface plasmon polariton propagating at an interface composed by vacuum and a Drude metal (plasma frequency $\omega_p = 9eV$).

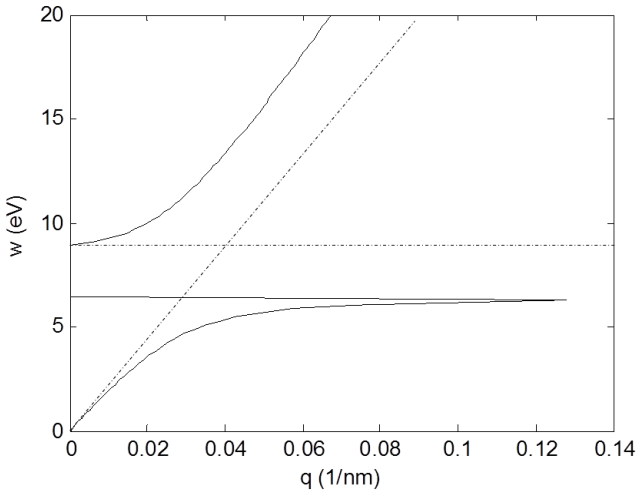

Figure 4.1: Dispersion relation of the plasmon polariton. Dashed lines represent the dispersion relation of a photon (called light line) and the dispersion relation of electrons in the metal (plasma frequency)

The lower branch of the polariton behaves like a photon at low frequency and tends to $\omega_p/\sqrt{2}$ at high frequencies. The upper branch of the polariton start from ω_p at low frequencies. The forbidden frequency gap between the upper and lower part of the polariton branches is the sign of an ultrastrong coupling.[145,146] In this framework, the width, in energy units, of the opened gap E_g can be linked to the coupling energy $\frac{h\omega_R}{\pi}$ through the equation:

$$E_g = \frac{(\frac{h\omega_R}{\pi})^2}{2\omega_p} \tag{4.2}$$

Where ω_R is the Rabi frequency describing the periodic energy exchange between the two coupled systems. The resolution of Maxwell equations plotted in figure 4.1 gives a gap opening of 2.6 eV which correspond to a Rabi frequency $\omega_R = 8.3 \times 10^{14}\ s^{-1}$. This frequency corresponds to a 360 nm wavelength photon propagating in free space. Energy exchanges between metal electrons and the electromagnetic field of the plasmon polariton quasiparticle are then about two times faster than their oscillation frequencies, and will be thus laid aside in the following.

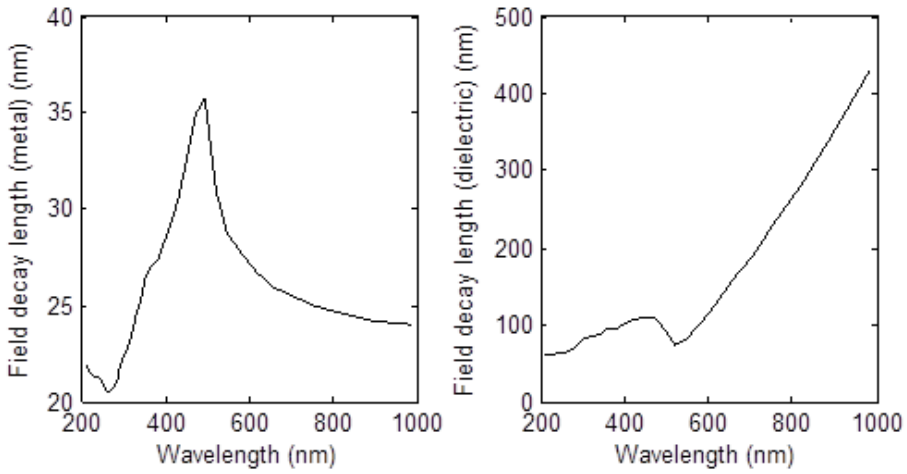

Figure 4.2: Field decay lengths from a gold/glass(n=1.5) interface inside the gold layer (left) and the vacuum layer (right). Gold permittivity were taken from Johnson and Christy.[147]

4.1.2 Field confinement and propagation length

Polarizability χ (or dielectric constant $\epsilon = 1+\chi$) properties of materials at the dielectric/metal interface dictate the characteristics of surface plasmon polariton: propagation length, field extension above and below the interface. Figure 4.2 displays the decay lengths of the fields from a gold/glass(n=1.5) interface inside the gold layer and the vacuum layer.

The plots in figure 4.2 show that such systems can confine electro-magnetic fields below the diffraction limit: for example, at a frequency corresponding to a 600 nm wavelength photon in free-space, the transverse decay length of the surface plasmon polariton field in the glass layer is 100 nm.

However, a major drawback goes with this strong confinement of light in plasmonic systems: electron motion in any metal is lossy due to Ohmic frictions that cause damping of the plasma oscillations. Furthermore, at high frequencies, interband metal electronic transitions can also absorb electromagnetic energy thus further reducing the propagation length of surface plasmon polaritons.

Figure 4.3 shows the propagation length of a surface plasmon polariton as a function of its wavelength for a gold/glass(n=1.5) interface together with the corresponding dielectric constant. As displayed by the imaginary part of the dielectric constant of gold, interband transitions prevent any propagation of the surface plasmon polariton below 500 nm. Above 600 nm, The combination of low light absorption by gold and highly negative real part of the gold permittivity increases the surface plasmon polariton propagation length to tenth of micrometers. Therefore practical uses of surface plasmon polaritons on gold are limited to the red to near-infrared (NIR) range (600-800 nm). Actually, longer-wavelength applications, cheaper metals such as aluminum are workable.

Since lossy metals are unavoidable, losses are the principal limitation to applications of plasmonic cavities or waveguides. This has two main consequences. First, more efficient gain media are required to compensate for the losses and potentially produce gain. Second, losses constrain plasmonic resonators to poor quality factor and thus to ultra-fast relaxation (typically 100 fs).

Since common gain media have a typical radiative lifetime of 1 ns, plasmonic lasers can be defined as class B lasers: the radiations are emitted by bursts.[148]

Further research on optical gain media is needed to engineer plasmonic properties aiming for a reduction of losses in such material.

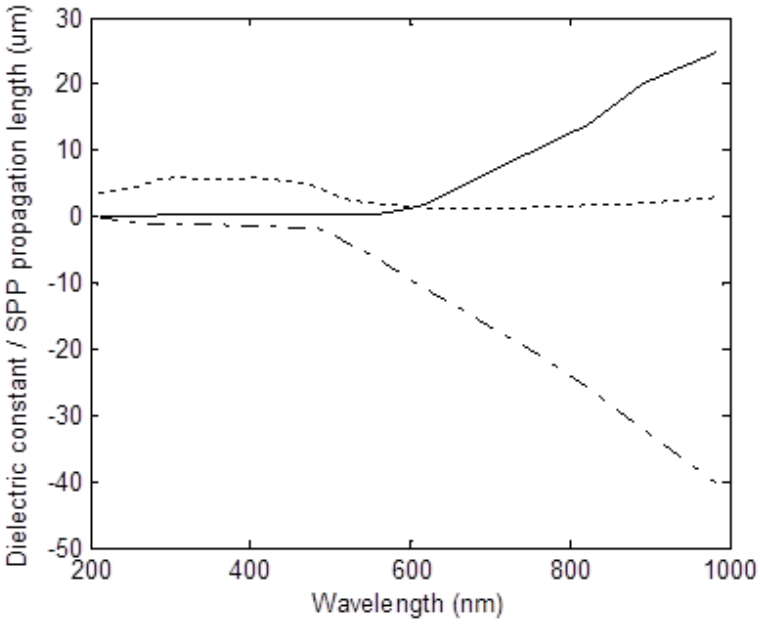

Figure 4.3: Real (long dash) and imaginary (short dash) part of the gold permittivity taken from Johnson and Christy.[147] Surface plasmon polariton propagation length at the gold/glass(n=1.5) interface.

4.1.3 Quality factor

The quality factor (Q-factor) is a practical figure to compare plasmonic resonators of different materials. It corresponds to the number of resonator oscillations before being damped. A quality factor for surface plasmon polariton Q_{spp} and for a local nanostructure Q_{loc} can be defined:[149]

$$Q_{spp} = -\frac{re(\epsilon)}{im(\epsilon)} \tag{4.3}$$

$$Q_{loc} = \frac{\omega \frac{dre(\epsilon)}{d\omega}}{2im(\epsilon)} \tag{4.4}$$

Q_{spp} is the ratio of the propagation length to the wavelength of a SPP propagating at the studied metal/vacuum interface. Q_{loc} is the number of local plasmon oscillations performed by the resonator before being totally damped.

We compare in figure 4.4 the quality factors of silver and gold SPPs computed from their experimental dielectric constant.[147]

Silver is known to have the best dielectric characteristics for visible plasmonics. It shows relatively low losses and the real part of its dielectric permittivity is sufficiently negative to end up with a good quality factor for the plasmonic resonance as shown in figure 4.4. However, the fast oxidation of any unprotected silver surface adds a technological complication for plasmonic applications of silver. Therefore, gold represent a good compromise in terms of dielectric properties and technological manipulation. Composite materials could be a strategy to engineer the dielectric properties and improve quality factor for local plasmon resonances or propagating surface plasmon polaritons.

4.2 Maxwell-Garnett materials

The Maxwell-Garnett approach aims at predicting the optical properties of an alloy that combines two materials. An effective dielectric constant ϵ_{eff} can be derived from the

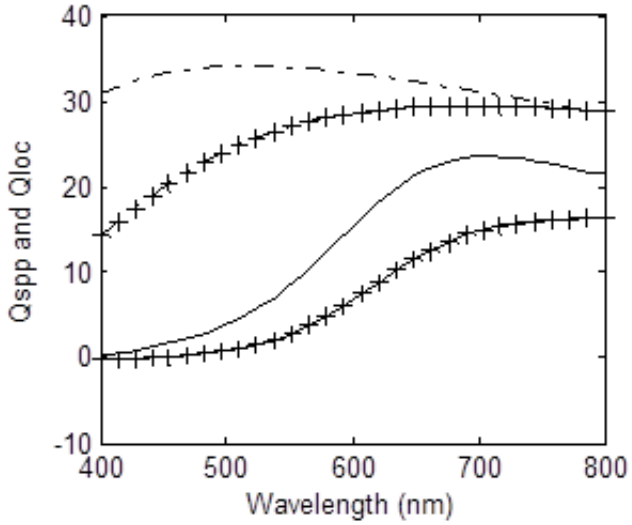

Figure 4.4: Q_{spp} (crosses) and Q_{loc} (no crosses) for silver (dash) and gold (plain) SPPs. Relative permittivity from Johnson and Christy.[147]

dielectric constant of matrix medium ϵ_m and inclusions ϵ_i knowing the volume fraction of the inclusions δ_i. This effective medium approximation assumes that inclusion domains are spatially separated. This approach is thus expected to be valid at low volume fractions. The effective dielectric constant can be written:

$$\epsilon_{eff} = \epsilon_m \frac{2\delta_i(\epsilon_i - \epsilon_m) + \epsilon_i + 2\epsilon_m}{2\epsilon_m + \epsilon_i + \delta_i(\epsilon_m - \epsilon_i)} \tag{4.5}$$

When the volume fraction is small, the effective dielectric constant has a pole for $2\epsilon_m + \epsilon_i = 0$. By considering a dielectric matrix with gold inclusions in the limit of low volume fractions, one retrieves the local plasmon resonance condition for gold nanospheres embedded in a dielectric matrix.

4.2.1 Glass inclusions.

An idea to reduce losses in a plasmonic material could consist in adding transparent inclusions which possibly would reduce the imaginary part of the plasmonic material relatively more than its real part. Figure 4.5 displays effective dielectric constant and Q_{spp} for a gold matrix with glass (n=1.5) inclusions with volume fractions varying from 0 to 0.75.

The imaginary part of the composite medium dielectric constant is computed to be lower than the pure gold medium case. However, the real part is more affected by the presence of the inclusions, resulting in a lower quality factor for the composite medium whatever the wavelength. The quality factor can eventually be negative due to a positive real part of the dielectric constant, meaning that the composite medium do not even display a resonance.

4.2.2 Absorber inclusions.

A second idea that we tested was to use a typical absorber (Lorentzian resonator) as inclusions. Considering a dense packing ($\rho = 1\ molecule/(2nm)^3$) of PTCDI molecules with a $\sigma = 3 \times 10^{-20}\ m^2$ absorption cross-section at resonance ($530\ nm$), the imaginary part of the absorber system dielectric constant is evaluated at resonance to:

$$Im(\epsilon_r) = \frac{3c\sigma\rho}{\omega_0} = 6 \tag{4.6}$$

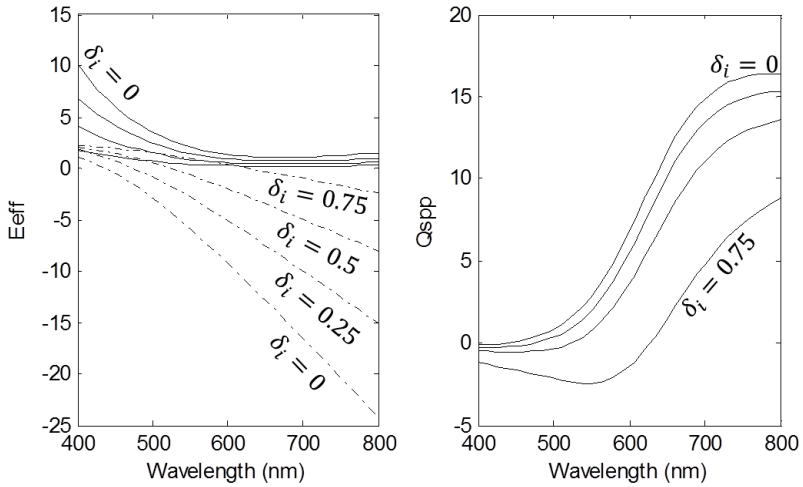

Figure 4.5: Left. Real (dash) and imaginary part of the effective dielectric constant obtained in the Maxwell-Garnett approach for a gold matrix and glass inclusions (volume fraction varying from 0 to 0.75). Right. Corresponding SPP quality factors.

Figure 4.6 displays the dielectric constant real and imaginary parts for a weak ($\rho = 1\ molecule/(4nm)^3$) and a strong absorber ($\rho = 1\ molecule/(2nm)^3$). As displayed in this figure, the dielectric constant of an absorber can be tuned with the amplitude of the absorption, and a negative real part of the dielectric constant can be obtained for strong absorbers.

Figure 4.7 (resp. 4.8) displays the effective permittivity and Q_{spp} in the Maxwell-Garnett model for a gold matrix and weak (resp. strong) absorber. In both cases, the ratio of the real part to the imaginary part of the effective dielectric constant does not improve plasmonic properties since Q_{spp} for the composite material is lower than for gold whatever the wavelength. However, the spectral selection of propagating wavelength by the presence of the absorber could be used as a band-pass filter for plasmons-based technology.

4.2.3 Gain medium inclusions.

A third idea consists in adding inclusions of gain medium to the gold matrix to compensate for losses. This gain medium can be viewed as a system presenting a population inversion, excited either electrically or optically.

Figure 4.9 displays the effective permittivity and Q_{spp} in the Maxwell-Garnett model for a gold matrix and the same weak absorber than previous figure with a 100% population inversion.

The real part and the imaginary part of the effective dielectric constant are weakly affected by the presence of the emitters. However, since the imaginary part (ie losses) tends to zero due to the emission of the inclusion material, Q_{spp} can diverge even for low inclusion volume fraction. Hence, high plasmon propagation lengths can be obtained in such material. Moreover, the band-pass action could be desirable from the plasmonic technology point of view.

Aside from this material research point of view, several design strategies can be used to minimize losses in plasmonic systems. Some modes, like the long-range surface plasmon in a metal-dielectric-metal structure are less damped because the electromagnetic field is localized outside the metal. However, the mode is then less spatially confined in the plasmonic system, and this drawback can be problematic from a miniaturization point of view.

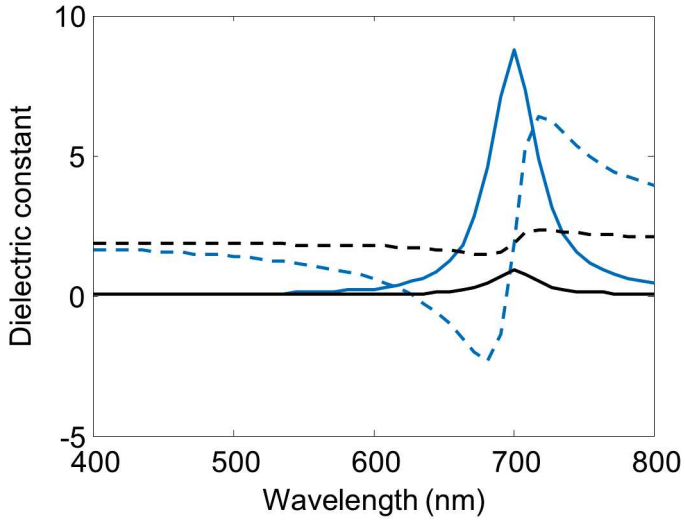

Figure 4.6: Comparison of the dielectric constant real (dash) and imaginary (plain) parts for a strong (blue) and a weak (black) absorber.

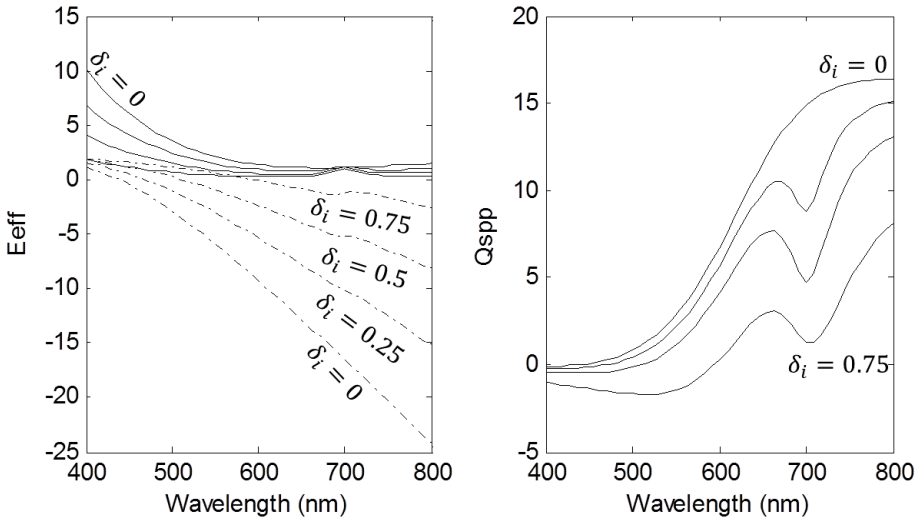

Figure 4.7: Left. Real (dash) and imaginary part of the effective dielectric constant obtained in the Maxwell-Garnett approach for a gold matrix and a weak absorber (volume fraction varying from 0 to 0.75). Right. Corresponding SPP quality factors.

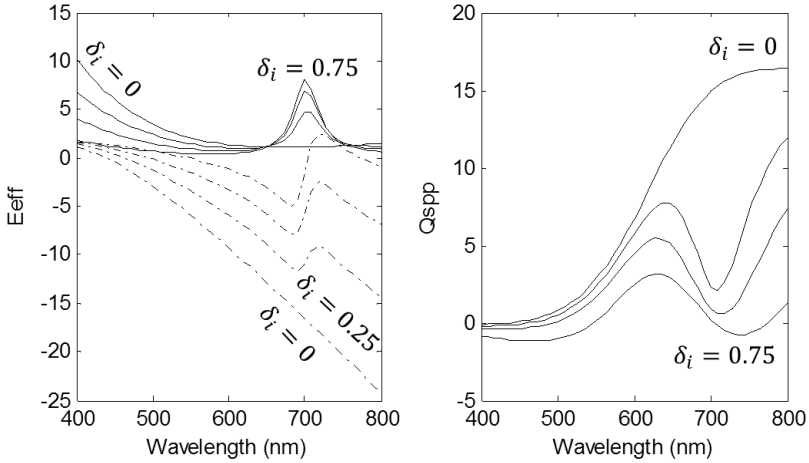

Figure 4.8: Left. Real (dash) and imaginary part of the effective dielectric constant obtained in the Maxwell-Garnett approach for a gold matrix and a strong absorber (volume fraction varying from 0 to 0.75. Right. Corresponding SPP quality factors.

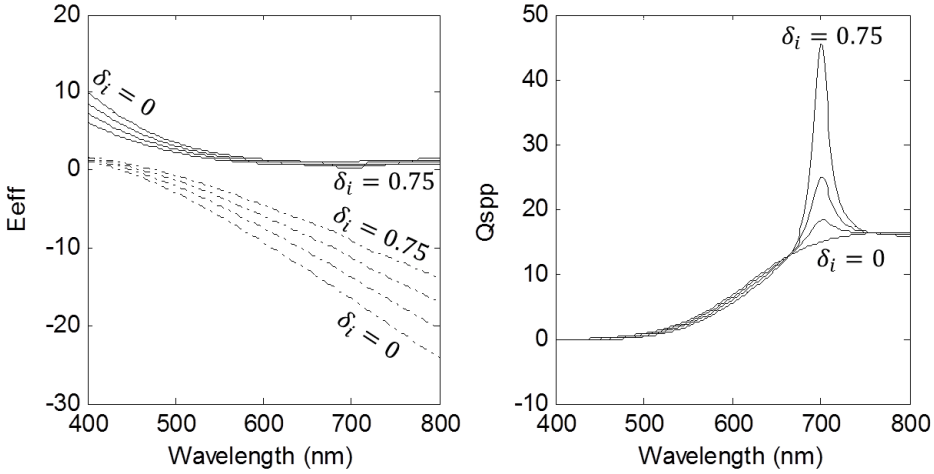

Figure 4.9: Left. Real (dash) and imaginary part of the effective dielectric constant obtained in the Maxwell-Garnett approach for a gold matrix and a weak emitter (volume fraction varying from 0 to 0.40. Right. Corresponding SPP quality factors.

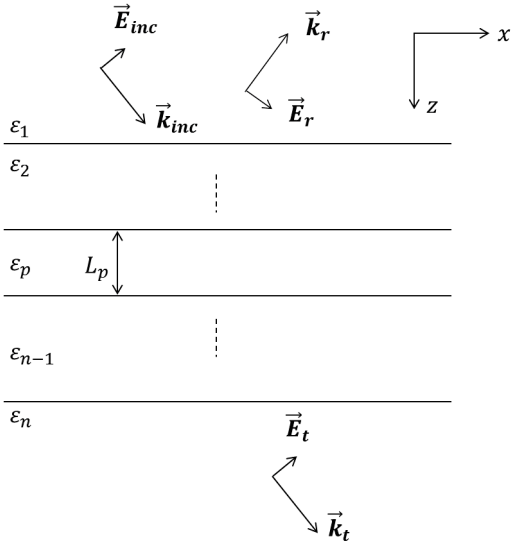

Figure 4.10: Description of the n-multilayer problem and notations.

4.3 Analysis of SPP dispersion relation

Engineering surface plasmon polaritons requires effective numeric and experimental tools to simulate and characterize their physical properties: frequency, propagation length, field extension... Moreover, the experimental characterization should tackle the fact that most of the plasmon systems are very small, typically on the order of a few micrometers or less. Most of the critical information about surface plasmon polaritons is embedded in the dispersion relation that results from solving Maxwell equation for this specific geometry. For a simple gold/dielectric interface, an analytic dispersion relation for the surface plasmon can be obtained. (cf. equation 4.1) However, analytic solution for the dispersion relation requires too complex calculations for a multilayer material.

Here we remind a numerical and an experimental tool to solve both numerically and experimentally Maxwell equations, finding the dispersion relation of surface plasmon polaritons at a precise spatial location (1 μm^2 precision) on a plasmonic system.

4.3.1 Numerical dispersion relation.

The transfer matrix approach is usually used to compute the optical reflection and transmission of a multilayer material when a beam is incident its surface.[150]

Scheme 4.10 describes the multilayer problem composed of n homogeneous layers with complex dielectric constant ϵ_i and extension L_i normal to the interfaces (ie in the z-direction). In the following, we consider uniquely transverse magnetic (TM) incident electromagnetic fields.

The wavevector projection on the x-axis, β, is continuous through all interfaces for the waves to propagate:

$$\beta = \overline{k}_p.\overline{x} = \overline{k}_{inc}.\overline{x} = k_{inc}sin(\theta_{inc}) \tag{4.7}$$

We then define k_{pz} the projection along the z-axis of the complex wavevector of the layer p:

$$k_{pz} = \sqrt{k_p^2 - \beta^2} \tag{4.8}$$

The TM propagating and counter propagating electric fields in the p layer can be deduced

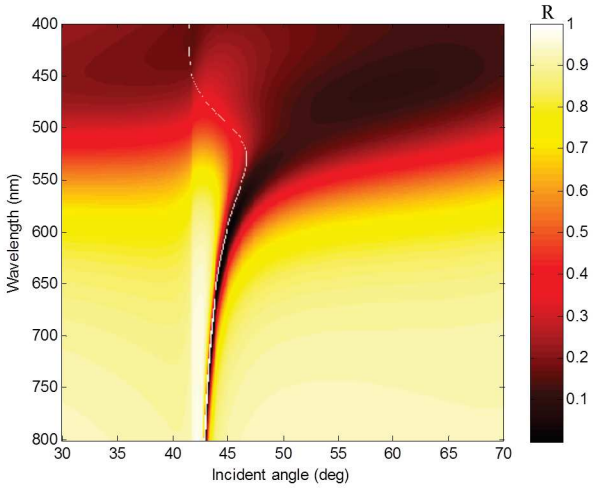

Figure 4.11: Reflection from a glass/gold (50 nm)/vacuum system as function of the wavelength and the incident angle of the incident electric field. Analytic dispersion relation for a SPP propagating at a gold/vacuum interface (white line).

from those in the p-1 layer thanks to the $D_{p-1,p}$ matrix derived from continuity equations:

$$D_{p-1,p} = \frac{1}{2}\begin{bmatrix} 1+n_{p-1,p} & 1-n_{p-1,p} \\ 1-n_{p-1,p} & 1+n_{p-1,p} \end{bmatrix} \tag{4.9}$$

$$n_{p-1,p} = \frac{\epsilon_{p-1}}{\epsilon_p}\frac{k_{pz}}{k_{p-1z}} \tag{4.10}$$

The propagation of the phase through the layer p of length L_p is carried out by the propagation matrix P_p:

$$P_p = \begin{bmatrix} exp(-ik_{pz}L_p) & 0 \\ 0 & exp(-ik_{pz}L_p) \end{bmatrix} \tag{4.11}$$

We then write the overall matrix M that links the reflected and transmitted electric field to the incident electric field:

$$\begin{bmatrix} E_{inc} \\ E_r \end{bmatrix} = M \begin{bmatrix} E_t \\ 0 \end{bmatrix} = \begin{bmatrix} M_{11} & M_{12} \\ M_{21} & M_{22} \end{bmatrix} \begin{bmatrix} E_t \\ 0 \end{bmatrix} = D_{1,2}P_2...D_{p-1,p}P_p...D_{n-1,n} \begin{bmatrix} E_t \\ 0 \end{bmatrix} \tag{4.12}$$

Reflected and transmitted fields and intensities can be deduced from the M matrix as follows:

$$t = \frac{1}{M_{11}} \qquad r = \frac{M_{21}}{M_{11}} \tag{4.13}$$

$$T = \frac{\epsilon_1}{\epsilon_n}\frac{k_{nz}}{k_{1z}} \times tt^* \qquad R = rr^* \tag{4.14}$$

Figure 4.11 displays the reflected intensity for a Kretschman configuration (glass / gold(50nm) / vacuum) as function of the wavelength and the incident angle of the incident electric field. Superposed to this figure is plotted in white the analytic dispersion relation for a gold/vacuum interface in the $\omega - \theta$ space.

A dip in the reflectivity appears above the total internal reflection angle at 41.8°. At 800 nm, this dip is located at 43° and this value increases as the wavelength decreases. This dip in the reflectivity is attributed to the coupling of the incident photon to the surface plasmon mode. The analytic dispersion curve matches perfectly the reflectivity

dip between 600 nm and 800 nm, validating our numerical implementation of the transfer matrix theory to compute the dispersion relation for more complex systems. Below 600 nm, the dip width increases due to gold interband transitions that shorten SPP propagation length. This region also corresponds to the transition from plasmon polariton to photon polariton, thus the analytic dispersion curve moves away from the reflectivity dip.
Interestingly, intrinsic and radiative loss terms Γ_i and Γ_r for the propagating plasmon polariton can be determined from the position, the height h and the width w of the dip by solving the following two equation system:[151]

$$h = \frac{4\Gamma_i\Gamma_r}{(\Gamma_i + \Gamma_r)^2} \tag{4.15}$$

$$w = \frac{\Gamma_i + \Gamma_r}{n_2 k_0 cos(\theta_r)} \tag{4.16}$$

Where $n_2 k_0$ is the incident wavevector onto the gold layer, and θ_r is the incident angle producing the reflectivity dip.

The transfer matrix method is a simple to implement and effective tool to predict the position in frequency and wavevector of the SPP mode. This figure permits to find the SPP wavelength from the wavector value of the reflectivity dip, and the SPP propagation length from intrinsic and radiative loss terms extracted from the characteristics of the reflectivity dip.

4.3.2 Experimental dispersion relation

An incident beam with an important wavevector at a given frequency is needed to phase-match the plasmon polariton wavevector and thus excites it. In the Kretschman configuration, the exciting beam is incident on the plasmonic waveguide coming from a prism at high angle of incidence. The plasmon polariton presence manifests itself by a dip in the reflectivity signal at a given angle above the total internal reflection condition for the prism/air interface.

However, this method is not efficient to locally characterize the SPP properties. We implement a microscopy analogue of the Kretschman configuration that allows the characterization of SPP properties at the micro scale. Scheme 4.12 describes the experimental set-up of the microscopy analogue of the Kretschman configuration. It is similar to the set-up used for example in ref.[152]

The prism in the traditional Kretschman configuration is replaced by the immersion oil of a high aperture objective. The reflected light is collected through the objective and analyzed in the Fourier plane. Thus, reflected light is experimentally decomposed on a wavevector basis. Moreover, the ability of the microscope objective to focus a collimated incident beam onto the substrate allows characterizing it at a precise location, typically with several microns precision. Since Maxwell equations are decoupled in frequency, we can shine white light (Tungsten incandescent lamp in our setup) on the system to characterize all frequencies at the same time knowing that the presence of multiple wavelengths will not perturb the solution of the problem for one wavelength. For the same reason, we can also send all wavevectors at the same time on the substrate. Since surface plasmon polaritons are uniquely excited by an incident TM electromagnetic field, a broadband polarizer is placed after the white source. The experimental dispersion relation is obtained by decomposing the reflectivity on a wavevector and a wavelength basis, as shown in the previous section. The detection of the signal in the Fourier plane decomposes the reflectivity on a wavevector basis. Figure 4.13 displays images of the Fourier plane for a reference glass sample and for 40 nm of gold deposited on top of this glass sample. A rough

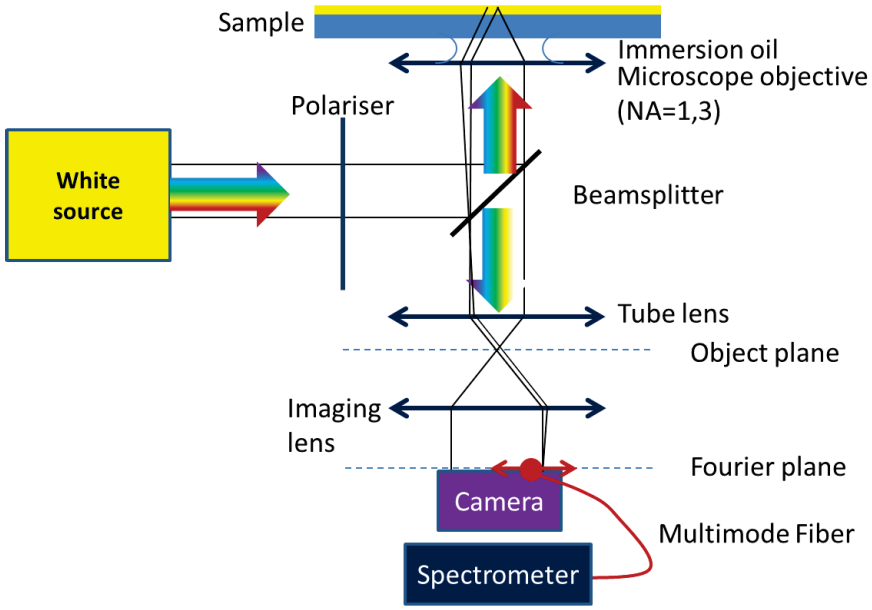

Figure 4.12: Description of the experimental set-up for obtaining the experimental SPP dispersion relation.

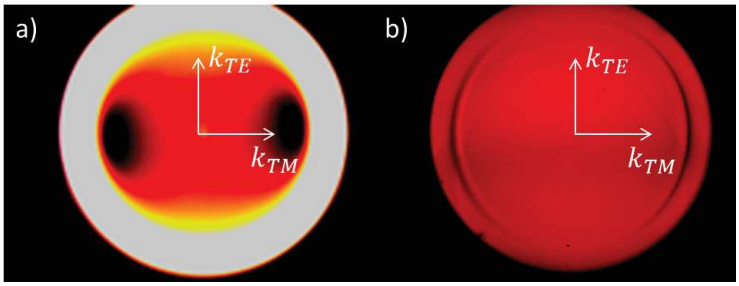

Figure 4.13: Experimental Fourier plane images obtained on a trichromatic camera with a linearly polarized white source illumination on a glass sample (a) and a glass sample coated with 40 nm of gold (b).

spectral information is acquired at each pixel of the image using a simple trichromatic color camera.

The first image (a) displays simultaneously the TE and TM intensity reflection dependence on the incident angle along the vertical and horizontal image axes respectively for a glass/air interface. Brewster incidences are visible as dark spots on the TM axis when the incident wavector k_i matches Brewster wavevectors $\pm k_B$. Above a certain incident wavector k_{TIR}, total internal reflection occurs and the light is entirely reflected by the glass/air interface. The coupling of the incident light to the surface plasmon polariton is visible along the TM axis on the image (b), taken for the same glass sample coated with 40 nm of gold. When k_i matches $\pm k_{SPP}$, a dip in the reflection occurs. The white source allows obtaining very clear images since interference patterns are blurred by the presence of multiple wavelength. However, the spectrum of the white source should be carefully selected to see the dip in the reflectivity since it can be distorted for wavelength around 500 nm and less.

A last step is needed to obtain the experimental dispersion relation. The decomposition of the reflectivity on a wavelength basis with a spectral resolution much better than the trichromic camera is performed by scanning a multimode fiber linked to a spectrometer

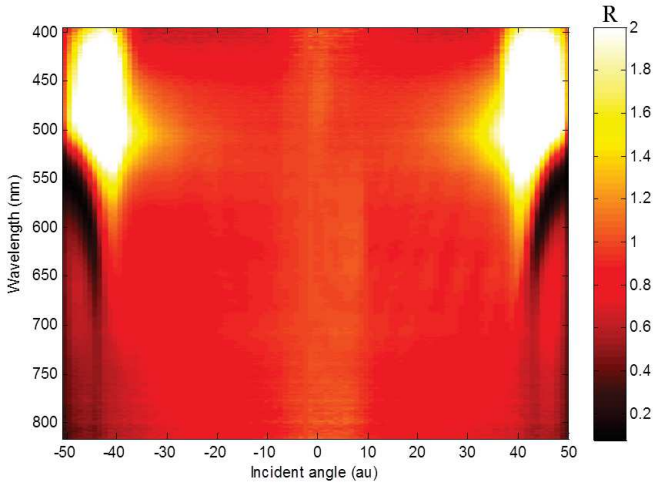

Figure 4.14: Experimental reflection from a glass sample coated with 40 nm of gold depending on the incident wavelength and angle with respect to the surface normal direction.

on the TM axis in the Fourier plane. The reflectivity function of the wavelength and the wavevector is then obtained by plotting spectra correlated to the position in the wavevector space. Figure 4.14 displays the intensity reflected by a glass sample coated with 40 nm of gold depending on the wavelength and angle with respect to surface normal direction of the incident electromagnetic waves.

The fiber has been scanned all along the TM axis in the Fourier plane, explaining the symmetry of the figure. The dip in the reflectivity is clearly visible at high incident angles. Saturated regions appear in the 550-400 nm range due to spectra normalization to the normal incident angle spectrum. In fact, due to interband transitions the reflectivity is much less than 1 in the 400-550 nm range at normal incidence (cf figure 1.11). The numerical aperture of the microscope objective limits the wavevector range. This can be problematic when a dielectric material is deposited on top of the gold layer, shifting the SPP band to higher wavevectors. Finally, the fiber entrance size limits the resolution on the incident angle axis. A greater extension of the image in the Fourier plane is needed to get a more precise dispersion relation of the SPP.

This experimental technique is an efficient tool to characterize surface plasmon polaritons properties and can be further calibrated with a diffraction grating for example to extract the dispersion relation of SPP.

4.4 High-Q plasmon modes

Engineering efficient plasmonic systems requires to carefully choose material. In the context of plasmonic cavities, one may wonder what geometry to adopt for the nanoparticle in order to maximize the quality factor of the plasmon resonance. For a single nanoparticle, the resonance frequency depends on the fraction of the plasmon energy inside the metal, and for this specific frequency the quality factor of the resonance is determined only by the complex dielectric function of the metal.[153]

However, electromagnetic interactions between individual units can be exploited to decrease internal metal losses and obtain high quality factor resonances.[154] The transition from a mode localized on a single nanoparticle to a Bloch mode delocalized on multiple nanoparticle changes the fraction of the plasmon energy inside the metal, and may lead to a high-Q plasmon mode.

In the following, we compute the quality factor of a nanorod and observe how it evolves

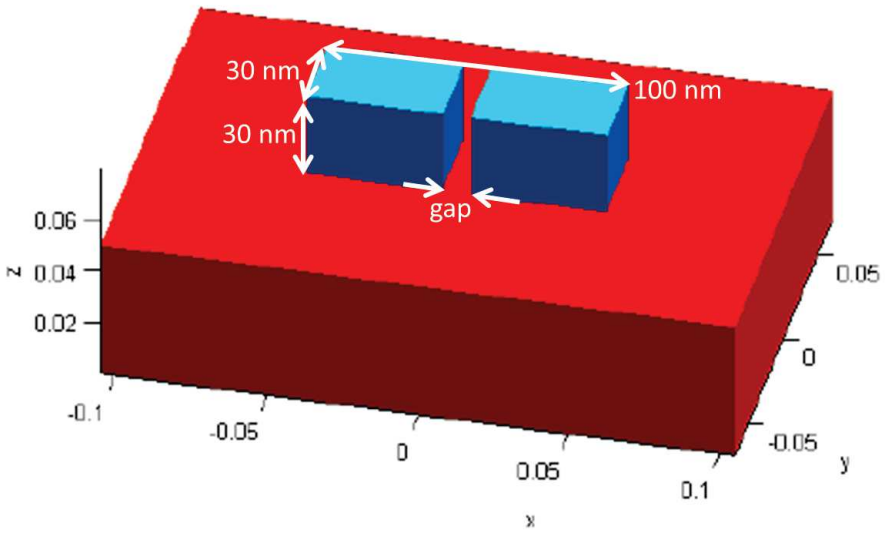

Figure 4.15: Gold nanorod with airgap on a glass substrate used for computations.

when a gap is opened in the middle of the nanorod. Scheme 4.15 displays the geometry of the rod and the gap varying from 0 to 5 nm.

We use the RETICOLO code, an implementation of a frequency-domain modal method known as the Rigorous Coupled Wave Analysis (RCWA) to compute the optical absorption of nanorods. Since it computes diffraction efficiencies and diffracted amplitudes of gratings composed of stacks of lamellar structures, we use perfectly matched layers to isolate nanoparticles from nearest neighbors. We also use a Granet transformation[155] to increase spatial resolution around permittivity function discontinuities and improve convergence rates.

Figure 4.16 displays the absorption spectra of a nanorod with an air gap varying from 0 to 5 nm. As the gap between the two rods increases, several effects are observed. First, the absorption resonance shifts toward the blue. The gap produces a consequent reduction of the nanorod aspect ratio. However, the reduction of the aspect ratio by a factor 2 is compensated by the in-phase coupling of the two rods that shifts the resonance to the red in a similar manner than J-aggregates.

Second, the absorption band decreases. This can be understood by the reduction of the number of electrons participating in the mode, therefore reducing the mode oscillator strength. Finally, a clear increase of the local plasmon resonance quality factor occurs when the gap increases, as displayed in 4.4. High quality factor plasmon resonances can therefore be obtained using in-phase coupling of small dipoles. A delocalized collective mode displaces the fraction of plasmon energy from metal to the dielectric environment.

Gap (nm)	0	1	2	3	4	5
Q_{loc}	14.3	16.5	17.5	18.9	22.1	23.9

A new resonance around 550 nm, not displayed in figure 4.16, appears as the gap increases. We assign this mode to the gap mode.

Opening gaps in a nanorod is an effective approach to obtain relatively high quality factors thanks to collective modes that are create by the in-phase coupling of small dipoles. However, opening 5 nm gaps in small nanorods seems unrealistic for the today available technology. One can draw a parallel with near-field dipole coupling in J-aggregates where the in-phase coupling of dye molecules creates an exciton mode delocalized on several molecules that displays a red-shifted resonance frequency with a smaller bandwidth and higher oscillator strength.

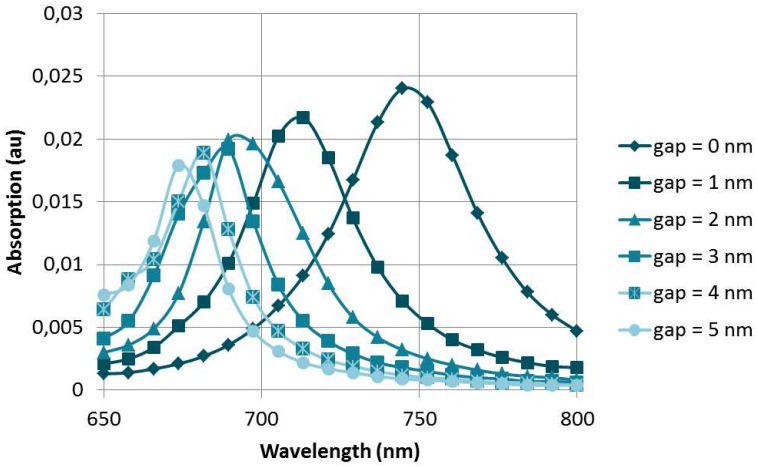

Figure 4.16: Gold nanorod absorption spectra when varying gap from 0 nm to 5 nm.

4.5 Conclusion

The electron damping in metals is the major issue in plasmonics for most of applications. Material research is needed to find ways to overcome or avoid these losses. We show that the Maxwell-Garnet and the Matrix transfer method are two useful theoretical approaches to conveniently predict exotic material dielectric properties and associated plasmon polariton characteristics. We experimentally demonstrate the possibility to measure the dispersion relation of plasmon polaritons. Finally, we show that the in-phase coupling of nano-rods can increase the quality factor of a local plasmon resonance, which is desired for example to amplify this mode through the interaction with emitters.

Chapter 5

Strongly coupled self-assembled dyes and plasmons

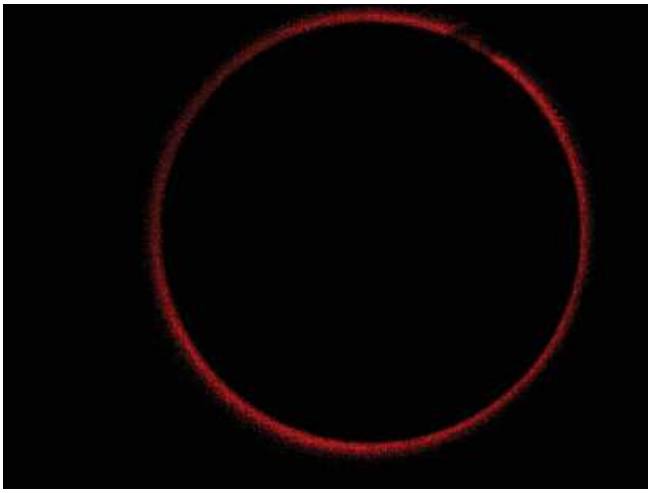

Back focal plane of the fluorescence from a self-assembled PTCDI-C7 thin film coupled to surface plasmon polaritons propagating at the gold surface.

The coupling between the dye molecules and the plasmon mode results in the dye emitting most of the light at a specific angle.

Contents

The coupling between light and matter allows controlling excited state radiative lifetime and spatial light emission patterns, to change the dynamics from incoherent to coherent, to create strongly non-linear systems active at low intensities. Such properties lead to the realization of single photons sources,[156] ultra-low threshold lasers,[157] photon blockade,[158] ultrafast all-optical switches.[159] All of these devices operate in the strong coupling regime where the interaction between an emitter and a specific electromagnetic mode dominates over the other interactions such as the interaction between the emitter and the continuum of vacuum modes.

Plasmonics exhibits several advantages for the realization of such components operating under strong coupling conditions. First, nano-fabrication techniques of plasmonic waveguides such as physical vapor deposition nanopatterning of gold are well known and controlled. Second, metal electrons confine electromagnetic modes at the metal surface. Since the dipole-photon coupling scales with the field-confinement volume V as $\sqrt{1/V}$,[160] plasmon modes can demonstrate very high coupling constants to dipoles up to the ultra-strong coupling regime.[161] Last, plasmonic systems coupled to organic dyes and quantum dots have demonstrated strong-coupling regime at room temperature proving the possibility to develop optical quantum devices operating under ambient conditions.[162,163,164]

Among all organic dye systems, dye aggregates are especially interesting since coherence effects between neighbor dyes resulting from intermolecular strong coupling can increase the dye system oscillator strength f at resonance. In such coherent collective excitations, the dipole moment scales as $\sqrt{N}$ where N represents the number of interacting dye molecules. Since the dipole-photon coupling scales as $\sqrt{f}$, collective excitations favor the strong coupling regime, in particular when coupled to a plasmonic waveguide.[165] However, this $\sqrt{N}$ factor does not impact the strength of the coupling when exciting the molecules, since the same phase is imposed to all the molecules by the excitation field. Depending on the orientation and the distances between the molecules within the aggregate, the collective excitation sees its resonance shifting toward higher (H-aggregate) or lower (J-aggregate) frequencies with respect to the isolated dye.

Therefore, the optimization of the interaction between a plasmonic mode and a dye system requires a precise control over intermolecular interactions inside the dye layer and thus their relative positioning and orientations. Furthermore, the precise positioning of dyes is also needed to increase the spatial and orientational overlap between dye dipoles and the plasmon mode electric field distribution and orientation: since the electric field of a plasmon polariton propagating at a metal surface is mainly normal to the surface, vertically oriented dye dipoles could further increase the interaction. In the meantime, the electric field of the plasmon polariton mode decays exponentially from the metal surface. Thus dye dipoles should be placed close to the surface to maximize the dye-plasmon interactions.

As a bottom-up approach, molecular self-assembly is the ultimate tool to control the arrangement of dye molecules with reference to each other. Furthermore, the molecular self-assembly approach also allows controlling the positioning of the assembled molecule with reference to the substrate surface, and vertically aligned molecules on top of a substrate can be obtained as demonstrated in chapter 1. Finally, the very high density of molecules in such systems confine photonic responsive elements in an extremely thin layer that is required to optimize the spatial overlap with the plasmon polariton mode.

Consequently, the self-assembly approach opens interesting prospects for the optimization of plasmon-organic dye coupling at the nanometer scale aiming at the development of optical quantum devices working under ambient conditions.

In this chapter, the coupling between a plasmon polariton mode propagating at a gold surface and a self-assembled N,N'-diheptyl-3,4,9,10-perylenedicarboximide (PTCDI-C7) thin film deposited by molecular beam epitaxy on top of the gold layer is studied.

The dispersion relation of this hybrid system is modeled numerically and characterized experimentally by probing the system reflectivity coefficient dependence on incidence angle and wavelength of an incident beam. The strong coupling regime is experimentally demonstrated. The emission is also investigated by leakage radiation microscopy and by numerical computations to clarify light-matter interactions with emitters displaying large Stokes shift.

5.1 Anti-crossing in self-assembled PTCDI on gold systems

Two oscillators can periodically exchange energy if they are interacting. This phenomenon can manifest itself in the framework of electromagnetic modes couplings principally at the crossing of the two systems dispersion relation curve, where the two systems are resonant in both frequency and wavevector domains. If the coupling is strong enough, the frequency at which the two systems exchange energy - called Rabi frequency - is large enough to remove the degeneracy of the two interacting states beyond their natural line widths. A high and a low energy coupled modes are then created corresponding to the two oscillators being either in-phase or out-of-phase. This results in an anti-crossing of the two oscillator system dispersion relation lines that is usually considered as a proof for strong coupling. An pedagogical detailed explanation of strong coupling in dye-surface plasmon polariton systems can be found in reference.[164]

In the previous chapter, the determination of the numerical and experimental dispersion relation of a plasmonic system has been presented. In the following, these two techniques will be used to give an insight into strong coupling between a dye thin film on top of a 40 nm thick gold film.

5.1.1 Tuning the Rabi frequency

The dielectric permittivity of the dye thin film is modeled as a lorentzian oscillator.The imaginary part is fitted from a transmission absorption measurement at normal incidence through the dye thin film. For example, a 30 nm thick PTCDI-C7 thin film absorbs $\sim 30\%$ of the incident light at resonance, as shown in chapter 1. The real part is then computed along Kramers-Kronig principle to obtain an off-resonant real part of the refractive index around 1.4, which corresponds to dense π-conjugated molecular medias. Dye dipoles inside the thin film are considered to be isotropically distributed.

Figure 5.1 displays the dispersion relation computed for a 30 nm thick dye thin film on top of a 40 nm thick gold layer. To get insight into the specific role of the real and imaginary parts of the dye dielectric constant in the coupling to plasmons polaritons, the real part of the dye thin film dielectric constant has been set to the constant value of 1.4^2 in figure 5.1 a), the imaginary part of the dye thin film dielectric constant has been set to zero in figure 5.1 b), and both real and imaginary parts of the dye thin film dielectric constant are regularly implemented in the simulation in figure 5.1 c). Notice that Kramers-Kronig relations are not verified anymore for the dielectric constant used in the two figures 5.1 a) and b), and thus does not represent a possible real physical system.

The presence of a dye layer with a uniform dielectric constant real part on top of the gold layer (figure 5.1 a)) changes the plasmon polariton dispersion relation in three ways. First, the reflectivity drop is uniformly shifted to higher wavectors. This results directly from the presence of a higher refractive index material on top of gold. Second, the reflectivity drop is enlarged in the wavevector direction close to the dye absorption band, for example at 700 nm.

Last, and more surprisingly, the drop in the reflectivity is reduced by a factor 10 from $R = 0.03$ for a gold/air interface to $R = 0.3$ for the gold/dye/air interface. One could

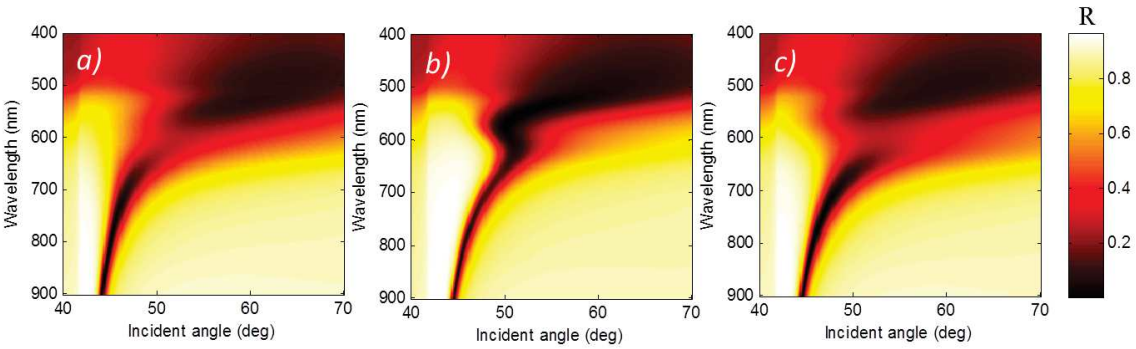

Figure 5.1: Calculated Reflection from a glass/gold (40 nm)/Absorber dye thin film (30nm) system as function of the wavelength and the incident angle of the incident electric field. a): $Re(\epsilon_{dye})$ set to 1.9, $Im(\epsilon_{dye})$ left unchanged . b): $Re(\epsilon_{dye})$ left unchanged, $Im(\epsilon_{dye})$ set to 0. c): No modification of ϵ_{dye}.

have expected to increase the reflectivity drop since more absorption occurs in the system with the addition of the absorbing layer ($A = 30\%$ for the dye layer at normal incidence). This is true if one integrates the reflectivity coefficient over wavevectors. However, since the reflectivity drop is significantly broadened by the dye absorption that shortens the plasmon polariton propagation length, the reflectivity drop peak is more important without than with the absorbing layer. From another point of view, the absorption is such that plasmons polaritons can't propagate and do not exist at this wavevector.

The presence of a dye layer with a null dielectric constant imaginary part on top of a gold layer is displayed in figure 5.1 b). Apart from a global shift to higher wavevectors produced by a high mean refractive index, the plasmon polariton dispersion relation displays an interesting feature around the dye resonant frequency. The variation of the refractive index function of the frequency due to the dye resonance is directly imprinted on the wavevector position of the reflectivity drop since this position is given by the value of the refractive index. This result can be derived from the analytical plasmon polariton dispersion relation at the interface between gold and a dye medium having both an infinite spatial expansion:

$$\beta = k_0 \sqrt{\frac{\epsilon_m \epsilon_{dye}}{\epsilon_m + \epsilon_{dye}}} \tag{5.1}$$

If $Im(\epsilon_{dye}) = 0$ and if $Re(\epsilon_{dye}) - 1 \ll Re(\epsilon_m)$ then the above equation can be rewritten:

$$\beta = n_{dye}(\lambda) \frac{2\pi}{\lambda} \sqrt{\frac{\epsilon_m}{\epsilon_m + 1}} \tag{5.2}$$

Figure 5.1 c) displays the reflection coefficient for the glass/gold (40nm)/ absorber dye thin film (30 nm) system with a dye dielectric constant complying with the Kramers-Kronig relation. This numerical simulation can be viewed as the combination of the two previous unphysical special cases. The real part of the dye dielectric constant is responsible for the position of the reflectivity drop in the 2D wavevector-wavelength space, whereas the imaginary part governs absorption and thus the reflection drop width and height. At dye resonance wavelength, the dye absorption is too strong to allow the propagation of surface plasmon polaritons and thus create the anti-crossing characteristic shape of the dispersion relation.

Since the anti-crossing strongly depends on the refractive index, one can control the energy exchange rate between systems through the choice of the proper refractive index. For example, figure 5.2 displays the dispersion relation of plasmon polaritons for a dye absorber thin film composed of either one resonator (figure 5.2 center) or two resonators

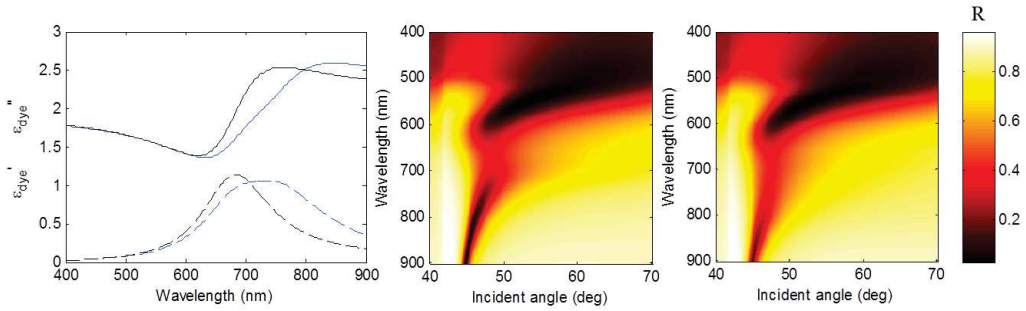

Figure 5.2: Left. Considered real and imaginary part of a one (black) and two (blue) absorber thin film dielectric constant. Calculated reflection coefficient from a glass/gold(40 nm)/dye (30nm)/vacuum system where the dye medium correspond to the black (center) and the blue (right) dielectric constant.

(figure 5.2 right) having close eigenfrequencies (figure 5.2 left). The anti-crossing in the two resonator system is much larger than for the one resonator system. Therefore, it is possible to tune the value of the opened gap E_g by acting on the difference between the natural frequencies of the two oscillators.

5.1.2 Experimental evidence of anti-crossing

A 30 nm thick PTCDI-C7 thin film is deposited on a 30 nm gold layer on a SiO2 substrate. AFM measurements, together with absorption and fluorescence spectra of this self-assembled PTCDI-C7 layer are detailed in chapters 1 and 2. Figure 5.3 a) displays the experimental reflection coefficient of TM polarized light incident on the system from the SiO2 side in a leakage radiation microscopy setup (see section 4.3), depending on the wavelength and the incidence angle of this incident light. The maximal incidence angle $\theta_{max} = 74.5°$ is fixed by the numerical aperture of the immersion objective, which corresponds here to $NA = 1.46$. A matrix transfer method simulating the experiment is displayed in figure 5.3 b). The absorption is modeled as a Lorentzian oscillator centered at $\lambda_{max} = 565\ nm$ with a 40 nm width (FWHM). The off-resonance refractive index is set to 1.6. For the simulation we assumed an isotropic orientational distribution of dye dipoles which is not the case in the real system, as shown in chapter 1.

Experimental data clearly show two branches of low reflectivity, symbolized by the black dots on the figure. The anticrossing wavelength ($\sim$ 565 nm) corresponds to the transition from the ground HOMO state to a Frenkel excitonic state delocalized on several dye molecules (0-F transition), sometimes considered as a hybrid charge-transfer Frenkel exciton. The anti-crossing width is measured to be 110 meV which is comparable with values reported for J-aggregates in other plasmonics systems.[164] The numerical simulation retrieves quite accurately the experimental reflectivity. It is interesting to note that plasmon polaritons couple with excitonic states delocalized on several dye units, creating a polariton which mixes plasmon propagating on gold and delocalized Frenkel excitons.

5.2 Luminescence of self-assembled PTCDI on gold

5.2.1 Strong coupling and Stokes shift

In the previous section, the dyes have been considered to be driven by an exciting electromagnetic field. In a two-state model, dyes emit the absorbed light at the same frequency. However, most of dyes molecules can't be considered as two state systems since they display a difference between band positions of the absorption and emission spectra. This

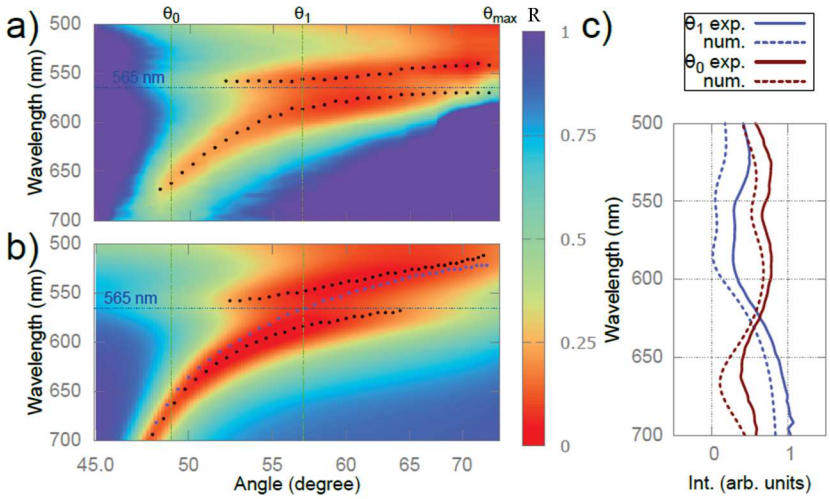

Figure 5.3: Reflection coefficient of the coupled system, (a) experimentally measured in the back focal plane and (b) obtained from numerical simulation. The dye absorption is modeled as a Lorentzian oscillator centered at 565 nm with a 40 nm width (FWHM). (c) Reflectivity spectra at $\theta_0 = 49°$ and $\theta_1 = 57°$. The dispersion relation of surface plasmon polariton propagating at a gold/dielectric (n=1.6) interface is plotted in dash blue. Experimental and numerical minima (black dashed lines) show a 110 meV anticrossing.

energy difference, referred to Stokes shift, results from the vibrational relaxation of the dye molecule. The full model describing a dye medium dielectric constant is required to account for absorption at one wavelength and emission at a lower energy. Since the dyes used in our experiments behave according to a four-state model, excited dyes display population inversion and thus act as a gain medium. A gain medium can be modeled with a negative polarizability imaginary part and a corresponding real part set up to verify the Kramers-Kronig relation. It corresponds to an electromagnetic field driven by the dyes. A fluorescence quantum efficiency can be introduced to set the oscillator strength of the fluorescence spectrum in comparison to the absorption spectrum. Instead of calculating the fluorescence emitted from a Hertz dipole, the effective gain is calculated for the excitation addressing each electromagnetic mode of the system.

Figure 5.4 displays the reflection coefficient of TM polarized light on a system composed of an emitting dye thin film (30 nm) on top of a gold layer (40 nm) deposited on

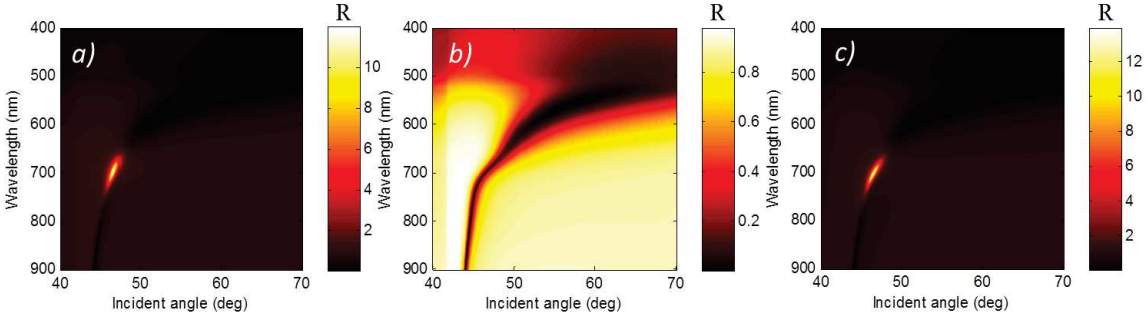

Figure 5.4: Reflection from a glass/gold (40 nm)/gain medium thin film (30nm) system as function of the wavelength and the incidence angle of the incident electric field. a): $Re(\epsilon_{dye}) = 1.9$, $Im(\epsilon_{dye})$ left unchanged. b): $Im(\epsilon_{dye}) = 0$, and the variation of $Re(\epsilon_{dye})$ has been exaggerated to see an effect. c): No modification of ϵ_{dye}.

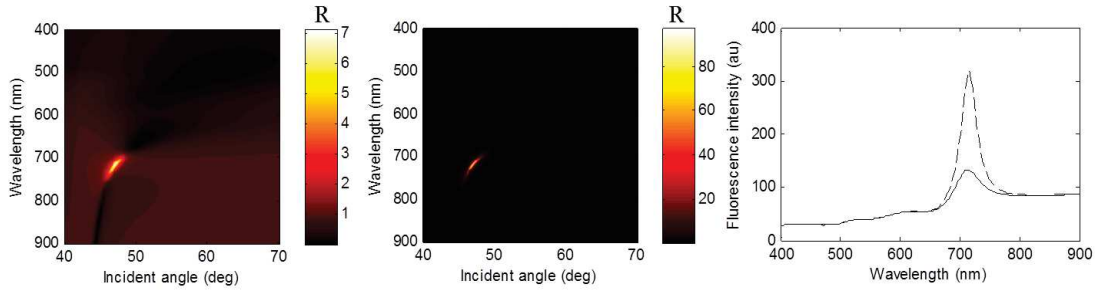

Figure 5.5: Reflection from a glass/gold (40 nm)/dye thin film (30nm) system as function of the wavelength and the incident angle of the incident electric field. The dye thin film absorbs light around 600 nm and fluoresces around 700 nm with a fluorescence quantum yield of 32% (left) and 38% (center).Right: Signal integration over wavevectors for left (plain) and right (dashed) figure.

SiO2. To get an insight into processes at play, $Re(\epsilon_{dye})$ is considered constant in Figure 5.4 a). It can thus not be considered as a physical system. Far from the dye resonance, no change in the SPP reflectivity drop is observed. At wavelengths close to the dye resonance, this simulation shows that most of the fluorescence signal of the dye layer is concentrated at the reflectivity drop wavevector position. In other words, the dyes of the gain medium mainly decay into the surface plasmon polariton mode.

In figure 5.4 b), $Im(\epsilon_{dye})$ has been set to zero and the variation of $Re(\epsilon_{dye})$ has been exaggerated to clearly identify the plasmon polariton dispersion curve dependence on the refractive index change. Instead of flattening the dispersion relation curve along a $\beta = \beta_{resonance}$ line as it is the case for an absorbing layer, the presence of the gain medium flattens the dispersion relation curve along a $\lambda = \lambda_{resonance}$ line. Since the gain medium layer drives the electromagnetic field, its polarization is ahead of phase in comparison to the field at low frequency. On the other hand, if the dye layer is absorbing the electromagnetic field, its polarization is delayed at low frequency. Therefore, dye layer refractive index variations as function of the frequency are inverted between the absorbing and the emitting case.

The refractive index variation of an gain medium thin film has the effect of increasing the density of plasmon polariton states at resonance wavelength but decreases the localisation of the polariton in the wavevector space.

Figure 5.4 c) displays the reflectivity with a physical ϵ_{dye}. The resulting figure is a combination of the effects described in the two previous paragraphs. Very high excited dye densities are required to see a modification of the dispersion relation curve. The main effect is the dye radiative decay into the SPP mode.

In the following, the dye thin film absorbs light around 600 nm and fluoresces at 700 nm to account for the Stokes shift with a 20% fluorescence quantum yield. Figure 5.5 displays the reflection coefficient of incident TM polarized electromagnetic waves on a system composed of a dye thin film (30 nm) on top of a gold layer (40 nm) deposited on SiO2.

In this case absorption and emission resonances are significantly separated in the frequency domain. The overall behavior of the system is a combination of the two previous sections. Below 650 nm, the anti-crossing is visible in the reflection of the exciting electromagnetic field. Above, 650 nm, the gain medium layer mainly excite the field in the surface plasmon polariton mode.

Thus, the Stokes shift major effect is to shift the emission from the anticrossing frequency resulting in a coupling of the gain medium to plasmon polaritons that are unperturbed by the absorption of the dyes.

An increase of the fluorescence quantum efficiency from 32% to 38% leads to a rapid augmentation of the fluorescence signal from 65 to 250, as shown in figure 5.5, going with a reduction of the fluorescence peak bandwidth from 45 nm to 30 nm. This directly results from the increase of the polariton propagation length that reduces the mode bandwidth. Ultimately, when the dye fluorescence compensates plasmon losses at the peak dye fluorescence wavelength, the polariton can propagate infinitely at this wavelength and the fluorescence signal tends to infinity.

5.2.2 Experimental wavevector resolved luminescence spectra

Experimental wavevector resolved emission spectra are taken by exciting the self-assembled PTCDI-C7 thin film on top of the gold layer with a 532 nm continuous wave laser (1 mW pumping power on a $\sim 1\ \mu m^2$ surface), collecting light by the SiO2 side of the sample through the immersion objective. The spectra are displayed in figure 5.6. Simultaneously, matrix transfer simulations are performed to model the experimental wavevector resolved data. From an experimental fluorescence spectrum at low fluence the PTCDI-C7 spectrum is modeled with two bands at 625 nm and 680 nm with an equivalent width. The absorption of a 30 nm thick PTCDI-C7 thin film is set to 30% in transmission, as measured in a transmission absorption measurement. The mean refractive index is set to 1.6. Finally, we consider a 10% radiative quantum yield.

The computed reflection coefficient resolved in wavelength and wavevector for the dye layer, which refractive index displays both absorption and fluorescence, shows a dip in the reflection along the surface plasmon polariton mode and an enhanced reflection at the crossing between the plasmon dispersion curve and the dye layer fluorescence frequency. The matrix transfer method requires the multi-layer system to be excited by an incident field that will reveal the dip in the reflection coefficient corresponding to the plasmon dispersion relation. This is not the case in the experimental wavevector resolved luminescence spectra because the gain medium is excited by a laser beam coming from the top of the system. Therefore, we implemented the following procedure to keep only the signature of the enhanced reflection produced by the emission of the gain layer in the computed reflection coefficient.

The enhanced reflection coefficient is obtained when the reflection coefficient computed without any fluorescence ($Im(\epsilon_d ye) = 0$, $Re(\epsilon_d ye)$ left unchanged) is subtracted from the reflection coefficient computed with the full dye layer dielectric characteristics.

It is worth noting that this procedure implies an in-phase emission of all emitters in the dye medium layer, which is questionable in the experiment.

The experimental wavevector resolved emission spectra in figure 5.6 show a clear concentration of the emission at a certain wavevector corresponding to an angle of $\sim 49°$. The superposition of the dispersion relation for the unexcited coupled plasmon polariton-dye system shows that the emission concentrates into the plasmon polariton mode. Below and above this resonance wavevector, two dye fluorescence bands can be identified at 610 nm and 680 nm. These bands correspond to the fluorescence of the PTCDI-C7 thin film on SiO2.

The matrix transfer simulation is in fair agreement with the experimental data. The emission is mainly detected in the plasmon polariton mode. Emission is also detected above the plasmon polariton wavevector. However, the computed signal for these wavevectors is significantly smaller than the experimental signal. This could result from a mismatch in the definition of the dye layer due to the anisotropy of the experimental system that the simulation does not take into account.

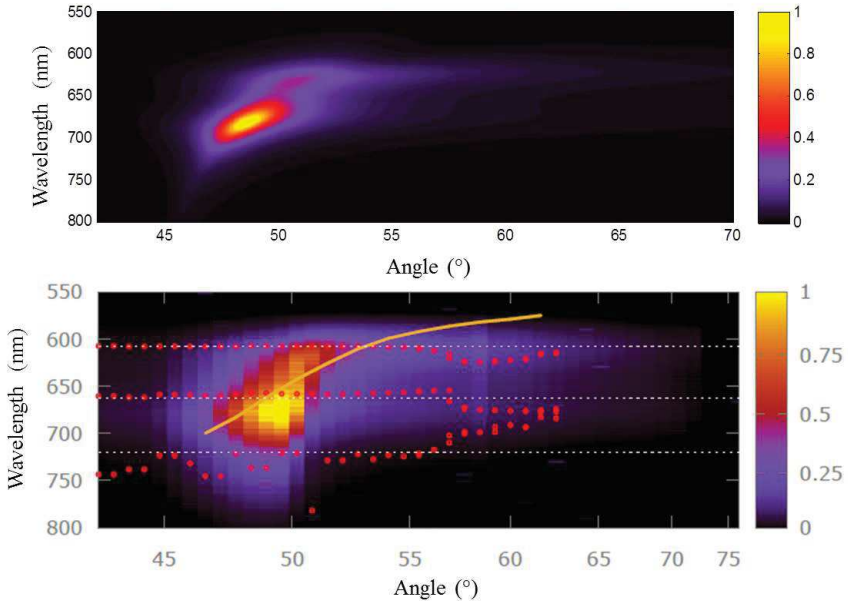

Figure 5.6: Top: Matrix transfer simulation computing the intensity emitted by the PTCDI-C7 layer on top of a gold film. Bottom: Wavevector-resolved emission spectrum of self-assembled PTCDI-C7 (30 nm thick) on top of a gold waveguide (40 nm) excited with a 532 nm CW laser. Dispersion of coupled SPP-molecule lower energy state (orange line). Red circles are the emission line centers resulting from the fit of the emission spectrum at the given wavevector. The three main components of the bare molecule emission spectrum are shown by white dotted lines.

5.3 Conclusion

The achievement of a strong coupling regime between plasmon polariton at a gold surface and a self-assembled dye thin film is possible under ambient conditions. The experimental determination of the polariton dispersion relation from a gold/self-assembled PTCDI-C7 thin film shows a 110 meV anti-crossing around the 560 nm absorption band of PTCDI-C7.

As determined with matrix transfer computations, the refractive index of the dye thin film is imprinted on the dispersion relation of the plasmon polariton. In the case of a non-excited dye film, the electromagnetic field drives the dye thus creating a "zig-zag" in the dispersion curve because the dye polarization is delayed with reference to the excitation electromagnetic field for frequencies below the its natural frequency and in advance of phase for frequencies greater than the natural frequency. The absorption of the film homogeneously broadens the polariton resonance by reducing the polariton propagation length and thus creates the anti-crossing since the polariton mode at dye absorption resonance is not allowed anymore.

In the case of an excited dye film, the dye medium drives the electromagnetic field thus creating a flattening of the dispersion relation of the polariton because the dye polarization is in advance of phase at low frequencies with reference to the electromagnetic field and delayed at high frequencies. At large excitation ratio, the optical gain of the dye reduces the width of the polariton band by increasing the polariton propagation length. Therefore, there is a concentration of the emission at the point where the polariton propagation length is the greatest.

Therefore, for emitter systems far from two energy level description one should not expect to remove the degeneracy between the coupled systems. Experimental wavevector resolved emission spectra of self-assembled PTCDI-C7 on gold confirm this vision and

show a clear concentration of the emission into the polariton mode.

Chapter 6

Supramolecular self-assemblies for plasmon amplification

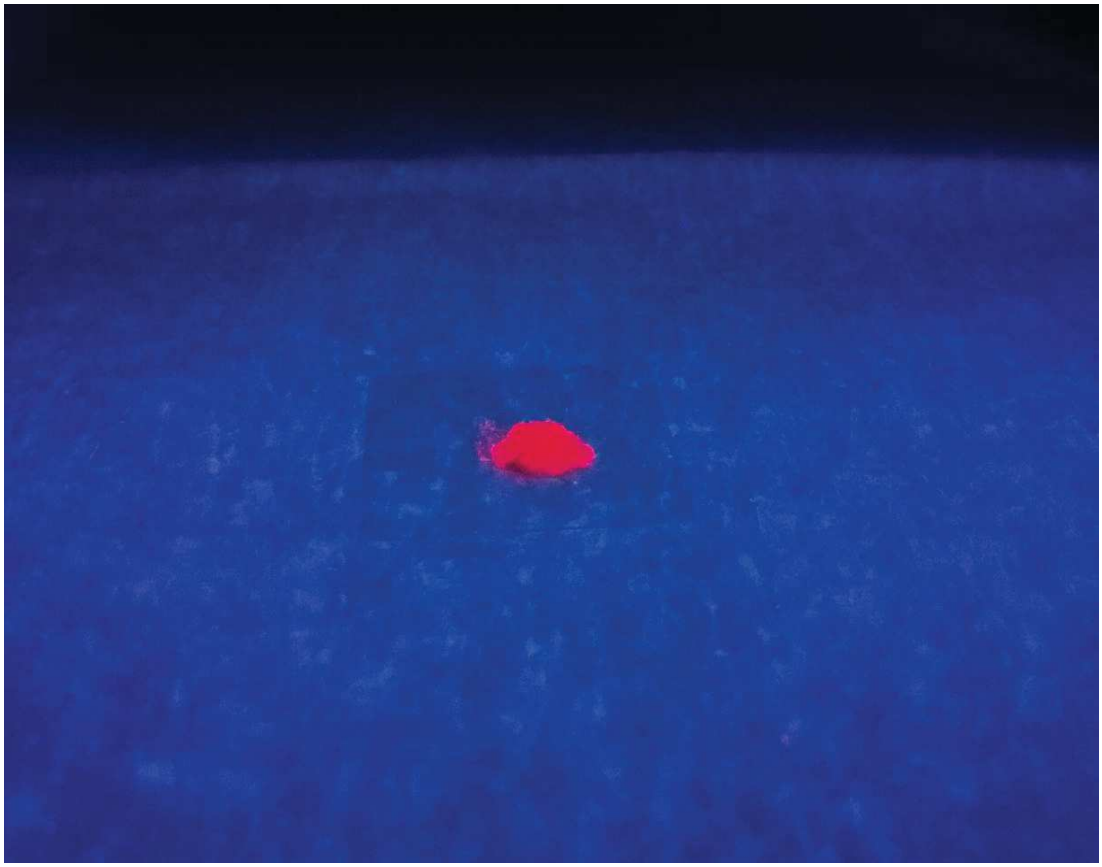

The perylene derivative PTCDI-C7 dye is fluorescent in its solid state: under UV light excitation, PTCDI-C7 powder displays a beautiful pink/red strong fluorescence.

Thanks to their very high molecular densities and the possibility to precisely control intermolecular distances and orientations, supramolecular self-assemblies could pave the way to efficient confined gain media that are desirable for the realization of nanolasers. How do the performances of these systems compare with conventional gain media? What are the limits of these systems?

Contents

Whereas most of the optical elements based on plasmonics produced up to now are passive (waveguides, couplers, etc.), a considerable effort is made to develop active components (amplifier, switch, etc.). In particular, the amplification of a plasmonic mode would lead to the development of a new category of plasmonic components, such as spasers, amplifiers, etc. Although some demonstrations of spaser[45 ,44] and plasmonic wave amplification[166] have already taken place, much of the work remains to be done in order to obtain a low threshold, reliable and efficient active component. Here, we evaluate the possibility of using molecular self-assemblies as optical gain medium in plasmonic systems to obtain the ultimate active plasmonic component.

6.1 Molecular self-assemblies as gain medium

6.1.1 Stimulated emission of plasmons

We consider a metal strip with a dielectric constant $\epsilon_m(\omega)$ covered by a gain medium consisting in a two-level energy quantum system assembly with a dielectric constant defined as $\epsilon_d(\omega)$. In the quasistatic regime, if the plasmon polariton propagation length is large compared with its wavelength, the number of surface plasmon polaritons N_n in the nth mode that propagate on the metal surface is given by the equation:[167]

$$\frac{dN_n}{dt} = (B_n - \gamma_n)N_n + A_n \tag{6.1}$$

Where the modified Einstein coefficients B_n and A_n represent respectively the stimulated and spontaneous plasmon emission by emitters present close to the metal surface, and which have a slightly different expression with reference to the case where emitters are positioned in an uniform medium. The parameter γ_n represent the plasmon relaxation rate. Considering an isotropic and uniform distribution of transition dipole moments d_{01} between the two states of emitters, Einstein coefficients can be written:

$$A_n = \frac{4\pi}{3\hbar}\frac{\epsilon_d - \epsilon'_m}{\epsilon_d \epsilon''_m} \mid d_{01} \mid^2 p_{an} q n \tag{6.2}$$

$$B_n = \frac{4\pi}{3\hbar}\frac{\epsilon_d - \epsilon'_m}{\epsilon_d \epsilon''_m} \mid d_{01} \mid^2 p_{bn} q n \tag{6.3}$$

Where ϵ'_m and ϵ''_m represent respectively the real and imaginary parts of the metal dielectric constant. The spatial overlap between the plasmon mode and the population inversion of the emitter is described by the dimensionless factor p_{bn}, and between the plasmon mode and the excited emitters by the factor p_{an}. Finally, q_n represents the dimensionless spectral overlap between the emitter transition and the plasmon mode.

Amplified spontaneous emission of surface plasmon polaritons(ASE) has been observed[166 ,168,169] in the near-IR range using gratings or working in the Kretschman configuration by optically pumping the gain medium.

When increasing the pumping power, such amplified spontaneous emission is characterized by a superlinear increase of the number of propagating plasmons in the amplified mode, and simultaneously a gain in their coherence. This effect manifests itself by a reduction of the spectral width of plasmons polaritons.[169]

Maximizing the number of plasmon polaritons in a given mode is directly linked to the maximization of Einstein coefficients which rule the number of propagating plasmon polaritons when an emitter interacts with a plasmonic waveguide.

The Einstein coefficient B_n can be decomposed in several factors. A dielectric factor $(\frac{\epsilon_d - \epsilon'_m}{\epsilon_d \epsilon''_m})$depending on the metal and the matrix containing emitters used can be isolated

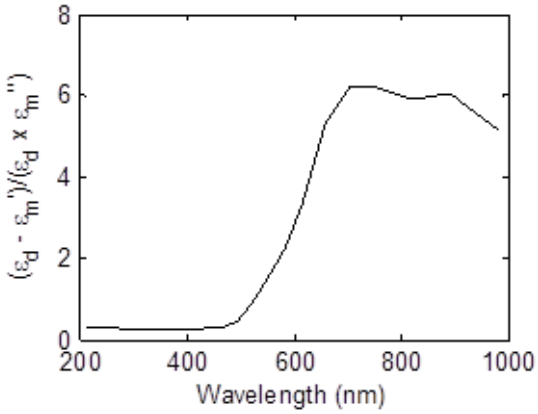

Figure 6.1: Dielectric factor of the Einstein coefficient for a gold/dielectric($\epsilon_d = 3$) interface. Gold dielectric constant from Johnson and Christy[147]

in the Einstein coefficient expression. Figure 6.1 displays the wavelength dependence of this dielectric factor for a gold/dielectric interface.

As the figures shows, the Einstein coefficient of an emitter on top of this gold waveguide is multiplied by a factor 3 if radiating at 700 nm instead of 600 nm, and by a factor 6 if radiating at 700 nm instead of 550 nm.

The second factor that can be isolated in the Einstein coefficient is the transition dipole moment d_{01}. The increase of transition dipole moments can be obtained by coupling in-phase emitters. In J-aggregates, such enhancement of the transition dipole moment is observable. A J-aggregate of N dyes has a transition dipole moment $\sqrt{N}$ times larger than the isolated dye,[52] and thus a J-aggregate of 10 dyes increases Einstein coefficients by one order of magnitude.

The third factor p_{an} (or p_{bn}) in the Einstein coefficient is the spatial overlap between excited emitters and plasmon modes. This spatial overlap can thus be enhanced by increasing the emitter density inside the plasmon mode. However, high molecular densities may lead to the Dexter or Förster quenching of excited states through the formation of aggregates. Thus, it exists an optimum density, which depends on the emitter characteristics, that maximizes the spatial overlap between the plasmon mode and emitters while preserving the excited state lifetime.

The fourth factor q_n in the Einstein coefficient is the spectral overlap. It describes the matching between the oscillator resonances and can be maximized by designing an emitter that radiates at the same frequency than the plasmon oscillation.

6.1.2 Molecular self-assemblies as gain media

Molecular self-assemblies can reach surface concentration of molecules over 0.5 $molecules/nm^2$, while avoiding aggregation of neighbor molecules. In comparison, quantum dots that can be used for gain media have typical sizes from 2 nm to 10 nm[170,.171] Molecular self-assemblies of organic dyes can thus be considered as good candidates to obtain the ultra-dense assembly of emitters that is needed to maximize the Einstein coefficients describing the spontaneous and stimulated rate of plasmon emission.

However, the monolayer thickness (around 1 nm) is much less than the surface plasmon polariton field extension in the dielectric medium (100 nm approximately for a gold/dielectric interface at 700 nm excitation wavelength). Molecular self-assemblies that exploit all the three spatial dimensions are needed to increase the number of emitters interacting with the surface plasmon mode.

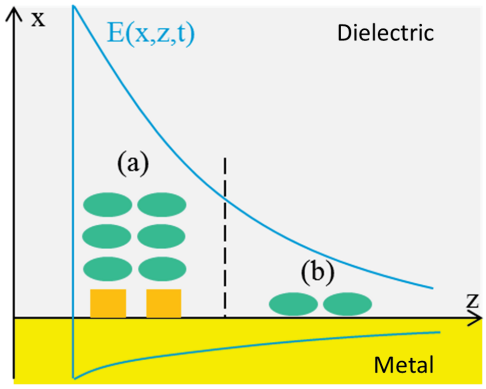

Figure 6.2: A 2D self-assembled dye (green) monolayer has a low spatial overlap with SPP electric field (b). The gain medium can be improved using 3D self-assemblies and using spacer that decouples the dyes from the surface. (a)

The flexibility in the design of assembling blocks could be exploited to form assemblies of J-aggregates. The transition dipole moments may then be maximized by in-phase couplings between emitters to obtain a highly efficient gain medium.

However, the surface close proximity could lead to quenching mechanisms such as Dexter transfer to the non-radiative metal electronic structure of the surface, or Förster transfer to dark modes that will relax the energy non radiatively. As shown in chapter 4, non-covalent self-assemblies can be designed so as to reduce charge transfer. A spacer between the active photonic part and the substrate surface can be used to avoid such quenching phenomena.

Finally, a molecular self-assembly takes place only on a surface. Therefore, this fabrication process inherently fulfills the requirement to cover a confined electromagnetic mode such as a local plasmon mode of a metal nanoparticle. The gain medium forms spontaneously without the need of expensive and complex fabrication processes.

Scheme 6.2 synthesize these considerations. The molecular self-assembly bottom-up approach could lead to highly efficient gain media through the design of J-aggregated dyes forming pillars that could self-assemble vertically on a substrate and that will be decoupled electronically from the surface by a spacer.

Table 6.1 compares three different gain media at a given optical pumping power the absorption cross-section, the pumping rate, the volume density of excited emitters, the spatial overlap between excited emitters and a plasmon polariton mode, and the effective linear gain.

The three compared gain media are:

- a CdSe quantum dots compact assembly. The quantum dots have a diameter of 2 nm and a molar absorptivity of $2 \times 10^5\ cm^{-1}mol^{-1}$.[167]

- A typical laser dye (HITC) in a PMMA matrix. The laser dye concentration is assumed to be $4 \times 10^{-2}\ mol \times L^{-1}$ and its molar absorptivity is $2 \times 10^5\ cm^{-1}mol^{-1}$. These parameters correspond to the gain medium used in.[172] It represents a trade-off between high concentrations that aggregate the dye molecules and thus change their photonic properties, and a low concentration that is not efficient in term of spatial overlap with the electromagnetic mode to amplify.

- A PTCDI molecular self-assembly monolayer. The molar absorptivity of the PTCDI molecule is $8,7 \times 10^4\ cm^{-1}mol^{-1}$. The PTCDI supramolecular network formed at an HOPG surface has a typical surface density of 0.5 $molecules/nm^2$. We assume that the gain medium has a 1 nm thickness, which correspond to the order of magnitude for the molecule thickness.

	CdSe	HITC	PTCDI monolayer	PTCDI pillar
$\sigma(m^2) \times 10^{20}$	7.6	7.6	3.3	33
$\tau(\%)$	0.26	0.36	0.11	1.1
$d_s(m^{-2}) \times 10^{-17}$			3.0	3.0
$d_v(m^{-3}) \times 10^{-25}$	2.2	2.4	30	3
Spatial overlap	1	1	0.01	0.1
$G(\mu m^{-1})$	0.45	0.66	0.019	1.9

Table 6.1: Comparison gain media characteristics for a CdSe quantum dot (2 nm diameter) compact assembly, a HITC laser dye in PMMA matrix system (the dye concentration is assumed to be $4 \times 10^{-2}\ mol \times L^{-1}$), a self-assembled PTCDI monolayer with a 0.5 $molecules/nm^2$ surface concentration, and self-assembled pillars composed of 10 PTCDI J-aggregated, the pillars displaying a 0.5 $molecules/nm^2$ surface concentration.σ: absorption cross-section, τ: pumping rate resulting from an excitation at a 1 W/mm^2 optical power (80 MHz repetition rate), d_s: emitter surface, d_v: emitter volume density, spatial overlap between excited emitters and a plasmon polariton mode with a 100 nm spatial extension above the metal surface, G: effective linear gain obtainable for a propagating plasmon polariton.

- Self-assembled pillars of 10 J-aggregated PTCDI. The supramolecular network is assumed to have the same arrangement on the surface than the PTCDI self-assembly. Stacks are considered to be 10 nm tall. The J-stacking of PTCDI increases the absorption cross section by 10 in comparison to one monolayer PTCDI. However, the volume density is divided by 10 in comparison of the self-assembled PTCDI system since we consider 10 nm high PTCDI pillars.

These systems are compared when excited by a femtosecond laser at a wavelength corresponding to the gain media peak absorption, with a 1 W/mm^2 optical power at a 80 MHz repetition rate. The pulse energy of such pump is then $1.25 \times 10^{-2}\ Jm^{-2}$.

The absorption and fluorescence cross-sections are considered to be identical, and are deducted from the molar absorptivity ϵ in $Lmol^{-1}cm^{-1}$ with the relation:

$$\sigma = 1000ln(10)\frac{\epsilon}{N_A} = 3.82 \times 10^{-21}\ \epsilon\ (cm^2) \tag{6.4}$$

The pumping rate τ is deducted from the absorption cross-section σ and the peak absorption energy from the gain medium $\hbar\omega_0$, and from the light energy density of the optical pump E:

$$\tau = \frac{\sigma E}{\hbar\omega_0} \tag{6.5}$$

The spatial overlap factor R represents the vertical overlap between the gain medium and the plasmon polariton electric field. It is computed by taking the ratio of the gain medium thickness to the plasmon polariton field characteristic extension above the surface, that we assume to be 100 nm.

Finally, the linear gain G (μm^{-1}) is calculated with the following equation:

$$G = \sigma\ d_v \tau R \tag{6.6}$$

Computations show in 6.1 that the absorption cross-section of PTCDI dye molecule is slightly lower than the absorption cross-section of CdSe quantum dots or HITC dye. However, the J-stacking of 10 PTCDI molecules can increase the absorption cross-section by an order of magnitude, which directly impacts the pumping rate and the gain that can

be obtained. The volume density of the self-assembled PTCDI monolayer is much larger than for the other compared systems. When J-aggregated, the PTCDI volume density loses an order of magnitude since one should consider J-aggregates and not PTCDI molecules alone anymore.

As displayed in the table 6.1, the gain that can be obtained from a molecular self-assembly monolayer is two orders of magnitudes below what can be obtained with volume gain media. These two orders of magnitude are directly linked with the fact the monolayer covers only 1% of the plasmon polariton field. The number of dye molecules that interact with the plasmon mode has to be increased in order to compete with traditional gain media.

Surprisingly, one should note that self-assembling 10 J-stacked PTCDI is sufficient to surpass the characteristics of traditional gain media by a factor of 3, and by an order of magnitude if 20 PTCDI are J-stacked. The full losses compensation for a gold plasmonic waveguide requiring a 2 μm^{-1} gain[173] will then be achievable at low pumping power (1.1 W/mm^2 at a 80 MHz repetition rate). The advantages of the J-stacked PTCDI system mainly result from the aggregation of the molecule which on the one hand allows to obtain many molecules interacting with the plasmon mode and, on the other hand, a high pumping rate at a given excitation power resulting from the collective behavior of the system. Furthermore, the J-aggregation can induce a concentration of the oscillator strength in the fluorescence spectrum that directly leads to an increase of the fluorescence cross-section and thus to an enhancement of the linear gain.

Molecular self-assemblies appear as an alternative for gain media currently used in the amplification of confined electromagnetic modes. These systems would be particularly suitable for the stimulated emission of plasmons thanks to high surface densities that can be obtained and to the possibility of creating J-aggregates that enhance assembled dye photonic properties. More specifically, the self-assembly of pillars formed by J-aggregation of dye molecules could be of great use for the development of plasmonic based amplifiers and lasers, and more generally for the amplification of confined electromagnetic modes.

6.2 Gain limitations in self-assembled thin films

Solid state organic gain media have been studied for a long time since they benefit from the advantages of organic material such as tunable, compact and low-cost sources while avoiding the inconvenient use of toxic solvents used in liquid dye lasers.[174] Moreover, the use of a solid state may improve the dye photostability by preventing the diffusion of oxygen and moisture[175] and decrease the lasing threshold by massively increasing the number of emitters interacting with the cavity electromagnetic mode,[157,176] which are two major limitation to the development of organic laser systems. However, photonics properties of dye molecules are usually radically different between the solid and the liquid phase since intermolecular interactions lead to fluorescence quenching[177] and absorption and fluorescence spectra redistribution over visible frequencies.

Reducing the intermolecular interactions such as π-stacking can be done by designing molecular geometries that isolate the emissive part from neighbors thanks to highly branched groups.[178] However, the introduction of these spacer groups increases the amorphous character of the thin film and decrease its molecular packing density. In the context of surface plasmon polariton amplification, the organization of the film plays an important role since the propagating mode electromagnetic field is mostly normal to the metal surface. Therefore, an anisotropic gain medium is needed to optimize the coupling from emitters to the plasmon polariton mode.

Perylene derivative 2,9-Diheptylanthra [2,1,9-def : 6,5,10-d'e'f'] diisoquinoline-1,3,8,10 (2H,9H) tetrone (PTCDI-C7) thin film grew by molecular beam epitaxy presents both

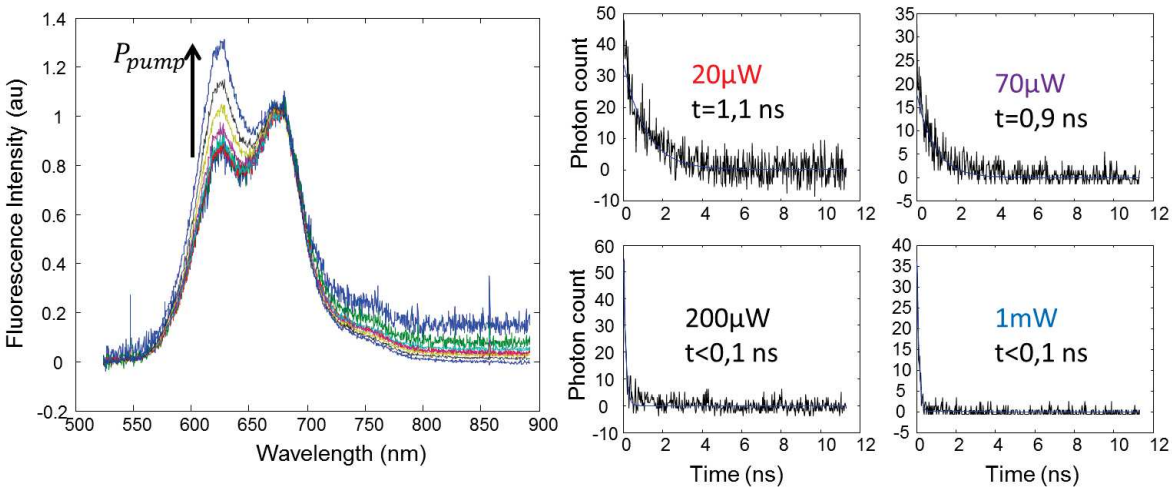

Figure 6.3: Left. Fluorescent spectra of a 30 nm PTCDI-C7 thin film on gold for increasing pumping power at 460 nm from 20 μW to 4 mW with reference to the same gold substrate without any molecules. The spectra have been normalized on the intensity of the 680 nm band. Right. Fluorescence decays at various pumping power.

an organization with the molecular main axis nearly normal to the substrate surface (see Chapter 1) and a relatively good fluorescence quantum efficiency ($QE \sim 10\%$) (see Chapter 2). It may thus be a good candidate to be used as a solid-state gain medium for plasmon polariton amplification. However, the compensation of the plasmonic losses requires high gain coefficients only achievable with large excitation ratios.

In the following, photodynamic properties of a 30 nm thick PTCDI-C7 thin film are studied to explore which physical phenomena limit its use as gain medium, such as exciton recombination at such high pumping rates.

6.2.1 Yield, spectrum and decay dependence on pump power

A 30 nm thick self-assembled PTCDI-C7 layer on top of various substrates (gold, SiO2 and ITO on SiO2) was excited at a 460 nm wavelength by a doubled Ti:Sapphire femtosecond laser focused onto the sample through a microscope objective (NA=0.6, x40). Fluorescence spectra were collected from a microscope immersion objective (NA=1.3, x100) on the other side of the sample. Figure 6.3 displays normalized fluorescence spectra for the PTCDI-C7 on gold hybrid system for pumping power ranging from 20 μW to 4 mW. Two clear bands are visible on the spectra at 620 nm and 680 nm and a shoulder can be distinguished at 720 nm. Surprisingly, the oscillator strength is redistributed from the 680 nm to the 620 nm band when increasing the pump power. A consequent reduction of the fluorescence lifetimes accompany this fluorescence spectrum redistribution, as shown in figure 6.3. At 20 μW pumping power, the fluorescence lifetime is estimated to 1.1 ns and decreases below 0,1 ns (setup detection limit) at 200 μW pumping power.

Figure 6.4 shows the variations of the two fluorescence bands intensities with reference to the pumping power in a logarithmic scale for the three different substrates. First, the PTCDI-C7 thin film on SiO2 fluorescence intensity at low pumping power is one order of magnitude larger than on ITO on SiO2 and two orders of magnitude larger than on gold. The coupling of emitters to dark modes of ITO and gold through a Forster mechanism can be invoked to explain such difference. Furthermore, the different nature of the three substrates could lead to small differences in the dye orientation with respect to the substrate during the assembly process and could then result in enhancing or decreasing

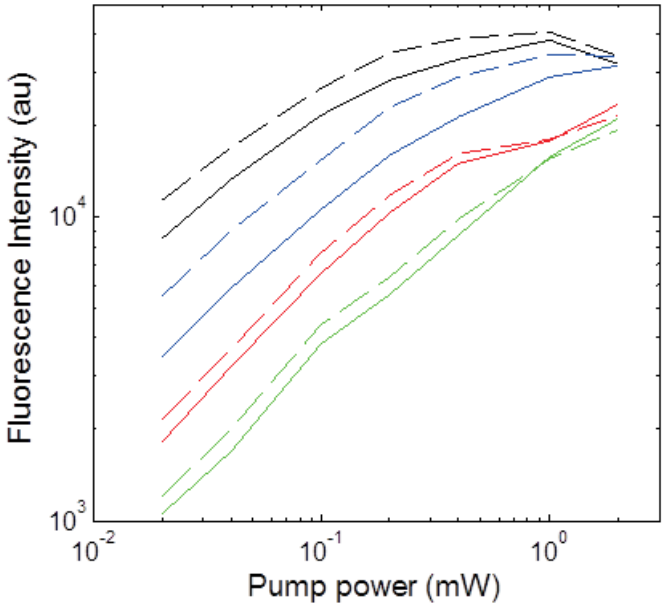

Figure 6.4: Fluorescence spectra band intensity dependence on pumping power for a 30 nm self-assembled PTCDI-C7 monolayer on glass (black), ITO on glass (blue) and gold (red when increasing pumping power, green when decreasing pumping power after the first pump ramp). Dash line represent the 0-1 transition, plain line the 0-0 transition.

the dye interaction with the incident electric field. Second, a clear non-linear dependence on pumping power is observed for the three systems: losses on fluorescence intensities increase with pumping power. However, these losses are not identical for the two main bands of the fluorescence spectra. For all three systems, the 680 nm band is more quenched at high pumping power than the 620 nm band. Two successive increasing and decreasing pumping power ramps confirm the reversibility of the observed phenomenon (Figure 6.4, red: increasing power ramp, green: decreasing power ramp) : the non-linear characteristic of the fluorescence intensity with pumping power is not related to a non-reversible process such as a bleaching of the emitters. However, the fluorescence intensity difference between the two successive pumping power ramps reveals a rapid bleaching of the optically active layer at 4 mW pumping power.

6.2.2 Time-resolved fluorescence spectra

Time-resolved fluorescence spectra have been performed for the 30 nm thick PTCDI-C7 thin film on ITO on SiO2 with a sub pico-second resolution by Valentin Maffeis (collaboration with LIDYL laboratory). The spectra are recorded using a combination of fluorescence upconversion in a nonlinear crystal and time-correlated single photon counting. A doubled femtosecond Ti:Sapphire laser is used as excitation source. Figure 6.5 displays spectra at various times after the exciting femtosecond pulse at 460 nm wavelength. Right after excitation, a rapid decrease of the fluorescence signal is observed in the 0 - 500 fs region. Thus, the excited dyes relax rapidly in a state where radiative transitions are hampered. This effect could be attributed to an H-aggregation effect of PTCDI-C7 where the lowest energy transition is forbidden due to the out-of-phase Coulombic coupling of dye dipoles.

The fluorescence spectra display a shift to the red between the 0 - 1 ps and the 1 - 10 ps region revealing an energy transfer between at least two excited states. Time-resolved fluorescence spectra at 50 fs, 500 fs, 1 ps and 9 ps displayed in figure 6.6 show this global

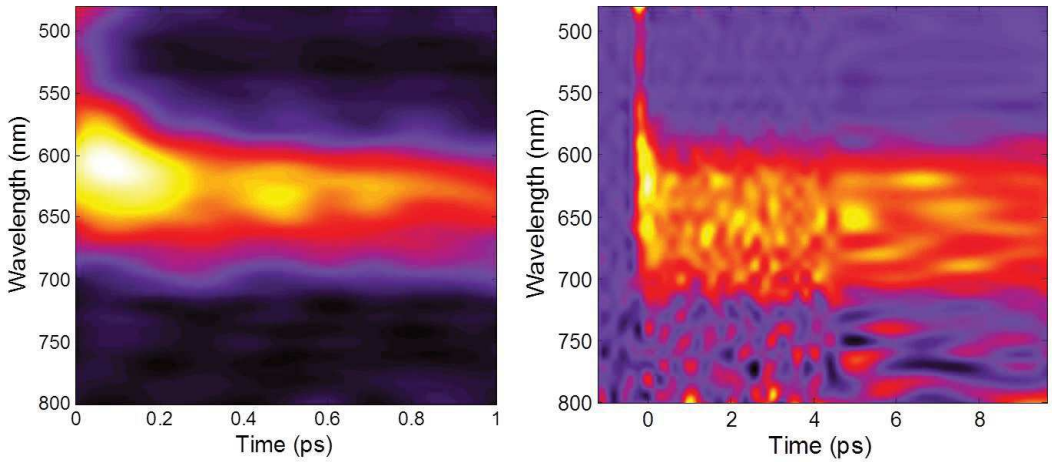

Figure 6.5: Experimental time-resolved fluorescence spectra for a 30 nm PTCDI-C7 thin film deposited on ITO on glass excited by a doubled femtosecond Ti:Sapphire laser at 460 nm.

redshift behavior. Between 100 and 500 fs, the fluorescence spectra reveal a unique band at 620 nm. At 1 ps, a shoulder at 680 nm appears continue to increase with time to match the 620 nm oscillator strength at 9 ps. The fluorescence band positions are consistent with previously obtained fluorescence spectra as measured in the continuous-wave regime superimposed in 6.6.

Fluorescence lifetime measurements in the picosecond regime at 620 nm, 680 nm and 720 nm are displayed in Figure 6.6. A multi-exponential fit reveals a short ($\tau_1 \sim 2\ ps$) and a long ($\tau_2 \sim 120\ ps$) lifetime for the PTCDI-C7 on ITO fluorescence spectrum with a major contribution from the long-lived state in the fluorescence spectrum. The fluorescence signal at 720 nm is too low to extract a meaningful fluorescence lifetime.

To summarize, the fluorescence mainly comes from the 620 nm band at short times after excitation. Interestingly, the fluorescence lifetime was found to decrease dramatically at large pumping power, meaning that most of the fluorescence coming from long times after the excitation was quenched. The increase of the 620 nm band in the fluorescence spectrum is then explained by time-resolved fluorescence spectra showing that the 620 nm band is stronger at short times after excitation. Furthermore, this consideration also explains the observed different partition of the oscillator strength over the 620 nm and 680 nm bands in the fluorescence spectra of PTCDI-C7 on SiO2, ITO and gold since ITO and gold reduce the fluorescence lifetime of the dyes through a Forster mechanism.

A model describing the electronic states and transition rates is built in the following section to get insight about the quenching mechanism that arises at high pumping power.

6.2.3 Electronic transition model

The active medium is modeled by a ground state G, and two excited state E_1 and E_2. The transition from E_1 (resp. E_2) to G correspond to the 620 nm (resp. 680 nm) fluorescence band observed experimentally. When a high energy photon is absorbed, the state of the system is E_1 after a rapid relaxation. From E_1 state, the system can either relax to the G state through a radiative γ_{1R} and non-radiative γ_{1NR} decay rate, or transfer its energy to the E_2 state (γ_t). The system can then relax to the G state through a radiative γ_{2R} and non-radiative γ_{2NR} decay rate. These transitions can be summarized in the following equations, where $\gamma_{1R} + \gamma_{1NR} = \gamma_1$ and $\gamma_{2R} + \gamma_{2NR} = \gamma_2$:

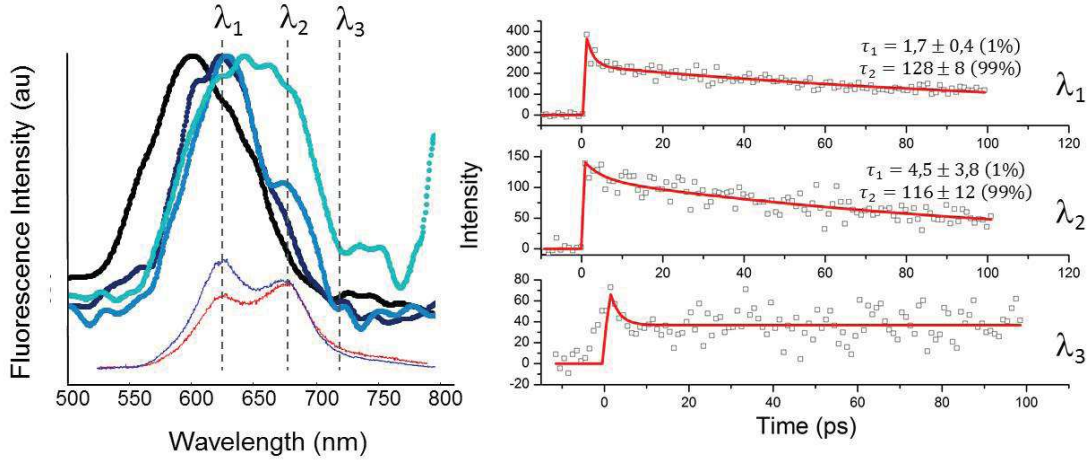

Figure 6.6: Left. Normalized experimental time-resolved fluorescent spectra at different time from 1 to 10 ps (noisy lines). Fluorescence spectra for 20 μW and 4 mW (resp. low noise red and blue curves) have been superimposed for easier comparison. Right. Fluorescence decays at 620 nm, 680 nm and 720 nm.

$$\begin{aligned} G &\xrightarrow{\Gamma} E_1 \\ E_1 &\xrightarrow{\gamma_1} G \\ E_1 &\xrightarrow{\gamma_t} E_2 \\ E_2 &\xrightarrow{\gamma_2} G \end{aligned} \tag{6.7}$$

Assuming a short lived (100 ps) E_1 state and a long-lived (1 ns) E_2 state, γ_1 and γ_2 can be set at low excitation rate to match the experimental fluorescence spectrum of the PTCDI-C7 thin film with a fluorescence quantum yield of 50% and a oscillator strength distribution over the spectrum corresponding to the figure 6.3.

The resulting time-resolved fluorescence spectra are displayed in figure 6.7 ($\gamma_{1R} = 5\times 10^9\ s^{-1}$, $\gamma_{1NR} = 5\times 10^9\ s^{-1}$, $\gamma_t = 15\times 10^9\ s^{-1}$, $\gamma_{2R} = 5\times 10^8\ s^{-1}$, $\gamma_{2NR} = 5\times 10^8\ s^{-1}$).

However, these linear processes are not sufficient to describe the dependence of the self-assembled PTCDI-C7 thin film fluorescence spectrum on pumping power. Non-linear recombination processes have to be introduced such as exciton recombination. If two neighbor molecules are in the excited state E_1, one molecule can decay in the G state by giving its energy to its neighbor. The other molecule will rapidly relax this energy returning in the E_1 state. Such mechanism are also possible between two molecules in the E_2 state, or one molecule in the E_1 state and another in the E_2 state. These non linear processes are associated with decay rates γ_{11}, γ_{22} and γ_{12} as follow:

$$\begin{aligned} E_1 + E_1 &\xrightarrow{\gamma_{11}} E_1 + G \\ E_1 + E_2 &\xrightarrow{\gamma_{12}} E_1 + G \\ E_2 + E_2 &\xrightarrow{\gamma_{22}} E_1 + G \end{aligned} \tag{6.8}$$

The experimental fluorescence signal dependence on pumping power shows a difference in the non-linearity for the two 620 nm and 680 nm bands that can only be explain by a difference in the non-linear recombination rate between the two states E_1 and E_2. Simulated non-linear rates depend on how pumping power is defined in the simulation.

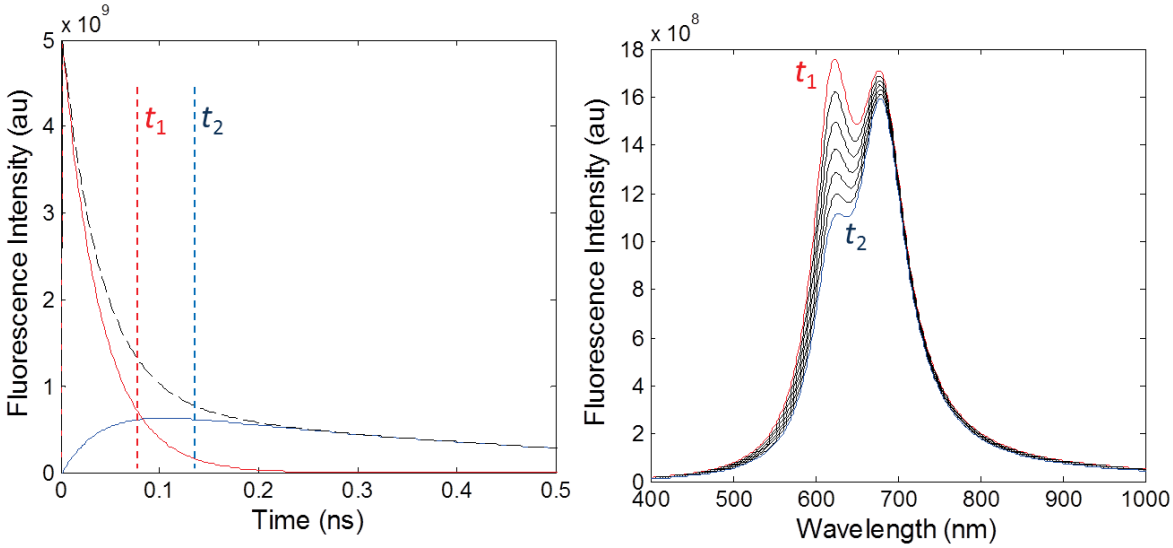

Figure 6.7: Left. Computer simulated time-resolved fluorescence intensity of the 620 nm band (red), the 680 nm band (blue) and the sum of these two bands (black). Computer simulated time resolved fluorescence spectra between times t_1 and t_2.

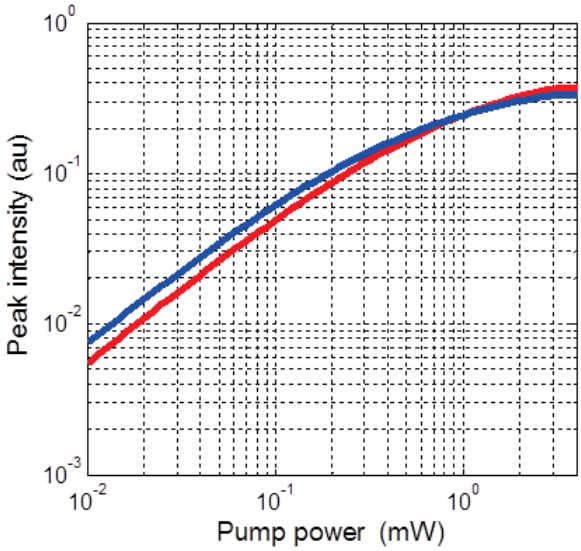

Figure 6.8: Computed fluorescence spectra band intensity dependance on pumping power. The red (resp. blue) line represent the 0-0 (resp. 0-1) transition.

We retrieve the experimental behavior for the fluorescence spectrum when setting $\gamma_{11} = 10^{11}\ s^{-1}$, $\gamma_{12} = 6 \times 10^9\ s^{-1}$ and $\gamma_{22} = 6 \times 10^9\ s^{-1}$, as displayed in figure 6.8.

The model can be summarized with the following set of equations describing the temporal evolution of the population N_G, N_1 and N_2 of the respective states G, E_1 and E_2:

$$\frac{dN_G}{dt} = (-\Gamma + \gamma_1)N_1 + \gamma_2 N_2 + \gamma_{11}N_1^2 + \gamma_{22}N_2^2 + \gamma_{12}N_1N_2 \tag{6.9}$$

$$\frac{dN_1}{dt} = (\Gamma - \gamma_1)N_G - \gamma_t N_2 - \gamma_{11}N_1^2 + \gamma_{12}N_1N_2 \tag{6.10}$$

$$\frac{dN_2}{dt} = -\gamma_2 N_G + \gamma_t N_1 - \gamma_{22}N_2^2 - \gamma_{12}N_1N_2 \tag{6.11}$$

The time-resolved fluorescence intensity at the instant t of the two bands then corresponds respectively to $\gamma_{1R}N_1(t)$ and $\gamma_{12}N_2(t)$. The pumping power is adjusted with the parameter $N_1(0)$, the population of the state E_1 just after the excitation by the incident laser beam. The two transitions are considered to be lorentzian using a width that fits the experimental spectra at low pumping power.

6.3 Conclusion

Supramolecular self-assemblies open the perspective to obtain highly efficient gain media thanks to a high concentration of dyes in the medium and the possibility to saturate the active medium at low excitation rate when molecules behave collectively forming J-aggregates. These system have the potential to surpass the gain of active media such as dyes in a polymer matrix or assemblies of quantum dots by at least one order of magnitude.

Self-assembled PTCDI-C7 thin films on top of various substrates have been optically characterized to probe their photonic properties as potential gain media for amplifying surface plasmon polaritons. Linear and non-linear non radiative recombination processes reduce the fluorescence quantum yield due to intermolecular interactions such as exciton-exciton recombination and therefore limit the performances of this active media, especially at high excitation rates. The fluorescence quantum yield estimated at 10% at low pumping rates decreases to 1% at high pumping rates. A careful design of the assembling building block should be undertaken to reduce these limiting effects by, for example, spacing the dyes while maintaining sufficient intermolecular interactions to form a self-assembled system.

Summary

As a bottom-up approach, supramolecular self-assembly allows the design of matter at the nanometer scale through the control of intermolecular distances and orientations. In this work, we have studied optical absorption, fluorescence and vibrational properties of two- and three-dimensional dye self-assemblies exploring how these photonic characteristics depend on intermolecular and molecule-substrate interactions.

In chapter 1, we have studied several dye self-assemblies on graphene forming well-defined two-dimensional networks with geometrical parameters characterized by STM experiments. Transmission absorption measurements have shown a rigid redshift of the absorption spectra in comparison to the same dyes dispersed in a toluene solution with minor modifications in the peak structure of the absorption spectra. We were able to observe a significant change in the oscillator strength distribution over the S0-S1 vibronic replicas by varying the intermolecular distances in self-assembled perylene derivative monolayers on graphene. We have attributed this effect to Coulombic dipole-dipole couplings between neighbor molecules. Self-assembled molecules with a dye group standing away from the graphene surface have displayed a smaller redshift of their optical absorption peak. Therefore, the modification of the dielectric environment due to the high refractive index of graphene and the spatial overlap between the sp^2 orbitals of graphene and the adsorbed dye have appeared to be the main phenomena altering the dye absorption spectrum once self-assembled on the graphene surface. We have demonstrated the possibility to extend these two-dimensional self-assemblies to three dimensions by evaporating perylene-dye derivatives at a slow deposition rate on heated surfaces.

Adsorbed dyes on graphene lose their fluorescence due to both Dexter and Förster type energy transfers toward non-radiative excited states. Nevertheless, we have shown in chapter 2 that a fluorescent molecular self-assembled monolayer on graphene has been obtained with the use of a 3D Janus tecton embedding a PTCDI dye spaced from a pedestal group steering the assembly at the graphene surface. We have demonstrated the first fluorescent functionalization of graphene with a self-assembled molecular monolayer. A multilayer self-assembled system with a 10% fluorescence quantum efficiency has been demonstrated, paving the way to self-assembled optical gain media.

The fluorescence quenching of self-assembled dyes by graphene has been exploited in chapter 3 to measure vibrational properties of self-assembled molecules by Raman spectroscopy. This have provided the opportunity to measure for the first time the Raman response of PTCDI, which is normally made impossible by its fluorescence both in solution and in solid state. A low frequency graphene-molecule coupled mode called "Mambo mode" has been demonstrated to appear in the Raman spectra of self-assembled molecules on graphene.

In chapter 4, we have described useful theoretical and experimental tools to predict and characterize plasmonic modes. We have experimentally determined the dispersion relation of a surface plasmon polariton propagating at the surface of a 40 nm thick gold waveguide. We have shown that the approach of Coulombic coupling between neighbor plasmon modes could enhance the quality factor of plasmonic modes.

Strong-coupling between a 30 nm thick self-assembled PTCDI-C7 layer and surface

plasmon polaritons propagating on a gold layer has been demonstrated in chapter 5. A 110 meV anti-crossing around the 560 nm absorption peak of PTCDI-C7 has been measured. Matrix-transfer computations have retrieved the absorption and emission response of the hybrid system. This strong-coupling regime has resulted from the high emitter density of the self-assembled gain medium and the orientation of the molecules inside the gain layer with respect to the electric field of the plasmon mode that have optimized the interaction between the gain medium and the surface plasmon mode. Since the self-assembled PTCDI-C7 have shown an important Stokes shift, absorption and fluorescence spectra did not overlap and no anti-crossing has been observed in emission. Matrix-transfer simulations have shown that this behavior is consistent with the picture of dyes driving the electromagnetic field.

Theoretical considerations have shown that dye self-assemblies could surpass traditional optical gain media by one order of magnitude. However, we have demonstrated in chapter 6 that intermolecular interactions such as exciton-exciton recombination have lowered consequently the fluorescence quantum efficiency of the 30 nm thick self-assembled PTCDI-C7 layer. Molecular building blocks should therefore be carefully designed to minimize such limiting interactions while keeping their self-assembling nature.

Synthèse

La miniaturisation des technologies optiques se heurte à la limite physique du confinement du champ électromagnétique à des échelles inférieures à la longueur d'onde. Cette limite pourrait être repoussée en étendant aux échelles optiques les antennes et guides métalliques utilisés pour les ondes Hertziennes. Ce nouveau domaine de l'optique, appelé plasmonique, ouvre la perspective du développement de nano-lasers par association d'un milieu optiquement actif à un résonateur plasmonique.

Toutefois, la distribution spatiale du champ électrique très spécifique des modes plasmoniques impose de nouvelles contraintes sur les milieux à gain. Les milieux optiquement actifs classiques doivent être repensés pour permettre le développement de nano-dispositifs optiques efficaces.

Dans cette thèse, nous explorons les possibilités d'utiliser les auto-assemblages supramoléculaires, dont les propriétés photoniques sont peu connues, comme milieux optiquement actifs de nouvelle génération pour les technologies optiques à l'échelle sub-longueur d'onde.

Au chapitre 1, nous étudions l'absorption optique de monocouches de dérivés de pérylène auto-assemblés à la surface du graphène. Nous montrons que les propriétés optiques des auto-assemblages de colorants à deux dimensions sur le graphène dépendent des interactions intermoléculaires et des interactions colorant-graphène, et peuvent être variées en changeant la géométrie de l'assemblage du colorant sur le graphène. Nous montrons comment obtenir un auto-assemblage tridimensionnel de dérivés de pérylène optimisant une interaction possible avec un plasmon polariton de surface.

Le deuxième chapitre traite de la fluorescence de couches auto-assemblées sur graphène. La première fonctionnalisation fluorescente non covalente du graphène par une monocouche auto-assemblée de colorant est démontrée, grâce à l'utilisation de tectons Janus. La fluorescence des auto-assemblages tridimensionnels optimisés pour l'interaction avec des plasmons polaritons de surface est étudiée.

Dans le troisième chapitre, nous explorons les propriétés vibrationnelles des monocouches auto-assemblées sur le graphène par des calculs de théorie de la fonctionnelle de la densité et des expériences de spectroscopie Raman. Nous montrons l'apparition d'un mode vibrationnel couplé entre les molécules adsorbés sur le graphène et le graphène lui-même, que nous nommons le mode "Mambo".

Le chapitre quatre présente les techniques théoriques (simulation par transfert de matrice, constante diélectrique de matériaux hybrides) et expérimentales permettant de caractériser les plasmons polaritons de surface dans le but de réduire les pertes des résonateurs plasmoniques. Nous proposons une stratégie lors du design du résonateur pour optimiser le facteur de qualité de la résonance.

Nous démontrons dans le chapitre cinq un régime de couplage fort entre des plasmons polaritons de surface et un auto-assemblage tridimensionnel de colorant ayant un important déplacement de Stokes. Les propriétés photoniques du système couplé sont étudiées expérimentalement et théoriquement par sa réponse en absorption et en émission, notamment pour explorer les liens entre anti-croisements et déplacement de Stokes.

Enfin, le chapitre six présente les conditions théoriques permettant d'amplifier des

plasmons polaritons de surface, et compare les performances de gain atteignable par les systèmes auto-assemblés aux milieux à gain traditionnels. Les limitations sur le gain des couches auto-assemblées sont étudiées expérimentalement par des spectres de fluorescence résolus dans le temps ainsi que par la dépendance du spectre de fluorescence avec la puissance de pompage du milieu. D'importantes pertes liées aux recombinaisons exciton-exciton sont caractérisées à fort taux de pompage, limitant l'efficacité de ce nouveau milieu à gain. Un modèle prenant en compte les effets linéaires et non-linéaires permettant d'expliquer la dynamique de fluorescence ainsi que le comportement du signal de fluorescence avec la puissance de pompe est proposé.

Appendix A

Dipole-field interactions theoretical calculations

A.1 Frequency to local electric field shifts relation demonstration

In a 1D framework, we model the molecule by a moving electron cloud and a static positive charge cloud. The electron cloud is defined by a homogeneous linear partition of a charge density $\rho_c$and a mass density ρ_m with spatial extension L. The global neutrality of the molecule requires same characteristics for the positive charges cloud. (see figure A.1)

We consider that the displacement of the electron cloud is small in comparison to L. Local charges appear only at the extremity of the molecule, meaning this model leads to a condensator geometry where the electric field between the two charges E_{in} is constant.

We apply Newton's law on a slice δx of negative charges:

$$\rho_m \delta x \frac{d^2x}{dt^2} = -\rho_c \delta x E_{in}$$

Since the barycenter of positive charges does not move, we find the differential equation for the dipole moment μ:

$$\mu = \rho_c x L$$
$$\frac{d^2\mu}{dt^2} = -\frac{\rho_c^2 L}{\rho_m} E_{in}$$

The condensator approximation allow to write the electric field E_{in} in terms of dipole moment and others constants:

$$E_{in} = \frac{\sigma}{\epsilon_0 \epsilon_r} = \frac{\rho_c x}{\epsilon_0 \epsilon_r S} = \frac{\mu}{\epsilon_0 \epsilon_r V}$$

Where σ is the surface charge density at the extremity of the molecule, and $V = SL$ the specific volume of charges at the extremity of the molecule. In the following, we note: $\beta = \epsilon_0 \epsilon_r V$.

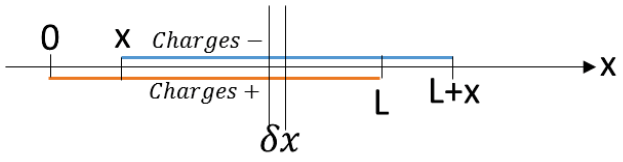

Figure A.1: 1D molecule model

The differential equation on the dipole moment can then be rewritten:

$$\frac{d^2\mu}{dt^2} = -\frac{\rho_c^2 L}{\rho_m \beta}\mu$$

Without any perturbation from the environment such as an incident electromagnetic wave or a retroaction of the environment through charge coupling, the electron cloud of the molecule is an harmonic oscillator with frequency $\omega_0 = \sqrt{\frac{\rho_c^2 L}{\rho_m \beta}}$

The differential equation on the dipole moment is modified with an incident electric field
$E_0 cos(\omega t)$ as the following:

$$\frac{d^2\mu}{dt^2} = -\frac{\rho_c^2 L}{\rho_m}(\frac{\mu}{\beta} + E_0 cos(\omega t))$$

We retrieve the usual lorentzian function for the dipole moment dependence on frequency:

$$\mu(t) = \mu_0(\omega) cos(\omega t)$$

$$\mu_0(\omega) = \frac{\rho_c^2 L}{\rho_m(\omega^2 - \omega_0^2)} E_0$$

If the environment produce a retroaction on the molecule creating the perturbative electric field $E_p = kE_{in}$ (where k can be complex to account for various delays in the retroaction), the harmonic oscillator have a shifted resonance frequency:

$$\omega_p^2 = (1 + k)\omega_0^2$$

The total electric field inside the molecule is in this case $E_p = E_{in} + kE_{in}$. The shifted resonance frequency ω_p can thus be related to the resonance frequency and the electric field for the lone molecule case as follow:

$$\frac{\omega_p}{\omega_0} = \sqrt{\frac{E_p}{E_{in}}}$$

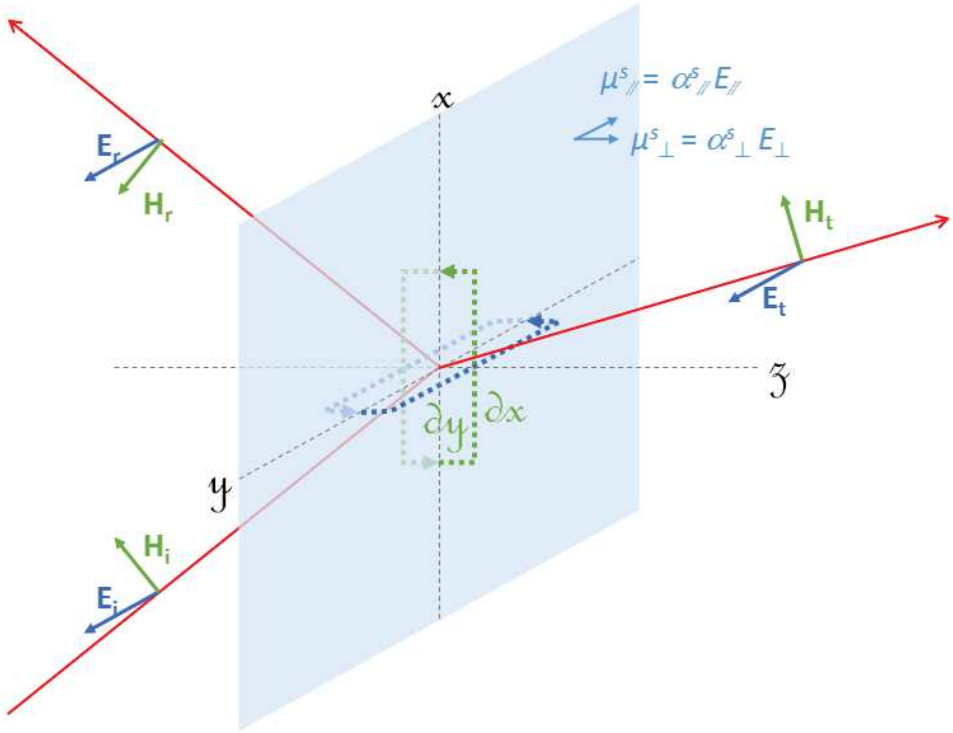

Figure A.2: Incident, reflected and transmitted electromagnetic fields on a molecular monolayer in a transverse electric configuration (TE).

A.2 Absorption of an oriented dipole monolayer

In this part, the reflection and transmission coefficients of a electromagnetic wave incident on a molecular monolayer are computed. Scheme A.2 describes the problem of the absorption of light by a molecular monolayer represented by polarizability α.

An incident electromagnetic $(\mathbf{E_i}, \mathbf{H_i}, \mathbf{k_i})$ field is directed onto the monolayer interface which transmits the field $(\mathbf{E_t}, \mathbf{H_t}, \mathbf{k_t})$ and reflects the field $(\mathbf{E_r}, \mathbf{H_r}, \mathbf{k_r})$.

A.2.1 Transverse electric polarization

The Maxwell-Faraday equation makes a link between the electric and the magnetic field:

$$\nabla \times \mathbf{E} = -\frac{\partial}{\partial t}\mathbf{B}$$

The electric field circulation on a path around the surface is null when the thickness t of the monolayer tends to 0.

$$\lim_{t \to 0} \int_0 \mathbf{E} \mathrm{dl} = 0$$

The contribution of the paths parallel to the surface is:

$$\int_{\parallel} \mathbf{E} \mathrm{dl} = E_1 \partial y - E_2 \partial y$$

The contribution of the paths perpendicular to the surface is null since $\mu_{\perp} = 0$. The equation on the electric field circulation then gives:

$$E_1 = E_2$$

The Maxwell-Ampere equation links the magnetic field to the electric displacement and the surface current:

$$\nabla \times \mathbf{H} = \mathbf{j} + \frac{\partial}{\partial t}\mathbf{D}$$

A surface current exists in the molecular monolayer:

$$\mathbf{j} = \frac{\partial}{\partial t}\mu = -i\omega\mu$$

Therefore, the circulation of magnetic field can be written:

$$\int_{\parallel} \mathbf{H}\mathrm{dl} = H_1\partial y - H_2\partial y = -i\omega\mu_{\parallel}\partial x$$

$$H_{2\parallel} - H_{1\parallel} = i\omega\mu_{\parallel}$$

Field continuity relationship can thus be written as:

$$E_i + E_r = E_t$$

$$H_i cos(\theta_1) - H_r cos(\theta_1) = H_t cos(\theta_2) - i\omega\mu_{\parallel}$$

For a plane wave propagating in the dielectric environment with refractive index n, the magnetic field continuity equation can be rewritten as:

$$E_i n_1 cos(\theta_1) - E_r n_1 cos(\theta_1) = E_t n_2 cos(\theta_2) - i\frac{\omega\alpha_{\parallel}}{\epsilon_0 c}E_t$$

Since the dipole moment is linked to the electric field by $mu\| = \alpha_{\parallel}E_t$.

The extended Fresnel coefficient is then:

$$\frac{E_t}{E_i} = \frac{2n_1 cos(\theta_1)}{n_2 cos(\theta_2) + n_1 cos(\theta_1) - i\frac{\omega\alpha_{\parallel}}{\epsilon_0 c}}$$

A.2.2 Transverse magnetic polarization

Scheme A.3 represents electromagnetic fields in the transverse magnetic (TM) polarization.

The electric field circulation by a parallel path to the surface can be written:

$$\int_{\parallel} \mathbf{E}\mathrm{dl} = E_{1\parallel}\partial x - E_{2\parallel}\partial x$$

The circulation by a perpendicular path is more complex. The interface thickness t is defined as the separation distance between two charged planes that are equivalent to the surface dipole distribution:

$$\mu_{\perp} = \sigma \mathrm{t}$$

Between these two planes, the electric field can be written:

$$E_{\mu_{\perp}} = \frac{\sigma}{\epsilon_0} = \frac{\mu_{\perp}}{2\epsilon_0 \mathrm{t}}$$

The electric field circulation is then calculated when the thickness tends to zero:

$$\int_0 \mathbf{E}\mathrm{dl} = \int_{\perp} \mathbf{E}\mathrm{dl} + \int_{\parallel} \mathbf{E}\mathrm{dl}$$

$$\lim_{\mathrm{t}\to 0} \int_{\perp} \mathbf{E}\mathrm{dl} = \frac{\mu_{perp}(x + \partial x}{\epsilon_0} - \frac{\mu_{perp}(x}{\epsilon_0}$$

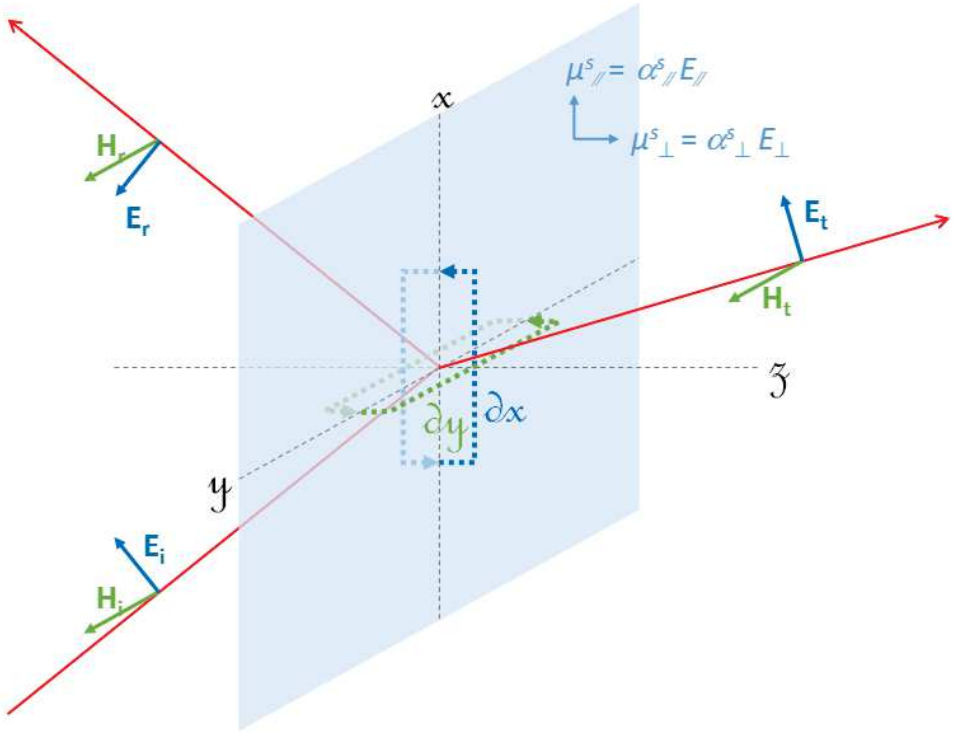

Figure A.3: Incident, reflected and transmitted electromagnetic fields on a molecular monolayer in a transverse magnetic configuration (TM).

Which simplifies to:

$$E_{2\|} - E_{1\|} = \frac{1}{\epsilon_0}\frac{\partial \mu_\perp(x)}{\partial x}$$

$$E_{2\|} - E_{1\|} = \frac{ik_x\mu_\perp}{\epsilon_0}$$

Surface current $\mathbf{j}$ exists and in the context of propagating plane wave at pulsation ω and this surface current can be written:

$$\mathbf{j} = \frac{\partial}{\partial t}\mu = -i\omega\mu$$

The circulation of magnetic field around the surface is then:

$$\int_0 \mathbf{H}\mathrm{d}\mathbf{l} = H_1\partial y - H_2\partial y = -i\omega\mu_\|\partial y$$

Continuity equations can be summarized:

$$E_{2\|} - E_{1\|} = \frac{ik_x\mu_\perp}{2\epsilon_0} = \frac{i\omega\mu_\perp}{\epsilon_0 c}n_2 sin(\theta_2)$$

$$H_2 - H_1 = i\omega\mu_\|$$

Since the electric field continuity equation depends on the dipolar moment $\mu_\perp$, one has to choose on which side of the interface the dipoles are located. If dipoles lay on the transmitted side, the continuity equation on the electric field can be written:

$$E_i cos(\theta_1) - E_r cos(\theta_1) = E_t cos(\theta_2) - \frac{i\omega\alpha_\perp}{\epsilon_0 c}n_2 (sin(\theta_2))^2 E_t$$

The resolution of the two equation system gives the extended Fresnel coefficient:

$$\frac{E_t}{E_i} = \frac{2\frac{cos(\theta_1)}{n_1}}{\frac{cos(\theta_1)}{n_1} + \frac{cos(\theta_2)}{n_2} - \frac{i\omega}{\epsilon_0 c n_2}(\frac{\alpha_\perp}{2} n_2 sin(\theta_2)^2 + \frac{\alpha_\parallel}{n_1} cos(\theta_1)cos(\theta_2))}$$

In the case of dipoles laying on the incident side of the surface, the electric field continuity equation and the Fresnel extended coefficient can be written:

$$E_i cos(\theta_1) - E_r cos(\theta_1) = E_t cos(\theta_2) - \frac{i\omega\alpha_\perp}{2\epsilon_0 c} n_2 sin(\theta_2)(E_i + E_r) sin(\theta_1)$$

$$\frac{E_t}{E_i} = \frac{2\frac{cos(\theta_1)}{n_1}}{\frac{cos(\theta_1)}{n_1} + \frac{cos(\theta_2)}{n_2} - \frac{i\omega}{\epsilon_0 c n_1}(\alpha_\perp n_2 sin(\theta_1)sin(\theta_2) - \frac{\alpha_\parallel}{n_2} cos(\theta_1)cos(\theta_2)) + \frac{\omega^2 \alpha_\perp \alpha_\parallel}{\epsilon_0^2 c^2 n_1} sin(\theta_2)sin(\theta_1)cos(\theta_2)}$$

Appendix B

Self-assembled systems on graphene absorption spectra

B.1 Table of experimental shifts and broadenings

Several supramolecular self-assemblies on graphene have been optically characterized by transmission absorption measurements. The principal absorption peak position and peak width in solution and self-assembled on graphene are synthetized in figure B.1. All of principal peaks are shifted to the red by a energy ranging from 50 to 500 meV when comparing the absorption of the self-assembled system on graphene to the same molecule diluted in a solution. Alternatively, the width of the principal peak is either increased or reduced depending on the system. The change in peak width (FWHM) ranges from -100 to 200 meV.

	Diluted in solution		Self-assembled on graphene		Peak shift : $\lambda_o g - \lambda_o s$		Peak broadening : $\Delta\lambda g - \Delta\lambda s$	
Molecule Name	$\lambda_o s$	$\Delta\lambda s$ (FWHM)	$\lambda_o g$	$\Delta\lambda g$ (FWHM)	(nm)	(meV)	(nm)	(meV)
PTCDI-C7	526	22	559	40	33	139	18	60
PTCDI-C8	526	22	560	40	34	143	18	60
PTCDI-C13	528	22	566	36	38	158	14	42
PTCDI-d	527	22	540	70	13	57	48	201
PTCDI-JT	528	20	540	64	12	52	44	184
TBC8	491	98	594	114	103	438	16	-89
TBC8-JT	495	88	536	116	41	192	28	56
P3DT	451	106	559	174	108	531	68	52
P3HT	453	102	570	154	117	562	52	-26
P3DDT	455	112	558	142	103	503	30	-106
P3PT-Br	450	104	540	152	90	459	48	14
P3DT-Br	438	116	540	172	102	535	56	13
P3PD-Br	452	108	564	152	112	545	44	-62
pCpT3	394	84	420	80	26	195	-4	-111
SQ-Bu2	638	20	684	40	46	131	20	45
PBDTTPD	532	104	582	108	50	200	4	-61

Figure B.1: Principal absorption peak position and width for various molecules diluted in a solution and self-assembled on graphene.

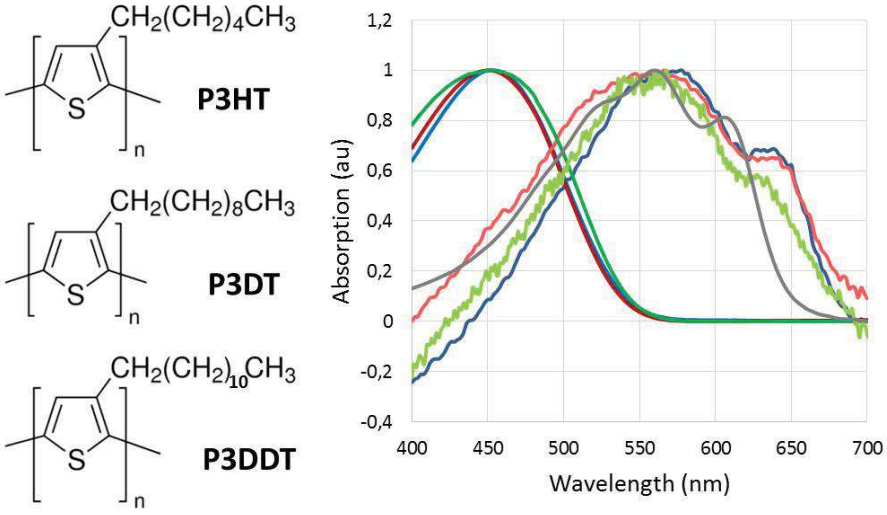

Figure B.2: Monomer molecular structure of polymers P3HT, P3DT and P3DDT. Transmission absorption spectra of P3HT (blue), P3DT (red) and P3DDT (green) diluted in a toluene solution (dark) and self-assembled on the graphene surface (light). The absorption spectrum of a P3HT microcrystal on a SiO2 substrate is also displayed in grey.

B.2 Polymers on graphene

Absorption spectra of polythiophene polymers P3HT, P3DT and P3DDT and polythiophene derivatives P3PT-Br, P3DT-Br and P3PDT-Br are displayed in figure B.2 and B.3. Once one the graphene surface, all polymer absorption spectra show an important $\sim 500\ meV$ redshift with reference to the absorption spectra taken with polymers diluted in a toluene solution. It is worth to note that most of the redshift should not result from interactions with the graphene surface since P3HT microcrystals on a glass substrate absorption spectrum displays the same shift to lower frequencies. (see figure B.2).

However, a difference exists when comparing the shoulder at 625 nm. First, absorption spectra of polymers on graphene display a 30 nm redshift with comparison to P3HT microcrystals. Second, the oscillator force of the 625 nm shoulder is decreased for polymers on graphene with reference to P3HT microcrystals. Interestingly, this shoulder is sensibly reduced for P3PT-Br, P3DT-Br and P3PDT-Br with comparison to the main absorption peak once on the graphene surface.

Density functional theory calculations have been performed to predict the effect of the polythiophene oligomer adsorption on a graphene surface on the polythiophene oligomer electronic density of states (DOS). Calculated DOS for P3HT and P3DT oligomer (10 monomers) in vacuum and adsorbed on a graphene surface are displayed in figure B.4. Calculated gaps for P3DT and P3HT oligomers are respectively 1.3 and 1.2 eV in vacuum. This result points out some imprecision with the calculation since absorption spectra in toluene solution show that the alkyl chain length do not interact with conjugated thiophene rings since absorption spectra peak at the same frequency for P3HT and P3DT. Once adsorbed on the graphene surface, figure B.4 shows that the electronic DOS is importantly modified. The calculation gives a 1.91 electron charge transfer from the P3HT oligomer to the graphene, representing 0.32% of the total number of valence electrons. As a result, for both calculated systems the whole DOS is shifted to higher energies. A 400 meV and 200 meV reduction of the HOMO-LUMO gap for P3DT and P3HT oligomers respectively accompanies the important modification of the DOS. The planarization of the polythiophene oligomer increasing the electron conjugation length could explain this effect. Our deposition technique needs to be improved to assure the formation of a polythiophene

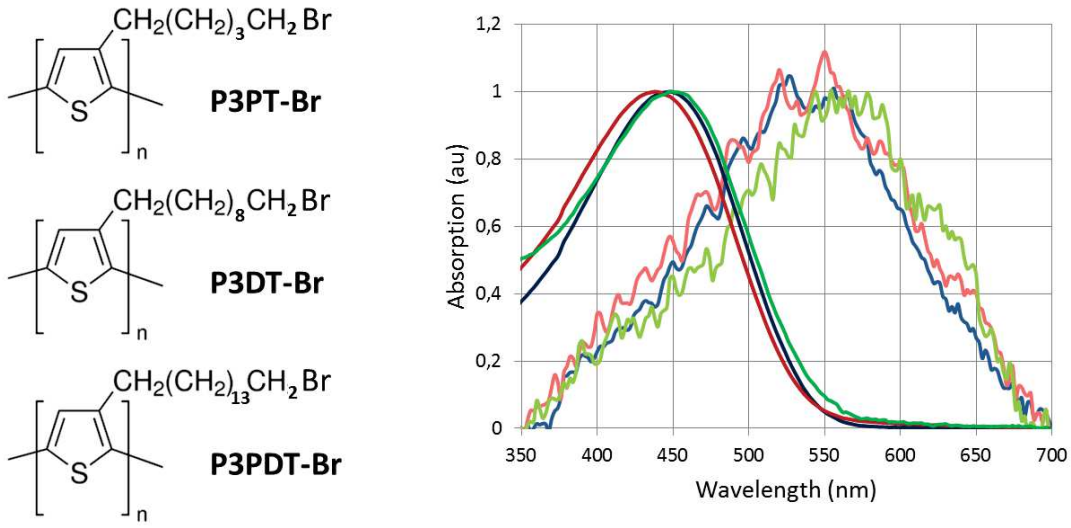

Figure B.3: Monomer molecular structure of polymers P3PT-Br, P3DT-Br and P3PDT-Br. Transmission absorption spectra of P3HT-Br (blue), P3DT-Br (red) and P3PDT-Br (green) diluted in a toluene solution (dark) and self-assembled on the graphene surface (light).

monolayer on the graphene surface detectable by transmission absorption spectroscopy. For now, we are not confident that a monolayer is formed therefore graphene-polythiophene interactions effects may be hidden by intermolecular interactions effects that have already been studied.[179]

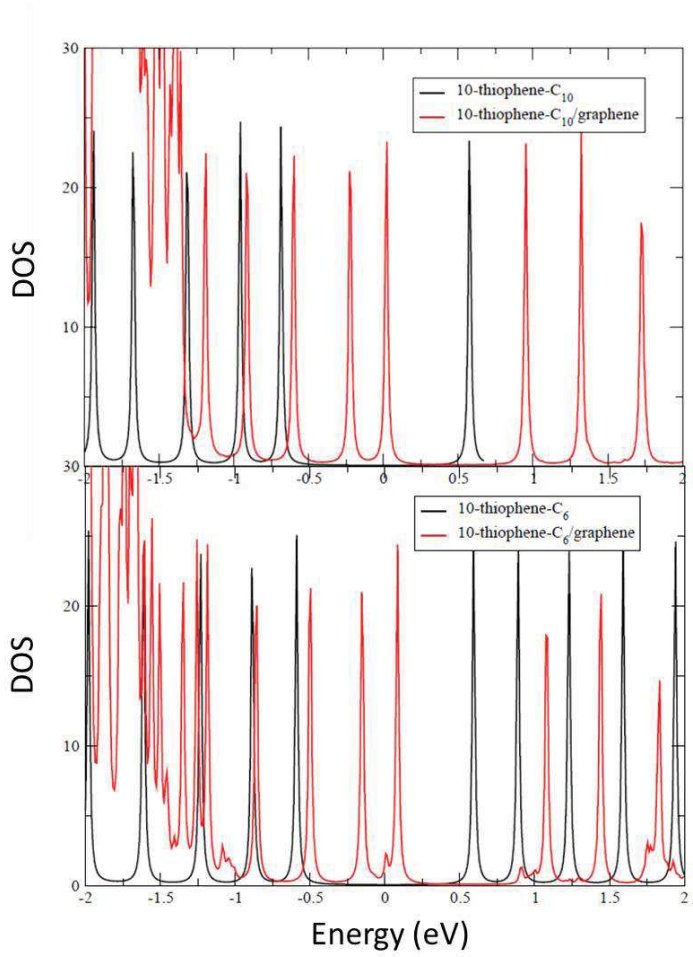

Figure B.4: Electronic density of states (DOS) for P3DT (top) and P3DT (bottom) oligomers (10 monomers) in vacuum (black) and adsorbed on a graphene surface.

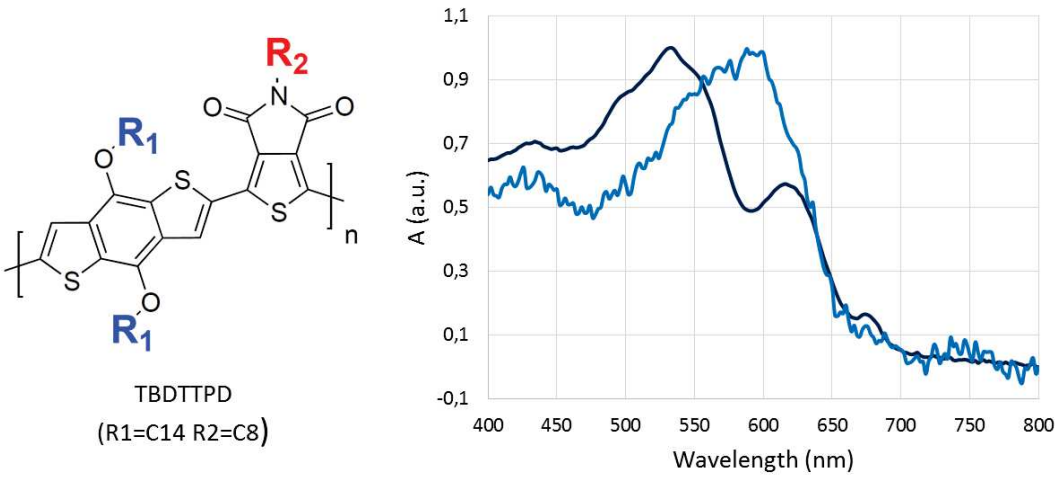

Figure B.5: Monomer molecular structure of PBDTTPD. Transmission absorption spectra diluted in a toluene solution (dark blue) and self-assembled on the graphene surface (light blue).

The optical absorption of PBDTTPD thin layer on graphene and in solution are displayed in figure B.5. The main absorption peak at 532 nm in solution is redshifted to 584 nm once on graphene, corresponding to a 208 meV redshift. Interestingly, the well-resolved structure at 616 nm present in the solution absorption spectrum disappears when the polymer is deposited on graphene.

B.3 Small molecules on graphene

Figure B.6 displays the absorption spectrum of a squaraine dye ($SQ-Bu_2$) drop casted on graphene. A 130 meV redshift of the principal absorption peak is observed accompanied by a 45 meV broadening of the peak. The idea is to find flat molecules to build multiple stacks of dye functionalized graphene. In a try to build such stacked system, it was not possible to reproduce this absorption spectrum and we obtained a much larger absorption peak that might result from the presence of aggregated molecules instead of adsorbed molecules on graphene.

Figure B.7 displays the absorption spectrum of a PTCDI derivative (PTCDI-d) on graphene. PTCDI-d carries a large dendron at one extremity and alkyl chain at the other extremity to try to lift the aromatic core from the graphene surface while retaining the molecule to the surface thanks to the alkyl chains present at the molecule extremity. The absorption spectrum is promising since the redshift of the 0-0 transition peak (528 nm in solution, 540 nm once on the graphene surface) is much lower than for other PTCDI derivatives such as PTCDI-C13, revealing lower interactions with the graphene surface (cf. Chapter 1). Further investigations should be done to precisely characterize the molecular self-assembly.

Figure B.8 displays the molecular structure and the absorption spectra of pCpT3 in a toluene solution and self-assembled on the graphene surface. The dye group of the molecule is separated from the graphene surface by a self-assembling pedestal group (cf Chapter 2) and a spacer group. This molecule has a very close structure from the TBC8-JT one. The same pedestal group is used, but the spacer group differs since a disulfur bridge is used in TBC8-JT. Finally, the pCpT3 dye group absorbs light in the 400 nm range whereas TBC8-JT absorbs light in the 500 nm range. A 195 meV redshift of the principal absorption peak is observed between pCpT3 diluted in a toluene solution and

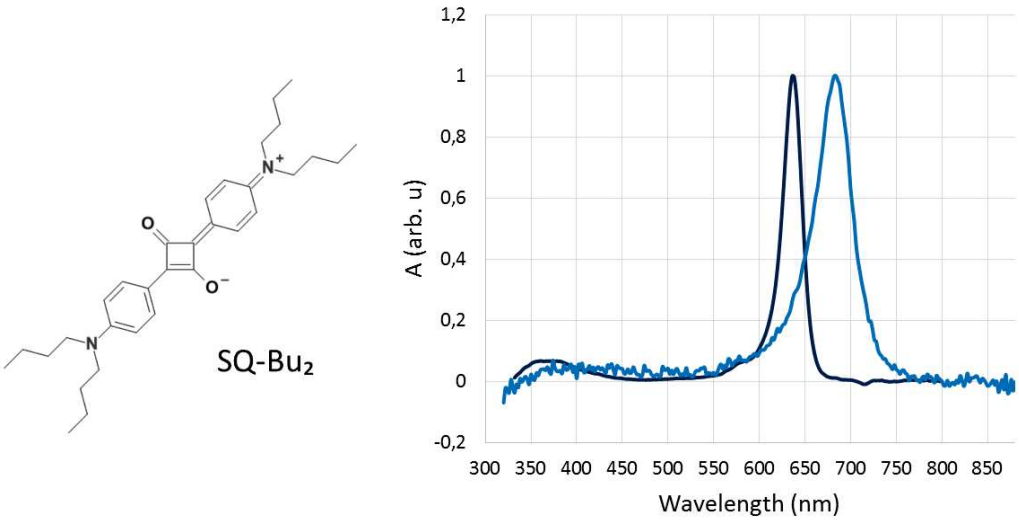

Figure B.6: Molecular structure of the squaraine dye $SQ - Bu_2$. $SQ - Bu_2$ transmission absorption spectrum diluted in a toluene solution (dark blue) and self-assembled on the graphene surface (light blue).

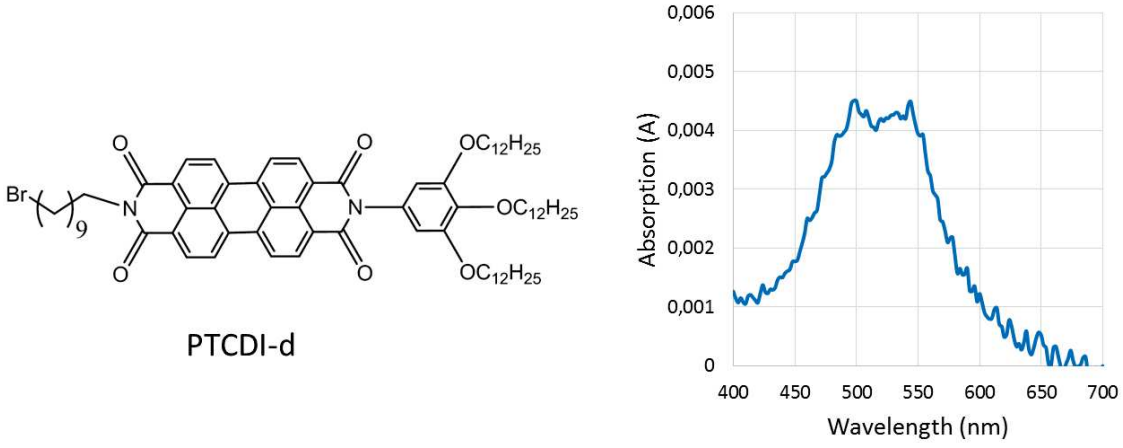

Figure B.7: Molecular structure of the perylene derivative dye PTCDI-d. PTCDI-d transmission absorption spectrum on the graphene surface.

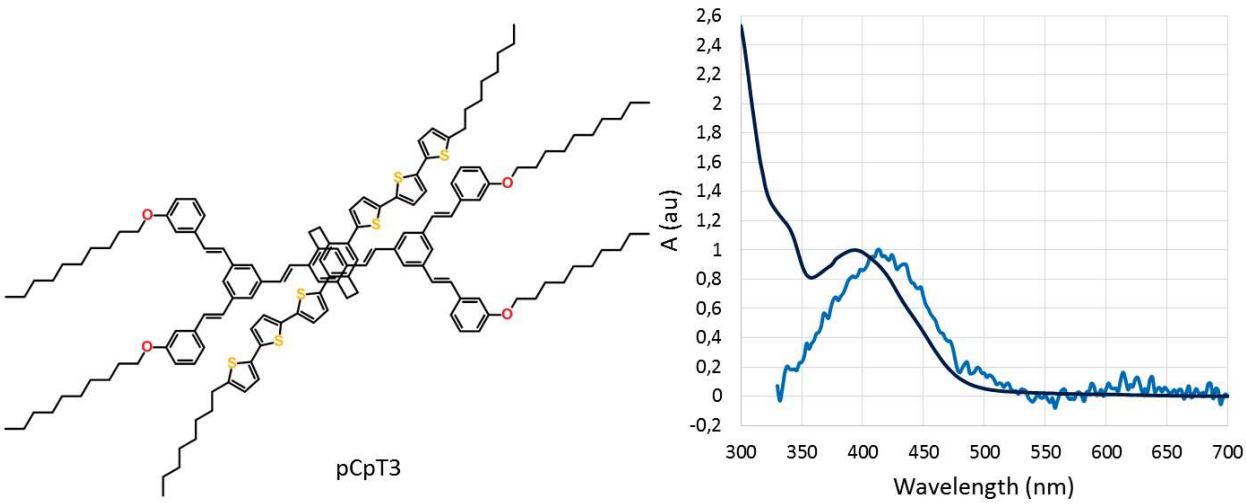

Figure B.8: Molecular structure of pCpT3. pCpT3 transmission absorption spectra diluted in a toluene solution (dark blue) and self-assembled on the graphene surface (light blue).

self-assembled on the graphene surface. It is surprisingly close to the 192 meV redshift obtained for the self-assembled TBC8-JT system.

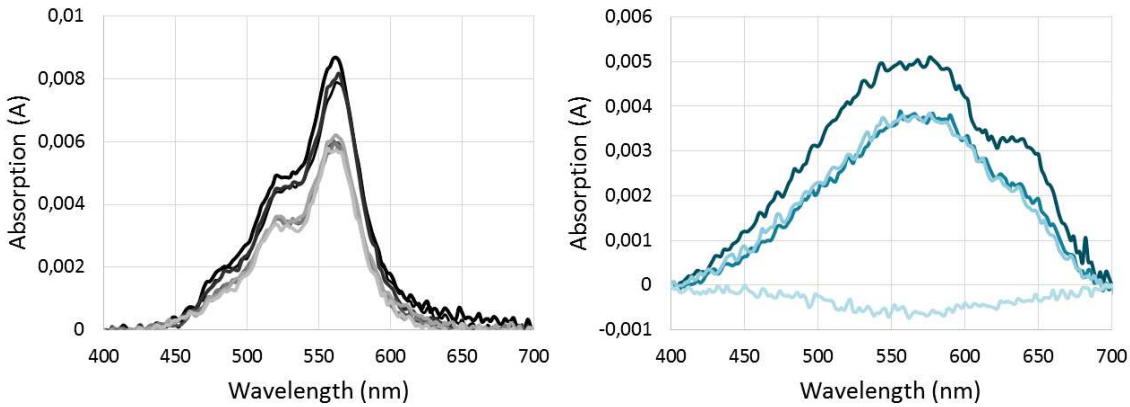

Figure B.9: Left. Absorption spectra for a self-assembled PTCDI-C13 monolayer on graphene after being placed at different temperature and pressure conditions. From dark black to light grey: (1) initial spectrum, (2) after 3h at 80°C, (3) after 3h at 80°C, (4) after 3d at 90°C, (5) after 3h at -20°C, (6) after 12h at $\sim 10^{-6}$ *mbar*, (7) after 12h at 90°C. Right. Absorption spectra for P3DT on graphene. From dark to light blue: (1) initial spectrum, (2) after 3h at 80°C, (3) after 3h at 80°C, (4) after 3d at 90°C.

B.4 Annealing effects on absorption spectra

Annealing effects have been explored for self-assembled PTCDI-C13 on graphene and P3DT deposited on the graphene surface. Figure B.9 displays the transmission absorption spectra for both systems after every different step. Samples were first placed for 3 hours at 80°C. Self-assembled PTCDI on graphene displayed a minor diminution of its absorption peak without disturbance of the spectrum. P3DT on graphene showed a 25% decrease of the peak absorption. A significant diminution of the shoulder at 625 nm is also visible after the annealing step revealing a shorter conjugation length (lower crystalline quality).[179] Samples are then placed a second time for 3 hours at a 80°C temperature. Absorption spectra are left unchanged. In a third step, samples were left at 90°C for three days. Figure B.9 shows that all P3DT material have been severely damaged during this annealing step since no visible absorption remains. The PTCDI-C13 self-assembly on graphene system displays a 25% decrease of the absorption spectrum after this step without any major redistribution of the absorption spectrum. Other steps are then tested on the PTCDI-C13 on graphene monolayer such as 12 hours at a $\sim 10^{-6}$ *mbar* pressure, -20°C for 3 hours and finally 90°C for 12 hours. Figure B.9 shows that the PTCDI-C13 on graphene absorption spectrum is left unchanged by these temperature and pressure conditions steps. These measures reveal an interesting stability for the PTCDI-C13 supramolecular network on graphene system.

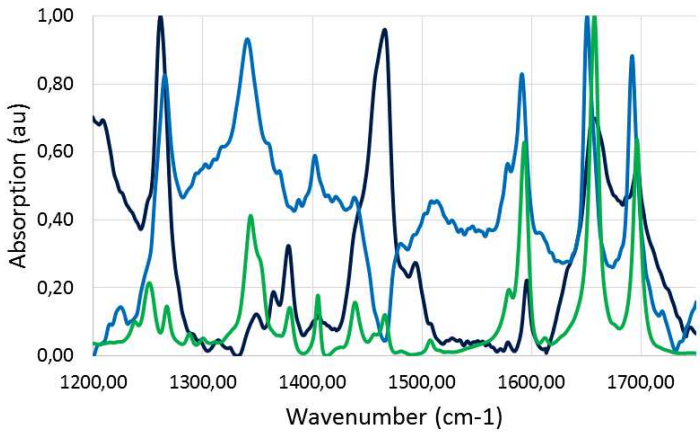

Figure B.10: FTIR spectra of PTCDI-C13 on graphene on quartz (light blue), evaporated on SiO2 (dark blue), and in KBr (green).

B.5 Vibrational spectra

B.5.1 PTCDI-C13 FTIR spectra

The infrared absorption spectrum of a self-assembled PTCDI-C13 on graphene on quartz, a mixture of PTCDI-C13 molecules and KBr and PTCDI-C13 microcrystals have been probed by FTIR. Spectra between 1200 cm^{-1} and 1750 cm^{-1} are displayed in figure B.10. All three spectra are different. Interestingly, PTCDI-C13 on graphene spectum displays some characteristics of both PTCDI-C13 on SiO2 and PTCDI-C13 in KBr spectra. For example, the 1260 cm^{-1} peak for PTCDI-C13 on graphene is also present in the PTCDI-C13 on SiO2 system, whereas it correspond to a doublet in the PTCDI-C13 in KBr spectrum. On the other side, the 1340 cm^{-1} PTCDI-C13 on graphene peak is also present in the PTCDI-C13 in KBr system spectrum whereas the PTCDI-C13 on SiO2 spectrum does not displays this resonance. Therefore, it seems that the self-assembled PTCDI-C13 on graphene displays vibrational modes corresponding either to an aggregated (PTCDI-C13 microcrystals on SiO2) or to an isolated state (PTCDI-C13 in KBr). This might correspond to in-plane or out-of-plane PTCDI-C13 resonance that are affected or not by the graphene presence.

B.5.2 Self-assembled TSB on graphene Raman spectra

Raman spectra of self-assembled TSB-C8 and TSB-C12 on graphene are displayed in figure B.11. At the exciting wavelength of 532 nm the TSB molecules do not absorb light. Therefore, the exciting radiation is mainly absorbed in the graphene layer and the experiment probes the properties of functionalized graphene by the TSB self-assembly. Raman spectra show that no new vibrational modes appear with this non-covalent functionalization. However, a broad peak in the 1000-1600 cm^{-1} range seems to appear. Interestingly, this broad peak seems to deplete the 2D peak, as it is the case for the D peak at 1350 cm^{-1} when defects are present in the graphene layer or for the 1440 cm^{-1} peak of non-resonant BS-C10 self-assembled on the graphene surface. Therefore, the TSB molecules adsorbed on graphene hybrid system do not seem to display a Raman active coupled vibrational mode. This can result from the symmetry of such possible mode that might result in a IR active mode uniquely. This can also results from the non-existence of the coupled mode since the alkyl chains at the extremity of the TSB molecule that are responsible from the adsorption on graphene may constrain the motion of the aromatic core above the graphene

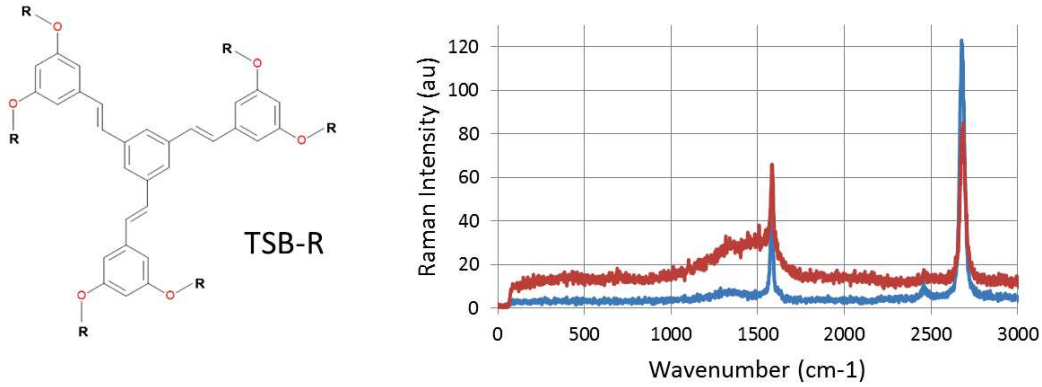

Figure B.11: Molecular structure of the TSB-R molecule ($R = C_8H_{17}$ or $R = C_{12}H_{25}$). Raman spectra of self-assembled TSB-C8 (blue) and TSB-C12 (red) self-assembled on the graphene surface.

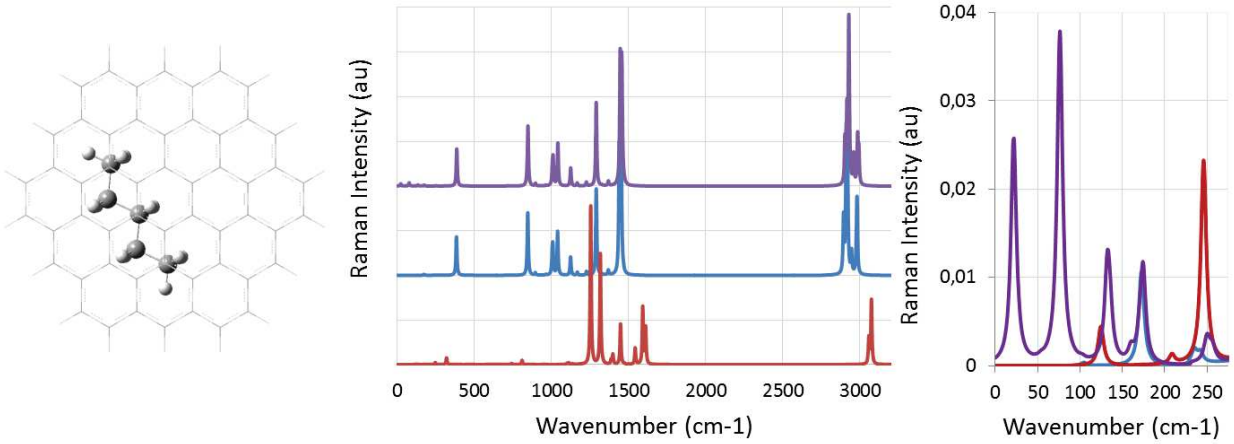

Figure B.12: Left. Adsorption of pentane on circumcoronene in a Groszek model.[?] Center. DFT calculated Raman spectra of circumcoronene in vacuum (red), pentane in vacuum (blue) and pentane adsorbed on circumcoronene (violet). The circumcoronene spectrum has been divided by 200 for clarity. Right. Zoom in the low frequency region of the DFT calculated Raman spectra.

surface.

DFT calculations have been performed with a pentane alkyl chain either isolated in vacuum or adsorbed on a circumcoronene molecule in a Groszek configuration[180] to model the adsorption of an alkyl chain on the graphene surface. Figure B.12 displays the Raman spectra obtained by these DFT calculations. Interestingly, three low-frequency mambo modes appear at 22, 76 and133 cm^{-1}. The non-resonant experiment of TSB on graphene should be able to reveal these modes since there should be coupled modes. However, the Raman intensity of these low frequency modes is quite low in comparison to the naphthalene on circumcoronene system. Furthermore, the flexibility of the alkyl chain could result in important inhomogeneous broadening of the coupled vibrations that might blurs resulting Raman peaks.

B.6 Gold nanoparticles coupled to SAM on the graphene surface

A gold thin film (6 nm thickness) has been evaporated on graphene, SiO2 and ITO on SiO2 to probe the formation of non-continuous gold films on these surfaces since the percolation thickness is usually larger ($\sim$ 20 nm). A scanning electron microscope image displayed in figure B.13 reveals the formation of well-defined gold nanoparticles on the graphene surface with radius ranging from 50 nm to 150 nm. Absorption spectra of the evaporated gold film on each systems is displayed in figure B.13. The absorption spectrum of the gold thin film on graphene peaks at 620 nm revealing a low aspect ratio (close to 1). Furthermore, the observed resonance width ($\Delta\lambda = 160\ nm = 510 mev$) indicates a high degree of homogeneity in the shape distribution of the gold nanoparticles.

PTCDI-C13 molecules have been deposited on the gold on graphene sample and then rinsed with toluene. Surprisingly, the transmission absorption spectrum of the new sample reveals a blue shift of the local plasmon resonance. From 620 nm without any molecules, it has been shifted to 595 nm. Considering the polarizability of the nanosphere in the electrostatic approximation (nanosphere radius ¡ 50 nm):[147]

$$\alpha(\omega) = 4\pi R^3 \frac{\epsilon_m - \epsilon_d}{\epsilon_m + 2\epsilon_d}$$

and the real part of the gold dielectric constant function of the frequency, a redshift should have been expected with the deposition of molecules that increases the dielectric constant of the environment. The peak width is still on the order of 500 meV.

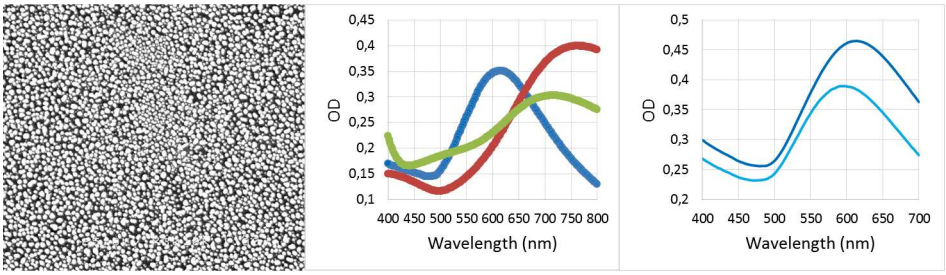

Figure B.13: 6 nm thick gold films evaporated simultaneously on a graphene, a SiO2 and a ITO on SiO2 substrate. Left MEB image of the gold thin film deposited on graphene. Center: Transmission absorption spectra of the gold thin film on graphene (blue), SiO2 (green) and ITO on SiO2 (red). Transmission absorption spectra of the gold thin film on graphene (dark blue) and the same gold thin film on graphene where PTCDI-C13 molecules have been self-assembled at the graphene surface between the gold nanoparticles.

Appendix C

Experimental methods

C.1 Materials

C.1.1 Graphene

The HOPG sample grade ZYB was purchased from SPI and the monolayer CVD graphene transferred onto transparent PET and fused silica samples were purchased from Megan-Technologies (Poland), Graphenea (Spain), and Graphene Supermarket (USA). Both have been transferred from their copper CVD substrate using the standard PMMA technique.[181] The CVD graphene is polycrystalline, with typically $1\mu m$ sized 2D domains. The PET/silica coverage by CVD graphene is ca. 95%. Suspended graphene on TEM grids were purchased from Graphene Supermarket (https://graphene-supermarket.com/).

C.1.2 Perylene derivatives

N,N'-Ditridecylperylene-3,4,9,10-tetracarboxylic diimide (PTCDI-C13), 2,9-Dihexylanthra[2,1,9-def:6,5,10-d'e'f']diisoquinoline-1,3,8,10(2H,9H)tetrone (PTCDI-C6), 2,9-Diheptylanthra[2,1,9-def:6,5,10-d'e'f']diisoquinoline-1,3,8,10(2H,9H)tetrone (PTCDI-C7),N,N'-Bis(1-hexylheptyl)-perylene-3,4:9,10-bis-(dicarboximide) (PTCDI-2C6), N,N'-Bis(2,5-di-tert-butylphenyl)-3,4,9,10-perylenedicarboximide (PTCDI-tBuPh), were purchased from Sigma-Aldrich and used as received. A phenyloctane (99%, Chemos GmbH) solvent was used for liquid–solid STM experiments and toluene (99.9%, Sigma-Aldrich) for monolayer depositions by drop casting or dip coating. All other molecules have been synthesized.

C.2 Deposition techniques

For drop-casting experiments, the concentrations were adjusted so that the applied $5\mu L$ droplet contains the quantity of molecules contained in a monolayer covering the entire $1cm^2$ substrate, given the monolayer surface-density measured by STM ($0.45 molecule per nm^2$). This target concentration evaluates to about $1.5 \times 10^{-5}\ mol\ L^{-1}$ and was adjusted with absorption spectroscopy applying the Beer-Lambert law with a molar absorptivity of $\epsilon = 87000\ L.mol^{-1}.cm^{-1}$ for various alkylated PTCDI [34]. For dip-coating experiments, the samples were immersed for 1 min in a toluene solution with the same concentration as for drop casting, and then gently rinsed with neat toluene for typically 5 min. The transferred monolayer CVD graphene remained unaltered even after prolonged immersion in toluene. Hence only the upper side of the graphene is exposed to the PTCDI solution. Molecular beam epitaxy have been performed at low deposition rate $\sim 300\ s/nm$ on heated substrates in vacuum ($\sim 10^{-6}\ mbar$). The deposition rate was measured with a quartz balance and the substrate temperature by a thermocouple.

C.3 STM experiments

The STM images were recorded under ambient conditions (ca. 300 K) with a custommade digital system by the immersion of a 250 μm mechanically cut tip of Pt/Ir (90/10) purchased from Goodfellow into a 5 μL droplet of solution. The scanning piezoelectric ceramic was calibrated by means of atomic resolution obtained on HOPG images in XY-directions and with flame annealed gold through the height of steps in the Z-direction. All the images were obtained at a quasi-constant current, i.e., in the variable-height mode. The images were corrected for the thermal drift by combining two successive images with downward and upward slow-scan directions.

C.4 Optical characterization

C.4.1 Absorption spectra

Optical absorption spectra at normal incidence were obtained with a Perkin-Elmer Lambda 650 spectrometer. Optical microspectroscopy was adapted on an Olympus IX71 microscope equipped with an Ocean Optics spectrometer QE-Pro. Variable incidence measurements were acquired on a custommade goniometer bench using the same spectrometer, by monitoring the absorption at its maximum.

C.4.2 Fluorescence spectra and lifetimes

Samples have been excited with a 532 nm continuous wave diode laser or a frequency doubled Ti:Sapphire femtosecond laser through an Olympus objective ($NA = 1.3$, $\times 100$, immersion oil), and a cooled Andor charge-coupled device (CCD) camera has been used to characterize the fluorescence signals. Lifetime measurements have been performed with a photon counting module (Hamamatsu MCP R3809U-50) and a triggering Si photodiode.

C.4.3 Raman spectra

Raman spectra were recorded on a Jobin Yvon Aramis Instrument. The sample was excited with a 532 nm CW diode laser through an Olympus objective ($NA = 0.9$, $\times$ 100).

C.5 Numerical computations

C.5.1 Molecular structure

Molecular mechanics calculations were performed with a chemical simulation software (Accelrys Discovery Dassault System BioVia).

C.5.2 DFT Calculations

All DFT calculations were performed using the Gaussian 09 set of programs in the gas phase employing the b3lyp functional with the 6-311+g(d,p) basis set. In the instances where two molecules are present in the same simulation, each molecule is assigned to a different layer by utilizing the oniom keyword.[182] In such simulations the molecule of spectroscopic interest is handled by the aforementioned functional and basis set, while the neighboring molecule is handled by the more computationally expedient uff molecular mechanics method.[183] For each computation, the molecules were first optimized and confirmed as minima during the frequency analysis. The optimal frequency scaling factor

of 0.9679 was applied to all computations, in accordance with prior analyses of the selected functional and method.[184]

Bibliography

[1] G. Binning, H. Rohrer, C. Gerber, and E. Weibel. Surface studies by scanning tunneling microscopy. *Physical Review Letters*, 49(1):57–61, 1982.

[2] G. Binnig, C. F. Quate, and C. Gerber. Atomic force microscope. *Physical Review Letters*, 56(9):930–933, 1986.

[3] D. W. Pohl, W. Denk, and M. Lanz. Optical stethoscopy - image recording with resolution lambda/20. *Applied Physics Letters*, 44(7):651–653, 1984.

[4] D. M. Eigler and E. K. Schweizer. Positioning single atoms with a scanning tunneling microscope. *Nature*, 344(6266):524–526, 1990.

[5] H. W. Kroto, J. R. Heath, S. C. Obrien, R. F. Curl, and R. E. Smalley. C-60 - buckminsterfullerene. *Nature*, 318(6042):162–163, 1985.

[6] A. Oberlin, M. Endo, and T. Koyama. Filamentous growth of carbon through benzene decomposition. *Journal of Crystal Growth*, 32(3):335–349, 1976.

[7] S. Iijima. Helical microtubules of graphitic carbon. *Nature*, 354(6348):56–58, 1991.

[8] K. S. Novoselov, A. K. Geim, S. V. Morozov, D. Jiang, Y. Zhang, S. V. Dubonos, I. V. Grigorieva, and A. A. Firsov. Electric field effect in atomically thin carbon films. *Science*, 306(5696):666–669, 2004.

[9] S. M. Kim, A. Hsu, M. H. Park, S. H. Chae, S. J. Yun, J. S. Lee, D. H. Cho, W. J. Fang, C. Lee, T. Palacios, M. Dresselhaus, K. K. Kim, Y. H. Lee, and J. Kong. Synthesis of large-area multilayer hexagonal boron nitride for high material performance. *Nature Communications*, 6, 2015.

[10] Z. C. He, C. M. Zhong, S. J. Su, M. Xu, H. B. Wu, and Y. Cao. Enhanced power-conversion efficiency in polymer solar cells using an inverted device structure. *Nature Photonics*, 6(9):591–595, 2012.

[11] L. T. Qu, Y. Liu, J. B. Baek, and L. M. Dai. Nitrogen-doped graphene as efficient metal-free electrocatalyst for oxygen reduction in fuel cells. *Acs Nano*, 4(3):1321–1326, 2010.

[12] B. J. Landi, M. J. Ganter, C. D. Cress, R. A. DiLeo, and R. P. Raffaelle. Carbon nanotubes for lithium ion batteries. *Energy and Environmental Science*, 2(6):638–654, 2009.

[13] C. G. Qiu, Z. Y. Zhang, M. M. Xiao, Y. J. Yang, D. L. Zhong, and L. M. Peng. Scaling carbon nanotube complementary transistors to 5-nm gate lengths. *Science*, 355(6322):271–+, 2017.

[14] S. Bae, H. Kim, Y. Lee, X. F. Xu, J. S. Park, Y. Zheng, J. Balakrishnan, T. Lei, H. R. Kim, Y. I. Song, Y. J. Kim, K. S. Kim, B. Ozyilmaz, J. H. Ahn, B. H. Hong, and S. Iijima. Roll-to-roll production of 30-inch graphene films for transparent electrodes. *Nature Nanotechnology*, 5(8):574–578, 2010.

[15] F. Bonaccorso, Z. Sun, T. Hasan, and A. C. Ferrari. Graphene photonics and optoelectronics. *Nature Photonics*, 4(9):611–622, 2010.

[16] K. Minami, Y. Kasuya, T. Yamazaki, Q. M. Ji, W. Nakanishi, J. P. Hill, H. Sakai, and K. Ariga. Highly ordered 1d fullerene crystals for concurrent control of macroscopic cellular orientation and differentiation toward large-scale tissue engineering. *Advanced Materials*, 27(27):4020–4026, 2015.

[17] J. H. Shen, Y. H. Zhu, X. L. Yang, and C. Z. Li. Graphene quantum dots: emergent nanolights for bioimaging, sensors, catalysis and photovoltaic devices. *Chemical Communications*, 48(31):3686–3699, 2012.

[18] B. S. Wong, S. L. Yoong, A. Jagusiak, T. Panczyk, H. K. Ho, W. H. Ang, and G. Pastorin. Carbon nanotubes for delivery of small molecule drugs. *Advanced Drug Delivery Reviews*, 65(15):1964–2015, 2013.

[19] J. P. Zhao, W. C. Ren, and H. M. Cheng. Graphene sponge for efficient and repeatable adsorption and desorption of water contaminations. *Journal of Materials Chemistry*, 22(38):20197–20202, 2012.

[20] A. D. Smith, F. Niklaus, A. Paussa, S. Vaziri, A. C. Fischer, M. Sterner, F. Forsberg, A. Delin, D. Esseni, P. Palestri, M. Ostling, and M. C. Lemme. Electromechanical piezoresistive sensing in suspended graphene membranes. *Nano Letters*, 13(7):3237–3242, 2013.

[21] K. Huang, G. P. Liu, Y. Y. Lou, Z. Y. Dong, J. Shen, and W. Q. Jin. A graphene oxide membrane with highly selective molecular separation of aqueous organic solution. *Angewandte Chemie-International Edition*, 53(27):6929–6932, 2014.

[22] L. L. Chang, Y. K. Choi, D. W. Ha, P. Ranade, S. Y. Xiong, J. Bokor, C. M. Hu, and T. J. King. Extremely scaled silicon nano-cmos devices. *Proceedings of the Ieee*, 91(11):1860–1873, 2003.

[23] L. Zang, Y. K. Che, and J. S. Moore. One-dimensional self-assembly of planar pi-conjugated molecules: Adaptable building blocks for organic nanodevices. *Accounts of Chemical Research*, 41(12):1596–1608, 2008.

[24] J. V. Barth, G. Costantini, and K. Kern. Engineering atomic and molecular nanostructures at surfaces. *Nature*, 437(7059):671–679, 2005.

[25] J. P. Zheng, J. J. Birktoft, Y. Chen, T. Wang, R. J. Sha, P. E. Constantinou, S. L. Ginell, C. D. Mao, and N. C. Seeman. From molecular to macroscopic via the rational design of a self-assembled 3d dna crystal. *Nature*, 461(7260):74–77, 2009.

[26] F. Charra and J. Cousty. Surface-induced chirality in a self-assembled monolayer of discotic liquid crystal. *Physical Review Letters*, 80(8):1682–1685, 1998.

[27] S. Griessl, M. Lackinger, M. Edelwirth, M. Hietschold, and W. M. Heckl. Self-assembled two-dimensional molecular host-guest architectures from trimesic acid. *Single Molecules*, 3(1):25–31, 2002.

[28] C. A. Palma, J. Bjork, M. Bonini, M. S. Dyer, A. Llanes-Pallas, D. Bonifazi, M. Persson, and P. Samori. Tailoring bicomponent supramolecular nanoporous networks: Phase segregation, polymorphism, and glasses at the solid-liquid interface. *Journal of the American Chemical Society*, 131(36):13062–13071, 2009.

[29] K. Tahara, S. Furukawa, H. Uji-I, T. Uchino, T. Ichikawa, J. Zhang, W. Mamdouh, M. Sonoda, F. C. De Schryver, S. De Feyter, and Y. Tobe. Two-dimensional porous molecular networks of dehydrobenzo 12 annulene derivatives via alkyl chain interdigitation. *Journal of the American Chemical Society*, 128(51):16613–16625, 2006.

[30] G. Schull, L. Douillard, C. Fiorini-Debuisschert, F. Charra, F. Mathevet, D. Kreher, and A. J. Attias. Single-molecule dynamics in a self-assembled 2d molecular sieve. *Nano Letters*, 6(7):1360–1363, 2006.

[31] D. Bleger, D. Kreher, F. Mathevet, A. J. Attias, G. Schull, A. Huard, L. Douillard, C. Fiorini-Debuischert, and F. Charra. Surface noncovalent bonding for rational design of hierarchical molecular self-assemblies. *Angewandte Chemie-International Edition*, 46(39):7404–7407, 2007.

[32] S. Kuhn, U. Hakanson, L. Rogobete, and V. Sandoghdar. Enhancement of single-molecule fluorescence using a gold nanoparticle as an optical nanoantenna. *Physical Review Letters*, 97(1), 2006.

[33] P. L. Stiles, J. A. Dieringer, N. C. Shah, and R. R. Van Duyne. Surface-enhanced raman spectroscopy. *Annual Review of Analytical Chemistry*, 1:601–626, 2008.

[34] W. L. Barnes, A. Dereux, and T. W. Ebbesen. Surface plasmon subwavelength optics. *Nature*, 424(6950):824–830, 2003.

[35] D. K. Gramotnev and S. I. Bozhevolnyi. Plasmonics beyond the diffraction limit. *Nature Photonics*, 4(2):83–91, 2010.

[36] J. N. Anker, W. P. Hall, O. Lyandres, N. C. Shah, J. Zhao, and R. P. Van Duyne. Biosensing with plasmonic nanosensors. *Nature Materials*, 7(6):442–453, 2008.

[37] J. Homola. Surface plasmon resonance sensors for detection of chemical and biological species. *Chemical Reviews*, 108(2):462–493, 2008.

[38] S. Kawata, Y. Inouye, and P. Verma. Plasmonics for near-field nano-imaging and superlensing. *Nature Photonics*, 3(7):388–394, 2009.

[39] L. R. Hirsch, R. J. Stafford, J. A. Bankson, S. R. Sershen, B. Rivera, R. E. Price, J. D. Hazle, N. J. Halas, and J. L. West. Nanoshell-mediated near-infrared thermal therapy of tumors under magnetic resonance guidance. *Proceedings of the National Academy of Sciences of the United States of America*, 100(23):13549–13554, 2003.

[40] S. A. Maier, M. L. Brongersma, P. G. Kik, S. Meltzer, A. A. G. Requicha, and H. A. Atwater. Plasmonics - a route to nanoscale optical devices. *Advanced Materials*, 13(19):1501–+, 2001.

[41] S. I. Bozhevolnyi, V. S. Volkov, E. Devaux, J. Y. Laluet, and T. W. Ebbesen. Channel plasmon subwavelength waveguide components including interferometers and ring resonators. *Nature*, 440(7083):508–511, 2006.

[42] H. A. Atwater and A. Polman. Plasmonics for improved photovoltaic devices. *Nature Materials*, 9(3):205–213, 2010.

[43] A. J. Haes and R. P. Van Duyne. A nanoscale optical blosensor: Sensitivity and selectivity of an approach based on the localized surface plasmon resonance spectroscopy of triangular silver nanoparticles. *Journal of the American Chemical Society*, 124(35):10596–10604, 2002.

[44] R. F. Oulton, V. J. Sorger, T. Zentgraf, R. M. Ma, C. Gladden, L. Dai, G. Bartal, and X. Zhang. Plasmon lasers at deep subwavelength scale. *Nature*, 461(7264):629–632, 2009.

[45] M. A. Noginov, G. Zhu, A. M. Belgrave, R. Bakker, V. M. Shalaev, E. E. Narimanov, S. Stout, E. Herz, T. Suteewong, and U. Wiesner. Demonstration of a spaser-based nanolaser. *Nature*, 460(7259):1110–U68, 2009.

[46] R. Carminati, J. J. Greffet, C. Henkel, and J. M. Vigoureux. Radiative and non-radiative decay of a single molecule close to a metallic nanoparticle. *Optics Communications*, 261(2):368–375, 2006.

[47] David Bleger, Fabrice Mathevet, David Kreher, Andre-Jean Attias, Amandine Bocheux, Sylvain Latil, Ludovic Douillard, Celine Fiorini-Debuisschert, and Fabrice Charra. Janus-like 3d tectons: Self-assembled 2d arrays of functional units at a defined distance from the substrate. *Angewandte Chemie-International Edition*, 50(29):6562–6566, 2011.

[48] D. Oelkrug, H. J. Egelhaaf, J. Gierschner, and A. Tompert. Electronic deactivation in single chains, nano-aggregates and ultrathin films of conjugated oligomers. *Synthetic Metals*, 76(1-3):249–253, 1996.

[49] E. G. McRae and M. Kasha. Enhancement of phosphorescence ability upon aggregation of dye molecules. *Journal of Chemical Physics*, 28(4):721–722, 1958.

[50] F. Wurthner, T. E. Kaiser, and C. R. Saha-Moller. J-aggregates: From serendipitous discovery to supramolecular engineering of functional dye materials. *Angewandte Chemie-International Edition*, 50(15):3376–3410, 2011.

[51] F. C. Spano. *Excitons in conjugated oligomer aggregates, films, and crystals*, volume 57 of *Annual Review of Physical Chemistry*, pages 217–243. Annual Reviews, Palo Alto, 2006.

[52] Frank C. Spano. The spectral signatures of frenkel polarons in h- and j-aggregates. *Accounts of Chemical Research*, 43(3):429–439, 2010.

[53] N. T. Fofang, T. H. Park, O. Neumann, N. A. Mirin, P. Nordlander, and N. J. Halas. Plexcitonic nanoparticles: Plasmon-exciton coupling in nanoshell-j-aggregate complexes. *Nano Letters*, 8(10):3481–3487, 2008.

[54] J. Dintinger, S. Klein, F. Bustos, W. L. Barnes, and T. W. Ebbesen. Strong coupling between surface plasmon-polaritons and organic molecules in subwavelength hole arrays. *Physical Review B*, 71(3):5, 2005.

[55] H. Fidder, J. Knoester, and D. A. Wiersma. Superradiant emission and optical dephasing in j-aggregates. *Chemical Physics Letters*, 171(5-6):529–536, 1990.

[56] V. V. Korolkov, S. A. Svatek, A. Summerfield, J. Kerfoott, L. X. Yang, T. Taniguchi, K. Watanabe, N. R. Champness, N. A. Besley, and P. H. Beton. van der waals-induced chromatic shifts in hydrogen-bonded two-dimensional porphyrin arrays on boron nitride. *Acs Nano*, 9(10):10347–10355, 2015.

[57] P. Suppan. Solvatochromic shifts - the influence of the medium on the energy of electronic states. *Journal of Photochemistry and Photobiology a-Chemistry*, 50(3):293–330, 1990.

[58] D. Markovitsi, N. Pfeffer, F. Charra, J. M. Nunzi, H. Bengs, and H. Ringsdorf. Charge-transfer complexes of discogenic molecules - a time-resolved study based on kerr ellipsometry. *Journal of the Chemical Society-Faraday Transactions*, 89(1):37–42, 1993.

[59] N. J. Hestand and F. C. Spano. Molecular aggregate photophysics beyond the kasha model: Novel design principles for organic materials. *Accounts of Chemical Research*, 50(2):341–350, 2017.

[60] C. Arrigoni, G. Schull, D. Bleger, L. Douillard, C. Fiorini-Debuisschert, F. Mathevet, D. Kreher, A. J. Attias, and F. Charra. Structure and epitaxial registry on graphite of a series of nanoporous self-assembled molecular monolayers. *Journal of Physical Chemistry Letters*, 1(1):190–194, 2010.

[61] Q. Y. Zhou, Y. B. Li, Q. Li, Y. B. Wang, Y. L. Yang, Y. Fang, and C. Wang. Switchable supramolecular assemblies on graphene. *Nanoscale*, 6(14):8387–8391, 2014.

[62] A. K. Geim and K. S. Novoselov. The rise of graphene. *Nature Materials*, 6(3):183–191, 2007.

[63] A. K. Geim. Graphene: Status and prospects. *Science*, 324(5934):1530–1534, 2009.

[64] Y. B. Zhang, Y. W. Tan, H. L. Stormer, and P. Kim. Experimental observation of the quantum hall effect and berry's phase in graphene. *Nature*, 438(7065):201–204, 2005.

[65] N. Petrone, C. R. Dean, I. Meric, A. M. van der Zande, P. Y. Huang, L. Wang, D. Muller, K. L. Shepard, and J. Hone. Chemical vapor deposition-derived graphene with electrical performance of exfoliated graphene. *Nano Letters*, 12(6):2751–2756, 2012.

[66] X. Wang, L. J. Zhi, and K. Mullen. Transparent, conductive graphene electrodes for dye-sensitized solar cells. *Nano Letters*, 8(1):323–327, 2008.

[67] T. Mueller, F. N. A. Xia, and P. Avouris. Graphene photodetectors for high-speed optical communications. *Nature Photonics*, 4(5):297–301, 2010.

[68] P. Matyba, H. Yamaguchi, G. Eda, M. Chhowalla, L. Edman, and N. D. Robinson. Graphene and mobile ions: The key to all-plastic, solution-processed light-emitting devices. *Acs Nano*, 4(2):637–642, 2010.

[69] Z. P. Sun, T. Hasan, F. Torrisi, D. Popa, G. Privitera, F. Q. Wang, F. Bonaccorso, D. M. Basko, and A. C. Ferrari. Graphene mode-locked ultrafast laser. *Acs Nano*, 4(2):803–810, 2010.

[70] B. Wang, X. Zhang, F. J. Garcia-Vidal, X. C. Yuan, and J. Teng. Strong coupling of surface plasmon polaritons in monolayer graphene sheet arrays. *Physical Review Letters*, 109(7), 2012.

[71] J. M. MacLeod and F. Rosei. Molecular self-assembly on graphene. *Small*, 10(6):1038–1049, 2014.

[72] B. Li, A. V. Klekachev, M. Cantoro, C. Huyghebaert, A. Stesmans, I. Asselberghs, S. De Gendt, and S. De Feyter. Toward tunable doping in graphene fets by molecular self-assembled monolayers. *Nanoscale*, 5(20):9640–9644, 2013.

[73] Ping Du, David Bleger, Fabrice Charra, Vincent Bouchiat, David Kreher, Fabrice Mathevet, and Andre-Jean Attias. A versatile strategy towards non-covalent functionalization of graphene by surface- confined supramolecular self-assembly of janus tectons. *Beilstein Journal of Nanotechnology*, 6:632–639, 2015.

[74] K. S. Mali, J. Greenwood, J. Adisoejoso, R. Phillipson, and S. De Feyter. Nanostructuring graphene for controlled and reproducible functionalization. *Nanoscale*, 7(5):1566–1585, 2015.

[75] J. M. MacLeod and F. Rosei. Molecular self-assembly on graphene. *Small*, 10(6):1038–1049, 2014.

[76] Z. X. Zhang, H. L. Huang, X. M. Yang, and L. Zang. Tailoring electronic properties of graphene by pi-pi stacking with aromatic molecules. *Journal of Physical Chemistry Letters*, 2(22):2897–2905, 2011.

[77] J. Park, W. H. Lee, S. Huh, S. H. Sim, S. B. Kim, K. Cho, B. H. Hong, and K. S. Kim. Work-function engineering of graphene electrodes by self-assembled monolayers for high-performance organic field-effect transistors. *Journal of Physical Chemistry Letters*, 2(8):841–845, 2011.

[78] X. M. Wang, J. B. Xu, W. G. Xie, and J. Du. Quantitative analysis of graphene doping by organic molecular charge transfer. *Journal of Physical Chemistry C*, 115(15):7596–7602, 2011.

[79] Qing Hua Wang and Mark C. Hersam. Nanofabrication of heteromolecular organic nanostructures on epitaxial graphene via room temperature feedback-controlled lithography. *Nano Letters*, 11(2):589–593, 2011.

[80] H. Yang, A. J. Mayne, G. Comtet, G. Dujardin, Y. Kuk, Ph Sonnet, L. Stauffer, S. Nagarajan, and A. Gourdon. Stm imaging, spectroscopy and manipulation of a self-assembled ptcdi monolayer on epitaxial graphene. *Physical Chemistry Chemical Physics*, 15(14):4939–4946, 2013.

[81] H. Ishii, K. Sugiyama, E. Ito, and K. Seki. Energy level alignment and interfacial electronic structures at organic metal and organic organic interfaces. *Advanced Materials*, 11(8):605–+, 1999.

[82] J. Hieulle and F. Silly. Localized intermolecular electronic coupling in two-dimensional self-assembled 3,4,9,10-perylenetetracarboxylic diimide nanoarchitectures. *Journal of Materials Chemistry C*, 1(30):4536–4539, 2013.

[83] Marco Gruenewald Roman Forker and Torsten Fritz. Optical differential reflectance spectroscopy on thin molecular films. *Annu. Rep. Prog. Chem., Sect. C: Phys. Chem.*, 108(34-68), 2012.

[84] H. Proehl, T. Dienel, R. Nitsche, and T. Fritz. Formation of solid-state excitons in ultrathin crystalline films of ptcda: From single molecules to molecular stacks. *Physical Review Letters*, 93(9):4, 2004.

[85] R. Forker, C. Golnik, G. Pizzi, T. Dienel, and T. Fritz. Optical absorption spectra of ultrathin ptcda films on gold single crystals: Charge transfer beyond the first monolayer. *Organic Electronics*, 10(8):1448–1453, 2009.

[86] T. U. Kampen, G. Salvan, M. Friedrich, D. A. Tenne, S. Park, and D. R. T. Zahn. Optical characterisation of ptcda films grown on passivated semiconductor substrates. *Applied Surface Science*, 166(1-4):387–391, 2000.

[87] T. Dienel, C. Loppacher, S. C. B. Mannsfeld, R. Forker, and T. Fritz. Growth-mode-induced narrowing of optical spectra of an organic adlayer. *Advanced Materials*, 20(5):959–+, 2008.

[88] M. Muller, A. Paulheim, A. Eisfeld, and M. Sokolowski. Finite size line broadening and superradiance of optical transitions in two dimensional long-range ordered molecular aggregates. *Journal of Chemical Physics*, 139(4):9, 2013.

[89] A. H. Schafer, C. Seidel, and H. Fuchs. The effect of annealing on the photoluminescence of epitaxial dme-ptcdi multilayers on ag(110). *Thin Solid Films*, 379(1-2):176–182, 2000.

[90] M. Meissner, M. Gruenewald, F. Sojka, C. Udhardt, R. Forker, and T. Fritz. Highly ordered growth of ptcda on epitaxial bilayer graphene. *Surface Science*, 606(21-22):1709–1715, 2012.

[91] Guillaume Schull, Herve Ness, Ludovic Douillard, Celine Fiorini-Debuisschert, Fabrice Charra, Fabrice Mathevet, David Kreher, and Andre-Jean Attiast. Atom substitution for marking and motion tracking of individual molecules by scanning tunneling microscopy. *Journal of Physical Chemistry C*, 112(36):14058–14063, 2008.

[92] Y. Kaneda, M. E. Stawasz, D. L. Sampson, and B. A. Parkinson. Stm investigations of the two-dimensional ordering of perylenetetracarboxylic acid n-alkyl-diimides on hopg and mos2 surfaces. *Langmuir*, 17(20):6185–6195, 2001.

[93] JW Verhoeven. Glossary of terms used in photochemistry (iupac recommendations 1996). *Pure and Applied Chemistry*, 68(12):2223–2286, 1996.

[94] A. E. Clark, C. Y. Qin, and A. D. Q. Li. Beyond exciton theory: A time-dependent dft and franck-condon study of perylene diimide and its chromophoric dimer. *Journal of the American Chemical Society*, 129(24):7586–7595, 2007.

[95] K. Balakrishnan, A. Datar, T. Naddo, J. L. Huang, R. Oitker, M. Yen, J. C. Zhao, and L. Zang. Effect of side-chain substituents on self-assembly of perylene diimide molecules: Morphology control. *Journal of the American Chemical Society*, 128(22):7390–7398, 2006.

[96] J. Mizuguchi and K. Tojo. Electronic structure of perylene pigments as viewed from the crystal structure and excitonic interactions. *Journal of Physical Chemistry B*, 106(4):767–772, 2002.

[97] T. Stauber, N. M. R. Peres, and A. K. Geim. Optical conductivity of graphene in the visible region of the spectrum. *Physical Review B*, 78(8):8, 2008.

[98] M. J. Dignam, M. Moskovits, and R. W. Stobie. Specular reflectance and ellipsometric spectroscopy of oriented molecular layers. *Transactions of the Faraday Society*, 67(587):3306–+, 1971.

[99] M. J. Dignam and M. Moskovites. Optical properties of sub-monolayer molecular films. *Journal of the Chemical Society-Faraday Transactions Ii*, 69(1):56–64, 1973.

[100] U. Heinemeyer, R. Scholz, L. Gisslen, M. I. Alonso, J. O. Osso, M. Garriga, A. Hinderhofer, M. Kytka, S. Kowarik, A. Gerlach, and F. Schreiber. Exciton-phonon coupling in diindenoperylene thin films. *Physical Review B*, 78(8), 2008.

[101] Frank C. Spano and Hajime Yamagata. Vibronic coupling in j-aggregates and beyond: A direct means of determining the exciton coherence length from the photoluminescence spectrum. *Journal of Physical Chemistry B*, 115(18):5133–5143, 2011.

[102] N. S. Bayliss and E. G. McRae. Solvent effects in organic spectra - dipole forces and the franck-condon principle. *Journal of Physical Chemistry*, 58(11):1002–1006, 1954.

[103] Cohen Claude Tannoudji, Diu Bernard, and Laloë Franck. Mécanique quantique. tome i. 1973.

[104] A. H. Castro Neto, F. Guinea, N. M. R. Peres, K. S. Novoselov, and A. K. Geim. The electronic properties of graphene. *Reviews of Modern Physics*, 81(1):109–162, 2009.

[105] Geraud Delport. *Non-convalent functionalization of carbon nanotubes: From the organization of surfactants to the self-assembly ofporphyrins.* PhD thesis, Université Paris-Saclay, 2016.

[106] X. Q. Tian, J. B. Xu, and X. M. Wang. Self-assembly of ptcda ultrathin films on graphene: Structural phase transition and charge transfer saturation. *Journal of Physical Chemistry C*, 114(49):20917–20924, 2010.

[107] A. J. Ferguson and T. S. Jones. Photophysics of ptcda and me-ptcdi thin films: Effects of growth temperature. *Journal of Physical Chemistry B*, 110(13):6891–6898, 2006.

[108] P. Jarvinen, S. K. Hamalainen, K. Banerjee, P. Hakkinen, M. Ijas, A. Harju, and P. Liljeroth. Molecular self-assembly on graphene on sio2 and h-bn substrates. *Nano Letters*, 13(7):3199–3204, 2013.

[109] C. Ludwig, B. Gompf, J. Petersen, R. Strohmaier, and W. Eisenmenger. Stm investigations of ptcda and ptcdi on graphite and mos2 - a systematic study of epitaxy and stm image-contrast. *Zeitschrift Fur Physik B-Condensed Matter*, 93(3):365–373, 1994.

[110] Ping Du, Maud Jaouen, Amandine Bocheux, Cyril Bourgogne, Zheng Han, Vincent Bouchiat, David Kreher, Fabrice Mathevet, Celine Fiorini-Debuisschert, Fabrice Charra, and Andre-Jean Attias. Surface-confined self-assembled janus tectons: A versatile platform towards the noncovalent functionalization of graphene. *Angewandte Chemie-International Edition*, 53(38):10060–10066, 2014.

[111] S. Le Liepvre, P. Du, D. Kreher, F. Mathevet, A. J. Attias, C. Fiorini-Debuisschert, L. Douillard, and F. Charra. Fluorescent self-assembled molecular monolayer on graphene. *Acs Photonics*, 3(12):2291–2296, 2016.

[112] F. Wurthner, C. R. Saha-Moller, B. Fimmel, S. Ogi, P. Leowanawat, and D. Schmidt. Perylene bisimide dye assemblies as archetype functional supramolecular materials. *Chemical Reviews*, 116(3):962–1052, 2016.

[113] J. P. Sun, A. D. Hendsbee, A. J. Dobson, G. C. Welch, and I. G. Hill. Perylene diimide based all small-molecule organic solar cells: Impact of branched-alkyl side chains on solubility, photophysics, self-assembly, and photovoltaic parameters. *Organic Electronics*, 35:151–157, 2016.

[114] P. R. L. Malenfant, C. D. Dimitrakopoulos, J. D. Gelorme, L. L. Kosbar, T. O. Graham, A. Curioni, and W. Andreoni. N-type organic thin-film transistor with high field-effect mobility based on a n,n-'-dialkyl-3,4,9,10-perylene tetracarboxylic diimide derivative. *Applied Physics Letters*, 80(14):2517–2519, 2002.

[115] L. C. Ma, Y. L. Guo, Y. G. Wen, Y. Q. Liu, and X. W. Zhan. High-mobility, air stable bottom-contact n-channel thin film transistors based on n,n '-ditridecyl perylene diimide. *Applied Physics Letters*, 103(20):4, 2013.

[116] Y. Zhong, M. T. Trinh, R. S. Chen, W. Wang, P. P. Khlyabich, B. Kumar, Q. Z. Xu, C. Y. Nam, M. Y. Sfeir, C. Black, M. L. Steigerwald, Y. L. Loo, S. X. Xiao, F. Ng, X. Y. Zhu, and C. Nuckolls. Efficient organic solar cells with helical perylene diimide electron acceptors. *Journal of the American Chemical Society*, 136(43):15215–15221, 2014.

[117] Y. Z. Lin and X. W. Zhan. Non-fullerene acceptors for organic photovoltaics: an emerging horizon. *Materials Horizons*, 1(5):470–488, 2014.

[118] R. D. Harcourt, K. P. Ghiggino, G. D. Scholes, and S. Speiser. On the origin of matrix elements for electronic excitation (energy) transfer. *Journal of Chemical Physics*, 105(5):1897–1901, 1996.

[119] C. Seidel, A. H. Schafer, and H. Fuchs. Oriented growth of dme-ptcdi on ag(110); an leed, xps. sfm and stm characterisation. *Surface Science*, 459(3):310–322, 2000.

[120] E. M. Purcell. Spontaneous emission probabilities at radio frequencies. *Physical Review*, 69(11-1):681–681, 1946.

[121] Q. Liu, Z. F. Liu, X. Y. Zhong, L. Y. Yang, N. Zhang, G. L. Pan, S. G. Yin, Y. Chen, and J. Wei. Polymer photovoltaic cells based on solution-processable graphene and p3ht. *Advanced Functional Materials*, 19(6):894–904, 2009.

[122] T. Sghaier, S. Le Liepvre, C. Fiorini, L. Douillard, and F. Charra. Optical absorption signature of a self-assembled dye monolayer on graphene. *Beilstein Journal of Nanotechnology*, 7:862–868, 2016.

[123] P. Anger, P. Bharadwaj, and L. Novotny. Enhancement and quenching of single-molecule fluorescence. *Physical Review Letters*, 96(11), 2006.

[124] A. Kasry, A. A. Ardakani, G. S. Tulevski, B. Menges, M. Copel, and L. Vyklicky. Highly efficient fluorescence quenching with graphene. *Journal of Physical Chemistry C*, 116(4):2858–2862, 2012.

[125] E. Dulkeith, A. C. Morteani, T. Niedereichholz, T. A. Klar, J. Feldmann, S. A. Levi, Fcjm van Veggel, D. N. Reinhoudt, M. Moller, and D. I. Gittins. Fluorescence quenching of dye molecules near gold nanoparticles: Radiative and nonradiative effects. *Physical Review Letters*, 89(20), 2002.

[126] D. Bleger, D. Kreher, F. Mathevet, A. J. Attias, G. Schull, A. Huard, L. Douillard, C. Fiorini-Debuischert, and F. Charra. Surface noncovalent bonding for rational design of hierarchical molecular self-assemblies. *Angewandte Chemie-International Edition*, 46(39):7404–7407, 2007.

[127] Ping Du, Maud Jaouen, Amandine Bocheux, Cyril Bourgogne, Zheng Han, Vincent Bouchiat, David Kreher, Fabrice Mathevet, Celine Fiorini-Debuisschert, Fabrice Charra, and Andre-Jean Attias. Surface-confined self-assembled janus tectons: A versatile platform towards the noncovalent functionalization of graphene. *Angewandte Chemie-International Edition*, 53(38):10060–10066, 2014.

[128] David Bleger, David Kreher, Fabrice Mathevet, Andre-Jean Attias, Imad Arfaoui, Germain Metge, Ludovic Douillard, Celine Fiorini-Debuisschert, and Fabrice Charra. Periodic positioning of multilayered 2.2 paracyclophane-based nanopillars. *Angewandte Chemie-International Edition*, 47(44):8412–8415, 2008.

[129] Hai-Feng Ji, Ravish Majithia, Xin Yang, Xiaohe Xu, and Karren More. Self-assembly of perylenedilmide and naphthalenediimide nanostructures on glass substrates through deposition from the gas phase. *Journal of the American Chemical Society*, 130(31):10056–+, 2008.

[130] S. R. Forrest. Ultrathin organic films grown by organic molecular beam deposition and related techniques. *Chemical Reviews*, 97(6):1793–1896, 1997.

[131] Jierong Cheng, Wei Li Wang, Hossein Mosallaei, and Efthimios Kaxiras. Surface plasmon engineering in graphene functionalized with organic molecules: A multiscale theoretical investigation. *Nano Letters*, 14(1):50–56, 2014.

[132] V. Bulovic, P. E. Burrows, S. R. Forrest, J. A. Cronin, and M. E. Thompson. Study of localized and extended excitons in 3,4,9,10-perylenetetracarboxylic dianhydride (ptcda) .1. spectroscopic properties of thin films and solutions. *Chemical Physics*, 210(1-2):1–12, 1996.

[133] S. R. Forrest. Ultrathin organic films grown by organic molecular beam deposition and related techniques. *Chemical Reviews*, 97(6):1793–1896, 1997.

[134] L. M. Malard, M. A. Pimenta, G. Dresselhaus, and M. S. Dresselhaus. Raman spectroscopy in graphene. *Physics Reports-Review Section of Physics Letters*, 473(5-6):51–87, 2009.

[135] Ryan Beams, Luiz Gustavo Cancado, and Lukas Novotny. Raman characterization of defects and dopants in graphene. *Journal of Physics-Condensed Matter*, 27(8), 2015.

[136] X. Ling, L. M. Xie, Y. Fang, H. Xu, H. L. Zhang, J. Kong, M. S. Dresselhaus, J. Zhang, and Z. F. Liu. Can graphene be used as a substrate for raman enhancement? *Nano Letters*, 10(2):553–561, 2010.

[137] G. Dent E. Smith. Modern raman spectroscopy: a practical approach. *John Wiley and Sons*, 2013.

[138] M. D. Williams, D. S. Bradshaw, and D. L. Andrews. Raman scattering mediated by neighboring molecules. *Journal of Chemical Physics*, 144(17):9, 2016.

[139] M. D. Williams, D. S. Bradshaw, and D. L. Andrews. Symmetry analysis of raman scattering mediated by neighboring molecules. *Journal of Chemical Physics*, 145(18):7, 2016.

[140] C. Rajesh, C. Majumder, H. Mizuseki, and Y. Kawazoe. A theoretical study on the interaction of aromatic amino acids with graphene and single walled carbon nanotube. *Journal of Chemical Physics*, 130(12):6, 2009.

[141] S. D. Chakarova-Kack, E. Schroder, B. I. Lundqvist, and D. C. Langreth. Application of van der waals density functional to an extended system: Adsorption of benzene and naphthalene on graphite. *Physical Review Letters*, 96(14):4, 2006.

[142] A. Srivastava and V. B. Singh. Theoretical and experimental studies of vibrational spectra of naphthalene and its cation. *Indian Journal of Pure and Applied Physics*, 45(9):714–720, 2007.

[143] R. S. Swathi and K. L. Sebastian. Resonance energy transfer from a dye molecule to graphene. *Journal of Chemical Physics*, 129(5), 2008.

[144] E. Zaborova, A. Six, H. Amokrane, F. Charra, F. Mathevet, A. J. Attias, and D. Kreher. Synthesis of new dithia 3.3 parapara-and metapara-cyclophane based tectons: toward an universal surface-confined 2d/3d molecular binding motif. *Pure and Applied Chemistry*, 88(10-11):1005–1025, 2016.

[145] P. Jouy, A. Vasanelli, Y. Todorov, A. Delteil, G. Biasiol, L. Sorba, and C. Sirtori. Transition from strong to ultrastrong coupling regime in mid-infrared metal-dielectric-metal cavities. *Applied Physics Letters*, 98(23), 2011.

[146] Y. Todorov, A. M. Andrews, R. Colombelli, S. De Liberato, C. Ciuti, P. Klang, G. Strasser, and C. Sirtori. Ultrastrong light-matter coupling regime with polariton dots. *Physical Review Letters*, 105(19), 2010.

[147] P. B. Johnson and R. W. Christy. Optical constants of noble metals. *Physical Review B*, 6(12):4370–4379, 1972.

[148] G. P. Puccioni and G. L. Lippi. Stochastic simulator for modeling the transition to lasing. *Optics Express*, 23(3):2369–2374, 2015.

[149] J David Jackson. *Electrodynamics*. Wiley Online Library, 1975.

[150] Max Born and Emil Wolf. *Principles of optics: electromagnetic theory of propagation, interference and diffraction of light*. Elsevier, 2013.

[151] E. M. Yeatman. Resolution and sensitivity in surface plasmon microscopy and sensing. *Biosensors and Bioelectronics*, 11(6-7):635–649, 1996.

[152] A. Hohenau, J. R. Krenn, A. Drezet, O. Mollet, S. Huant, C. Genet, B. Stein, and T. W. Ebbesen. Surface plasmon leakage radiation microscopy at the diffraction limit. *Optics Express*, 19(25):25749–25762, 2011.

[153] F. Wang and Y. R. Shen. General properties of local plasmons in metal nanostructures. *Physical Review Letters*, 97(20):4, 2006.

[154] Wei Zhou, Montacer Dridi, Jae Yong Suh, Chul Hoon Kim, Dick T. Co, Michael R. Wasielewski, George C. Schatz, and Teri W. Odom. Lasing action in strongly coupled plasmonic nanocavity arrays. *Nature Nanotechnology*, 8(7):506–511, 2013.

[155] G. Granet. Reformulation of the lamellar grating problem through the concept of adaptive spatial resolution. *Journal of the Optical Society of America a-Optics Image Science and Vision*, 16(10):2510–2516, 1999.

[156] N. Somaschi, V. Giesz, L. De Santis, J. C. Loredo, M. P. Almeida, G. Hornecker, S. L. Portalupi, T. Grange, C. Anton, J. Demory, C. Gomez, I. Sagnes, N. D. Lanzillotti-Kimura, A. Lemaitre, A. Auffeves, A. G. White, L. Lanco, and P. Senellart. Near-optimal single-photon sources in the solid state. *Nature Photonics*, 10(5):340–345, 2016.

[157] P. B. Deotare, T. S. Mahony, and V. Bulovic. Ultracompact low-threshold organic laser. *Acs Nano*, 8(11):11080–11085, 2014.

[158] K. M. Birnbaum, A. Boca, R. Miller, A. D. Boozer, T. E. Northup, and H. J. Kimble. Photon blockade in an optical cavity with one trapped atom. *Nature*, 436(7047):87–90, 2005.

[159] T. Volz, A. Reinhard, M. Winger, A. Badolato, K. J. Hennessy, E. L. Hu, and A. Imamoglu. Ultrafast all-optical switching by single photons. *Nature Photonics*, 6(9):605–609, 2012.

[160] L. C. Andreani, G. Panzarini, and J. M. Gerard. Strong-coupling regime for quantum boxes in pillar microcavities: Theory. *Physical Review B*, 60(19):13276–13279, 1999.

[161] T. Schwartz, J. A. Hutchison, C. Genet, and T. W. Ebbesen. Reversible switching of ultrastrong light-molecule coupling. *Physical Review Letters*, 106(19), 2011.

[162] D. E. Gomez, K. C. Vernon, P. Mulvaney, and T. J. Davis. Surface plasmon mediated strong exciton-photon coupling in semiconductor nanocrystals. *Nano Letters*, 10(1):274–278, 2010.

[163] A. I. Vakevainen, R. J. Moerland, H. T. Rekola, A. P. Eskelinen, J. P. Martikainen, D. H. Kim, and P. Torma. Plasmonic surface lattice resonances at the strong coupling regime. *Nano Letters*, 14(4):1721–1727, 2014.

[164] P. Torma and W. L. Barnes. Strong coupling between surface plasmon polaritons and emitters: a review. *Reports on Progress in Physics*, 78(1):013901 (34 pp.)–013901 (34 pp.), 2015.

[165] J. Bellessa, C. Bonnand, J. C. Plenet, and J. Mugnier. Strong coupling between surface plasmons and excitons in an organic semiconductor. *Physical Review Letters*, 93(3), 2004.

[166] P. M. Bolger, W. Dickson, A. V. Krasavin, L. Liebscher, S. G. Hickey, D. V. Skryabin, and A. V. Zayats. Amplified spontaneous emission of surface plasmon polaritons and limitations on the increase of their propagation length. *Optics Letters*, 35(8):1197–1199, 2010.

[167] D. J. Bergman and M. I. Stockman. Surface plasmon amplification by stimulated emission of radiation: Quantum generation of coherent surface plasmons in nanosystems. *Physical Review Letters*, 90(2), 2003.

[168] Y. H. Chen, J. F. Li, M. L. Ren, B. L. Wang, J. X. Fu, S. Y. Liu, and Z. Y. Li. Direct observation of amplified spontaneous emission of surface plasmon polaritons at metal/dielectric interfaces. *Applied Physics Letters*, 98(26):3, 2011.

[169] A. Marini, A. V. Gorbach, D. V. Skryabin, and A. V. Zayats. Amplification of surface plasmon polaritons in the presence of nonlinearity and spectral signatures of threshold crossover. *Optics Letters*, 34(18):2864–2866, 2009.

[170] C. A. Leatherdale, W. K. Woo, F. V. Mikulec, and M. G. Bawendi. On the absorption cross section of cdse nanocrystal quantum dots. *Journal of Physical Chemistry B*, 106(31):7619–7622, 2002.

[171] Jinjun Sun and Ewa M. Goldys. Linear absorption and molar extinction coefficients in direct semiconductor quantum dots. *Journal of Physical Chemistry C*, 112(25):9261–9266, 2008.

[172] J. K. Kitur, G. Zhu, and M. A. Noginov. Low-threshold stimulated emission of surface plasmons polaritons. *Journal of Optics*, 16(11), 2014.

[173] Mark I. Stockman. Nanoplasmonics: past, present, and glimpse into future. *Optics Express*, 19(22):22029–22106, 2011.

[174] S. Chenais and S. Forget. Recent advances in solid-state organic lasers. *Polymer International*, 61(3):390–406, 2012.

[175] D. Ding, K. Li, B. Liu, and B. Z. Tang. Bioprobes based on aie fluorogens. *Accounts of Chemical Research*, 46(11):2441–2453, 2013.

[176] V. G. Kozlov, V. Bulovic, P. E. Burrows, and S. R. Forrest. Laser action in organic semiconductor waveguide and double-heterostructure devices. *Nature*, 389(6649):362–364, 1997.

[177] B. Valeur. *Molecular Fluorescence*. Wiley-VCH Verlag GmbH. i., 2001.

[178] R. D. Xia, W. Y. Lai, P. A. Levermore, W. Huang, and D. D. C. Bradley. Low-threshold distributed-feedback lasers based on pyrene-cored starburst molecules with 1,3,6,8-attached oligo(9,9-dialkylfluorene) arms. *Advanced Functional Materials*, 19(17):2844–2850, 2009.

[179] Jenny Clark, Jui-Fen Chang, Frank C. Spano, Richard H. Friend, and Carlos Silva. Determining exciton bandwidth and film microstructure in polythiophene films using linear absorption spectroscopy. *Applied Physics Letters*, 94(16), 2009.

[180] A. J. Groszek. Selective adsorption at graphite/hydrocarbon interfaces. *Proceedings of the Royal Society of London Series a-Mathematical and Physical Sciences*, 314(1519):473, 1970.

[181] X. L. Liang, B. A. Sperling, I. Calizo, G. J. Cheng, C. A. Hacker, Q. Zhang, Y. Obeng, K. Yan, H. L. Peng, Q. L. Li, X. X. Zhu, H. Yuan, A. R. H. Walker, Z. F. Liu, L. M. Peng, and C. A. Richter. Toward clean and crackless transfer of graphene. *Acs Nano*, 5(11):9144–9153, 2011.

[182] S. Dapprich, I. Komaromi, K. S. Byun, K. Morokuma, and M. J. Frisch. A new oniom implementation in gaussian98. part i. the calculation of energies, gradients, vibrational frequencies and electric field derivatives. *Journal of Molecular Structure-Theochem*, 461:1–21, 1999.

[183] A. K. Rappe, C. J. Casewit, K. S. Colwell, W. A. Goddard, and W. M. Skiff. Uff, a full periodic-table force-field for molecular mechanics and molecular-dynamics simulations. *Journal of the American Chemical Society*, 114(25):10024–10035, 1992.

[184] M. P. Andersson and P. Uvdal. New scale factors for harmonic vibrational frequencies using the b3lyp density functional method with the triple-xi basis set 6-311+g(d,p). *Journal of Physical Chemistry A*, 109(12):2937–2941, 2005.

université PARIS-SACLAY | ÉCOLE DOCTORALE Ondes et Matière (EDOM)

Titre : Auto-assemblages supramoléculaires pour la plasmonique : une approche ascendante pour la réalisation de nano-systèmes photoniques efficaces.

Mots clés : Nanophotonique, auto-assemblages supramoléculaires, graphène, plasmonique, couplage fort

Résumé : Dans cette thèse, nous avons étudié les propriétés photoniques et vibrationnelles de monocouches moléculaires auto-assemblées sur graphène et la possibilité d'utiliser des multicouches auto-assemblées de pérylène comme milieu à gain pour l'amplification de plasmons. Le graphène, en tant que matériau transparent et conducteur, a permis pour la première fois de corréler la géométrie du réseau de l'auto-assemblage supramoléculaire avec ses propriétés optiques, grâce à la microscopie à effet tunnel et à des mesures de spectroscopiques optiques et Raman. En comparant plusieurs colorants auto-assemblés sur le graphène, nous avons mis en lumière les effets des interactions intermoléculaires et des interactions colorant-graphène sur le spectre d'absorption du colorant adsorbé. Le transfert d'énergie rapide des colorants vers la couche de graphène par les mécanismes de Förster et de Dexter empêche toute relaxation radiative du colorant.

Néanmoins, nous avons démontré la première fonctionnalisation fluorescente non-covalente du graphène par une monocouche de colorants auto-assemblée en mettant en place une stratégie à base d'espaceurs. Nous avons exploité l'extinction rapide de la fluorescence des colorants par le graphène pour étudier les spectres Raman des auto-assemblages moléculaires sur graphène, et nous avons révélé l'apparition d'un mode vibrationnel couplé entre les molécules adsorbées et le substrat de graphène. Nous avons démontré le régime de couplage fort entre un auto-assemblage tri-dimensionnel de pérylène et un plasmon polariton de surface en optimisant l'orientation et l'organisation des molécules de colorant par rapport au champ électrique du mode de plasmon. Nous avons prouvé que les milieux de gain auto-assemblés en agrégats-J peuvent théoriquement conduire à des milieux de gain efficaces pour l'amplification de plasmons. Cependant, nous avons révélé expérimentalement que les recombinaisons exciton-exciton limitent le taux de pompage à des fluences élevées dans ces milieux denses.

Title : Supramolecular self-assemblies for plasmonics : a bottom-up approach to efficient photonics nanodevices

Keywords : Nanophotonics, supramolecular self-assemblies, graphene, plasmonics, strong-coupling,

Abstract: In this work, we have studied the photonic and vibrational properties of self-assembled molecular monolayers on graphene and the possibility to use perylene self-assembled multilayers as a gain medium for plasmon amplification. Graphene, as a transparent and conductive material, has offered for the first time to correlate the self-assembly structure as deduced from scanning tunneling microscopy to photonic properties as analyzed by optical and Raman spectroscopy measurements.By comparing several self-assembled dyes on graphene we have shed light on how intermolecular and dye-graphene interactions modify the absorption spectrum of the adsorbed dye.Fast Förster and Dexter energy transfer from the adsorbed dyes to the graphene layer prevent any radiative decay of the dye. Nevertheless, we have demonstrated the first fluorescent non-covalent functionalization of graphene by a supramolecular self-assembled monolayer using a spacer approach.

We have exploited the fast dye fluorescence quenching by graphene to study Raman spectra of self-assembled dye on graphene, and we have shown the appearance of a coupled vibrational mode between the adsorbed molecules and the graphene substrate. We have demonstrated the strong-coupling regime between a three-dimensional perylene self-assembly and a propagating plasmon polariton by optimizing the orientation and the organisation of the dye molecules compared to the electric field of the plasmon mode. We have shown that J-aggregated self-assembled gain media may theoretically lead to efficient gain media for plasmon amplification. However, we experimentally demonstrated that exciton-exciton recombination limits the achievable pumping rate at high fluences in such dense media.

Université Paris-Saclay
Espace Technologique / Immeuble Discovery
Route de l'Orme aux Merisiers RD 128 / 91190 Saint-Aubin, France